Renner-Teller effects and Vibronic Coupling: Full-dimensional Nonadiabatic Dynamics of Linear carbon chains and Cyanobenzene

A thesis submitted during 2025 to the
University of Hyderabad
in partial fulfillment of the award of a Ph.D. degree in
School of Chemistry
by

Mamilwar Rani
(Reg. No. 18CHPH21)

Under the supervision of

Prof. Susanta Mahapatra

School of Chemistry

University of Hyderabad

Hyderabad – 500 046

Telangana

India

October – 2025

CERTIFICATE

This is to certify that the thesis entitled **"Renner-Teller Effects and Vibronic Coupling: Full-dimensional Nonadiabatic Dynamics of Linear carbon chains and Cyanobenzene"** submitted by **Mamilwar Rani** bearing Registration Number **18CHPH21** in partial fulfilment of the requirements for award of Doctor of Philosophy in the School of Chemistry is a bonafide work carried out by her under my supervision and guidance.

This thesis is free from Plagiarism and has not been submitted previously in part or in full to this or any other University or Institution for award of any degree or diploma.

Further, the student has the following publication before submission of the thesis/monograph for adjudication and has produced evidence for the same in the form of acceptance letter or the reprint in the relevant area of his research: (Note: At least one publication in referred journal is required)

1. Mamilwar Rani, Arun Kumar Kanakati and S. Mahapatra*, Photoionization Bands of Cyanogen: Multi-Mode Vibronic Coupling and Renner-Teller Effects, *ChemPhysChem*., **24**, e202200882(2023), (Chapter 3 in the Ph. D thesis).

and

has made presentations in the following conferences:

1. Poster presentation in 'DAE Symposium on Current Trends in Theoretical Chemistry (CTTC-2020)' Sep 2021, BARC, Mumbai, India.
2. Poster presentation in '17th Theoretical Chemistry Symposium (TCS-2021)', Dec 2021, IISER Kolkata, India.
3. Oral presentation in '20th Annual In-House Symposium CHEMFEST-2023.'
4. Poster presentation in 'Quantum System in Chemistry, Physics, and Biology (QSCP-XXVI)', Oct 2023, Ashoka University, India.
5. Attended workshop, 'MCTDH Summer School July-2023', Heidelberg, Germany.

Further, the student has passed the following courses towards fulfilment of coursework requirement for Ph.D. / was exempted from doing coursework (recommended by Doctoral Committee) on the basis of the following courses passed during his M.Phil. Program and the M.Phil. Degree was awarded:

Course	Code Name	Credits	Pass/Fail
1. Research Proposal	CY801	4	Pass
2. Instrumentation and Computer Applications Lab	CY802/507	4	Pass
3. Instrumental Methods-A	CY805	4	Pass
4. Instrumental Methods-B	CY806	4	Pass

Susanta Mahapatra
Senior Professor
School of Chemistry
University of Hyderabad
Hyderabad-500046, TS, India.

Supervisor

21/10/25

SCHOOL OF CHEMISTRY
University of Hyderabad
Hyderabad-500 046.

Head of the Department

Dean of School

DECLARATION

I Mamilwar Rani hereby Declare that this thesis entitled **"Renner-Teller effects and Vibronic Coupling: Full-dimensional Nonadiabatic Dynamics of Linear carbon chains and Cyanobenzene"** submitted by me under the guidance and supervision of **Prof. Susanta Mahapatra** is a bonafide research work. I also declare that it has not been submitted previously in part or in full to this University or any other University or Institution for the award of any degree or diploma. I hereby agree that my thesis can be deposited in Shodhganga/INFLIBNET. A report on plagiarism statistics from the University Librarian is enclosed.

Date : 21. 10. 2025

Name : MAMILWAR RANI

Regd. No.: 18CHPH21

Thesis Title: **Renner-Teller effects and Vibronic Coupling: Full-dimensional Nonadiabatic Dynamics of Linear carbon chains and Cyanobenzene**

Student Regd. No.: **18CHPH21**
Supervisor: **Prof. Susanta Mahapatra**
School: **School of Chemistry**

The research presented in this thesis aligns with the **Sustainable Development Goals (SDGs)**, with primary focus on **SDG-9: Industry, Innovation and Infrastructure.**

The thesis aligns most strongly with SDG 9, emphasizes the importance of building resilient infrastructure, promoting inclusive and sustainable industrialization, and fostering innovation. This research contributes to these objectives through its advancement of fundamental molecular science, which forms the backbone of technological innovation in materials, energy, and chemical industries. At the heart of this study lies an in-depth exploration of nonadiabatic molecular dynamics, focusing on Renner–Teller effects and vibronic coupling, phenomena that describe the intricate interactions between electronic and nuclear motions within molecules. By developing a full-dimensional understanding of these effects in carbon-based systems such as linear carbon chains and cyanobenzene, the research enhances our ability to predict, control, and manipulate molecular behavior under different energetic conditions. Such knowledge is essential for the rational design of new materials with tailored electronic and optical properties. This work directly supports innovation in fields such as quantum chemistry, photophysics, and materials science. Carbon chains and aromatic molecules play crucial roles in developing organic semiconductors, molecular electronics, and photonic devices, technologies that form the foundation of modern sustainable industries. By improving theoretical and computational methods that describe molecular interactions, the research contributes to the scientific infrastructure that enables future breakthroughs in nanotechnology, optoelectronics, and renewable energy materials. Moreover, the thesis represents a model of research-driven innovation, where advances in fundamental science stimulate progress in applied technology. The methodologies developed, such as high-precision simulations and nonadiabatic dynamics modeling, are not limited to specific systems but can be extended to a wide range of molecular materials. This fosters cross-disciplinary collaboration between chemistry, physics, and engineering, reinforcing SDG 9's focus on innovation ecosystems. Ultimately, this research embodies the spirit of SDG 9 by advancing scientific knowledge that supports sustainable industrial development. Through its contributions to understanding molecular processes and enabling the design of advanced materials, the study helps pave the way for a future where innovation and sustainability coexist, driving progress toward a more resilient and technologically advanced society.

Acknowledgements

I would like to express my sincere gratitude to my supervisor, Prof. Susanta Mahapatra, who has been not only my PhD mentor but also my faculty during my MSc, laying the foundation of my understanding in quantum chemistry. I deeply admire his professional accomplishments and respect him as a kind and compassionate human being.

I am deeply grateful to Prof. Durga Prasad, Prof. Barik, Prof. T. P. Radha Krishna, Prof. Basavaiah, and my M.Sc. project guide Prof. Abani K. Bhuyan for their invaluable guidance and encouragement. I would also like to sincerely thank all the faculty members of the Integrated Masters course for their constant support throughout my studies. My heartfelt appreciation goes to the non-teaching staff of the School of Chemistry for their assistance and cooperation.

I would like to express my heartfelt gratitude to two remarkable individuals, the late S. Narsing Reddy and S. Mallikarjun Prasad, my intermediate teachers. They changed my perception on education, offering constant support and guidance. Their influence is one of the key reasons I am where I am today.

I would like to thank my labmates Dr. Arpita Ghosh, Dr. Sugata Goswami, Dr. Rudraditya, Dr. Arun, Dr. Jay Krishna, Dr. Ajay, Daradi, Md. Alamgir, Ajay kumar, Shreyan and Dr. Shavez. Arpita di has made my initial days so smooth and Sugata daa has always been a well-wisher. I would like to specially thank my friend Alamgir, for being a constant support inside and outside the lab and for all the chit chats that helped ease our frustration and sometimes created new ones. I thank Yarram Ajay Kumar for being a stress burster in the lab, at least to me, and for being an encyclopedia of politics.

Through all my ups and downs in this journey, this very close friend of mine Dr. Vamshi, has pushed me beyond my limits. I am very grateful for his constant support and for being an unpaid therapist. I would like to thank Dr. Vamshi, Seema Nagarajan, and Dr. Vinay for giving me the best memories that I would cherish forever.

My hostel life would not be beautiful without Swathi, Seema, Manasa, and Sandya. The nightouts, the never ending gossips and the emotional moments we shared are etched in my HCU dairies.

My special thanks to Dr. Maruthi and Nivruthi for always showering love and affection.

Thanks for always being kind and empathetic.

Now, I would like to thank my Intergrated friends Ramadevi, Yasaswini, Radha, Subash, Priyanka, Sharanya, Reshma, Vinay, Vinod, Karthik, Kumar, Revathi, spandana, Priyavardhan and Venky. All these people have made my HCU life so special and beautiful. I thank Rama, Subash, Vinay and Pinky for being my strength and for being my shadow in all the shady things.

I express my heartfelt thanks to this extremely important person, Dr. Srikanth, for guiding me at every step and for never letting me fall. I thank him for all the meaningful discussions of academics and for the meaningless discussions about daily stories of my life. Thanks for existing.

I thank all my maternal and paternal family members, for understanding my absence in all the occasions. For not bothering my parents about my marriage, this means a lot. I thank my grand parents Mamilwar Venkatesham, Kamshalya, Potdar Venkatesham, and Veerama for giving such beautiful family tree for our generation. I thank Vittal mama, Sarada atthama, Hanumandla mama, Vijaya atthama, Krishna mama, and Laxmi atthama, Krishna mama and Sukanya atthama, Brahmayya mama and Vijaya laxmi atthama, Sudarshan mama and Shobha atthama. I thank Vaman peddananna, Shobha peddamma, chandrakala peddama, Chandrashekar kaka and Vasanta pinni. My healtfelt thanks to all my cousins Santhanna, Rajanna, Prasad, Praveen, Damodhar, ramakka, prasanna, Sai vardhan and Minnu. I would like to thank my other cousins I spent my good time with, Pushpa, Ujwala, meenu, Swathi, Jyothi, Gajju, Manisha, Monika, Bintu, Sweety, Sanjanna and Sathish anna.

Now I would like to thank my siblings Chinni, Vani, and Sappy without whom I am incomplete. They have given me wings to fly and trained me to face the world. Although Chinni is the youngest one, she protects me from the vicious things and people. She could declare a war if my eyes are wet. Vani and Sappy, they treat me like one of their children. I would like to thank two other special people, Prasad bava and Krishna bava, they are my brothers from another mother. I thank vani akka and krishna bava for treating me like their kid without even adopting me. I specially thank the bundle of joy and unconditional love in my life, from these little champs Hari, Shivu, Vishu and Ammu.

I would now like to express my deepest gratitude to my superheroes, Nanna and amma. They

have always been the pillar of my strength and I remain profoundly thankful for their unwavering support. Coming from a humble background, they have shown me that resilience, hardwork, and kindness make a person truly exceptional. I will always be grateful for their unique presence and inspiration in my life. Their battles with the society and silent sacrifices have paved the way for me to reach this point. I am forever indebted for their love.

I would like to thank myself for **never giving up**. Along this journey, I have sacrificed many family gatherings, festivals and important moments. I remember wiping my own tears and sometimes walked into hospitals alone, yet chose to keep moving forward. I did not mind appearing worn out or underdressed, for I was committed to what I wanted. I appreciate myself for having the courange to reach out to my friends during difficult times. Beyond the support of all the wonderful people in my life, I believe it is fair to acknowledge my own role in reaching this point.

This thesis is dedicated to my parents - Mamilwar Gangadhar and Susheela. And to my younger sister, Mamilwar Krishnaveni.

Contents

List of Figures

List of Tables

Abbreviations

BO	Born-Oppenheimer
VIEs	vertical ionization energies
EOMIP-CCSD	Equation-of-motion coupled cluster singles and doubles Ionization Potential
XMCQDPT	extended multiconfiguration quasi-degenerate perturbation theory
CI	Conical Intersections
VC	Vibronic coupling
RT	Renner-Teller
PES	potential energy surfaces
DOF	degrees of freedom
JT	Jahn-Teller
QVC	quadratic vibronic coupling
LVC	linear vibronic coupling
MCTDH	multi-configuration time-dependent Hartree
ML-MCTDH	multi layer multi-configuration time-dependent Hartree
WP	wave packet
BN	Benzonitrile
PAHs	polycyclic aromatic hydrocarbons
ISM	Interstellar Medium
TDSE	time-dependent Schrödinger equation
TISE	time-independent Schrödinger equation
NACT	non-adiabatic coupling term
ADT	adiabatic-to-diabatic transition
KEO	Kinetic energy operator
DVR	discrete variable representation
SPFs	single-particle functions

aug-cc-pVTZ	augmented-correlation consistent polarized Valence Triple Zeta
MP2	Møller-Plesset perturbation
cc-pVDZ	correlation consistent polarized valence double Zeta
DNDCs	dimensionless normal displacement coordinates
IREPs	irreducible representations
aug-cc-pVDZ	augmented correlation-consistent polarized valence double-zeta
B3LYP	Becke 3-parameter, Lee, Yang, and Parr

Chapter 1

Introduction

The study of chemical reactions mediated by light energy is known as photochemistry[4]. Numerous fundamental mechanisms in this nature are initiated by photochemical reactions. Among them, one of the most important photochemical reactions is photosynthesis. The process is driven by the absorption of sunlight by chlorophyll in the leaves in presence of carbon dioxide and water. As a result, the starch stores the absorbed energy as chemical energy[5]. A thorough understanding of photochemical processes and the ability to regulate them will help us in the creation of artificial experimental photochemical systems that closely resemble natural ones, such as sunscreens[6], solar cells[7], photostat machines[8] and so on.

Theoretically, it became feasible to find solutions to mysterious chemistry issues like what occurs when two substances mix, why a certain product is generated, whether a product will develop at all, and if so, when - it might be seconds or even years! Furthermore, the capacity to create new materials and investigate the characteristics of matter were made available. Comparing today's kitchen to that of our ancestors highlights the advancements in chemistry over time. The impact of technology on daily life is subjective, but it has undoubtedly altered our way of existence. The understanding of molecular processes at the atomic level made all of this practical. The development of science has been greatly supported by theory and experimentation, which frequently inspires experimentalists to conduct new and challenging studies. When discussing molecules, the two components, electrons and nuclei, are readily identifiable that contribute to chemistry. Their mass and, consequently, the time scale of motion are the primary distinctions between these two components. The Schrödinger equation for the two cases can be independently solved. This approach, which is well-known as the

Born-Oppenheimer (BO) or adiabatic approximation[9;10;11;12], has served as the fundamental basis for molecular chemistry, whether it is in energetics, kinetics, or spectroscopy. *Electronic structure theory* is the area of study that deals with electron motion, whereas *nuclear dynamics* is the theory that deals with nuclei motion[11].

Simple yet elegant physical models can be used to understand the complexity of nature. When the previously mentioned BO approximation begins to fail in specific situations, one such complexity emerges. This occurs more frequently than one may imagine. Nonadiabatic processes are those in which the motion of nuclei and electrons can no longer be handled separately due to their mass difference ($\text{Mass}_{el} > \text{Mass}_{nu}$ by a factor of 10^3). Even though these processes have been understood for a long time, Köppel, Domcke, and Cederbaum's introduction of vibronic models in the 1980s marked the beginning of theoretical advancements for addressing them[11].

Vibronic models offer a compact representation of potential energy surfaces in close energetic proximity, making them an excellent tool for studying nonadiabatic processes. High-level *ab initio* electronic structure methods can be used to obtain the parameters of the model responsible for the coupled motion of electrons and nuclei. In the work presented here, the vertical ionization energies (VIEs) and vibronic model parameters will be obtained using the Equation-of-motion coupled cluster singles and doubles Ionization Potential (EOMIP-CCSD) method[13;14] and extended multiconfiguration quasi-degenerate perturbation theory (XMCQDPT) framework[15;16;17]. By fixing the nuclear motion and by treating the electronic motions for several fixed nuclear configurations potential energy surfaces can be constructed as first step. Then the obtained potential surfaces provide force field for the nuclear dynamics of molecular systems of our interest[10;11].

Important to say, the electronic structure components of any nonadiabatic process only account for half of the total. Solving the nuclear motion problem is necessary to ascertain the experimental observables. This will be done by using both the time-dependent wavepacket propagation technique and time-independent diagonalization method. **Cyanogen (C_2N_2)**, **Carbon Monohydride, $C_{2n}H^-$ ($n = 1-4$)** linear carbon chain series, and **Cyanobenzene (C_6H_5CN)** are the vibronic model systems of our interest. Each belonging to different symmetry point group and give us an opportunity to understand the role of symmetry on electronic degeneracies, vibrational couplings, and the overall manifestation of nonadiabatic

effects. These species are highly interesting and are significant in the astrophysical environment. The goal is to replicate the photoelectron spectra of these species and compare the theoretical findings with the existing experimental literature.

1.1 Outset of the theory

In polyatomic systems, the ground electronic state is generally well separated from the other excited states. The excited states can be very close in energy and thus leading to strong coupling between the electronic states. As a consequence, the electronic states intersect with each other leading to the formation of *conical intersections (CI)*[18;19;20] and breakdown of adiabatic approximation. In such situations, we are compelled to include the couplings between electronic and vibrational motions. Such couplings are termed as **vibronic coupling (VC)**. VC has vital role in polyatomic molecular systems, having close lying electronic states and many nuclear degrees of freedom. Also, VC has great importance in molecular spectroscopy, specially in absorption and photoelectron spectroscopy[11;21;22;23].

As mentioned earlier, CIs can be formed when two electronic states intersect and forms a double cone topography. Whereas in other case, instead of intersecting, the electronic states coincide and gives a glancing type of topography which is termed as *Renner-Teller (RT) effect or RT coupling.* RT type of coupling is common for degenerate electronic states of linear systems with axial symmetry. According to Wigner and von Neumann's non crossing rule[24], potential energy surfaces (PES) of diatomic molecules cannot cross unless they have different symmetry or spin multiplicity. There should be at least two nuclear degrees of freedom (DOF) for two electronic states to be degenerate when spin-orbit coupling is excluded. In 1934, nonadiabatic couplings in the excited electronic states of linear system CO_2 was reported by Renner[18]. Then in 1937, Teller has shown how nonradiative decay in photophysics are mediated through CIs[19]. The internal conversion dynamics was first carried out by Köppel et al. by performing quantum dynamics simulations[25], since then CIs provided deep insights in predicting the physical phenomena and significant ultrafast mechanisms for various photo-chemical reactions[26].

The Jahn-Teller (JT) effect is an unique type of VC among the trigonal and tetragonal systems[11;20;27;28;29;30;31]. In 1937, Jahn and Teller, have came up with the concept of instability and spontaneous distortion of nuclear configuration along the asymmetric vibrational modes

in an orbitally degenerate electronic states (Γ)[20;27]. The mentioned JT effect has vital role in the complex electronic spectra of JT active systems. Like JT systems, linear molecules do experience instabilities in the degenerate electronic states along the bending vibrational modes. The VC that exists in linear molecules is called as RT coupling and this is one of the best examples that explains the violation of BO approximation. In its most basic form, this vibronic interaction is caused by a coupling between the nuclear angular momentum coupled to the bending vibration and the electronic orbital angular momentum in linear molecules in orbitally degenerate Π electronic states[32]. An extra dipole moment is created in the molecular plane when the molecule is bent, raising the electronic degeneracy. Nonetheless, the motion on both potential surfaces is connected by a coriolis-type interaction between electronic and vibrational angular momentum. The breakdown of the adiabatic approximation results from this singularity behavior at the linear configuration. A review by Rosmus and Chambaud[33] is advised for an in-depth account of the RT effect.

All of the previous instances make use of perturbation theory. When a nonadiabatic coupling is sufficiently strong, perturbative strategies are known to fail. It appears that the multimode dynamics of linear polyatomic molecules can be systematically understood using the quadratic vibronic coupling (QVC) technique, which was originally developed by Köppel, Domcke, and Cederbaum[34]. A higher degree of sophistication has been attained in the literature through theoretical investigations of VC effects in molecular systems[11;25]. Typically, the theoretical approach relies on the linear vibronic coupling (LVC) scheme, which is frequently improved by quadratic vibronic coupling terms[11;28;29;30]. Using a diabatic electronic basis, this sustains linear or quadratic terms while expanding the potential energy matrix in a Taylor series in appropriate displacement coordinates. The nuclear motion and the relevant coupling constants are calculated using an ab initio quantum dynamical approach. Different electronic spectra's vibrational structures have been investigated as time-independent observables. In the interacting manifold of electronic states, time-dependent quantities of interest are frequently electronic populations. The strong nonadiabatic couplings among the electronic states drives the electronic population transfer indicating the internal conversion dynamics[11].

1.2 Organisation of the Thesis

The thesis is organised as follows:

Chapter 1: This chapter gives a brief introduction to the thesis. The photo-induced vibronic interactions in the vibronic models are introduced. The vibronic models of interest are **Cyanogen (C_2N_2)**, **carbon monohydride, $C_{2n}H^-$ ($n = 1-4$)** linear carbon chain series, and **cyanobenzene (C_6H_5CN)** which are of different symmetry point groups ($D_{\infty h}$, $C_{\infty v}$ and C_{2v}) respectively. The essential development of theory, required approximations and their breakdown consequences are mentioned in this chapter.

Chapter 2: A thorough theoretical basis for a multistate-multimode vibronic coupling scheme is provided in chapter 2 of this thesis. In order to study the RT and PRT interactions in multimode molecular systems, the idea of adiabatic approximation and the requirement for a diabatic electronic basis are covered. This chapter also includes a detailed discussion of the vibronic coupling including degenerate vibrational modes and degenerate electronic states. A few illustrative examples are provided to illustrate how to construct a diabatic electronic Hamiltonian using basic symmetry selection principles. It is presented how to compute the vibronic eigenvalue spectrum using the Lanczos algorithm[23] to solve the time-independent Schrodinger problem numerically. Using multi-configuration time-dependent Hartree (MCTDH) method[35] and multi layer multi-configuration time-dependent Hartree (ML-MCTDH) method[36;37;38;39], the computation of complicated vibronic spectra of molecules with significant electronic states using all the vibrational DOF is demonstrated by a time-dependent wave packet (WP) propagation approach.

Chapter 3: A thorough theoretical analysis of the electronically excited six states and associated photoelectron spectrum of the Cyanogen molecule is presented in chapter 3. An in-depth understanding of the electronic bands, one-dimensional PESs, and vibrational assignments is provided by combining precise *ab initio* calculations with sophisticated WP propagation techniques. Investigations are being done to examine the vibronic coupling in cyanogen's six electronic states. Among the six electronic states, two are degenerate Π states and two are non-degenerate Σ states. Using the vibronic coupling theory and the symmetry selection rules, a 6x6 diabatic model Hamiltonian is built in terms of the normal coordinates of vibrational modes. Comprehensive *ab initio* quantum chemistry computations are used to estimate the Hamiltonian parameters. A thorough analysis of the topography of cyanogen's

first six electronic states is conducted, and CIs are established. The WP propagation method is used to do the nuclear dynamics computations on the coupled electronic surfaces. It comes to light that the theoretical findings agree well with the experimentally known photoelectron spectrum.

Chapter 4: Over the past couple of decades, bare carbon clusters, or C_n, have been the subject of in-depth experimental and theoretical research. A little less study has been paid to the related carbon monohydrides, C_nH, which are crucial for combustion and interstellar chemistry. The interstellar medium has been found to include a number of C_nH chains. Furthermore, the diffuse interstellar bands could be candidates for C_nH radicals. The existence of close-lying $^2\Sigma$ and $^2\Pi$ electronic states, however, makes it challenging to perform vibrational and electronic spectroscopy on these open shell species. The ground state of C_2H is $\widetilde{X}^2\Sigma_1$ electronic state, for instance, interacts strongly with the adjacent $\widetilde{A}^2\Pi$ state. The $^2\Sigma$ and $^2\Pi$ states in C_4H are almost degenerate. The $^2\Pi$ state is the ground state in C_6H and C_8H; a low-lying $^2\Sigma$ state is anticipated in each instance, though its term values are unknown in the reports. The impact of vibronic interactions on the vibronic structure of each state is theoretically investigated. The interactions between the doubly degenerate and non-degenerate electronic states of $C_{2n}H$ (n=1-4) species are evaluated. This work discusses the pattern in which nonadiabatic couplings and Renner-teller effects alter as chain length increases.

Chapter 5: Accurately understanding the many-body quantum effects for complex molecules is a major difficulty in theoretical chemical physics and physical chemistry. It is anticipated that the most basic aromatic CN-substituted hydrocarbon, cyanobenzene or benzonitrile (BN), will serve as the foundation for polycyclic aromatic hydrocarbons (PAHs). Apparently, no specific PAH has been discovered in the Interstellar Medium (ISM), despite the fact that PAHs are known to be a class of interstellar molecules. Radio telescopes and other astronomical methods can identify the BN's spectral signature in the ISM because of its polarity caused by the CN-group and permanent dipole moment. This work uses a cutting-edge theoretical technique to treat the first eight low-lying electronic states of the cyanobenzene radical cation. The EOMIP-CCSD and XMCQDPT approaches are used to calculate the corresponding PESs using CFOUR and GAMESS program modules. The diabatic model Hamiltonian, which includes all eight electronic states and all DOFs, is used to study their vibronic coupling. Lastly, the extremely effective MCTDH and ML-MCTDH technique is

used to perform the nuclear dynamics. According to their CIs and vibronic coupling constants, all vibronic interactions of the states that make up the manifold have been identified and described. The results of the simulated spectrum reflect the available experimental data quite well. The study of population dynamics has made it possible to have discussions about nonradiative decay channels.

Chapter 6: The main conclusions, contributions, and insights from the study are compiled in this chapter. Future directions are discussed briefly.

Chapter 2

Theoretical methodology

The theoretical approaches and strategies employed to accomplish the objectives mentioned in the introduction are briefly described in this chapter. We'll divide the whole non-relativistic time-dependent Schrödinger equation (TDSE) into two components: the nuclear TDSE and the electronic TISE. To solve the electronic time-independent Schrödinger equation (TISE), ab initio quantum chemistry techniques will be employed. The techniques for determining the non-adiabatic coupling terms (NACTs) are described. We will present the interaction between molecules and light and talk about the adiabatic-to-diabatic transition (ADT). The nuclear Schrödinger equation will be solved numerically using both time-dependent and time-independent approaches.

2.1 Born-oppenheimer approximation

The BO approximation relies on the idea that nuclear motion is slower than electronic motion because of the significant mass difference between nuclei and electrons. By distinguishing nuclear and electronic motions, the BO approximation simplifies the solution. Because of the low electron mass in relation to the nuclear one, the fast-moving electrons in the BO approximation can instantly re-adapt to the changing nuclear geometry. Consequently, the TISE for the electronic Hamiltonian is solved initially. While keeping the nuclei fixed, the electronic problem is solved. The PESs are determined by using quantum chemistry methods to calculate the electronic energies for each fixed nuclear configuration. The second stage involves performing nuclear dynamics on one or more selected PESs[9;11;12].

In the entire space of electronic $\{q\}$ and nuclear $\{Q\}$ coordinates, the TISE can be expressed as

$$\hat{H}(q,Q)\Psi(q,Q) = E\Psi(q,Q) \tag{2.1}$$

where the molecular Hamiltonian, wavefunction, and energy are denoted by $\hat{H}(q,Q)$, $\Psi(q,Q)$, and E, respectively. The expression for the molecular Hamiltonian is

$$\hat{H} = -\frac{\hbar^2}{2}\sum_A \frac{\nabla_A^2}{m_A} - \frac{\hbar^2}{2m_{el}}\sum_i \nabla_i^2 + \sum_A \sum_{B>A} \frac{Z_A Z_B e^2}{r_{AB}} - \sum_A \sum_i \frac{Z_A e^2}{r_{iA}} + \sum_i \sum_{i>j} \frac{e^2}{r_{ij}} \tag{2.2}$$

where A and B in the Eq. 2.2 stand for nuclei and i and j are for electrons. The nuclei and electron masses are given as M_A and m_{el}, e is the electron charge, Z_A is the atomic number of the A^{th} nuclei. The first term on the RHS of the Eq. 2.2 is the kinetic energy (KE) of nuclei and second term is of electron, respectively. The third, fourth, and fifth terms are potential energies between the pair of nucleus-nucleus, electron-nucleus and electron-electron respectively. For simplicity, the above equation can be represented as

$$\hat{H} \equiv T_N + T_{el} + V_{N-N} + V_{N-el} + V_{el-el} \tag{2.3}$$

Within the BO approximation, the total molecular wavefunction can be expressed as:

$$\Psi_i(q,Q) = \sum_{i=1}^{N} \Phi_i(q;Q)\chi_i(Q) \tag{2.4}$$

Eq. 2.4, can be exact only when the considered number of eigenstates are infinite (i.e., N $\rightarrow \infty$). In chemistry applications, energetically close electronic states are taken into consideration. In the product of electronic wave functions $\Phi_i(q;Q)$ and nuclear wave functions $\chi_i(Q)$, the electronic wave function depends on the electronic, q and nuclear coordinates Q while the nuclear wave function depends solely on the nuclear coordinate. The presence of interaction term of electron-nucleus in the Eq. 2.2, makes it difficult for the separation of q and Q variables. That's when the BO approximation is invoked, in which the electronic and nuclear motions are treated independently based on their significant mass difference. In quantum chemistry modules, the electronic schrödinger equation is solved and the PESs can

be generated by fixing the nuclear positions ($\mathcal{T}_N = 0$).

$$\hat{H}_{el}\Phi(q;Q) = V_i(Q)\Phi_i(q;Q) \tag{2.5}$$

In Eq. 2.5, $\hat{H}_{el}$ represents the electronic Hamiltonian part i.e., $T_{el}+V_{N-el}+V_{el-el}$ and $V_i(Q)$ is the electronic potential energy obtained by solving the Eq. 2.5. By solving Eq. 2.4 and 2.5, and by left multiplying the complex conjugate of $\Phi(q,Q)$ and integrating over the electronic coordinate leads to coupled differential equation for $\chi_i(Q)$ expansion coefficients

$$[\hat{T}_N(Q) + \hat{V}_j(Q) - E]\chi_j(Q) = \sum_{i=1}^{\infty} \hat{\Lambda}_{ij}\chi_i(Q) \tag{2.6}$$

The term $\hat{\Lambda}_{ij}$ in Eq. 2.6 represents the nonadiabatic coupling operator between the electronic states i and j and is expressed as

$$\sum_i \hat{\Lambda}_{ij}(Q) = -\int dq\Phi_i^*(q;Q)[T_N, \Phi_j(q;Q)] \tag{2.7}$$

The coupling between the electronic states causes the nuclear kinetic energy operator to acquire non-diagonal form in this formulation. Decomposition of the nonadiabatic operator coupling $\hat{\Lambda}_{ij}$ is[11;40]

$$\hat{\Lambda}_{ij}(Q) = -\sum_{n=1}^{m} \frac{\hbar^2}{M_n} F_{ij}^n(Q)\frac{\partial}{\partial Q_i} - \sum_{n=1}^{m} \frac{\hbar^2}{2M_n} G_{ij}^n(Q) \tag{2.8}$$

In Eq. 2.8, M_n represents the nuclear masses, F_{ij}^n(Q) is the derivative coupling and G_{ij}^n(Q) is the scalar coupling. This nonadiabatic operator ($\hat{\Lambda}_{ij}$) affects the solution of the nuclear Schrödinger equation, particularly for polyatomic molecules where several nuclear DOF must be taken into account. In the adiabatic approximation, the nonadiabatic operators are disregarded ($\hat{\Lambda}_{ij} = 0$)[9;12;10]. This approximation relies on the assumption that the kinetic energy operator (KEO) of the nuclei acts as a minor perturbation to the electronic motion. A more practical approach, referred to as the Born-Huang approximation[41], involves neglecting only the off-diagonal elements of the nonadiabatic operators $\hat{\Lambda}_{ij}$. By applying the Hellmann-Feynman theorem[42;43;44;45], the vector coupling term can be expressed as

$$F_{ij}^n(Q) = \frac{\langle\Phi_j(q;Q)|\nabla_i\mathcal{H}_{el}(q;Q)|\Phi_i(q;Q)\rangle}{V_i(Q) - V_j(Q)}, \tag{2.9}$$

In some circumstances, especially when the energy levels of the electronic states are identical, the adiabatic approximation fails. When two electronic states become exactly degenerate ($i = j$) at a CI, the adiabatic approximation fails because the derivative coupling terms (F_{ij} in Eq. 2.8) become infinite. Due to this singularity, the electronic nature abruptly changes since the electronic states and their energies are no longer smooth analytic functions of nuclear coordinates. They feature a cusp at the degeneracy in their energy surfaces[46].

The adiabatic electronic foundation is insufficient for numerical solution of the nuclear Schrödinger equation due to the singularity of the derivative coupling. An alternative electronic basis, referred to as the diabatic electronic basis, is reported in order to solve this problem. In this case, an adequate unitary transformation transforms the sharply fluctuating kinetic coupling found in the adiabatic basis into a smoothly varying potential coupling[11;47;48;49]. This is the version of the nuclear Schrödinger equation (Eq. 2.6) in this diabatic basis[50].

$$[T_N(Q) + U_j(Q) - E]\chi_j = \sum_{i \neq j} U_{ij}(Q)\chi_i(Q) \tag{2.10}$$

$$\sum_j U_{ij}(Q) = \int dq \Phi_i^*(q;Q)[T_{el} + V(Q)]\Phi_j(q;Q) \tag{2.11}$$

For the diabatic electronic wave function, the term $\Phi(q;Q)$ is used. Over electronic coordinates q, the integration is performed. The only distinction between Eqs. 2.6 and 2.11 is that in U_{ij}, the diverging kinetic coupling of Eq. 2.6 is converted into a smooth potential coupling. On a diabatic basis, the wave function and energy both restore the analytic continuation as a function of Q since the diverging kinetic coupling may be "ideally" eliminated (completely). While the off-diagonal elements, U_{ij} (Q), define the coupling between them, the diagonal elements, $U_j(Q)$, of the U matrix explain the diabatic electronic states. The states retain their electronic nature in this representation and become smooth across the nuclear coordinate space as a result of analytic continuation. As was discussed before, the dynamics cannot be studied using the adiabatic electronic description, despite it being more realistic. Consequently, a diabatic electronic representation can be obtained for all practical applications, like molecular spectroscopy[11;48;51].

The diabatic electronic wavefunction generated via appropriately transforming the equivalent adiabatic $\psi(q;Q)$ ones.

$$\varphi(q;Q) = S(Q)\psi(q;Q) \tag{2.12}$$

$$S(Q) = \begin{pmatrix} cos\theta(Q) & sin\theta(Q) \\ -sin\theta(Q) & cos\theta(Q) \end{pmatrix} \tag{2.13}$$

The matrix $S(Q)$ is referred to as the adiabatic-to-diabatic transformation (ADT) matrix, with $\theta(Q)$ representing the transformation angle. This transformation is constructed under the condition that the first-order derivative couplings, described in Eq. 2.8, must be zero in the transformed (diabatic) representation for all values of the nuclear coordinates[52;53].

The mathematical equations for the transformation matrix are produced by this condition[52;54;51].

$$\frac{\partial S}{\partial Q_i} + A^{(i)} S = 0 \tag{2.14}$$

As given in Eq. 2.8, the entries of the derivative coupling matrix $A^{(i)}$ depend on first-order terms. Importantly, a unique solution to this equation exists only if the electronic states under consideration are from a finite subspace[53]. Consequently, strictly diabatic electronic states cannot be rigorously defined for polyatomic molecular systems[53]. Due to this limitation, several approximation methods have been devised to construct diabatic electronic states[54;55;56].

The idea of a diabatic electronic basis was introduced early in scientific literature, initially in the study of electron-nuclear coupling during atomic collisions[57] and later in molecular spectroscopy[58]. However, constructing such states for polyatomic molecules is particularly challenging because the problem depends on multiple nuclear coordinates rather than just one. As a result, numerous mathematical approximation techniques have been proposed to address this issue[52;53;55;56;59;60;61;62].

2.2 Vibronic Hamiltonian

All theoretical investigations presented in this thesis employ a diabatic electronic representation. In this framework, the nuclear kinetic energy operator becomes diagonal, while electronic state couplings arise from the off-diagonal elements of the potential energy operator. Unlike adiabatic representations where potential energy surfaces (PESs) exhibit avoided crossings with discontinuous behavior, diabatic PESs appear as smooth, intersecting curves.

The vibronic Hamiltonian for the excited states is expressed using dimensionless normal coordinates derived from the electronic ground state of the corresponding neutral reference species. Following conventional methodologies[12;57;31;63], these normal coordinates[64] describe small-amplitude vibrational motions near the equilibrium geometry of the electronic ground state (assuming a closed-shell molecule with a well-defined structure). The normal coordinates are formally defined as follows:

$$Q = L^{-1}\delta R \tag{2.15}$$

For a N-atom system, internal displacements δR (comprising bond length and angle changes) form a vector of dimension $3N-6$ ($3N-5$ for linear geometries). These connect to normal coordinates through the transformation matrix L of the Wilson FG-matrix approach[64]. The practical implementation utilizes dimensionless normal coordinates Q_i, which are obtained by scaling the mass-weighted coordinates q_i resulting from force field diagonalization[64] :

$$Q_i = (\omega_i/\hbar)^{1/2} q_i \tag{2.16}$$

The term ω_i represents the harmonic frequency corresponding to the i^{th} vibrational mode. These frequencies characterize the normal displacement coordinates (Q) relative to the equilibrium configuration ($Q = 0$) of the reference state.

The vibronic Hamiltonian, which governs the quantum mechanical behavior of a molecule upon photo-excitation, is formulated as:

$$\hat{H} = (H_0)\mathbf{I_n} + W(Q) \tag{2.17}$$

In this expression, H_0 (defined as $T_N + V_0$) represents the zero-order, or unperturbed, Hamiltonian corresponding to the electronic ground state. When expressed in terms of the dimensionless normal mode displacement coordinates, the kinetic and potential energy operators of H_0, under the harmonic approximation, are given by:

$$T_N = -\frac{1}{2}\sum_i \omega_i \left[\frac{\partial^2}{\partial Q_i^2}\right] \tag{2.18}$$

$$V_0 = \frac{1}{2}\sum_i \omega_i Q_i^2 \tag{2.19}$$

In Eq. 2.17, the term $\mathbf{I}_n$ denotes an $n \times n$ identity matrix, where n corresponds to the number of electronic states involved in the nuclear dynamics analysis. The operator ΔH represents the change in electronic energy resulting from excitation or ionization relative to the reference Hamiltonian H_0. The components of $W(Q)$ define the diabatic potential energy surfaces (PESs), denoted by U_{nn}, as well as the coupling PESs U_{nm} between adjacent electronic states. Notably, the off-diagonal elements U_{nm} account for nonadiabatic interactions within the molecular system. These PES elements are typically expanded in a Taylor series with respect to the normal displacement mode coordinates Q_i as follows:

$$U_{nn} = E_n + \sum_i \kappa_i^{(n)} Q_i + \frac{1}{2!}\sum_{i,j} \gamma_{ij}^{(n)} Q_i Q_j + ... \tag{2.20}$$

$$U_{nm} = \sum_i \lambda_i^{nm} Q_i + ...(n \neq m) \tag{2.21}$$

The term E_n refers to the vertical excitation or ionization energy of the system - defined as the energy gap between the ground state potential energy surface (PES) and that of the n^{th} vibronically active electronic state, evaluated at the ground-state equilibrium geometry ($Q = 0$). The parameter $\kappa_i^{(n)}$ represents the gradient of the potential energy surface for the n^{th} electronic state along the i^{th} vibrational mode; it gives the driving force for structural reorganization in the excited state relative to the ground state. The coefficient $\gamma_{ij}^{(n)}$ accounts for changes in vibrational frequencies upon excitation and represents the quadratic intra-state vibronic coupling, which includes effects such as Duschinsky rotation. The term $\lambda_i^{(nm)}$ denotes the linear vibronic coupling between the n^{th} and m^{th} electronic states. In systems with high molecular symmetry, many of these coupling terms vanish due to symmetry constraints. The selection rules governing the presence of non-zero linear coupling elements are determined by the symmetry properties of the involved vibrational modes and electronic states.

$$\Gamma_n \otimes \Gamma_{Q_i} \otimes \Gamma_m \supset \Gamma_A \tag{2.22}$$

Here, Γ_n and Γ_{Q_i} denote the irreducible representations of the n^{th} electronic state and the i^{th} vibrational mode, respectively. In the case of quadratic coupling, the nonzero terms obey the symmetry condition $\Gamma_n \otimes \Gamma_{Q_i} \otimes \Gamma_{Q_j} \otimes \Gamma_m \supset \Gamma_A$. Analogous symmetry requirements apply

to all higher-order coupling terms.

2.3 Vibronic Hamiltonian for linear systems

Polyatomic molecules classified under the $D_{\infty h}$ and $C_{\infty v}$ point groups exhibit both degenerate electronic states and degenerate vibrational modes. In such systems, formulating the molecular Hamiltonian for investigating vibronic coupling is particularly challenging. This is primarily due to the fact that electronic state degeneracy highlights a significant limitation of the Born-Oppenheimer adiabatic approximation. Vibronic coupling in orbitally degenerate Π electronic states in linear molecules results from the coupling between the vibrational angular momentum associated with bending modes and the electronic orbital angular momentum. Bending the molecule within its plane causes a dipole moment to be created, which splits the electronic degeneracy. In principle, vibrational modes of δ symmetry can lift orbital degeneracy through first-order vibronic coupling. However, in linear molecules, such δ-type vibrational modes are absent, which results in the vanishing of first-order coupling between the components of a Π electronic state. Nonetheless, since $(\pi_g)^2 = (\pi_u)^2 = \delta_g$, second-order coupling becomes possible via vibrational modes of π symmetry. This second-order interaction effectively removes the degeneracy of the Π states and gives rise to the Renner-Teller (RT) effect.

The Hamiltonian in Eq. 2.17, for a linear system with $D_{\infty h}$ symmetry is constructed within the harmonian approximation, and the H_0 elements are written as

$$\mathcal{T}_N = -\frac{1}{2}\sum_{i\,\in\,\sigma_g^+,\,\sigma_u^+}\omega_i\frac{\partial^2}{\partial Q_i^2} - \frac{1}{2}\sum_{i\,\in\,\pi_g,\,\pi_u}\omega_i\left(\frac{\partial^2}{\partial Q_{ix}^2}+\frac{\partial^2}{\partial Q_{iy}^2}\right) \tag{2.23}$$

and

$$\mathcal{V}_0 = \frac{1}{2}\sum_{i\,\in\,\sigma_g^+,\,\sigma_u^+}\omega_i Q_i^2 + \frac{1}{2}\sum_{i\,\in\,\pi_g,\,\pi_u}\omega_i\left(Q_{ix}^2+Q_{iy}^2\right) \tag{2.24}$$

The elements of $W(Q)$ of Eq. 2.17, are expressed as

$$\begin{aligned} H_{j_x/j_y} &= E_0^j + \sum_{i\,\in\,\sigma_g^+} \kappa_i^j Q_i + \sum_{i\,\in\,\sigma_g^+,\,\sigma_u^+} \gamma_i^j Q_i^2 + \sum_{i\,\in\,\sigma_g^+} \zeta_i^j Q_i^3 + \sum_{i\,\in\,\sigma_u^+} \xi_i^j Q_i^4 \\ &+ \sum_{i\,\in\,\pi_g,\,\pi_u} [\gamma_i^j (Q_{i_x}^2 + Q_{i_y}^2)] + \sum_{i\,\in\,\pi_g,\,\pi_u} [\xi_i^j (Q_{i_x}^2 + Q_{i_y}^2)^2] + \sum_{i\,\in\,\pi_g,\,\pi_u} [\sigma_i^j (Q_{i_x}^2 + Q_{i_y}^2)^3] \\ &\pm \sum_{i\,\in\,\pi_g,\,\pi_u} \eta_i^j (Q_{i_x}^2 - Q_{i_y}^2) \pm \sum_{i\,\in\,\pi_g,\,\pi_u} \delta_i^j (Q_{i_x}^4 - Q_{i_y}^4) \pm \sum_{i\,\in\,\pi_g,\,\pi_u} \rho_i^j (Q_{i_x}^6 + Q_{i_x}^4 Q_{i_y}^2 - Q_x^2 Q_y^4 - Q_{i_y}^6) \\ &\quad ;\, j \,\in\, \Pi_{g,u} \end{aligned} \tag{2.25}$$

$$\begin{aligned} H_j &= E_0^j + \sum_{i\,\in\,\sigma_g^+} \kappa_i^j Q_i + \sum_{i\,\in\,\sigma_g^+,\,\sigma_u^+} \gamma_i^j Q_i^2 + \sum_{i\,\in\,\pi_g,\,\pi_u} [\gamma_i^j (Q_{i_x}^2 + Q_{i_y}^2)] + \\ &\sum_{i\,\in\,\pi_g,\,\pi_u} [\xi_i^j (Q_{i_x}^2 + Q_{i_y}^2)^2] + \sum_{i\,\in\,\pi_g,\,\pi_u} [\sigma_i^j (Q_{i_x}^2 + Q_{i_y}^2)^3] \quad ;\, j \,\in\, \Sigma_{g,u} \end{aligned} \tag{2.26}$$

$$\begin{aligned} H_{j_x - j_y} &= \sum_{i\,\in\,\pi_g,\,\pi_u} [2\eta_i^j (Q_{i_x} Q_{i_y}) + 2\delta_i^j (Q_{i_x}^3 Q_{i_y} + Q_{i_x} Q_{i_y}^3) + \\ &\quad 2\rho_i^j (Q_{i_x}^5 Q_{i_y} + Q_{i_x} Q_{i_y}^5 + 2Q_{i_x}^3 Q_{i_y}^3)] \quad ;\, j \,\in\, \Pi_{g,u} \end{aligned} \tag{2.27}$$

$$H_{j-k} = \sum_{i\,\in\,\sigma_u^+} \lambda_i^{j-k} Q_i \quad ;j-k \,\in\, \Pi_g - \Pi_u, \Sigma_g - \Sigma_u \tag{2.28}$$

$$H_{j_x - k/j_y - k} = \sum_{i\,\in\,\pi_{g/u}} \lambda_i^{j-k} Q_{ix/iy} \;; j-k \,\in\, \Pi_{g/u} - \Sigma_{u/g} \tag{2.29}$$

In eqs. (2.25-2.29), the vertical ionization energy (VIE) corresponding to the j^{th} electronic state is represented by E_0^j. The components associated with degenerate vibrational modes and electronic states are identified as x and y. The symbol κ_{ij} denotes the linear intrastate vibronic coupling parameter along vibrational modes of σ_g^+ symmetry. The parameters η_{ij}, δ_{ij}, and ρ_{ij} represent the second-, fourth-, and sixth-order RT coupling constants, respectively, for the j^{th} electronic state along the doubly degenerate vibrational modes π_g and π_u.

The linear coupling between two different electronic states j and k via the i^{th} vibrational mode is given by λ_i^{j-k}. For a single electronic state j, the second-, third-, fourth-, and sixth-order intrastate coupling parameters along the i^{th} mode are denoted by γ_{ij}, ζ_{ij}, ξ_{ij}, and σ_{ij},

respectively. The superscripts '+' and '−' indicate the x and y components of the degenerate vibrational states.

The relative signs of all elements in the diabatic electronic Hamiltonian are determined using symmetry-based invariance principles. A comprehensive derivation of the RT Hamiltonian for the Π state is provided in the Appendix I.

2.4 Nuclear dynamics

The nuclear dynamics of molecular systems are significantly determined by vibronic coupling. This thesis concentrates on a quantum mechanical explanation of nuclear motion. Either time-independent or time-dependent approaches can be used to solve the nuclear Schrödinger equation, which is necessary for accurately describing such quantum dynamics. A common method involves constructing the total wave function using stationary basis functions while allowing their expansion coefficients to vary with time. However, this approach becomes computationally prohibitive for systems with many degrees of freedom, as both memory usage and computational time scale exponentially. To address this challenge, the Multi-Configuration Time-Dependent Hartree (MCTDH) method, developed by Meyer, Manthe, and Cederbaum in 1990[65], offers an efficient solution. It utilizes a multi-configurational representation of the wave function to solve the time-dependent Schrödinger equation effectively.

The time-independent method is used to accurately determine the positions of vibronic energy levels, while the time-dependent approach helps in simulating the broad spectral envelope and tracking the evolution of electronic populations across coupled electronic states. Spectral intensities are estimated using Fermi's golden rule.

$$I(E) \quad = \quad \sum_{n} \left| \langle \Psi_n^f | \hat{T} | \Psi_0^i \rangle \right|^2 \delta(E - E_n^f + E_0^i). \tag{2.30}$$

The transition dipole operator, represented by the symbol $\hat{T}$, describes how the electron interacts with the external electromagnetic field of energy E during the photoionization process. While $|\Psi_v^f\rangle$ is the final vibronic state of the ionized or electronically excited molecule, with energy E_v^f, $|\Psi_0^i\rangle$ is the initial vibronic ground state (which serves as the reference) with energy

E_0^i. The ground electronic state reads as

$$|\Psi_0^i\rangle = |\Phi_0^i\rangle|\chi_0^i\rangle \tag{2.31}$$

where $|\Phi_i^{el}\rangle$ represents the electronic part of the wave function, and $|\chi_i^0\rangle$ denotes the vibrational ground-state wave function. Similarly, the final vibronic state is described by:

$$|\Psi_n^f\rangle = \sum_m |\Phi_f^m\rangle|\chi_n^m\rangle \tag{2.32}$$

The expression for the spectral intensity in Eq. 2.30 can be written as[11]

$$P(E) = \sum_{n,m} |\tau^m \langle\chi_n^m|\chi_0^i\rangle|^2 \delta(E - E_n^f + E_0^i) \tag{2.33}$$

here,

$$\tau^m = \langle\Phi^m|\hat{T}|\Phi^0\rangle \tag{2.34}$$

represents the diabatic electronic basis's transition dipole matrix elements. Assuming that the Condon approximation is valid in this basis, these are treated as constants[66].

2.5 Time-independent method

The photoionization spectrum can be obtained through a quantum mechanical approach that involves time-independent matrix diagonalization, which entails solving the eigenvalue problem associated with the time-independent vibronic Schrödinger equation.

$$H|\Psi_n^f\rangle = E_n|\Psi_n^f\rangle \tag{2.35}$$

The solution involves expressing the vibronic eigenstates $|\Psi_n^f\rangle$ as a linear combination of basis functions constructed from the direct product of harmonic oscillator states associated with the electronic ground state[11].

$$|\Psi_n^f\rangle = \sum_{|K_i\rangle} a^n_{K_1\ldots K_l}|K_1\rangle|K_2\rangle\ldots|K_l\rangle|\varphi_n\rangle \tag{2.36}$$

The state $|K_i\rangle$ represents the K^{th} vibrational level of the i^{th} mode, and $|\varphi_n\rangle$ corresponds to the electronic wavefunction. In numerical implementations, the harmonic oscillator basis for each vibrational mode is truncated appropriately to ensure computational efficiency. When the Hamiltonian is represented in the direct product harmonic oscillator basis, it acquires a highly sparse structure. This sparse matrix is efficiently tridiagonalized using the Lanczos algorithm[23]. The diagonal elements of the resulting eigenvalue matrix indicate the positions of the vibronic transitions, while the associated intensities are calculated by squaring the first component of the corresponding Lanczos eigenvectors[11;67]. To simplify the evaluation of transition dipole matrix elements, the generalized Condon approximation is applied within the diabatic electronic representation[66].

To account for the natural linewidth observed in experimental vibronic spectra, the discrete stick spectra derived from matrix diagonalization are typically broadened using a Lorentzian line shape function[11] with a full width half maximum, Γ.

$$L(E) = \frac{1}{\pi} \frac{\frac{\Gamma}{2}}{E^2 + (\frac{\Gamma}{2})^2} \tag{2.37}$$

2.6 Time-dependent method

Within the time-dependent framework, the spectral intensity described in Eq. 2.30 corresponds to the Fourier transform of the wavepacket's time autocorrelation function as it evolves on the final electronic potential energy surface[11;68].

$$\begin{aligned} I(E) &\approx 2Re \sum_{m=1}^{N} \int_0^{\infty} e^{\frac{iEt}{\hbar}} \langle \chi^m(0) | \tau^{\dagger} e^{-\frac{iEt}{\hbar}} \tau | \chi^m(0) \rangle dt, \\ &\approx 2Re \sum_{m=1}^{N} \int_0^{\infty} e^{\frac{iEt}{\hbar}} C^m dt. \end{aligned} \tag{2.38}$$

Here, $C_m = \langle \chi^m(0) | \chi^m(t) \rangle$ denotes the time autocorrelation function of the wavepacket that was initially launched on the m^{th} electronic state. The total spectrum is then obtained by summing the individual spectral contributions resulting from wavepacket propagation on each electronic surface.

2.7 Wave packet propagation via the MCTDH algorithm

As the number of electronic and vibrational degrees of freedom increases, the matrix diagonalization method becomes computationally infeasible. For large molecular systems or those with intricate vibronic coupling, this approach often proves impractical. In such cases, wavepacket propagation using the Multi-Configuration Time-Dependent Hartree (MCTDH) framework has proven to be a highly effective alternative[69;65;70;35]. This grid-based technique employs discrete variable representation (DVR), fast Fourier transforms, and advanced integration algorithms. Its efficient multiset wavefunction ansatz enables flexible grouping of vibrational modes, helping to mitigate the curse of dimensionality. Within this framework, the wavefunction of a nonadiabatic system is formulated as[65;70;35]:

$$|\Psi(t)\rangle = \sum_{j_1} \dots \sum_{j_p} A_{j_1,\dots,j_p}(t) \prod_{k=1}^{p} |\varphi_{j_k}^{(k)}(t)\rangle \tag{2.39}$$

The summation runs over every possible configuration of single-particle functions, $|\varphi_{j_k}^{(k)}(t)\rangle$ for each of the p single-particle groups (k=1,2,…,p). The upper bound j_k in each sum limits the subspace defined by the SPFs within the k^{th} group. By applying a variational principle, the solution to the time-dependent Schrödinger equation is obtained through the time evolution of the expansion coefficients $A_{j_1}, \dots, j_p(\alpha)$. In this framework, multidimensional functions are represented using one-dimensional components, following the principles of the mean-field or Hartree approximation. This strategy enhances computational efficiency by minimizing the size of the required basis set. Additionally, multidimensional single-particle functions (SPFs) are constructed by carefully selecting coordinate groupings, which effectively reduces the number of particles considered and lowers computational demands.

Although significantly more advanced than traditional methods, the MCTDH approach is still limited to systems with only a few dozen degrees of freedom. To overcome this limitation, the multi-layer MCTDH (ML-MCTDH) method was introduced, which employs a hierarchical and dynamically contracted structure of basis functions derived from the original SPFs. This layered representation offers a flexible and efficient description of the full wavefunction, enabling accurate quantum simulations for systems with substantially more degrees of freedom than previously possible[36;39;71]. For a comprehensive understanding of the methodology and computational procedures, readers are encouraged to consult the re-

search publications[36;39;71;72;37;73;38;74;75;76;77;78;79;80;81].

The ML-MCTDH method utilizes a hierarchical structure in which effective modes are recursively defined. At the top level, the wavefunction is represented by time-dependent functions (first layer), governed by equations derived from the Dirac–Frenkel variational principle. Rather than relying on fixed basis functions, each of these functions is further expanded in terms of lower-dimensional, time-dependent functions (second layer), also optimized variationally. This recursive process continues through additional layers, ultimately terminating in either time-independent functions or the lowest level of time-dependent functions. This multi-tiered structure grants ML-MCTDH remarkable flexibility and enables a compact, efficient representation of the full wavefunction[36;39;71].

$$|\Psi(t)\rangle = \sum_{j_1} \dots \sum_{j_p} A_{j_1,\dots,j_p}(t) \prod_{k=1}^{p} |\varphi_{j_k}^{(k)}(t)\rangle \tag{2.40}$$

$$|\varphi_{j_k}^{(k)}(t)\rangle = \sum_{i_1} \dots \sum_{i_{Q(k)}} B^{k,j_k}_{i_1,\dots,i_{Q(k)}}(t) \prod_{q=1}^{Q(k)} |v_{i_q}^{(k,q)}(t)\rangle \tag{2.41}$$

$$|v_{i_q}^{(k,q)}(t)\rangle = \sum_{\alpha_1} \dots \sum_{\alpha_{M(k,q)}} C^{k,q,i_q}_{\alpha_1,\dots,\alpha_{M(k,q)}}(t) \prod_{\gamma=1}^{M(k,q)} |\xi_{\alpha_\gamma}^{(k,q,\gamma)}(t)\rangle \tag{2.42}$$

Eq. 2.40 includes a summation over all combinations of single-particle functions (SPFs) $|\varphi_{j_k}^{(k)}(t)\rangle$ for $k = 1, 2, ..., p$ corresponding to each single-particle (SP) group. In Eq. 2.41, the hierarchy is extended as each SPF from the first level (L1) undergoes another time-dependent multiconfigurational expansion, forming what are called level-two (L2) SPFs. Each L1-SP group contains $Q(k)$ L2-SP groups, and the function $|v_{i_q}^{(k,q)}(t)\rangle$ denotes a L2-SPF in the q^{th} group of the k^{th} L1-SP group. Eq. 2.42, introduces a third layer (L3), continuing the recursive expansion. This hierarchical construction can be extended to an arbitrary number of layers. The expansion coefficients at each layer are labeled $A_{j_1},...,j_p(t)$ for L1, $B^{(k,jk)}_{i_1,\dots,i_{Q(k)}}(t)$ for L2, and $C^{(k,q,iq)}_{\alpha_1,\dots,\alpha_{M(k,q)}}(t)$ for L3. At the deepest level, the SPFs are represented using fixed (time-independent) basis functions. Throughout this thesis, all quantum dynamical calculations are performed using the Heidelberg MCTDH program package[82].

Chapter 3

Photoionization Bands of Cyanogen: Multi-Mode Vibronic Coupling and Renner-Teller Effects

ABSTRACT

Multi-mode vibronic coupling in the $\widetilde{X}^2\Pi_g$, $\widetilde{A}^2\Sigma_g^+$, $\widetilde{B}^2\Sigma_u^+$ and $\widetilde{C}^2\Pi_u$ electronic states of Cyanogen radical cation ($C_2N_2^+$) is investigated with the aid of *ab initio* quantum chemistry and first principles quantum dynamics methods. The electronic degenerate states of Π symmetry of $C_2N_2^+$ undergo Renner-Teller (RT) splitting along degenerate vibrational modes of π symmetry. The RT split components form symmetry allowed conical intersections with those from nearby RT split states or with non-degenerate electronic states of Σ symmetry. A parameterized vibronic Hamiltonian is constructed using standard vibronic coupling theory in a diabatic electronic basis and symmetry rules. The parameters of the Hamiltonian are derived from *ab initio* calculated adiabatic electronic energies. The vibronic spectrum is calculated, assigned and compared with the available experimental data. The impact of various electronic coupling on the vibronic structure of the spectrum is discussed.

3.1 Introduction

Nitriles (RCN, where R is a organic group) are known to have presence in a wide range of astrophysical environments[83]. Considerable attention is paid on cyanopolyynes (HC_nN; n=3, 5, 7,...) because of their possible signatures in the interstellar medium[84;85;86;87;88]. CN radical is thought to be a predominant species in the evolution of prebiotic molecules and it was spectroscopically detected at different wavelengths in a variety of astrophysical objects like cometary coma[89;90], stellar and interstellar environments[91;92]. Symmetric cyanopolyynes (NC(C≡C)CN) are reported to be present in space and was detected by radioastronomy. Cyanogen (C_2N_2), is the smallest in the family that was reported to be observed in Titan's atmosphere[93].

The present work is aimed to study the electronic spectroscopy and nonadiabatic interactions in the low-lying electronic states of $C_2N_2^+$. At equilibrium minimum, the neutral C_2N_2 molecule belongs to the $D_{\infty h}$ symmetry point group in its electronic ground state. In linear molecules, the vibronic coupling in orbitally degenerate Π electronic states is caused by coupling between the electronic orbital angular momentum and the nuclear vibrational angular momentum associated with bending vibration. The bending of molecule in the molecular plane develops dipole moment which lifts the electronic degeneracy. Breakdown of the adiabatic approximation occurs in this situation[34]. Since the adiabatic basis fails to describe the nuclear motion of a linear molecule within its degenerate states, adiabatic approximation is inapplicable for the theory of Renner-Teller (RT) effect. In order to overcome these difficulties, a diabatic electronic basis can be used[34]. The details related to the Hamiltonian is discussed in 'Vibronic Hamiltonian' section.

Numerous experimental and theoretical investigations have been carried out on the molecular structure and infrared (IR) spectrum of the C_2N_2 molecule. The geometry of the molecule has been experimentally determined by Moller and Stoichff[94] and Maki[95]. Molecular structures, *ab initio* frequencies, IR intensities, dipole moment derivatives have been derived from quantum chemistry calculations[96]. Raman intensities of the normal modes and basis set dependence was investigated taking electron correlation into account[96]. Ionization potentials were calculated in different orders of the perturbation expansion of self-energy. The sequence of orbitals given by the Hatree-Fock (HF) calculations is $1\pi_g$, $1\pi_u$, $5\sigma_g$ and $4\sigma_u$ in

the increasing order of energy. When correlation and reorganisation effects were included, interchange of $5\sigma_g$ and $4\sigma_u$ orbitals with $1\pi_u$ was observed[97]. This is also observed for N_2 molecule where the $3\sigma_g$ and $1\pi_u$ orbitals change their energetic order when going from a HF level of low accuracy to more accurate methods[98]. The mismatch of the order of bands obtained using HF level of theory with the experimental spectra has been reported[98].

The photoelectron spectra of C_2N_2 was recorded and calibrated using the 127° electrostatic energy analyser[1] and $^2P_{1/2}$ and $^2P_{3/2}$ peaks from Xenon, respectively. Cyanogen can be easily synthesized by reacting potassium cyanide with copper sulphate in aqueous medium[1]. The first band ($\widetilde{X}^2\Pi_g$) in the photoelectron spectrum of C_2N_2 corresponds to removal of an electron from the $1\pi_g$ orbital. The $C_2N_2^+$ has a vibrational frequency of 2120 cm^{-1} which appeared in the spacing of the peaks in the $\widetilde{X}^2\Pi_g$ band. The vibrational structure of the fourth band is well interpreted as a series of doublets of simultaneous excitation of two vibrational modes. The symmetric stretching mode frequency of C-C bond is 710 cm^{-1}. The two orbitals $5\sigma_g$ and $4\sigma_u$, which are associated with the nitrogen "lone pairs" are not degenerate. Two peaks associated with these orbitals are assigned as 0←0 components of the band at 14.49 eV and 14.86 eV, respectively. According to the reports, the former one corresponds to a vibrational series with an average spacing of 0.23 eV (1860 cm^{-1}) associated with the C≡N symmetric stretching vibrational mode, ν_1[1].

Detailed study on the vibronic structure of $C_2N_2^+$ has not been reported till date to the best of our knowledge. In the present work, the ambiguity in the position of the bands obtained at the HF level of theory is resolved by using higher level *ab initio* quantum chemistry calculations. In order to achieve this goal, potential energy surfaces (PESs) of the first four low-lying $\widetilde{X}^2\Pi_g$, $\widetilde{A}^2\Sigma_g^+$, $\widetilde{B}^2\Sigma_u^+$ and $\widetilde{C}^2\Pi_u$ electronic states are calculated using equation of motion ionization potential coupled cluster singles and doubles (EOMIP-CCSD) method[13;14] with augmented-correlation consistent polarized Valence Triple Zeta (aug-cc-pVTZ) basis set[99] using CFOUR suite of program package[100]. The nuclear dynamics in the four electronic states is investigated using a vibronic coupling model derived with the aid of the standard vibronic coupling theory[34]. The latter is based on a diabatic electronic basis and a Taylor series expansion of the elements of the diabatic electronic matrix employing symmetry se-

lection rules. The nuclear dynamics calculations are performed quantum mechanically by both matrix diagonalization and wave packet propagation techniques. The vibronic energy levels and their assignments are precisely determined by the matrix diagonalization results. On the other hand, the time-dependent wave-packet (WP) propagation results yield the broad band spectra and also provide the detailed mechanistic aspects of the decay of the excited electronic states. All these calculations are carried out with the aid of multi-configuration time-dependent Hartree (MCTDH) method developed at Heidelberg[65;70;35]. The theoretical results are discussed in detail in relation to the available experimental data.

3.2 Electronic Structure Calculations

The second-order Møller-Plesset perturbation (MP2) theory[101] is used to optimize the geometry of the reference neutral C_2N_2 molecule in its electronic ground state with aug-cc-pVTZ basis set[99]. The calculations are carried out using Gaussian 09 suite of program[102]. The equilibrium geometry converged to the $D_{\infty h}$ point group symmetry and it is shown in Figure 3.1. The canonical molecular orbitals ($1\pi_g$, $1\pi_u$, $5\sigma_g$ and $4\sigma_u$ in the order of increasing energy) of the optimized configuration of C_2N_2 are shown in Figure 3.2. The optimized geometry data are given in Table 3.1 and compared with the available literature data[103;96;104;94]. At the same level of theory, harmonic vibrational frequencies (ω_i) are calculated at the equilibrium geometry of the ground electronic state. The mass-weighted normal displacement coordinates are calculated which are further multiplied by the factor $\sqrt{\omega_i/\hbar}$[105] in order to obtain them in dimensionless form (Q_i). The obtained harmonic frequency of seven vibrational modes, their symmetry and mode designation are listed in Table 3.2 along with the existing literature data[103;96;104;106;107]. The PESs of the first four low-lying electronic states of $C_2N_2^+$ are calculated along the dimensionless normal displacement coordinates of the reference electronic ground state of C_2N_2. The EOMIP-CCSD[13;14] method and the aug-cc-pVTZ basis set is used to determine the adiabatic potential energies and these calculations are carried out using CFOUR suite of program[100]. In CFOUR, the calculations are carried out in D_{2h} symmetry. The correlation table of $D_{\infty h}$ to D_{2h} is used to derive the electronic terms and symmetry representation of vibrational modes. The vertical ionization energies (VIEs) are calculated along the dimensionless normal displacement coordinates of individual vibrational mode for nuclear geometries, $Q_i = \pm 0.10$ and $\pm$ 0.25 to $\pm$ 5.0 with a spacing of 0.25.

The VIEs calculated at the equilibrium geometry of the reference state are listed in Table 3.3 and are compared with the previous reports[1]. In the MRCI calculations the active space consists of 12 electrons and 6 valence orbitals. It is clear from Table 3.3 that, our theoretical results are in good agreement with the available experimental data[1]. Also, Table 3.3 reveals that, at the vertical configuration electronic states $\widetilde{A}^2\Sigma_g^+$, $\widetilde{B}^2\Sigma_u^+$ and $\widetilde{C}^2\Pi_u$ are energetically close. Therefore, the vibronic coupling may become an important mechanism in driving the nuclear dynamics in these electronic states.

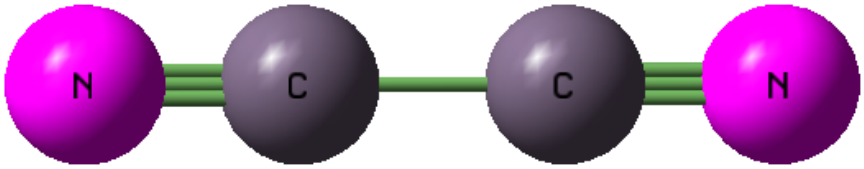

Figure 3.1: Equilibrium minimum geometry of C_2N_2 optimized at the MP2 level of theory and aug-cc-pVTZ basis set.

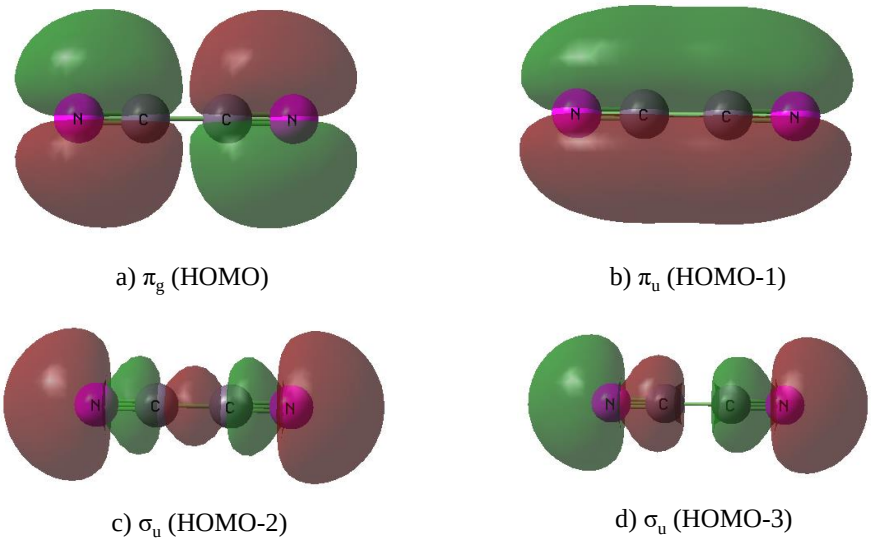

Figure 3.2: Canonical molecular orbitals (HOMO to HOMO-3) of C_2N_2. The red and green lobes shown in the above pictures represent positive and negative phases respectively.

Table 3.1: Bond lengths (in Angstrom unit) of the equilibrium structure of electronic ground state of C_2N_2 compared with the available literature data.

	This work (MP2/aug-cc-pVTZ)	MP2/6-311G* [103]	MP2/D95 [96]	B3LYP/6-311G(d) [104]	CISD/D95 [96]	Expt. [94]
C≡N	1.175	1.178	1.218	1.155	1.177	1.15
C - C	1.378	1.381	1.404	1.375	1.401	1.38

Table 3.2: Symmetry, designation and vibrational frequencies (in cm^{-1}) of C_2N_2 of its ground electronic state.

Symm.	Mode	MP2/aug-cc-pVTZ	MP2/6-311G* [103]	MP2/D95 [96]	B3LYP/6-311G(d) [104]	Expt.	Schematic description
σ_g^+	ν_1	2238	2248	2128	2440	2374 [106]	C≡N symmetric stretch
	ν_2	857	857	808	887	862 [106]	C-C symmetric stretch
σ_u^+	ν_3	2047	2047	1875	2266	2191 [106]	C≡N asymmetric stretch
π_g	ν_4	497	501	526	573	503 [107]	trans bending
π_u	ν_5	232	223	233	260	233 [107]	cis bending

Table 3.3: VIE (in eV) of the $\widetilde{X}^2\Pi_g$, $\widetilde{A}^2\Sigma_g^+$, $\widetilde{B}^2\Sigma_u^+$ and $\widetilde{C}^2\Pi_u$ states of $C_2N_2^+$ calculated at the reference equilibrium geometry of C_2N_2 and compared with the available experimental data.

States	$\widetilde{X}^2\Pi_g$	$\widetilde{A}^2\Sigma_g^+$	$\widetilde{B}^2\Sigma_u^+$	$\widetilde{C}^2\Pi_u$	Method
VIE	13.64	14.72	15.12	15.98	EOMIP-CCSD
	13.33	14.79	15.21	15.46	OVGF
	13.44	15.52	15.92	15.96	MRCI
	13.36	14.49	14.86	15.47	Expt. [1]

3.3 Vibronic Hamiltonian

A vibronic Hamiltonian of the coupled $\widetilde{X}^2\Pi_g$-$\widetilde{A}^2\Sigma_g^+$-$\widetilde{B}^2\Sigma_u^+$-$\widetilde{C}^2\Pi_u$ electronic states of $C_2N_2^+$ is developed here. Dimensionless normal displacement coordinates of vibrational modes introduced in the previous section, symmetry selection rule and a diabatic electronic basis are employed in the construction [11]. Irreducible representations of seven vibrational modes of

C_2N_2 in $D_{\infty h}$ equilibrium point group read Eq. 3.1.

$$\Gamma_{vib} = 2\sigma_g^+ + \sigma_u^+ + \pi_g + \pi_u \tag{3.1}$$

In the $D_{\infty h}$ point group, the symmetrized direct product of the electronic states Π_g, Σ_g^+, Σ_u^+ and Π_u reads

$$\Pi_{g/u} \otimes \Pi_{g/u} = \delta_g + \sigma_g^+ \tag{3.2a}$$

$$\Pi_g \otimes \Pi_u = \delta_u + \sigma_u^+ \tag{3.2b}$$

$$\Pi_{g/u} \otimes \Sigma_{g/u}^+ = \pi_g \tag{3.2c}$$

$$\Pi_{g/u} \otimes \Sigma_{u/g}^+ = \pi_u \tag{3.2d}$$

$$\Sigma_g^+ \otimes \Sigma_u^+ = \sigma_u^+ \tag{3.2e}$$

The Condon active totally symmetric (σ_g^+) vibrational modes, cannot lift the degeneracy of Π_g as well as Π_u electronic states. However, the orbital degeneracy can be lifted in first order by the vibrational modes of δ symmetry. Because of the absence of δ symmetry vibrational modes in linear systems, the first-order coupling between the components of Π state vanishes[108]. However since, $(\pi_g)^2 = (\pi_u)^2 = \delta_g$, they can be coupled in second-order through the vibrational modes of π symmetry. This leads to a lifting of the degeneracy of Π states and gives rise to the RT effect. From the symmetry rules given in Eqs. 3.2a-3.2e, it can be seen that the components of the RT split Π states can undergo coupling among themselves and also with the non-degenerate Σ states along vibrational modes of π symmetry. The σ_u^+ vibrational modes, can give rise to first-order coupling between the Σ states. Based on the stated coupling recipe, the vibronic Hamiltonian is constructed in a diabatic electronic basis

following standard vibronic coupling theory and can be expressed symbolically as

$$\mathcal{H} = \mathcal{H}_0\mathbf{1_6} + \begin{pmatrix} H_{\widetilde{X}x} & H_{\widetilde{X}x-\widetilde{X}y} & H_{\widetilde{X}x-\widetilde{A}} & H_{\widetilde{X}x-\widetilde{B}} & H_{\widetilde{X}x-\widetilde{C}x} & 0 \\ & H_{\widetilde{X}y} & H_{\widetilde{X}y-\widetilde{A}} & H_{\widetilde{X}y-\widetilde{B}} & 0 & H_{\widetilde{X}y-\widetilde{C}y} \\ & & H_{\widetilde{A}} & H_{\widetilde{A}-\widetilde{B}} & H_{\widetilde{A}-\widetilde{C}x} & H_{\widetilde{A}-\widetilde{C}y} \\ & & & H_{\widetilde{B}} & H_{\widetilde{B}-\widetilde{C}x} & H_{\widetilde{B}-\widetilde{C}y} \\ & & & & H_{\widetilde{C}x} & H_{\widetilde{C}x-\widetilde{C}y} \\ & & & & & H_{\widetilde{C}y} \end{pmatrix} \tag{3.3}$$

In Eq. (3.3) , $\mathcal{H}_0 = \mathcal{T}_N + \mathcal{V}_0$, represents the unperturbed Hamiltonian of the reference electronic ground state of C_2N_2. Its elements within the harmonic approximation are given in Eqs. 3.4 and 3.5 as

$$\mathcal{T}_N = -\frac{1}{2}\sum_{i\,\in\,\sigma_g^+,\,\sigma_u^+}\omega_i\frac{\partial^2}{\partial Q_i^2} - \frac{1}{2}\sum_{i\,\in\,\pi_g,\,\pi_u}\omega_i\left(\frac{\partial^2}{\partial Q_{ix}^2}+\frac{\partial^2}{\partial Q_{iy}^2}\right) \tag{3.4}$$

and

$$\mathcal{V}_0 = \frac{1}{2}\sum_{i\,\in\,\sigma_g^+,\,\sigma_u^+}\omega_i Q_i^2 + \frac{1}{2}\sum_{i\,\in\,\pi_g,\,\pi_u}\omega_i\left(Q_{ix}^2+Q_{iy}^2\right) \tag{3.5}$$

In Eq. (3.3), the term $\mathbf{1_6}$ represents a 6×6 diagonal unit matrix. The diagonal elements of matrix Hamiltonian in Eq. (3.3) represent the diabatic energies of the above mentioned electronic states of the radical cation and the off-diagonal elements represent the coupling between electronic states. Around the optimized minimum geometry at, **Q=0**, the matrix elements are expanded in a standard Taylor series as given below[11]

$$\begin{aligned} H_{j_x/j_y} = {} & E_0^j + \sum_{i\,\in\,\sigma_g^+}\kappa_i^j Q_i + \sum_{i\,\in\,\sigma_g^+,\,\sigma_u^+}\gamma_i^j Q_i^2 + \sum_{i\,\in\,\sigma_g^+}\zeta_i^j Q_i^3 + \sum_{i\,\in\,\sigma_u^+}\xi_i^j Q_i^4 \\ & + \sum_{i\,\in\,\pi_g,\,\pi_u}[\gamma_i^j(Q_{i_x}^2+Q_{i_y}^2)] + \sum_{i\,\in\,\pi_g,\,\pi_u}[\xi_i^j(Q_{i_x}^2+Q_{i_y}^2)^2] + \sum_{i\,\in\,\pi_g,\,\pi_u}[\sigma_i^j(Q_{i_x}^2+Q_{i_y}^2)^3] \\ & \pm \sum_{i\,\in\,\pi_g,\,\pi_u}\eta_i^j(Q_{i_x}^2-Q_{i_y}^2) \pm \sum_{i\,\in\,\pi_g,\,\pi_u}\delta_i^j(Q_{i_x}^4-Q_{i_y}^4) \pm \sum_{i\,\in\,\pi_g,\,\pi_u}\rho_i^j(Q_{i_x}^6+Q_{i_x}^4Q_{i_y}^2-Q_x^2Q_y^4-Q_{i_y}^6) \\ & ;\, j \in \widetilde{X},\widetilde{C} \end{aligned} \tag{3.6}$$

$$H_j = E_0^j + \sum_{i \in \sigma_g^+} \kappa_i^j Q_i + \sum_{i \in \sigma_g^+,\, \sigma_u^+} \gamma_i^j Q_i^2 + \sum_{i \in \pi_g,\, \pi_u} [\gamma_i^j (Q_{i_x}^2 + Q_{i_y}^2)] + \sum_{i \in \pi_g,\, \pi_u} [\xi_i^j (Q_{i_x}^2 + Q_{i_y}^2)^2] + \sum_{i \in \pi_g,\, \pi_u} [\sigma_i^j (Q_{i_x}^2 + Q_{i_y}^2)^3] \quad ; j \in \widetilde{A}, \widetilde{B} \tag{3.7}$$

$$H_{j_x - j_y} = \sum_{i \in \pi_g,\, \pi_u} [2\eta_i^j (Q_{i_x} Q_{i_y}) + 2\delta_i^j (Q_{i_x}^3 Q_{i_y} + Q_{i_x} Q_{i_y}^3) + 2\rho_i^j (Q_{i_x}^5 Q_{i_y} + Q_{i_x} Q_{i_y}^5 + 2Q_{i_x}^3 Q_{i_y}^3)] \quad ; j \in \widetilde{X}, \widetilde{C} \tag{3.8}$$

$$H_{j-k} = \sum_{i \in \sigma_u^+} \lambda_i^{j-k} Q_i \quad ; j-k \in \widetilde{X} - \widetilde{C}, \widetilde{A} - \widetilde{B} \tag{3.9}$$

$$H_{j_x - k/j_y - k} = \sum_{i \in \pi_{g/u}} \lambda_i^{j-k} Q_{ix/iy} \; ; j-k \in \widetilde{X} - \widetilde{A}, \widetilde{X} - \widetilde{B}, \widetilde{A} - \widetilde{C}, \widetilde{B} - \widetilde{C} \tag{3.10}$$

In Eqs. (6-10), the VIE for the *j*th electronic state is given by E_0^j. The components of degenerate vibrational modes and electronic states are labelled with *x* and *y*. The quantity, κ_i^j is the linear intrastate coupling parameter along the vibrational modes of σ_g^+ symmetry. The second, fourth and sixth-order RT coupling parameters of the *j*th electronic state along the degenerate vibrational modes (π_g and π_u) are denoted by η_i^j, δ_i^j and ρ_i^j, respectively. The linear inter-state coupling parameter of the *j* and *k* electronic states along the *i*th vibrational mode is given by λ_i^{j-k}. For the *j*th electronic state along the *i*th vibrational mode, the second, third, fourth and sixth-order intrastate coupling parameters are given by γ_i^j, ζ_i^j, ξ_i^j and σ_i^j, respectively. The + and - signs are for the *x* and *y* components of the degenerate state, respectively. By using the invariance principle for various symmetry operations, relative signs are assigned to all the elements of the diabatic electronic Hamiltonian matrix. A full derivation of the RT Hamiltonian of the Π state is given in the Appendix I.

3.4 Nuclear Dynamics

The spectral intensity of the $\widetilde{X}^2\Pi_g$, $\widetilde{A}^2\Sigma_g^+$, $\widetilde{B}^2\Sigma_u^+$ and $\widetilde{C}^2\Pi_u$ electronic states of $C_2N_2^+$ is calculated by the Fermi's golden rule

$$I(E) = \sum_{v} \left| \langle \Psi_v^f | \hat{T} | \Psi_0^i \rangle \right|^2 \delta(E - E_v^f + E_0^i). \tag{3.11}$$

In Eq. (11), the wave function of the initial vibronic ground state of C_2N_2 (with energy E_0^i), is represented by $|\Psi_0^i\rangle$, and the wave function of the final (f) vibronic state with energy E_v^f is represented by $|\Psi_v^f\rangle$.

The quantity $\hat{T}$ represents the transition dipole operator. The ground vibronic state is written as

$$|\Psi_0^i\rangle \quad = \quad |\Phi_0^0\rangle|\mathbf{0}\rangle, \tag{3.12}$$

where $|\Phi_0^0\rangle$, denote the diabatic electronic state and $|\mathbf{0}\rangle$ is the ground vibrational component of the wave function of the reference electronic ground state C_2N_2. The vibrational component ($|\mathbf{0}\rangle$) in Eq. (12), is defined to be the direct product of harmonic oscillator functions of the reference state. A matrix diagonalization method using the Lanczos algorithm is used to calculate $I(E)$ in the time-independent framework[109;110]. The eigenvalues are the exact position of the vibronic energy levels and squared first component of the Lanczos eigenvectors defines the relative intensity[11;111;66].

The spectral intensity transforms to the Fourier transform of time autocorrelation function of the WP evolving on the final electronic state in a time-dependent framework in Eqs. (13-14) as

$$I(E) \approx 2Re \sum_{m=1}^{6} \int_0^\infty e^{iEt/\hbar} \langle \chi^m(0)|\tau^\dagger \; e^{-i\mathcal{H}t/\hbar} \; \tau|\chi^m(0)\rangle dt, \tag{3.13}$$

$$\approx 2Re \sum_{m=1}^{6} |\tau^m|^2 \int_0^\infty e^{iEt/\hbar} \; C^m(t) \; dt. \tag{3.14}$$

The time autocorrelation function of the WP constructed on the m^{th} electronic state of $C_2N_2^+$ is given by, $C^m(t) = \langle \Psi^m(t=0)|\Psi^m(t)\rangle$. At $t = 0$, $|\Psi_0^i\rangle$ is the initial WP, which is vertically promoted to the final state $|\Psi_0^m\rangle$, and evolves thereafter according to the time-dependent Schrödinger equation. The transition dipole matrix is represented by τ: $\tau^\dagger = (\tau^{\widetilde{X}}, \tau^{\widetilde{A}}, \tau^{\widetilde{B}}$ and $\tau^{\widetilde{C}})$, where $\tau^m = \langle \Phi^m|\hat{T}|\Phi^0\rangle$. In a diabatic electronic basis, the matrix elements of $\hat{T}$ are treated as constant and are assumed to be independent of the nuclear coordinates within the generalized Condon approximation[66]. Finally, by combining the partial spectra obtained by propagating WP on individual electronic states, the composite spectrum is obtained.

Using the MCTDH method, WP propagation calculations are done[65;70;35]. The multiset formalism of MCTDH allows vibrational degrees of freedom (DOF) to be combined into a "particle" (p). Using

this ansatz the MCTDH wave function is given as

$$\Psi(q_1,...,q_p,t) \;=\; \sum_{j_1=1}^{n_1}...\sum_{j_p=1}^{n_p} A_{j_1,...j_p}(t)\prod_{k=1}^{p}\varphi_{j_k}^{(k)}(q_k,t). \tag{3.15}$$

The set of DOF combined in a single particle is $q_k = (Q_i, Q_j, ..)$, and the MCTDH expansion coefficients are $A_{j_1,...j_p}$ in Eq. (15). The single particle functions (SPFs), $\varphi_{jk}^{(k)}$, are the time-dependent basis functions, and the number of SPFs are denoted by n_k. SPFs are expressed in a primitive time-independent basis to solve the MCTDH equations of motion. The primitive basis is represented in a discrete variable representation (DVR) with HO basis. Readers are referred to the original research articles[65;70;35] for further information on this method and algorithm.

3.5 Results and Discussion

3.5.1 Adiabatic potential energy surfaces and Renner-Teller splitting

In this section, the topography of the adiabatic PESs of the first four electronic states of $C_2N_2^+$ is examined. The energy order of the electronic states is $\widetilde{X}^2\Pi_g < \widetilde{A}^2\Sigma_g^+ < \widetilde{B}^2\Sigma_u^+ < \widetilde{C}^2\Pi_u$. The potential curves of the electronic states mentioned above are examined along the dimensionless normal displacement coordinates of both totally symmetric (σ_g^+) and degenerate (π_g and π_u) vibrational modes. Along the coordinate of σ_g^+ vibrational mode, one dimensional cuts of the multidimensional PESs of $C_2N_2^+$ are shown in panels (a) and (b) of Figure 3.3. The *ab initio* computed adiabatic electronic energies and those obtained using the vibronic model developed in this study are shown by dots and solid lines, respectively, in these plots. As can be seen from Figure 3.3, the calculated *ab initio* energies are well represented by the present theoretical model. We find, up to a third-order Taylor expansion of the Hamiltonian is appropriate along the σ_g^+ vibrational modes to accurately reproduce the *ab initio* energies. The totally symmetric (σ_g^+) vibrational modes do not lift the electronic degeneracy of the $\widetilde{X}^2\Pi_g$ and $\widetilde{C}^2\Pi_u$ electronic states. But, they can tune the energy minimum relative to the equilibrium minimum of the electronic ground state of C_2N_2 ($Q = 0$) and therefore modify the energy gap between the electronic states. In contrast to the σ_g^+ vibrational modes, the degenerate π_g and the π_u vibrational modes split the electronic degeneracy of the $\widetilde{X}^2\Pi_g$ and $\widetilde{C}^2\Pi_u$ electronic states when distorted along them. Such splitting can be seen in the potential energy curves plotted in panels (a) and (b) of Figure 3.4 along the degenerate π_g and π_u modes, respectively. It can be seen from Figures 3.3 and 3.4 that, both the degenerate $\widetilde{X}^2\Pi_g$ and $\widetilde{C}^2\Pi_u$ electronic states are energetically well separated from the $\widetilde{A}^2\Sigma_g^+$ and $\widetilde{B}^2\Sigma_u^+$ states [cf. Table 3.3]. In case of $\widetilde{X}^2\Pi_g$ and $\widetilde{C}^2\Pi_u$ electronic states, the coupling strength ($k^2/2\omega^2$) of ν_1 and ν_2 vibrational modes is quite large [cf. Table 3.4]. Along ν_1 vibrational mode,

$\widetilde{X}^2\Pi_g$ electronic state undergoes curve crossing with $\widetilde{A}^2\Sigma_g^+$ and $\widetilde{B}^2\Sigma_u^+$ states [cf. Figure 3.3(a)]. The minimum of the degenerate $\widetilde{X}^2\Pi_g$ state shifts (relative to equilibrium at $Q = 0$) to a large extent along the strongest Condon active, C≡N symmetric stretching vibrational mode (ν_1). The minimum of the $\widetilde{C}^2\Pi_u$ electronic state shifts towards the negative displacement along the ν_1 mode, just as the $\widetilde{X}^2\Pi_g$ state. The $\widetilde{X}^2\Pi_g$ electronic state is energetically well separated from the other states along the C-C symmetric stretching mode (ν_2). It can be seen from Figure 3.3(b), that the equilibrium minimum of the $\widetilde{B}^2\Sigma_u^+$ and $\widetilde{C}^2\Pi_u$ states shifts in opposite directions along C-C symmetric stretching vibrational mode (ν_2). The displacement of the reference equilibrium minimum of both $\widetilde{B}^2\Sigma_u^+$ and $\widetilde{C}^2\Pi_u$ states are largest along ν_2 which appears to be a strong Condon active mode in these states [cf. Tables 3.4 and 3.5]. The adiabatic PESs along the σ_u^+ mode are shown in Figure 3.5.

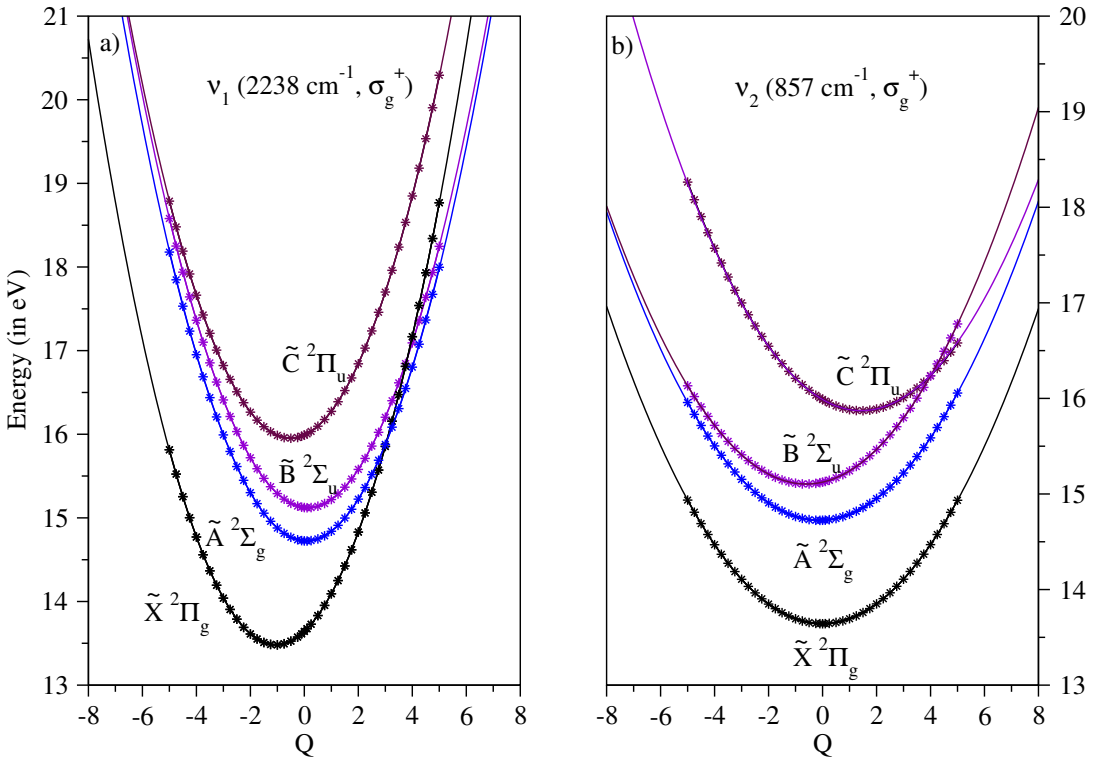

Figure 3.3: Adiabatic potential energy cuts of the $\widetilde{X}^2\Pi_g$, $\widetilde{A}^2\Sigma_g^+$, $\widetilde{B}^2\Sigma_u^+$ and $\widetilde{C}^2\Pi_u$ electronic states of $C_2N_2^+$ along the totally symmetric (σ_g^+) vibrational modes ν_1 and ν_2. The energies calculated from the present vibronic model and computed *ab initio* energies are represented by solid lines and points, respectively.

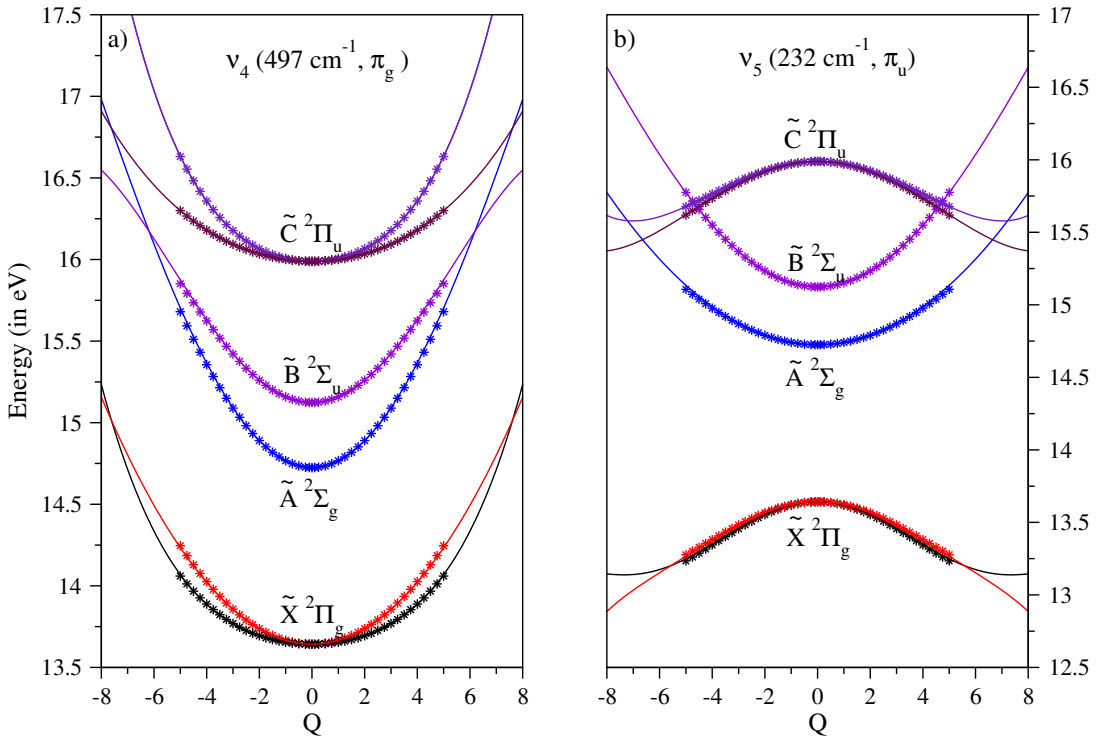

Figure 3.4: Adiabatic potential energy cuts of the $\widetilde{X}^2\Pi_g$, $\widetilde{A}^2\Sigma_g^+$, $\widetilde{B}^2\Sigma_u^+$ and $\widetilde{C}^2\Pi_u$ electronic states of $C_2N_2^{+}$ along the degenerate π_g and π_u vibrational modes. The energies obtained from the present vibronic model and computed *ab initio* energies are represented by solid lines and points, respectively.

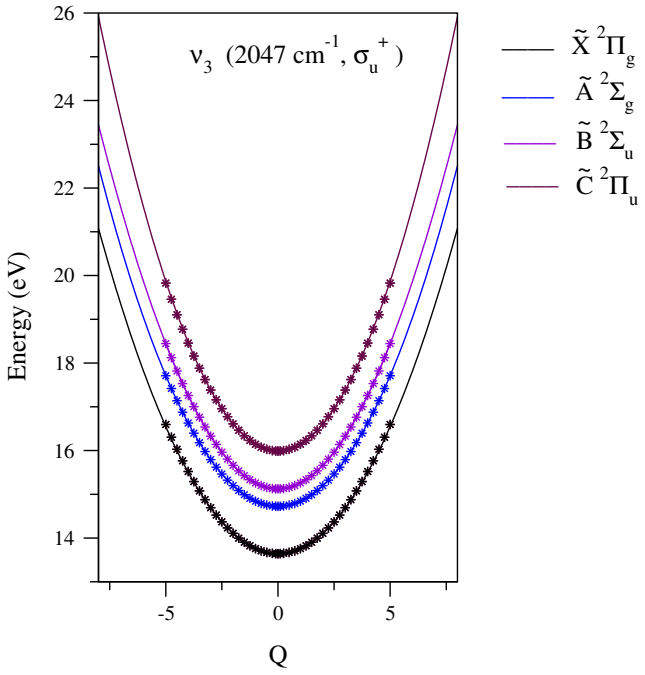

Figure 3.5: Adiabatic potential energy cuts of the $\widetilde{X}^2\Pi_g$, $\widetilde{A}^2\Sigma_g^+$, $\widetilde{B}^2\Sigma_u^+$ and $\widetilde{C}^2\Pi_u$ electronic states of $C_2N_2^+$ along the σ_u^+ vibrational mode, ν_3. The energies calculated from the present vibronic model and computed *ab initio* are represented by solid lines and points, respectively.

Table 3.4: Linear (κ_i), quadratic (γ_i and η_i), cubic (ζ_i), quartic (ξ_i and δ_i) and sixth-order (σ_i and ρ_i) coupling constants of the Hamiltonian for the $\widetilde{X}^2\Pi_g$ and $\widetilde{C}^2\Pi_u$ electronic states of $C_2N_2^+$. The values in the square brackets indicate dimensionless excitation strengths. All the values are given in the eV units.

Symmetry	Mode	κ_i	γ_i (η_i)	ζ_i	ξ_i (δ_i)	σ_i (ρ_i)
$\widetilde{X}^2\Pi_g$						
σ_g^+	ν_1	0.3063 [0.61]	0.0070	-0.0004		
	ν_2	0.0004 [0.00]	-0.0014	-0.0000		
σ_u^+	ν_3	-	-0.0107	-		
π_g	ν_4	-	-0.0130(0.0058)	-	0.0001(-0.0001)	-0.0000(0.0000)
π_u	ν_5	-	-0.0361(0.0019)	-	0.0003(-0.0000)	-0.0000 (0.0000)
$\widetilde{C}^2\Pi_u$						
σ_g^+	ν_1	0.1437 [0.13]	0.0031	-0.0004		
	ν_2	-0.1635 [1.18]	-0.0041	-0.0000		
σ_u^+	ν_3	-	0.0283	-		
π_g	ν_4	-	-0.0161(0.0035)		0.0001(-0.0001)	
π_u	ν_5	-	-0.0317(0.0006)		0.0001(0.0000)	

Table 3.5: Linear (κ_i), quadratic (γ_i), cubic (ζ_i), quartic (ξ_i) and sixth-order (σ_i) coupling constants of the Hamiltonian for the $\widetilde{A}^2\Sigma_g^+$ and $\widetilde{B}^2\Sigma_u^+$ electronic states of $C_2N_2^+$. The values in the square brackets indicate dimensionless excitation strengths. All the values are given in the eV units.

Symmetry	Mode	κ_i	γ_i	ζ_i	ξ_i	σ_i
$\widetilde{A}^2\Sigma_g^+$						
σ_g^+	ν_1	-0.0195 [0.00]	-0.0042	0.0000		
	ν_2	0.0117 [0.00]	-0.0018	0.0000		
σ_u^+	ν_3	-	-0.0087	-	0.0000	
π_g	ν_4	-	-0.0108	-	-0.0001	-0.0000
π_u	ν_5	-	0.0020	-	-0.0000	-0.0000
$\widetilde{B}^2\Sigma_u^+$						
σ_g^+	ν_1	-0.0350 [0.00]	-0.0071	0.0000		
	ν_2	0.0645 [0.18]	0.0001			
σ_u^+	ν_3	-	0.0076	-	0.0000	
π_g	ν_4	-	0.0042	-	-0.0002	
π_u	ν_5	-	0.0131	-	-0.0000	

Along the coordinates of the degenerate π_g and π_u vibrational modes, the potential energy curves of $\widetilde{X}^2\Pi_g$, $\widetilde{A}^2\Sigma_g^+$, $\widetilde{B}^2\Sigma_u^+$ and $\widetilde{C}^2\Pi_u$ electronic states of $C_2N_2^+$ are plotted and shown in Figure 3.4. As in Figure 3.3, the points and the solid lines in Figure 3.4 represents the *ab initio* electronic energy data and the energy obtained from the vibronic coupling model developed in section 'Vibronic Hamiltonian', respectively. These two data sets are in excellent agreement over a large nuclear displacement. We note that upto sixth-order Taylor expansion of the Hamiltonian is found to be appropriate along the degenerate modes to represent the *ab initio* electronic energies extremely well. Distortions along the degenerate modes (π_g and π_u) split the electronic degeneracy of the $\widetilde{X}^2\Pi_g$ and $\widetilde{C}^2\Pi_u$ electronic states. The splitting of the degeneracy can be seen from Figure 3.4. It can be seen from Figure 3.4(b), that the $\widetilde{A}^2\Sigma_g^+$ and $\widetilde{B}^2\Sigma_u^+$ electronic states intersect with $\widetilde{C}^2\Pi_u$ state at longer displacement along the RT active bending vibrational mode ν_5. Also, the adiabatic PESs of both $\widetilde{X}^2\Pi_g$ and $\widetilde{C}^2\Pi_u$ electronic states along the low frequency π_u mode exhibits a non-linear equilibrium geometry. This leads to an extended progressions in both $\widetilde{X}^2\Pi_g$ and $\widetilde{C}^2\Pi_u$ vibronic bands along this mode and will be discussed later in the text. In addition, the coupling of the RT split components of $\widetilde{C}^2\Pi_u$ state seems to be strong with the $\widetilde{B}^2\Sigma_u^+$ state through the modes of π_g symmetry. The data given in Table 3.3, show that $\widetilde{A}^2\Sigma_g^+$, $\widetilde{B}^2\Sigma_u^+$ and $\widetilde{C}^2\Pi_u$ electronic states are relatively close in energy. So, vibronic coupling among them can be expected to play major role in the nuclear dynamics in these electronic states. The interplay of RT and general vibronic coupling in the manifold of $\widetilde{X}^2\Pi_g$-$\widetilde{A}^2\Sigma_g^+$-$\widetilde{B}^2\Sigma_u^+$-$\widetilde{C}^2\Pi_u$ electronic states of $C_2N_2^+$ on its vibronic structure is discussed in section 'Interanal Conversion Dynamics'.

Energetic minimum of RT coupled surfaces, $V_{min}^{(c)}$, and the minimum of other intersections are calculated with the help of MATHEMATICA program package[112]. The results obtained are listed in Table 3.6 in a matrix array. In the latter, the numbers in the diagonal and off-diagonal represent the minimum of a state and the minimum of the intersection seam, respectively. The energetic minimum of $\widetilde{X}^2\Pi_g$, $\widetilde{A}^2\Sigma_g^+$, $\widetilde{B}^2\Sigma_u^+$ and $\widetilde{C}^2\Pi_u$ states occur at ∼13.47 eV, ∼14.72 eV, ∼15.10 eV and ∼15.83 eV, respectively. The $\widetilde{X}^2\Pi_g$-$\widetilde{A}^2\Sigma_g^+$, $\widetilde{X}^2\Pi_g$-$\widetilde{B}^2\Sigma_u^+$ and $\widetilde{X}^2\Pi_g$-$\widetilde{C}^2\Pi_u$ intersection minimum occurs at high energy. The data suggest that, the coupling of $\widetilde{X}^2\Pi_g$ state with $\widetilde{A}^2\Sigma_g^+$, $\widetilde{B}^2\Sigma_u^+$ and $\widetilde{C}^2\Pi_u$ states will have insignificant role in the nuclear dynamics of the $\widetilde{X}^2\Pi_g$ electronic state. The energetic minimum of the $\widetilde{A}^2\Sigma_g^+$, $\widetilde{B}^2\Sigma_u^+$ and $\widetilde{C}^2\Pi_u$ electronic states are relatively close to each other, the seam minimum of $\widetilde{A}^2\Sigma_g^+$-$\widetilde{B}^2\Sigma_u^+$ intersections is at higher energy whereas, the seam minimum of $\widetilde{B}^2\Sigma_u^+$-$\widetilde{C}^2\Pi_u$ intersections occurs just ∼0.18 eV above the $\widetilde{C}^2\Pi_u$ state minimum. Also, coupling between $\widetilde{B}^2\Sigma_u^+$-$\widetilde{C}^2\Pi_u$ electronic states occurs through π_g vibrational mode and this coupling is expected to have a significant role in the nuclear dynamics.

Table 3.6: Estimated energy (in eV) of the equilibrium minimum (diagonal elements) and minimum of the seam of various conical intersections (off-diagonal elements) of the electronic states of $C_2N_2^+$ within a quadratic coupling model.

	$\widetilde{X}^2\Pi_g$	$\widetilde{A}^2\Sigma_g^+$	$\widetilde{B}^2\Sigma_u^+$	$\widetilde{C}^2\Pi_u$
$\widetilde{X}^2\Pi_g$	13.47	16.48	17.66	25.15
$\widetilde{A}^2\Sigma_g^+$	-	14.72	18.49	17.10
$\widetilde{B}^2\Sigma_u^+$	-	-	15.10	16.01
$\widetilde{C}^2\Pi_u$	-	-	-	15.83

3.5.2 Vibronic band structure of the $\widetilde{X}^2\Pi_g$, $\widetilde{A}^2\Sigma_g^+$, $\widetilde{B}^2\Sigma_u^+$ and $\widetilde{C}^2\Pi_u$ states Of $C_2N_2^+$

Uncoupled state spectrum and the Renner-Teller effect in $\widetilde{C}^2\Pi_u$ electronic state :

The vibrational energy level structure of the uncoupled $\widetilde{X}^2\Pi_g$, $\widetilde{A}^2\Sigma_g^+$, $\widetilde{B}^2\Sigma_u^+$ and $\widetilde{C}^2\Pi_u$ states of $C_2N_2^+$ is examined first in order to illustrate the influence of nonadiabatic coupling on the vibronic structure of the photoionization bands of C_2N_2. The calculations are carried out by taking two totally symmetric vibrational modes (ν_1 and ν_2) in a time-independent matrix diagonalization approach using Lanczos algorithm[109]. The convergence of the stick spectrum is ensured in terms of the vibrational basis and the number of Lanczos iterations. Table 3.7 lists the vibrational basis functions utilized in each computation. The calculated stick spectrum of $\widetilde{X}^2\Pi_g$ and $\widetilde{C}^2\Pi_u$ states are convoluted with 30 meV, $\widetilde{A}^2\Sigma_g^+$ with 15 meV and $\widetilde{B}^2\Sigma_u^+$ with 25 meV full width at the half maximum (FWHM) Lorentzian line shape function to generate the spectral envelopes shown in the respective figures. Later in the text, the coupling among the states is included, and discussed in relation to the experimental results. Panels (a) and (b) of Figure 3.6, portray the uncoupled spectrum of non-degenerate $\widetilde{A}^2\Sigma_g^+$ and $\widetilde{B}^2\Sigma_u^+$ states, respectively. The fundamentals of C-C, ν_2 and C≡N, ν_1 symmetric vibrational modes are excited in both the states. Peak spacings of ∼842 cm^{-1}, ∼2205 cm^{-1} and ∼857 cm^{-1}, ∼2182 cm^{-1} corresponding to the fundamental of ν_2 and ν_1 vibrational modes are found in the spectrum of $\widetilde{A}^2\Sigma_g^+$ and $\widetilde{B}^2\Sigma_u^+$ electronic states, respectively. The excitation of ν_2 vibration forms dominant progressions in the uncoupled state spectrum of $\widetilde{A}^2\Sigma_g^+$ and $\widetilde{B}^2\Sigma_u^+$ electronic states. The overtones of ν_2 are found at ∼1684 cm^{-1} and ∼1715 cm^{-1} in the spectrum of $\widetilde{A}^2\Sigma_g^+$ and $\widetilde{B}^2\Sigma_u^+$ states, respectively. In case of $\widetilde{B}^2\Sigma_u^+$ electronic state, a combination peak of ν_1 and ν_2 appears at ∼3039 cm^{-1}.

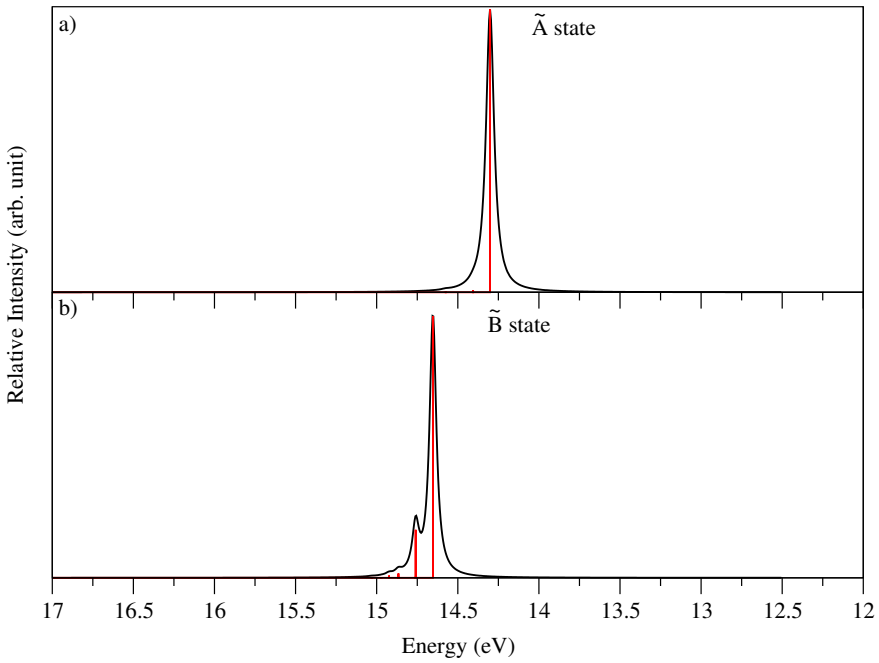

Figure 3.6: Vibrational energy level spectrum of the uncoupled $\widetilde{A}^2\Sigma_g^+$ (panel (a)) and $\widetilde{B}^2\Sigma_u^+$ (panel (b)) electronic states $C_2N_2^+$ computed with the vibrational modes of σ_g^+ symmetry.

Table 3.7: Number of HO basis functions along vibrational modes, the dimension of the secular matrix and the number of Lanczos iterations used to calculate the converged theoretical stick spectrum of $\widetilde{X}^2\Pi_g$ and $\widetilde{C}^2\Pi_u$ states of $C_2N_2^+$ shown in various figures.

Vibrational modes	(HO basis functions)	Dimension of the matrix	Lanczos iterations	Figure(s)
ν_1, ν_2	(38,26)	1008	10000	panel a of Figure 3.6
	(26,38)	1008	10000	panel b of Figure 3.6
	(26,38)	1008	10000	panel a of Figure 3.7
ν_{4x}, ν_{4y}	(26,38)	1008	10000	panel b of Figure 3.7
ν_{5x}, ν_{5y}	(38,26)	1008	10000	panel c of Figure 3.7

In panel (a) of Figure 3.7, the vibronic band structure of the degenerate $\widetilde{X}^2\Pi_g$ and $\widetilde{C}^2\Pi_u$ electronic states calculated with symmetric vibrational modes is shown. The symmetric C≡N stretch, ν_1, forms an extended progression in the $\widetilde{X}^2\Pi_g$ electronic state, as shown in Figure 3.7(a). The fundamental, first overtone and the second overtone of this vibrational mode appear at ∼2304, ∼4609 and ∼6914

cm^{-1}, respectively. The fundamentals of ν_1 and ν_2 appear at ∼2261 and ∼886 cm^{-1}, respectively, in the $\widetilde{C}^2\Pi_u$ band. In addition to the fundamental modes in the $\widetilde{C}^2\Pi_u$ state, the first overtone, second overtone and third overtone of ν_2 appear at ∼1772, ∼2658 and ∼3544 cm^{-1}, respectively. Several combination peaks of ν_1 and ν_2 vibrational modes are also identified in this state.

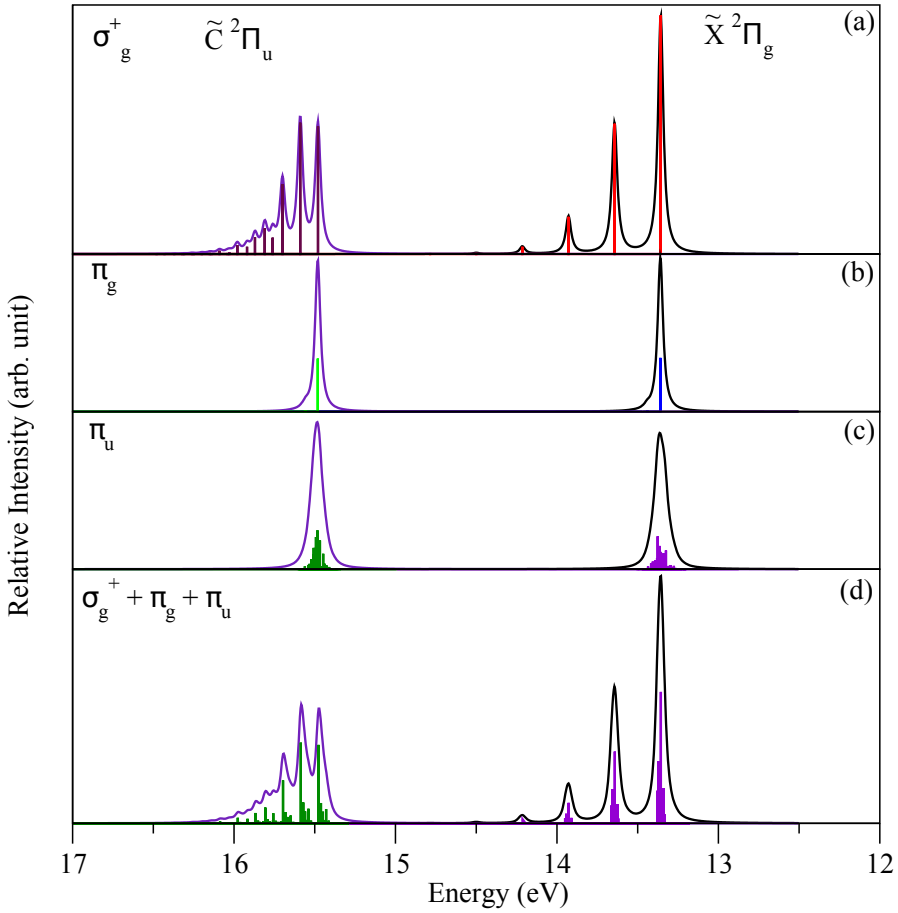

Figure 3.7: Vibrational energy spectrum of the $\widetilde{X}^2\Pi_g$ and $\widetilde{C}^2\Pi_u$ electronic states of $C_2N_2^+$ computed with the symmetric σ_g^+ (panel (a)), degenerate π_g and π_u (panel (b) and panel (c) vibrational modes. The convoluted spectrum of the panels (a), (b) and (c) is shown in panel (d) (see text for details)..

The Hamiltonian of the degenerate electronic states ($\widetilde{X}^2\Pi_g$ and $\widetilde{C}^2\Pi_u$) are separable in terms of symmetric (σ_g^+) and degenerate (π_g and π_u) vibrational modes when the bilinear coupling terms are ignored. Accordingly, the partial spectra computed with the totally symmetric [cf. panel (a) of Figure 3.7] and degenerate (π_g and π_u) [cf. panels (b) and (c) of Figure 3.7] vibrational modes separately, can be convoluted to obtain the composite vibronic band structure of the state. The composite vibronic structure of the $\widetilde{X}^2\Pi_g$ and $\widetilde{C}^2\Pi_u$ states, presented in panel (d) of Figure 3.7, reveals a weak contribution of the degenerate vibrational modes. The entire spectral envelope is similar to that obtained with

the symmetric vibrational modes as shown panel (a) of Figure 3.7. As discussed in previous section, the PESs, of both $\widetilde{X}^2\Pi_g$ and $\widetilde{C}^2\Pi_u$ states along π_u mode exhibits a non-linear equilibrium geometry [cf. Figure 3.4(b). The results obtained in the dynamics calculations are shown in Figure 6. It is to be noted that π_u mode exhibits an extended vibrational progression and its impact on the overall band structure is very small because of low intensity of individual vibronic lines. The experimental photoelectron bands of cyanogen[1] reveal that the bands due to $\widetilde{X}^2\Pi_g$ and $\widetilde{C}^2\Pi_u$ electronic states exhibit considerable vibrational structure, whereas, that due to $\widetilde{A}^2\Sigma_g^+$ and $\widetilde{B}^2\Sigma_u^+$ electronic states show only little vibrational structure. The C≡N symmetric stretching, ν_1 mode is excited in the $\widetilde{X}^2\Pi_g$ state and the C-C symmetric stretching mode, ν_2 forms dominant progression in the $\widetilde{C}^2\Pi_u$ electronic state [cf. Table 3.4]. The ν_1 vibrational mode has the strongest excitation strength in the $\widetilde{X}^2\Pi_g$ state, as can be seen from the data given in Table 3.4. The fundamental of ν_1 appears at ∼2120 cm^{-1} in the experimental results of Baker *et al.*[1], as compared to the present theoretical estimate of ∼2304 cm^{-1}. The above-mentioned all the electronic states vibrational progressions are given in Table 3.8. The block-improved relaxation approach implemented in the MCTDH package is used to calculate vibronic wave functions in order to validate the assignments[113;114]. Appropriate reduced dimensional space of normal coordinates are considered and a few of the wave function probability densities of the vibrational levels $\widetilde{X}^2\Pi_g$ and $\widetilde{C}^2\Pi_u$ states are plotted in Figures 3.8 and 3.9, respectively.

Table 3.8: A few vibrational energy levels (in cm^{-1}) of the $\widetilde{X}^2\Pi_g$, $\widetilde{A}^2\Sigma_g^+$, $\widetilde{B}^2\Sigma_u^+$ and $\widetilde{C}^2\Pi_u$ electronic states of $C_2N_2^+$ obtained from the uncoupled state calculations using the EOMIP-CCSD energy data. The assignment of the levels carried out by examining the nodal pattern of the wavefunctions is included in the table.

$\widetilde{X}^2\Pi_g$		$\widetilde{A}^2\Sigma_g^+$		$\widetilde{B}^2\Sigma_u^+$		$\widetilde{C}^2\Pi_u$	
Energy	Assignment	Energy	Assignment	Energy	Assignment	Energy	Assignment
0	0_0^0	0	0_0^0	0	0_0^0	0	0_0^0
845	$\nu_{2_0}^1$	842	$\nu_{2_0}^1$	857	$\nu_{2_0}^1$	886	$\nu_{2_0}^1$
1691	$\nu_{2_0}^2$	1684	$\nu_{2_0}^2$	1715	$\nu_{2_0}^2$	1772	$\nu_{2_0}^2$
2304	$\nu_{1_0}^1$	2205	$\nu_{1_0}^1$	2181	$\nu_{1_0}^1$	2261	$\nu_{1_0}^1$
2536	$\nu_{2_0}^3$			2573	$\nu_{2_0}^3$	2658	$\nu_{2_0}^3$
4609	$\nu_{1_0}^2$			3039	$\nu_{1_0}^1+\nu_{2_0}^1$	3147	$\nu_{1_0}^1+\nu 2_0^1$
6914	$\nu_{1_0}^3$					3544	$\nu_{2_0}^4$
						4033	$\nu_{1_0}^1+\nu_{2_0}^2$
						4430	$\nu_{2_0}^5$

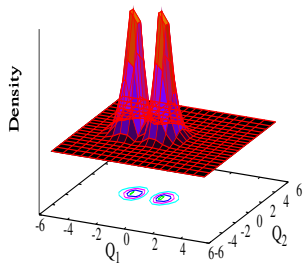

a) 2303 cm^{-1}

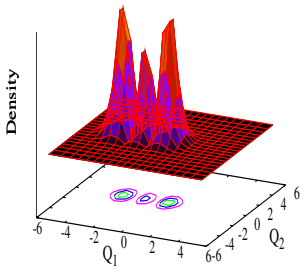

b) 4607 cm^{-1}

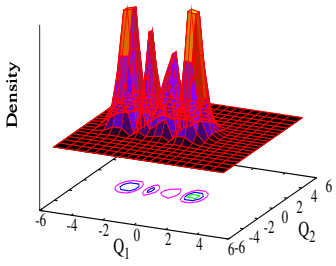

c) 6911 cm^{-1}

Figure 3.8: Probability density of vibronic wave functions of the $\widetilde{X}^2\Pi_g$ electronic state of $C_2N_2^+$ as a function of nuclear coordinate. Panels a, b, c represent the fundamental, first and second overtone of ν_1 mode, respectively.

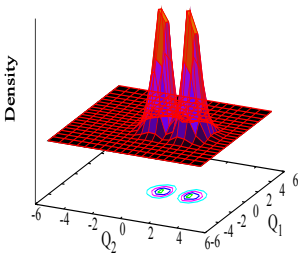

d) 885 cm^{-1}

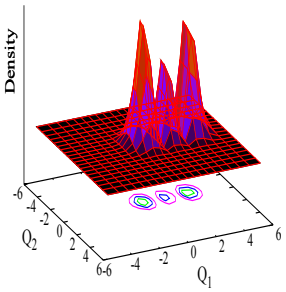

e) 1771 cm^{-1}

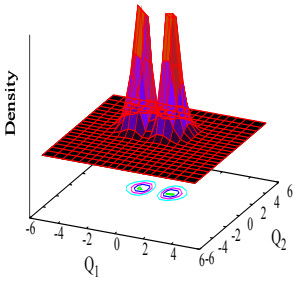

f) 2260 cm^{-1}

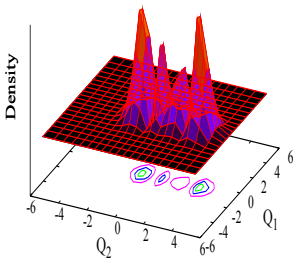

g) 2656 cm^{-1}

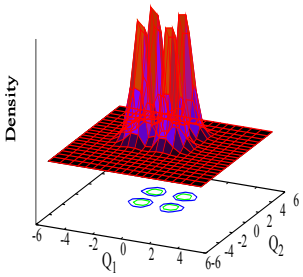

h) 3146 cm^{-1}

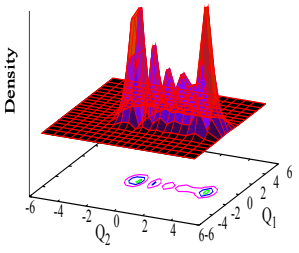

i) 3542 cm^{-1}

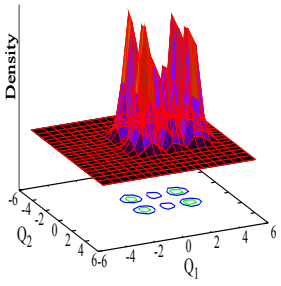

j) 4031 cm^{-1}

Figure 3.9: Probability density of vibronic wave functions of the $\widetilde{C}^2\Pi_u$ electronic state of $C_2N_2^+$ as a function of nuclear coordinate. Panels d and f represent the fundamentals of ν_2 and ν_1, respectively. panels e, g and h are first, second and third overtones of ν_2. panels i and j are combinations of modes ν_1 and ν_2.

Coupled States Spectrum and Time-Dependent Dynamics

The coupling of the $\widetilde{X}^2\Pi_g$, $\widetilde{A}^2\Sigma_g^+$, $\widetilde{B}^2\Sigma_u^+$ and $\widetilde{C}^2\Pi_u$ states through vibrational modes σ_u^+, π_g and π_u symmetry as mentioned in section 'Electronic Structure Calculations' is included in this section. The coupling parameters given in the Table 3.10 reveal that the coupling strengths of the π_g vibrational mode in the $\widetilde{X}^2\Pi_g$-$\widetilde{A}^2\Sigma_g^+$ electronic manifold is large. Whereas, along the π_u mode both $\widetilde{X}^2\Pi_g$-$\widetilde{B}^2\Sigma_u^+$ and $\widetilde{A}^2\Sigma_g^+$-$\widetilde{C}^2\Pi_u$ coupling strengths are much larger. The $\widetilde{X}^2\Pi_g$ state is energetically well separated from the $\widetilde{A}^2\Sigma_g^+$, $\widetilde{B}^2\Sigma_u^+$ and $\widetilde{C}^2\Pi_u$ states, as explained in section 'Adiabatic potential energy surfaces and Renner-Teller splitting', and its intersection with the other states occurs at higher energies [cf. Table 3.6]. As a result its coupling with the $\widetilde{A}^2\Sigma_g^+$, $\widetilde{B}^2\Sigma_u^+$ and $\widetilde{C}^2\Pi_u$ states is unlikely to have any impact on the nuclear dynamics in these states. On the basis of coupling strength and various test calculations, seven ($2\sigma_g^+$+σ_u^++π_g+π_u) modes are included in the nuclear dynamics. The dynamical calculations were carried out by propagating WP on six electronic states (two components of the RT split $\widetilde{X}^2\Pi_g$ and $\widetilde{C}^2\Pi_u$ states plus $\widetilde{A}^2\Sigma_g^+$, $\widetilde{B}^2\Sigma_u^+$ states), using the MCTDH program modules[115]. The initial WP corresponding to the vibronic ground state of the reference neutral molecule is vertically promoted to each of the ionic states and propagated in the coupled manifold of $\widetilde{X}^2\Pi_g$-$\widetilde{A}^2\Sigma_g^+$-$\widetilde{B}^2\Sigma_u^+$-$\widetilde{C}^2\Pi_u$ electronic states for 200 fs. The numerical details of the vibrational basis functions used in the WP propagation calculations are listed in Table 3.9. The time autocorrelation functions obtained from six WP calculations are combined, damped with an exponential function, $e^{(-t/\tau_r)}$ (with τ = 33 fs) and Fourier transformed to calculate the composite vibronic band. The vibronic band structure of the $\widetilde{X}^2\Pi_g$-$\widetilde{A}^2\Sigma_g^+$-$\widetilde{B}^2\Sigma_u^+$-$\widetilde{C}^2\Pi_u$ coupled electronic states of $C_2N_2^+$ obtained from these calculation is presented in Figure 3.10 along with the available experimental[1] spectrum. It can be seen from Figure 3.10 that the theoretical results are in good accord with the experimental findings. The vibronic bands of the individual electronic states are well separated and the nonadiabatic coupling effect appears to be weak. Some impact of the nonadiabatic coupling appears in the detailed band structure of the $\widetilde{A}^2\Sigma_g^+$ and $\widetilde{B}^2\Sigma_u^+$ electronic states. In addition to this we explicitly checked the convergence test of MCTDH calculations by varying the size of the basis and the corresponding results are shown in Figures 3.11 and 3.13.

Table 3.9: First column denotes the vibrational degrees of freedom (DOF) which are combined to form particles. Second column represents the number of primitive basis functions for each DOF. Third column represents the number of single particle functions (SPFs) for each electronic state.

Normal modes	Primitive Basis	SPF Basis
ν_1, ν_2	20, 10	10, 10, 8, 8, 10, 10
ν_{4x}, ν_{4y}	12, 12	10, 10, 8, 8, 10, 10
ν_{5x}, ν_{5y}	18, 18	8, 8, 8, 8, 6, 6
ν_3	16	10, 10, 8, 8, 10, 10

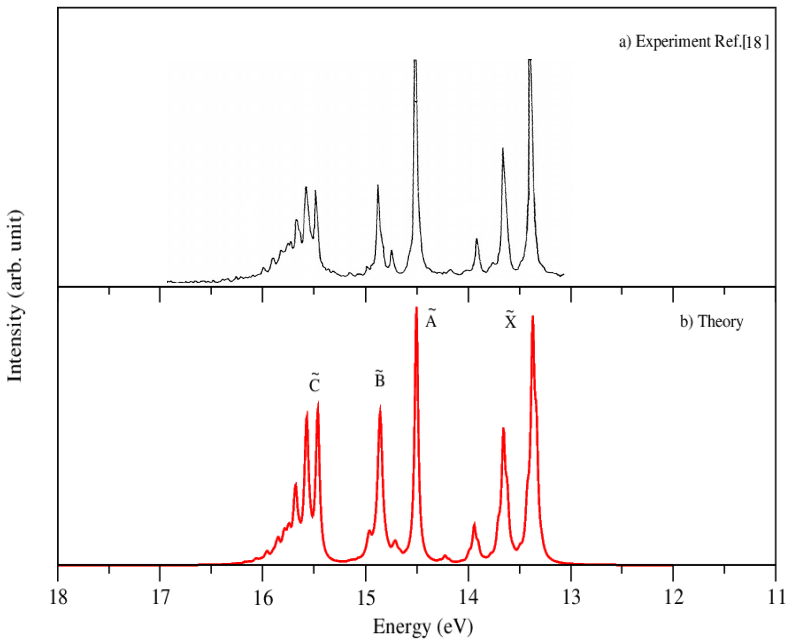

Figure 3.10: Vibronic band structure of the coupled $\widetilde{X}^2\Pi_g$-$\widetilde{A}^2\Sigma_g^+$-$\widetilde{B}^2\Sigma_u^+$-$\widetilde{C}^2\Pi_u$ electronic states of $C_2N_2^+$. Relative intensity(in arbitrary units) is plotted as a function of the energy of the vibronic states of $C_2N_2^+$. The experimental results of Ref.[1] is shown in panel (a) and the present theoretical results are shown in panel (b). The experimental spectrum in panel (a) is reproduced with permission from Ref.[1]. Copyright (2017) Royal Society (for scanned images).

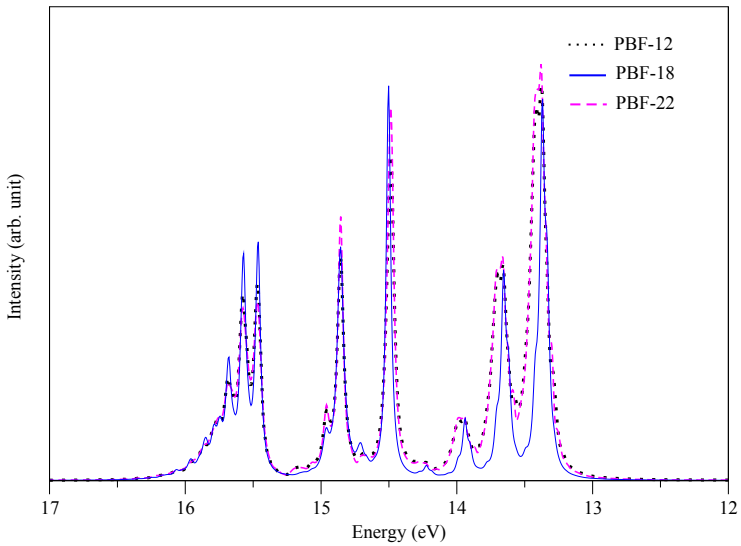

Figure 3.11: Convergence behaviour of the vibronic spectrum with respect to the number of basis functions along the π_u mode in the MCTDH calculations.

Table 3.10: Interstate coupling parameters (in eV) of the vibronic Hamiltonian of Eqs. (10) and (11) for the $\widetilde{X}^2\Pi_g$, $\widetilde{A}^2\Sigma_g^+$ $\widetilde{B}^2\Sigma_u^+$ and $\widetilde{C}^2\Pi_u$ electronic states of $C_2N_2^+$ estimated from the *ab initio* electronic structure results (see text for details).

Symmetry	Mode	Frequency	λ_i^{A-B}	λ_i^{X-C}
σ_u^+	ν_3	0.2538	0.0601(0.03)	0.2058(0.33)
π_g			λ_i^{X-A}	λ_i^{B-C}
	ν_4	0.0617	0.1260(2.08)/0.0984(1.27)	0.0915(1.09)/0.0701(0.64)
π_u			λ_i^{X-B}	λ_i^{A-C}
	ν_5	0.0288	0.2003(24.18)/0.1933(22.52)	0.1365(11.23)/0.1336(10.76)

3.6 Internal Conversion Dynamics

Time-dependence of the diabatic (column(i)) and adiabatic (column(ii)) electronic populations of $C_2N_2^+$ in the coupled six ($\widetilde{X}^2\Pi_g$-$\widetilde{A}^2\Sigma_g^+$-$\widetilde{B}^2\Sigma_u^+$-$\widetilde{C}^2\Pi_u$) states including seven ($2\sigma_g^+$+σ_u^++π_g+π_u) vibrational modes shown in Figures 3.12 and 3.14 are examined in this section in order to better understand the nonadiabatic coupling effects on the dynamics. The diabatic and adiabatic electronic populations for an initial location of the WP on the x-component of the $\widetilde{X}^2\Pi_g$ state shown in panel (a) and (b) of Figure 3.12, respectively. At t=0, the diabatic population starts from 1.0 at the x-component of the

$\widetilde{X}^2\Pi_g$ state and that of the y-component starts at 0.0, as shown in panel (a) of Figure 3.12. Because a diabatic state is an admixture of the two adiabatic states, the initial location of the WP on the diabatic x-component of the $\widetilde{X}^2\Pi_g$ state corresponds to ~50:50 population of the two (x and y) adiabatic states [cf. panel (b) of Figure 3.12]. The adiabatic population flow between x and y-components of the $\widetilde{X}^2\Pi_g$ state is much smaller in magnitude as compared to the diabatic populations. The population of the x-component flows to the y-component in time. That is, WP switches between the RT split components of the $\widetilde{X}^2\Pi_g$ state and only a small portion of the population is transferred to $\widetilde{A}^2\Sigma_g^+$, $\widetilde{B}^2\Sigma_u^+$ and $\widetilde{C}^2\Pi_u$ state in this case [cf. panel (a) of Figure 3.12].

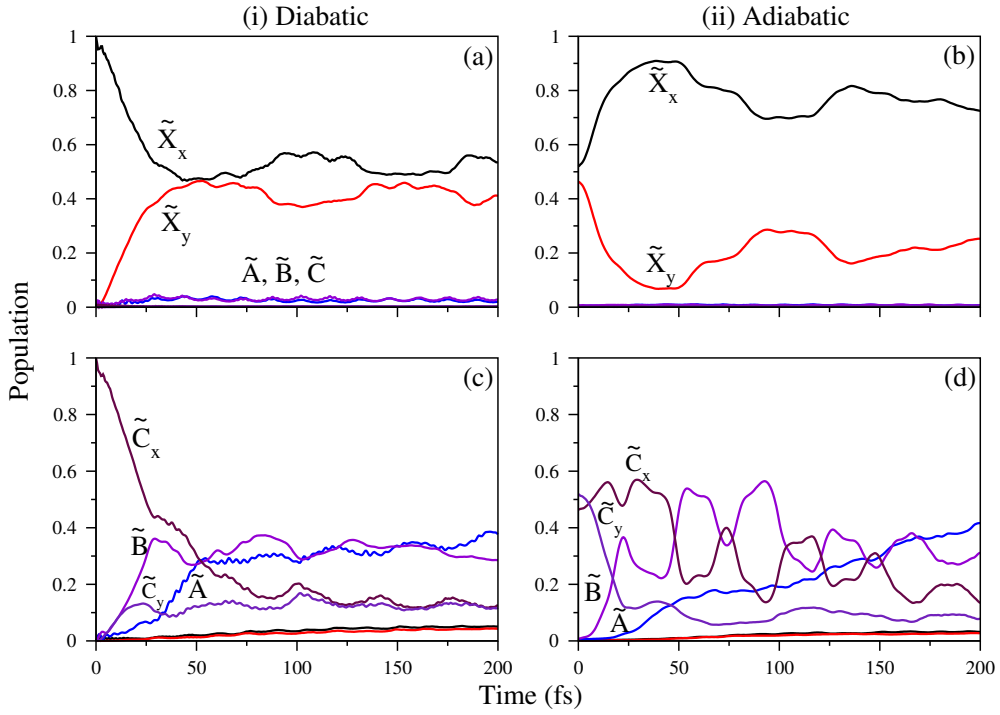

Figure 3.12: Time dependence of diabatic (panels (a) and (c)) and adiabatic (panels (b) and (d)) electron populations in the $\widetilde{X}^2\Pi_g$-$\widetilde{A}^2\Sigma_g^+$-$\widetilde{B}^2\Sigma_u^+$-$\widetilde{C}^2\Pi_u$ coupled states nuclear dynamics of $C_2N_2^+$. The initial (at t=0) WP is located on the x-component of $\widetilde{X}^2\Pi_g$ and $\widetilde{C}^2\Pi_u$ states as indicated in the panels.

When the WP is initially placed on the x-component of the $\widetilde{C}^2\Pi_u$ state, the diabatic (i) and adiabatic (ii) electron population dynamics becomes more complicated and involved, as can be seen from panels (c) and (d) of Figure 3.12, respectively. In the diabatic case, most of the population flows to both the $\widetilde{A}^2\Sigma_g^+$ and $\widetilde{B}^2\Sigma_u^+$ electronic [cf. panel (c) of Figure 3.12] states. This is because of nonadiabatic coupling between $\widetilde{A}^2\Sigma_g^+$-$\widetilde{B}^2\Sigma_u^+$, $\widetilde{B}^2\Sigma_u^+$-$\widetilde{C}^2\Pi_u$ and $\widetilde{A}^2\Sigma_g^+$-$\widetilde{C}^2\Pi_u$ states along σ_u^+, π_g and π_u vibrational modes, respectively [cf. Table 3.10]. Also, the minimum of $\widetilde{B}^2\Sigma_u^+$-$\widetilde{C}^2\Pi_u$ conical intersections is only ~0.18 eV above the $\widetilde{C}^2\Pi_u$ state minimum [cf. Table 3.6]. At t=0, the diabatic and adiabatic popula-

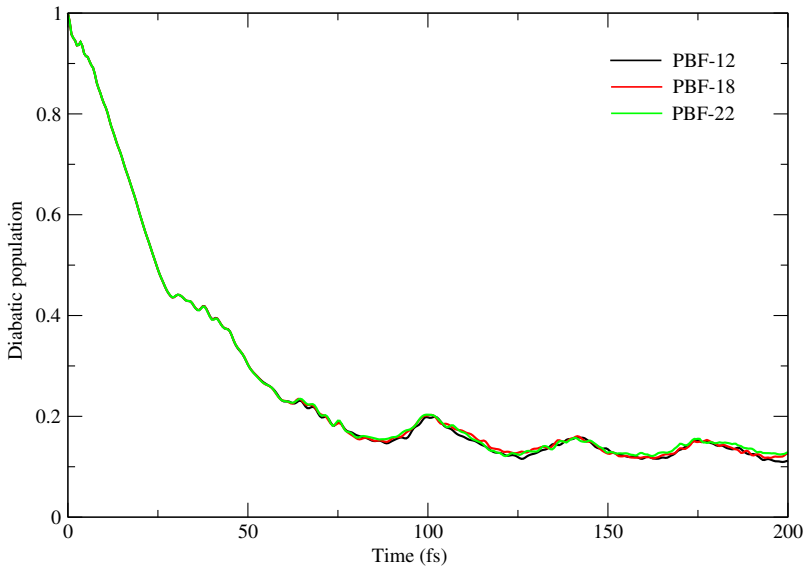

Figure 3.13: Convergence behaviour of the diabatic electronic calculations with respect to the number of basis functions along the π_u mode in the MCTDH calculations.

tions of the x-component of the $\widetilde{C}^2\Pi_u$ state start from 1.0 and ∼0.46, respectively [cf. panel (c) and (d) of Figure 3.12]. In this case population also flows to the $\widetilde{A}^2\Sigma_g^+$ and $\widetilde{B}^2\Sigma_u^+$ electronic states in addition to the flow of populations back and forth between the x and y-components of the $\widetilde{C}^2\Pi_u$ state. The initial decay of the population relates to a life-time of $\sim$ 39 fs of the $\widetilde{C}^2\Pi_u$ state in the diabatic picture.

The electronic population dynamics for an initial transition of the WP to the $\widetilde{A}^2\Sigma_g^+$ state in both diabatic (i) and adiabatic (ii) situations are shown in panels (a) and (b) of Figure 3.14, respectively. The internal conversion of electronic population is minor in this case. This is due to the energetic minimum of the $\widetilde{X}^2\Pi_g$-$\widetilde{A}^2\Sigma_g^+$, $\widetilde{A}^2\Sigma_g^+$-$\widetilde{B}^2\Sigma_u^+$ and $\widetilde{A}^2\Sigma_g^+$-$\widetilde{C}^2\Pi_u$ conical intersections occur $\sim$ 1.76, $\sim$ 3.77 and $\sim$ 2.38 eV above the minimum of the $\widetilde{A}^2\Sigma_g^+$ state, respectively [cf. Table 3.6]. Because of this, when the WP is initially prepared on the $\widetilde{A}^2\Sigma_g^+$ state, it hardly accesses these high energy CIs. Also, when the electronic states are energetically well separated the initial adiabatic and diabatic populations become nearly same. Therefore, both diabatic and adiabatic population profiles may show similar behaviour if the coupling is small. In addition, the $\widetilde{X}^2\Pi_g$-$\widetilde{A}^2\Sigma_g^+$ coupling is small and $\widetilde{A}^2\Sigma_g^+$-$\widetilde{C}^2\Pi_u$ coupling is strong (however they are energetically well separated) [see Tables 3.10 and 3.6]. These considerations imply a long lived nature of the $\widetilde{A}^2\Sigma_g^+$-state (or slow decay). Considering the vibronic mixing of $(g-u)$ $\widetilde{A}^2\Sigma_g^+$ and $\widetilde{C}^2\Pi_u$ states, the radiative emission of $C_2N_2^+$ from the $\widetilde{A}^2\Sigma_g^+$ state is expected. Until now there is no experimental report on this and certainly it calls for future experiments.

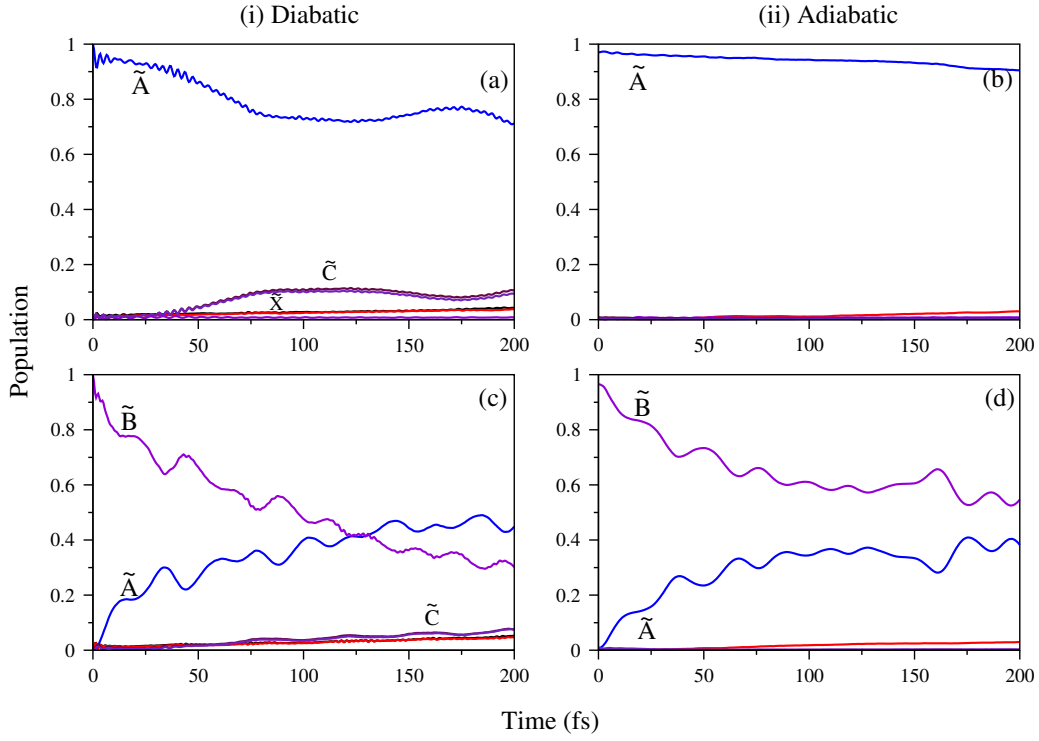

Figure 3.14: Time dependence of diabatic (panels (a) and (c)) and adiabatic (panels (b) and (d)) electron populations in the $\widetilde{X}^2\Pi_g$-$\widetilde{A}^2\Sigma_g^+$-$\widetilde{B}^2\Sigma_u^+$-$\widetilde{C}^2\Pi_u$ coupled states nuclear dynamics of $C_2N_2^+$. The initial (at t=0) WP is located on the $\widetilde{A}^2\Sigma_g^+$ and $\widetilde{B}^2\Sigma_u^+$ states, respectively as indicated in the panels.

The WP initially prepared on the diabatic and adiabatic $\widetilde{B}^2\Sigma_u^+$ state is shown in panels (c) and (d) of Figure 3.14, respectively. In the diabatic picture, the internal conversion takes place to the $\widetilde{A}^2\Sigma_g^+$ state via the $\widetilde{A}^2\Sigma_g^+$-$\widetilde{B}^2\Sigma_u^+$ conical intersections. These states are moderately coupled through the vibrational mode ν_3 of σ_u^+ symmetry [see Table 3.10]. Also, at the Franck-Condon region both $\widetilde{A}^2\Sigma_g^+$ and $\widetilde{B}^2\Sigma_u^+$ states are energetically close and all other states are far apart [cf. Table 3.3]. So, the population moves back and fourth between $\widetilde{A}^2\Sigma_g^+$-$\widetilde{B}^2\Sigma_u^+$ states in time. At longer times, population of both $\widetilde{A}^2\Sigma_g^+$ and $\widetilde{B}^2\Sigma_u^+$ states become equal ($\sim$ 0.4) and very minimal amount of population is transfered to the $\widetilde{X}^2\Pi_g$ and $\widetilde{C}^2\Pi_u$ states Figure 3.14]. A non-radiative decay rate of $\sim$ 104 fs can be estimated from the population curve of the $\widetilde{B}^2\Sigma_u^+$-state [cf. panel (c) of Figure 3.14] in the diabatic picture.

3.7 Conclusions

The nonadiabatic coupling effects in the vibronic structure and dynamics of $\widetilde{X}^2\Pi_g$, $\widetilde{A}^2\Sigma_g^+$, $\widetilde{B}^2\Sigma_u^+$ and $\widetilde{C}^2\Pi_u$ electronic states of cyanogen radical cation is investigated in this article. The theoretical results are compared with the experimental recording of Baker *et al.*[1]. The equilibrium geometry of the reference electronic ground state of the neutral C_2N_2 is optimized at the MP2/aug-cc-pVTZ level of theory using Gaussian-09 suit of program. The reference electronic ground state has $D_{\infty h}$ point group symmetry at its equilibrium minimum. When the correlation and reorganization effects are added, the ordering of the MO's changes as compared to the calculations at the HF level. Using EOMIP-CCSD *ab initio* quantum chemistry method, the potential energy surfaces of the $\widetilde{X}^2\Pi_g$, $\widetilde{A}^2\Sigma_g^+$, $\widetilde{B}^2\Sigma_u^+$ and $\widetilde{C}^2\Pi_u$ electronic states of $C_2N_2^+$ are computed along the dimensionless normal displacement coordinates of the electronic ground state of C_2N_2 . At the Franck-Condon geometry, it is found that the electronic states $\widetilde{A}^2\Sigma_g^+$, $\widetilde{B}^2\Sigma_u^+$ and $\widetilde{C}^2\Pi_u$ are energetically close. Both the RT effect in the doubly degenerate electronic states and their interactions with the nondegenerate states are examined and discussed. A coupled state vibronic Hamiltonian is developed in a diabatic electronic basis in terms of dimensionless normal displacement coordinate of vibrational modes using the electronic structure results.

Time-independent and time-dependent quantum mechanical approaches are used to study nuclear dynamics from first principles. The vibronic band structures are reported and progressions of vibrational modes are assigned and compared with the experiment. It is found that the C≡N symmetric stretching mode, ν_1 of σ_g symmetry forms progression in all four electronic states of $C_2N_2^+$. In the first vibrational band due to $\widetilde{X}^2\Pi_g$ state, C≡N stretching vibrational mode ν_1 is strongly excited at $\sim$2304 cm^{-1} and it is in agreement with the experimental estimate of Baker *et al.*[1] of $\sim$2120 cm^{-1}. Due to very weak RT coupling, RT active degenerate vibrational modes are not excited in this band.

The second and third bands are due to $\widetilde{A}^2\Sigma_g^+$ and $\widetilde{B}^2\Sigma_u^+$ states, respectively. These two bands show only little vibrational structure. Only C-C symmetric stretching, ν_2 vibrational mode excited in the $\widetilde{B}^2\Sigma_u^+$ state. The fourth band due to the $\widetilde{C}^2\Pi_u$ state exhibits considerable vibrational structure. In this band, the C-C stretching, ν_2 vibrational mode is strongly excited and the C≡N stretching mode ν_1 is moderately excited.

The diabatic and adiabatic electronic populations in the $\widetilde{X}^2\Pi_g$-$\widetilde{A}^2\Sigma_g^+$-$\widetilde{B}^2\Sigma_u^+$-$\widetilde{C}^2\Pi_u$ coupled states dynamics are further examined to better understand the nonadiabatic coupling effects. Due to RT coupling, the WP moves back and forth between the RT split (x and y) components of the $\widetilde{X}^2\Pi_g$ state. The

scenario is different when WP is placed on the $\widetilde{A}^2\Sigma_g^+$ state, no internal conversion takes place since the $\widetilde{X}^2\Pi_g$-$\widetilde{A}^2\Sigma_g^+$ and $\widetilde{A}^2\Sigma_g^+$-$\widetilde{B}^2\Sigma_u^+$ conical intersections occur at higher energies. Due to this, the WP stays for longer times in this state and is predicted to have radiative emission which can be validated in future experimental measurements. The initial location of the WP on the $\widetilde{B}^2\Sigma_u^+$ state reveals the population transfer between the $\widetilde{A}^2\Sigma_g^+$-$\widetilde{B}^2\Sigma_u^+$ states throughout the timescale. This is due to the nona-diabatic coupling of $\widetilde{A}^2\Sigma_g^+$-$\widetilde{B}^2\Sigma_u^+$ through ν_3 vibrational mode. The dynamics is more complex when WP is placed on the *x*-component of the $\widetilde{C}^2\Pi_u$ state. Due to strong vibronic mixing, the population flows nonradiatively to all the electronic states in this case.

Chapter 4

A Full-dimensional Investigation of Vibronic Coupling and Renner-Teller Effects in Linear Carbon Monohydrides, $C_{2n}H^{-}$ $(n = 1 - 4)$ of Astrophysical interest

ABSTRACT

In this work, electronic structure and quantum dynamics of astrophysically important linear carbon monohydrides, $C_{2n}H^{-}$ for $n = 1 - 4$ is investigated by constructing a multi-state and multi-mode vibronic coupling model. The latter relies on the standard vibronic coupling theory and symmetry rules and a diabatic electronic basis. Three energetically low-lying electronic states of neutral radical species ($C_{2n}H$, $n = 1 - 4$) are probed and dynamical investigations are carried by both a time-dependent and time-independent quantum mechanical methods. The impact of conical intersections and glacing degeneracies are thoroughly examined and their existence is confirmed in conjunction with available experimental results. It is observed that the Renner-Teller (RT) effect leading to glancing degeneracy decreases with increasing n. In contrast, the effect of conical intersections of the RT split states with the energetically higher non-degenerate electronic states increases with increasing n. Moreover, the outcomes of the present theoretical results are in excellent accord with the experiment.

4.1 Introduction

The ubiquitous carbon in the form of bare carbon clusters, C_n^-, carbon monohydrides, C_nH^-, carbon hydrides, $C_nH_n^-$, and their corresponding neutral radicals are known to be abundant in interstellar medium (ISM)[116] and hydrocarbon combustion processes[117]. These compounds also serve as building blocks for the formation of larger hydrocarbons, longer carbon chains and rings[118]. Interestingly, the anionic species $C_{2n}H^-(n = 1-4)$ are among the first ones to be detected in the ISM and circumstellar media, and believed to be formed through radiative attachment[119]. These species have been studied through various spectroscopic techniques[120]. Among them, the photoelectron (PE) spectroscopy was employed as a major tool, as it provided with the crucial details of the ground and excited electronic states of the corresponding neutral species, $C_{2n}H$ $(n = 1-4)$[121]. The early experimental PE spectra of $n = 1$ species was reported in 1991[122]. Later, other scientific groups investigated the subsequent $n = 2, 3,$ & 4 species[2] employing the same tool. Simultaneously, theoretical studies have been conducted in order to explore the details of electronic structure of $C_{2n}H$[123;124;125;126]. These joint efforts, established a linear structure and strong acetylenic nature of the electronic ground state of both neutral and anionic species[127]. Furthermore, ambiguity in the assignment of vibronic structure of the electronic bands was attributed to the possible existence of Renner-Teller (RT) coupling along the molecular axis and conical intersections (CIs) along the bending vibrational modes.

Although the mentioned efforts are successful in eliminating the problematic assignment of peaks in the electronic band associated with the first excited state, the apparent effects of RT coupling and CIs are seldomly discussed in the literature. Apart from these effects, for all neutral species the ground and first excited electronic states belong to either a $^2\Sigma^+$ or a $^2\Pi$ terms. The energetic ordering of these low-lying $^2\Pi$ and $^2\Sigma^+$ states in the neutral species varies with the chain length[2;124]. While the longer chains, $n = 3, 4$, have $^2\Pi$ ground state, the C_2H and C_4H radicals have $^2\Sigma^+$ ground-state. Due to strong vibronic coupling and the energetic closeness of these two states in C_2H and C_4H, leads significant complexity in their observed electronic spectrum. Furthermore, vibronic coupling in the longer chains with $\widetilde{X}^2\Pi$ ground states has not been studied so far.

The C_4H is the most controversial species with experimental results favouring $^2\Sigma^+$ ground state, while the theoretical results[126] reported near degeneracy between $^2\Pi$ and $^2\Sigma^+$ states. More recently, the $\widetilde{A}^2\Pi$-$\widetilde{X}^2\Sigma$ splitting in C_4H[128] was estimated to be $\sim$213 cm^{-1}. In contrast, the present study reveals that except for C_2H, rest of the species possess $^2\Pi$ ground state (details are elaborated later in the text). As a corroborating evidence, the HOMO, HOMO-1, and HOMO-2 molecular orbitals of the anionic species $C_{2n}H^-(n = 1-4)$ corresponding to three energetically low-lying electronic

states of neutral species ($C_{2n}H(n = 1-4)$) are presented in Figs.4.1 and 4.2. In addition, the energy difference between the frontier orbitals of anionic species generally decreases with increasing n as shown in Fig. 4.3. Hence it would be intriguing to explore how this trend correlates with effects due to RT coupling and CIs.

Overall, a comprehensive and detailed analysis seems necessary in case of $C_{2n}H^-$ ($n = 1-4$) linear carbon chain series. Therefore in this work, a vibronic coupling approach is undertaken to address the ambiguity in the assignment of ground electronic state through electronic structure calculations and to elucidate the effects of RT coupling and CIs through nuclear dynamics calculations. For this purpose, state-of-the-art *ab initio* electronic structure methods are employed in order to establish the relevant potential energy surfaces and parameterize the constructed vibronic Hamiltonian. Extensive nuclear dynamics calculations are carried out to unravel features observed in each photodetachment bands. Finally, the theoretical results are compared with the available experimental findings to confirm the validity of the present vibronic coupling models.

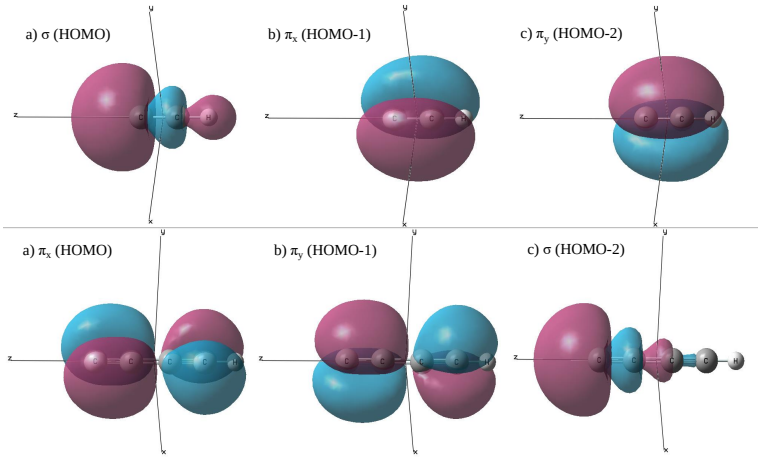

Figure 4.1: The canonical molecular orbitals shown in the first and second row are the (HOMO to HOMO-2) of C_2H^- and C_4H^-, respectively. The pink and blue lobes in the above pictures represent positive and negative phases, respectively.

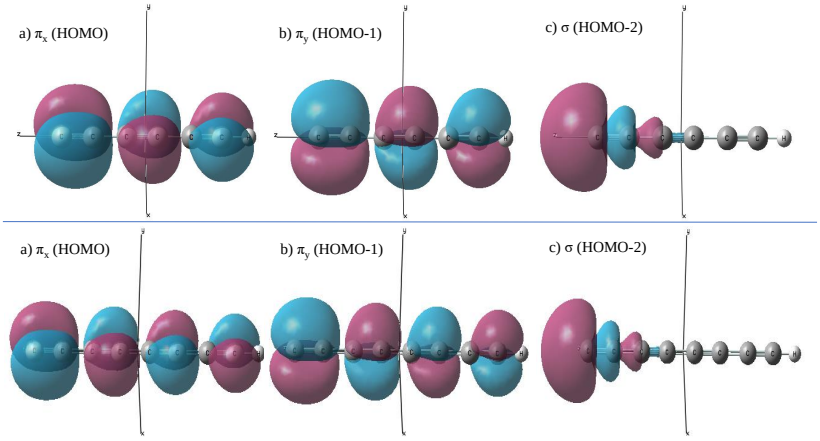

Figure 4.2: Same label as Fig. 4.1 of C_6H^- and C_8H^-, respectively.

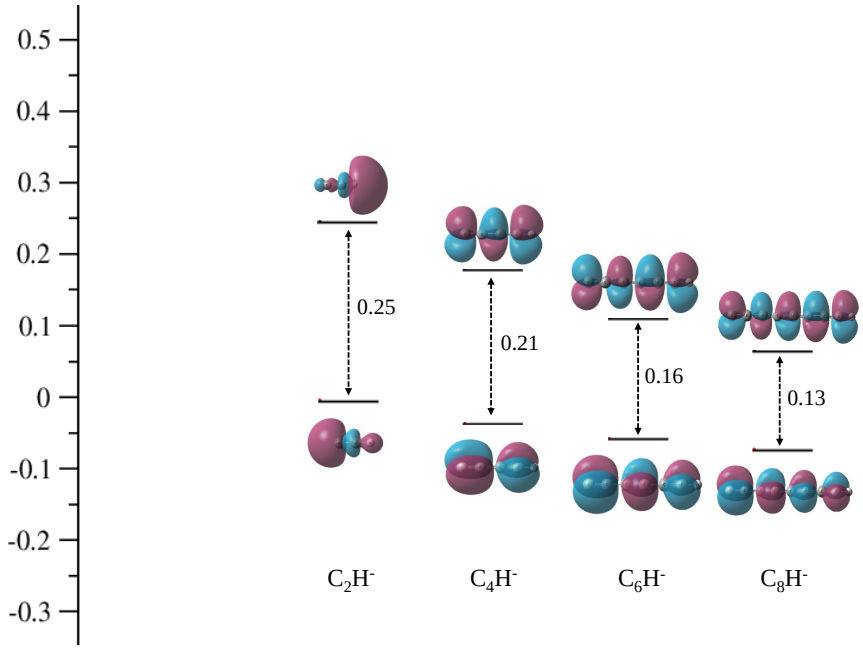

Figure 4.3: Schematic representation of HOMO-LUMO energy difference of $C_{2n}H^-(n = 1 - 4)$.

4.2 Computational Details

4.2.1 Electronic Structure

The equilibrium geometry of the electronic ground state of $C_{2n}H^-$ $(n = 1 - 4)$ (the reference geometry) is optimized by the Becke-3-parameter (exchange), Lee, Yang, and Parr (B3LYP) density functional method using the correlation consistent polarized valence double— ζ (cc-pVDZ) basis set of Dunning [129]. By diagonalizing the kinematic and force constant matrices of the reference equilibrium geometry, the harmonic frequency (ω_k) of vibrational modes and their dimensionless normal

displacement coordinates (DNDCs), (Q_k) are determined[105]. In these coordinates the reference geometry corresponds to **Q=0**. Table 4.1 lists the frequencies (cm^{-1}) and symmetries of $C_{2n}H^-$ (n=1-4). The Gaussian-09[102] suite of programs, is used for these calculations. The optimized equilibrium structure of the electronic ground state of the linear chains belongs to $C_{\infty v}$ symmetry point group. The normal vibrational modes of the $C_{\infty v}$ symmetry point group of linear carbon monohydride chains, $C_{2n}H^-$ (that is, $2n+1 = N$), belong to the following irreducible representations (IREPs) as illustrated in the Appendix II.

$$\Gamma_{\text{vibrational}} = \quad (N-1)\sigma + (N-2)\pi \tag{4.1}$$

Table 4.1: Symmetry, designation and vibrational frequencies (in cm^{-1}) of $C_{2n}H^-$ of its ground electronic state.

C_2H^-	Symmetries	Modes	B3LYP/cc-pVDZ
	σ^+	ν_1	3363
	σ^+	ν_2	1902
	π	ν_3	568
C_4H^-	Symmetries	Modes	B3LYP/cc-pVDZ
	σ^+	ν_1	3493
	σ^+	ν_2	2182
	σ^+	ν_3	1989
	σ^+	ν_4	910
	π	ν_5	623
	π	ν_6	438
	π	ν_7	251
C_6H^-	Symmetries	Modes	B3LYP/cc-pVDZ
	σ^+	ν_1	3487
	σ^+	ν_2	2230
	σ^+	ν_3	2150
	σ^+	ν_4	1985
	σ^+	ν_5	1208
	σ^+	ν_6	640
	π	ν_7	576
	π	ν_8	497
	π	ν_9	461
	π	ν_{10}	268
	π	ν_{11}	111
C_8H^-	Symmetries	Modes	B3LYP/cc-pVDZ
	σ^+	ν_1	3485
	σ^+	ν_2	2238
	σ^+	ν_3	2205
	σ^+	ν_4	2104
	σ^+	ν_5	1987
	σ^+	ν_6	1354
	σ^+	ν_7	946
	σ^+	ν_8	493
	π	ν_9	577
	π	ν_{10}	531
	π	ν_{11}	507
	π	ν_{12}	462
	π	ν_{13}	281
	π	ν_{14}	167
	π	ν_{15}	64

It is also evident from the results given in the Appendix II, that these linear molecules lack vibra-

tions with angular momentum greater than one. Therefore, the vibrational modes belong to σ and π symmetry only. Along the DNDC of each vibrational mode, the vertical ionization energies (VIEs) of the electronic states of $C_{2n}H^-$ $(n = 1-4)$ are computed. The CFOUR suite of program [100] and cc-pVDZ basis set are employed for this purpose using the equation of motion ionization potential coupled cluster singles and doubles (EOM-IP-CCSD) method [13;14]. These calculations are carried out in C_{2v} symmetry. The symmetry representation of vibrational modes and electronic terms are derived using the $C_{\infty v}$-C_{2v} correlation table, which is provided in the Appendix II. Table 4.2 lists the VIEs computed at the reference equilibrium geometry for energetically low-lying three electronic states of $C_{2n}H$ $(n = 1-4)$. The VIEs are calculated along all Q's for -5.00 (0.25) +5.00. Table 4.2 shows that all the electronic states of considered carbon chains belong to either a Σ^+ and Π term. As the length of the carbon chain increases, the energy of the HOMO decreases (see Fig. 4.3). It indicates an increase of the vertical ionization energy with chain length (cf. Fig. 4.3 and Table 4.2). It is therefore logical to anticipate that vibronic coupling would be playing crucial role in the nuclear dynamics since the states are energetically extremely near to their surrounding states (see Table 4.2). At the configuration of $C_{\infty v}$ symmetry, the Π electronic state is orbitally degenerate. When the linear chain is bent, this degeneracy splits, resulting in the RT effect. It is possible for the RT split components to couple with the nondegenerate state and give rise to NAC effects.

Table 4.2: VIEs (in eV) of the $\widetilde{X}$ and $\widetilde{A}$ states of $C_{2n}H^-$ calculated at the reference equilibrium geometry of $C_{2n}H$ and compared with the available experimental data.

Molecule	$\widetilde{X}^2\Sigma$	$\widetilde{A}^2\Pi$	Method
C_2H	2.77	3.29	EOMIP-CCSD
	2.96		Exp.[2]
	$\widetilde{X}^2\Pi$	$\widetilde{A}^2\Sigma$	
C_4H	3.60	3.71	EOMIP-CCSD
	3.55		Exp.[2]
C_6H	3.84	4.25	EOMIP-CCSD
	3.80		Exp.[2]
C_8H	4.03	4.63	EOMIP-CCSD
	3.96		Exp.[2]

4.3 Theoretical Framework

4.3.1 The Hamiltonian

The current study examines the photoionization of $C_{2n}H^-$ ($n = 1-4$) of the lowest two doublet electronic states of $C_{2n}H$ ($n = 1-4$). According to the calculations (vide supra), the ground and first ionized electronic states of C_2H are observed to be $\widetilde{X}^2\Sigma$ and $\widetilde{A}^2\Pi$ respectively. On the contrary, the ground and first ionized electronic states of C_4H, C_6H, and C_8H are observed to be $\widetilde{X}^2\Pi$ and $\widetilde{A}^2\Sigma$. Further, the vibrational modes of each molecular system are classified into totally symmetric (σ^+) and asymmetric (π) modes. The vibrational modes of the mentioned four molecular systems (using the Eq. 4.1) transform according to the irreducible representations (IREPs) as follows:

$$\Gamma_{n=1,\text{vib}} = 2\sigma + 1\pi \tag{4.2}$$

$$\Gamma_{n=2,\text{vib}} = 4\sigma + 3\pi \tag{4.3}$$

$$\Gamma_{n=3,\text{vib}} = 6\sigma + 5\pi \tag{4.4}$$

$$\Gamma_{n=4,\text{vib}} = 8\sigma + 7\pi \tag{4.5}$$

The symmetry rule[11], $\Gamma_R \otimes \Gamma_k \otimes \Gamma_S \supset \sigma$, directs the first-order connection between the electronic states R and S via vibrational mode k. IREPs are represented by the symbol Γ. The symbol σ^+ represents the totally symmetric IREP of the linear molecule with $C_{\infty v}$ symmetry. This rule indicates that the latter vibrational modes are active in the specified electronic states ($R = S$). Now, the symmetrical direct product transforms in accordance with $\Pi^2 = \sigma + \delta$ for the degenerate Π state. The δ symmetry vibrational modes can lift orbital degeneracy in the first-order of the Π state, while the totally symmetric vibrational modes cannot. The first-order RT coupling diminishes in linear molecules due to the absence of vibrational mode of δ symmetry (see the Appendix II). The π mode can, however, be RT active in the Π state in second-order, since $\pi^2 \supset \delta$. The Π state's RT split components may experience a PRT-style coupling with the neighboring nondegenerate Σ^+ state according to

$$\Sigma^+ \otimes \Pi = \pi \tag{4.6}$$

Eq. 4.6, demonstrates that direct coupling of Σ^+ and Π state couples in first-order through π vibrational mode.

According to the vibronic coupling theory, the vibronic model Hamiltonian is built in a diabatic elec-

tronic basis using the above mentioned coupling recipe[11]. It may be represented symbolically as

$$\mathcal{H} = \mathcal{H}_0 1_3 + \begin{pmatrix} W_{11} & W_{12} & W_{13} \\ & W_{22} & W_{23} \\ & & W_{33} \end{pmatrix} \tag{4.7}$$

The unperturbed Hamiltonian of the reference electronic ground state of $C_{2n}H^-$ is denoted by the equation $\mathcal{H}_0 = \mathcal{T}_N + \mathcal{V}_0$. Within the harmonic approximation, its components are provided by

$$\mathcal{T}_N = -\frac{1}{2}\sum_{i \in \sigma^+} \omega_i \frac{\partial^2}{\partial Q_i^2} - \frac{1}{2}\sum_{i \in \pi} \omega_i \left(\frac{\partial^2}{\partial Q_{ix}^2} + \frac{\partial^2}{\partial Q_{iy}^2} \right) \tag{4.8}$$

and

$$\mathcal{V}_0 = \frac{1}{2}\sum_{i \in \sigma^+} \omega_i Q_i^2 + \frac{1}{2}\sum_{i \in \pi} \omega_i \left(Q_{ix}^2 + Q_{iy}^2 \right) \tag{4.9}$$

The term 1_3 in Eq. 4.7 implies a 3×3 diagonal unit matrix. The diabatic energies of the aforementioned electronic states of the $C_{2n}H$ are represented by the diagonal components of the matrix Hamiltonian in Eq. (4.7), while the coupling between the electronic states is represented by the off-diagonal elements. The matrix elements are extended in a typical Taylor series around the optimized minimum geometry at $Q = 0$, as shown below[11].

$$\begin{aligned} W_{R_x/R_y} = {} & E_0^R + \sum_{i \in \sigma^+} \kappa_i^R Q_i + \sum_{i \in \sigma^+} \gamma_i^R Q_i^2 + \sum_{i \in \sigma^+} \zeta_i^R Q_i^3 + \sum_{i \in \sigma^+} \xi_i^R Q_i^4 \\ & + \sum_{i \in \pi} [\gamma_i^R (Q_{i_x}^2 + Q_{i_y}^2)] + \sum_{i \in \pi} [\xi_i^R (Q_{i_x}^2 + Q_{i_y}^2)^2] + \sum_{i \in \pi} [\sigma_i^R (Q_{i_x}^2 + Q_{i_y}^2)^3] \\ & \pm \sum_{i \in \pi} \eta_i^R (Q_{i_x}^2 - Q_{i_y}^2) \pm \sum_{i \in \pi} \delta_i^R (Q_{i_x}^4 - Q_{i_y}^4) \pm \sum_{i \in \pi} \rho_i^R (Q_{i_x}^6 + Q_{i_x}^4 Q_{i_y}^2 - Q_x^2 Q_y^4 - Q_{i_y}^6) \end{aligned} \tag{4.10}$$

$$; \; R \in \Pi \tag{4.11}$$

$$\begin{aligned} W_R = {} & E_0^R + \sum_{i \in \sigma^+} \kappa_i^R Q_i + \sum_{i \in \sigma^+} \gamma_i^R Q_i^2 + \sum_{i \in \pi} [\gamma_i^R (Q_{i_x}^2 + Q_{i_y}^2)] + \\ & \sum_{i \in \pi} [\xi_i^R (Q_{i_x}^2 + Q_{i_y}^2)^2] + \sum_{i \in \pi} [\sigma_i^R (Q_{i_x}^2 + Q_{i_y}^2)^3] \quad ; \; R \in \Sigma^+ \end{aligned} \tag{4.12}$$

$$W_{R_x-R_y} = \sum_{i \in \pi} 2\eta_i^R(Q_{i_x}Q_{i_y}) + 2\delta_i^R(Q_{i_x}^3Q_{i_y} + Q_{i_x}Q_{i_y}^3) + 2\rho_i^R(Q_{i_x}^5Q_{i_y} + Q_{i_x}Q_{i_y}^5 + 2Q_{i_x}^3Q_{i_y}^3) \quad ; j \in \Pi \tag{4.13}$$

$$W_{R_x-S/R_y-S} = \sum_{i \in \pi} \lambda_i^{R-S} Q_{ix/iy} \; ; R - S \in \Sigma^+ - \Pi \tag{4.14}$$

The VIE for the R^{th} electronic state in the equations above is provided by E_0^R. The subscripts x and y stand for the constituents of degenerate vibrational modes and electronic states, respectively. Along the vibrational modes of σ^+ symmetry, the linear intrastate coupling parameter is represented by the value κ_i^R. Along the degenerate vibrational mode π, the Rth electronic state's second, fourth, and sixth-order RT coupling characteristics are represented by η_i^R, δ_i^R and ρ_i^R, respectively. For the R and S electronic states along the ith vibrational mode, the linear inter-state coupling value is λ_i^{R-S}. The second, third, fourth, and sixth-order intrastate coupling parameters for the Rth electronic state along the ith vibrational mode are denoted by γ_i^R, ζ_i^R, ξ_i^R and σ_i^R respectively. The x and y components of the degenerate state are represented by the + and - signs, respectively. All of the diabatic electronic Hamiltonian matrix elements are given relative signs by using the invariance principle for different symmetry operations.

4.3.2 Nuclear Dynamics

The time-independent spectral calculations[109;110] are carried out for the first three electronic states of $C_{2n}H$ ($n = 1 - 4$) with the aid of Fermi's golden rule:

$$I(E) = \Sigma_v |\langle \Psi_v^f | \hat{T} | \Psi_0^i \rangle|^2 \delta(E - E_v^f + E_0^i), \tag{4.15}$$

where, the terms Ψ_v^f and Ψ_0^i represent the final and initial vibronic ground state possessing E_v^f and E_0^i energies respectively for each the molecular system of our concern here. The term $\hat{T}$ is the transition dipole operator. Further, the initial vibronic state is expanded as a product of diabatic electronic state ($|\Phi_0^0\rangle$) and its vibrational component ($|0\rangle$) as depicted below

$$|\Psi_0^i\rangle = |\Phi_0^0\rangle|0\rangle. \tag{4.16}$$

Wherein, $|0\rangle$ is further expressed in terms of a direct product of harmonic oscillator functions of the reference molecules of each molecular system. Consequently, a matrix diagonalization is carried out following Lanczos algorithm as implemented in the MCTDH module program[11;111;66].

The time-dependent spectral calculations are carried out for the first three electronic states of $C_{2n}H$ ($n = 1 - 4$) by the aid of transformed Fermi's golden rule:

$$\begin{aligned} I(E) &\approx 2Re\ \Sigma_{m=1}^{3} \int_0^{\infty} e^{\frac{iEt}{\hbar}} \langle \chi^m(0)|\tau^{\dagger} e^{-\frac{iEt}{\hbar}} \tau|\chi^m(0)\rangle dt, \\ &\approx 2Re\ \Sigma_{m=1}^{3} |\tau^m|^2 \int_0^{\infty} e^{\frac{iEt}{\hbar}} C^m dt. \end{aligned} \tag{4.17}$$

Here, the initial wave packet (Ψ_0^i) is vertically promoted to the final state (Ψ_0^m) through time evolution propagation scheme. This process is monitored over time through the autocorrelation functions, $C^m(t) = \langle \Psi^m(t=0)|\Psi^m(t)\rangle$. In this context, the transition dipole matrix is denoted by τ as following:

$$\tau^{\dagger} = (\tau^{\tilde{X}}, \tau^{\tilde{A}}), \tag{4.18}$$

with $\tau^m = \langle \Phi^m|\hat{T}|\Phi^0\rangle$. The subsequent computations of wave packet propagation are performed with the MCTDH module program[66;70;65;35].

4.4 Results and Discussion

4.4.1 Potential energy surfaces

To comprehensively understand nuclear dynamics, it is essential to analyze electronic potential energy surfaces (PESs). Within the framework of vibronic coupling theory, we study the potential energy cuts (PECs), derived from electronic structure calculations (vide supra), as functions of the DNDCs corresponding to each vibrational degree of freedom presented in Figs. 4.4, 4.5, 4.6, 4.7, 4.8, 4.9, and 4.10. Concerning the PECs presented in all the figures, the adiabatic electronic energies computed *ab initio* are represented by points, while those derived from the vibronic coupling model discussed in Section 5.2.2 are represented by solid lines. It can be seen that the *ab initio* electronic energies are in good agreement with those calculated from the theoretical model. In general, the energy gap between the electronic states is altered by the vibrational modes of σ^+ symmetry, also referred as Condon active modes, which adjust the electronic energy minimum away from the reference geometries of the electronic ground states of $C_{2n}H^-$ (at $Q = 0$).

For detailed analysis, consider the PECs for the three lowest electronic states of C_2H ($\widetilde{X}^2\Sigma$ & $\widetilde{A}^2\Pi$) as shown in (a), (b) and (c) panels of Fig. 4.4, corresponding to $2\sigma^+$ (ν_1 and ν_2) and the third panel for the degenerate π vibrational modes (ν_3 and ν_4). Despite their near proximity along the ν_1 mode, the three electronic states did not intersect at any distortion and had a little shift in the minima with

respect to $Q = 0$. This demonstrates that the Frack-Condon activity of ν_1 vibrational mode is weak which is also reflected in the intrastate coupling value in Table 4.3. The excitation strength along ν_1 mode in both the $\widetilde{X}^2\Sigma$ and $\widetilde{A}^2\Pi$ states is zero as shown in square brackets. On the contrary, along ν_2, the two electronic states exhibit shifting of their corresponding minima in the opposite directions with respect to $Q = 0$ along with a crossing. This proves that ν_2 is strongly Frack-Condon active. Justifying this, the intrastate coupling value in Table 4.3 shows a value of 0.34 and 0.21 for ν_2 mode in $\widetilde{X}^2\Sigma$ and $\widetilde{A}^2\Pi$ states respectively. The mentioned curve crossings among the potential cuts might eventually form conical intersections (CIs) in multidimensions. Along the degenerate ν_3 and ν_4, π modes, the degeneracy of $\widetilde{A}^2\Pi$ state is lifted as anticipated. It is evident that the degenerate $\widetilde{A}^2\Pi$ electronic state's RT-splitting is significant which is consistent with the magnitude of second-order RT coupling parameter displayed in Table 4.3.

Table 4.3: Linear (κ_i), quadratic (γ_i and η_i), cubic (ζ_i), quartic (ξ_i and δ_i) and sixth-order (σ_i and ρ_i) coupling constants of the Hamiltonian for the $\widetilde{X}^2\Sigma$ and $\widetilde{A}^2\Pi$ electronic states of C_2H. The values in the square brackets indicate dimensionless excitation strengths. All the values are given in the eV units.

Symm.	Mode	Freq. (eV)	κ_i	γ_i (η_i)	ζ_i	ξ_i (δ_i)
$\widetilde{X}^2\Sigma$						
σ^+	ν_1	0.4170	-0.0258 [0.00]	0.0094	-0.0007	0.0012
σ^+	ν_2	0.2358	0.1963 [0.34]	-0.0065	0.0002	-0.0003
π	ν_3	0.0705	-	-0.0098	-	0.0108
$\widetilde{A}^2\Pi$						
σ^+	ν_1	0.4170	0.0371 [0.00]	0.0086	0.0003	0.0007
σ^+	ν_2	0.2358	-0.1552 [0.21]	0.0191	-0.0024	0.0006
π	ν_3	0.0705	-	0.0550 (-0.0457)	-	-0.0060 (0.0107)

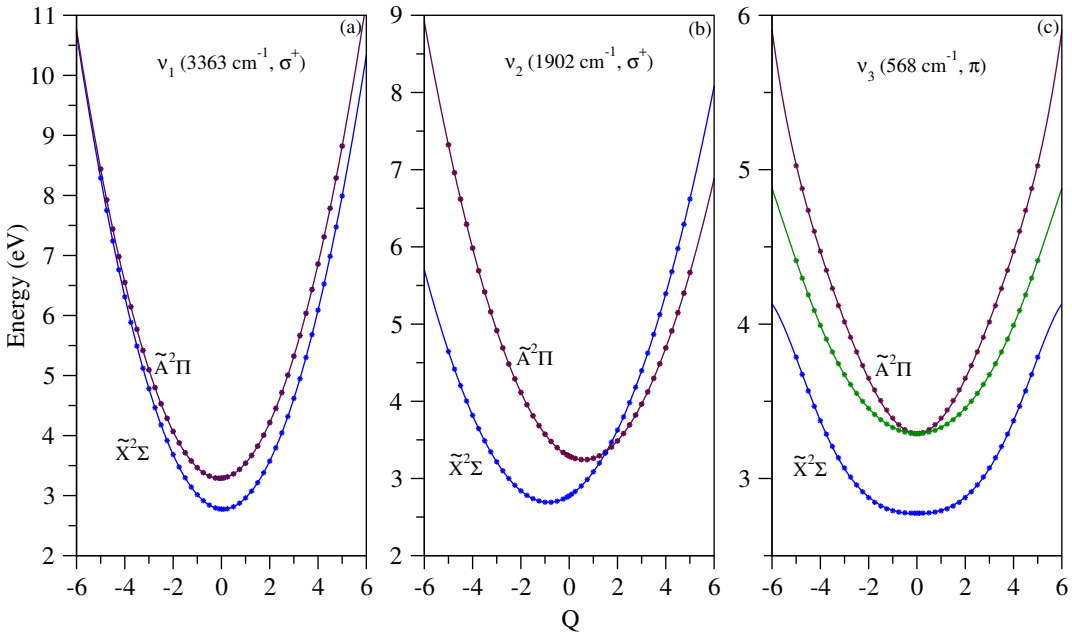

Figure 4.4: Adiabatic potential energies along the totally symmetric vibrational modes (σ^+) and degenerate mode (π) of the electronic states $\widetilde{X}^2\Sigma$ and $\widetilde{A}^2\Pi$ of C_2H. Solid lines and dots, respectively, represent the energies derived from the current vibronic model and calculated *ab initio* energies.

In Fig. 4.5, the PECs for the three lowest electronic states of C_4H ($\widetilde{X}^2\Pi$ & $\widetilde{A}^2\Sigma$) are shown in (a)-(d) panels corresponding to $4\sigma^+$ ($\nu_1 - \nu_4$) vibrational modes. Here, the electronic states are energetically quite close as compared to its smaller counterpart C_2H system corroborating for the minute energy difference in the VIE values of Table 4.2. Along ν_1 mode, the shift in the minima is negligible with respect to $Q = 0$, proving it's weak Franck-Condon activity as also seen in Table 4.4, while along ν_2, ν_3 and ν_4 modes, a noticeable shift is seen, with clear crossing between the electronic states. Accordingly, strong Franck-Condon activity is witnessed here along ν_2 and ν_3 modes in the intrastate coupling values presented in Table 4.4. Fig. 4.6 exhibits PECs along the degenerate π modes in (a)-(c) panels. Although the second-order RT coupling value (see Table 4.4) is somewhat lower compared to that of the degenerate state of C_2H, the RT-splitting of the $\widetilde{X}^2\Pi$ state is nevertheless substantial. The PECs of the degenerate state $\widetilde{X}^2\Pi$ showing symmetric double well nature along ν_5 and ν_7 modes, with two symmetric minima at the distorted geometries. These modes' unusual double well character will have a substantial impact on the nuclear dynamics on the electronic states in addition to being the coupling modes.

Table 4.4: Linear (κ_i), quadratic (γ_i and η_i), cubic (ζ_i), quartic (ξ_i and δ_i) and sixth-order (σ_i and ρ_i) coupling constants of the Hamiltonian for the $\widetilde{X}^2\Pi$ and $\widetilde{A}^2\Sigma$ electronic states of C_4H. The values in the square brackets indicate dimensionless excitation strengths. All the values are given in the eV units.

Symm.	Mode	Freq. (eV)	κ_i	γ_i (η_i)	ζ_i	ξ_i (δ_i)	σ_i (ρ_i)
$\widetilde{X}^2\Pi$							
σ^+	ν_1	0.4331	-0.0159 [0.00]	0.0018	-0.00007	0.0006	
σ^+	ν_2	0.2705	-0.1397 [0.13]	-0.0094	-0.0007	0.0016	
σ^+	ν_3	0.2466	0.1219 [0.12]	0.0031	-0.0002	-0.00002	
σ^+	ν_4	0.1128	0.0203 [0.01]	-0.0049	0.0007	0.00008	
π	ν_5	0.0773	-	-0.0374 (-0.0268)	-	0.0195 (0.0159)	-0.0111 (-0.0093)
π	ν_6	0.0542	-	0.0363 (0.0159)	-	-0.0046 (-0.0090)	0.0039 (0.0050)
π	ν_7	0.0311	-	-0.0481 (0.0155)	-	0.0142 (-0.0124)	-0.0074 (0.00001)
$\widetilde{A}^2\Sigma$							
σ^+	ν_1	0.4331	-0.0312 [0.00]	0.0021	0.00005	0.0006	
σ^+	ν_2	0.2705	0.1727 [0.20]	-0.0039	-0.0040	-0.0009	
σ^+	ν_3	0.2466	-0.1107 [0.10]	-0.0087	-0.0007	-0.00006	
σ^+	ν_4	0.1128	0.0640 [0.16]	0.0016	0.0005	-0.000007	
π	ν_5	0.0773	-	0.0431	-	-0.0175	0.0096
π	ν_6	0.0542	-	0.0586	-	-0.0061	0.0046
π	ν_7	0.0311	-	0.0789	-	-0.0216	0.00001

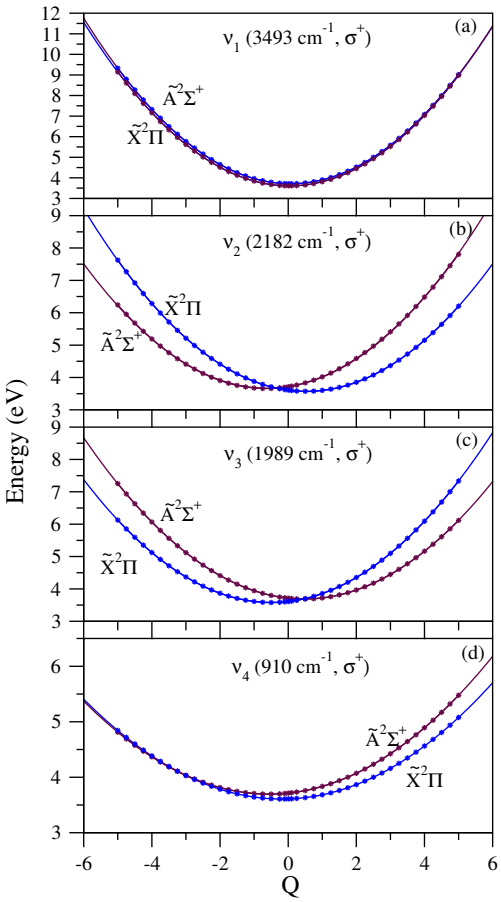

Figure 4.5: Adiabatic potential energies along the totally symmetric vibrational modes (σ^+) of the electronic states $\widetilde{X}^2\Pi$ and $\widetilde{A}^2\Sigma$ of C_4H. Solid lines and dots, respectively, represent the energies derived from the current vibronic model and calculated *ab initio* energies.

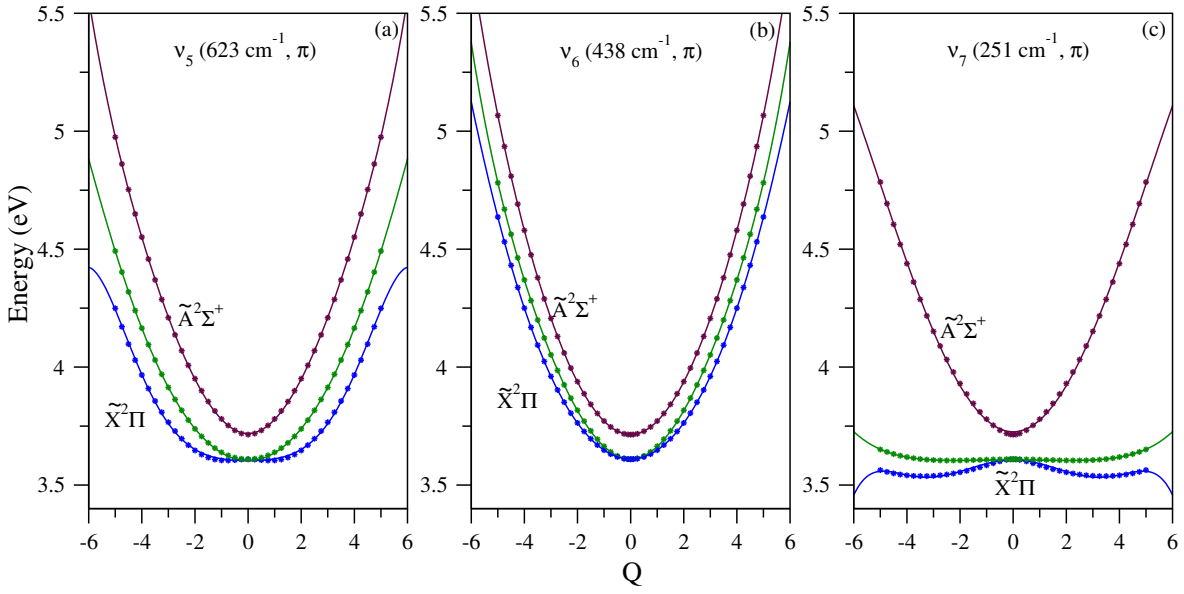

Figure 4.6: Adiabatic potential energies along the degenerate vibrational modes (π) of the electronic states $\widetilde{X}^2\Pi$ and $\widetilde{A}^2\Sigma$ of C_4H. Solid lines and dots, respectively, represent the energies derived from the current vibronic model and calculated *ab initio* energies.

In Fig. 4.7 and Fig. 4.9, the PECs for the three lowest electronic states of C_6H and C_8H ($\widetilde{X}^2\Pi$ & $\widetilde{A}^2\Sigma$) are shown in panels (a) - (f) and (a) - (h) corresponding to $6\sigma^+$ ($\nu_1-\nu_6$) and $8\sigma^+$ ($\nu_1-\nu_7$ and ν_{11}), respectively. As the length of the carbon chain increases, it is evident that the energy gap between the electronic states has been decreasing (see Table 4.2). Consequently, we could observe curve crossings between the possible PECs. Furthermore, it is noticed that as the length of the carbon chain increases, the excitation strength ($\kappa_i^2/2\omega_i^2$) of the symmetric modes decreases, lowering Condon activity. Panels (a)-(e) and (a)-(g) in Fig. 4.8 and Fig. 4.10 display the PECs of the degenerate π modes of C_6H and C_8H, respectively. Compared with the PECs to the lower carbon chains discussed previously, it is evident that the splitting of degenerate states is not as considerable. Furthermore, the amount of second-order RT coupling values shown in Tables 4.5 and 4.6 aligns with the splitting observed in the respective figures.

Table 4.5: Linear (κ_i), quadratic (γ_i and η_i), cubic (ζ_i), quartic (ξ_i and δ_i) and sixth-order (σ_i and ρ_i) coupling constants of the Hamiltonian for the $\widetilde{X}^2\Pi$ and $\widetilde{A}^2\Sigma$ electronic states of C_6H. The values in the square brackets indicate dimensionless excitation strengths. All the values are given in the eV units.

Symm.	Mode	Freq. (eV)	κ_i	γ_i (η_i)	ζ_i	ξ_i (δ_i)	σ_i (ρ_i)
$\widetilde{X}^2\Pi$							
σ^+	ν_1	0.4323	-0.0198 [0.00]	0.0016	-0.0001	0.0004	
σ^+	ν_2	0.2765	-0.1024 [0.06]	-0.0299	-0.0002	0.0030	
σ^+	ν_3	0.2666	0.1092 [0.08]	-0.0028	-0.0003	0.00005	
σ^+	ν_4	0.2461	0.1011 [0.08]	0.0067	0.0004	0.0000	
σ^+	ν_5	0.1497	0.0090 [0.00]	-0.0041	-0.0004	0.00004	
σ^+	ν_6	0.0794	0.0273 [0.06]	-0.0025	0.00019	0.0000	
π	ν_7	0.0715	-	-0.0117 (0.0026)	-	0.0046 (-0.0016)	0.0000 (0.0000)
π	ν_8	0.0616	-	-0.0057 (0.0049)	-	0.0003 (-0.0005)	0.0000 (0.0000)
π	ν_9	0.0572	-	0.03115 (-0.0093)	-	-0.0053 (0.0040)	0.0000 (0.0000)
π	ν_{10}	0.0332	-	-0.0276 (0.0055)	-	0.0057 (-0.0043)	0.0000 (0.0000)
π	ν_{11}	0.0137	-	-0.0076 (0.0001)	-	0.0008 (-0.0001)	0.0000 (0.0000)
$\widetilde{A}^2\Sigma$							
σ^+	ν_1	0.4323	-0.0225 [0.00]	0.0017	-0.00006	0.0003	
σ^+	ν_2	0.2765	0.1666 [0.18]	-0.0014	-0.0057	-0.0010	
σ^+	ν_3	0.2666	-0.0928 [0.06]	-0.0063	0.0006	-0.00005	
σ^+	ν_4	0.2461	-0.1603 [0.21]	-0.0091	0.00002	0.00003	
σ^+	ν_5	0.1497	-0.0390 [0.03]	0.0014	-0.00003	0.0000	
σ^+	ν_6	0.0794	0.0344 [0.09]	0.0006	0.0001	0.0000	
π	ν_7	0.0715	-	0.0138	-	0.0009	0.0000
π	ν_8	0.0616	-	0.0103	-	-0.0016	0.0000
π	ν_9	0.0572	-	0.0374	-	-0.0030	0.0000
π	ν_{10}	0.0332	-	0.0694	-	-0.0103	0.0000
π	ν_{11}	0.0137	-	0.0344	-	-0.00145	0.0000

Table 4.6: Linear (κ_i), quadratic (γ_i and η_i), cubic (ζ_i), quartic (ξ_i and δ_i) and sixth-order (σ_i and ρ_i) coupling constants of the Hamiltonian for the $\widetilde{X}^2\Pi$ and $\widetilde{A}^2\Sigma$ electronic states of C_8H. The values in the square brackets indicate dimensionless excitation strengths. All the values are given in the eV units.

Symm.	Mode	Freq. (eV)	κ_i	γ_i (η_i)	ζ_i	ξ_i (δ_i)	σ_i (ρ_i)
$\widetilde{X}^2\Pi$							
σ^+	ν_1	0.4321	-0.0177 [0.00]	0.0012	-0.0001	0.0003	
σ^+	ν_2	0.2772	-0.0916 [0.05]	-0.0088	0.0007	0.0003	
σ^+	ν_3	0.2734	-0.0816 [0.04]	-0.0412	-0.0004	0.0051	
σ^+	ν_4	0.2609	-0.0801 [0.04]	-0.0003	-0.0006	0.00005	
σ^+	ν_5	0.2463	0.0978 [0.07]	0.0049	0.0002	-0.00003	
σ^+	ν_6	0.1679	-0.0063 [0.00]	-0.0031	0.0002	0.00001	
σ^+	ν_7	0.1173	0.0011 [0.00]	-0.0021	0.0001	0.00001	
σ^+	ν_{11}	0.0611	0.0237 [0.07]	-0.0017	0.00009	0.0000	
π	ν_8	0.0716	-	-0.0090 (-0.0003)	-	0.0037 (-0.00059)	0.0000 (0.0000)
π	ν_9	0.0658	-	0.0007 (-0.0009)	-	0.0006 (0.0000)	0.0000 (0.0000)
π	ν_{10}	0.0628	-	0.0236 (-0.0043)	-	-0.0037 (0.0021)	0.0000 (0.0000)
π	ν_{12}	0.0573	-	0.0061 (0.0023)	-	0.0003 (-0.0002)	0.0000 (0.0000)
π	ν_{13}	0.0348	-	-0.0173 (0.0023)	-	0.0030 (-0.0020)	0.0000 (0.0000)
π	ν_{14}	0.0207	-	-0.0070 (0.0008)	-	0.0008 (-0.0002)	0.0000 (0.0000)
π	ν_{15}	0.0080	-	-0.0036 (-0.00008)	-	0.00019 (0.0000)	0.0000 (0.0000)
$\widetilde{A}^2\Sigma$							
σ^+	ν_1	0.4321	-0.0173 [0.00]	0.0012	-0.00006	0.0002	
σ^+	ν_2	0.2772	0.0757 [0.03]	-0.0061	-0.0004	-0.0001	
σ^+	ν_3	0.2734	0.1687 [0.19]	-0.0005	-0.0075	-0.0017	
σ^+	ν_4	0.2609	0.1570 [0.18]	-0.0013	-0.0014	-0.0002	
σ^+	ν_5	0.2463	-0.1530 [0.19]	-0.0114	-0.0001	0.00006	
σ^+	ν_6	0.1679	0.0498 [0.04]	0.0008	-0.00002	-0.00001	
σ^+	ν_7	0.1173	0.0246 [0.02]	0.0011	0.0001	0.0000	
σ^+	ν_{11}	0.0611	0.0185 [0.04]	0.0001	0.00005	0.0000	
π	ν_8	0.0716	-	0.0055	-	0.0037	0.0000
π	ν_9	0.0658	-	0.0057	-	0.0009	0.0000
π	ν_{10}	0.0628	-	0.0253	-	-0.0018	0.0000
π	ν_{12}	0.0573	-	-0.0009	-	0.00046	0.0000
π	ν_{13}	0.0348	-	0.0589	-	-0.0054	0.0000
π	ν_{14}	0.0207	-	0.0315	-	-0.0013	0.0000
π	ν_{15}	0.0080	-	0.0258	-	-0.0005	0.0000

The stationary points corresponding to the equilibrium minimum of a state and the energy minimum of the seam of different CIs are calculated by MATHEMATICA program package [112] and are

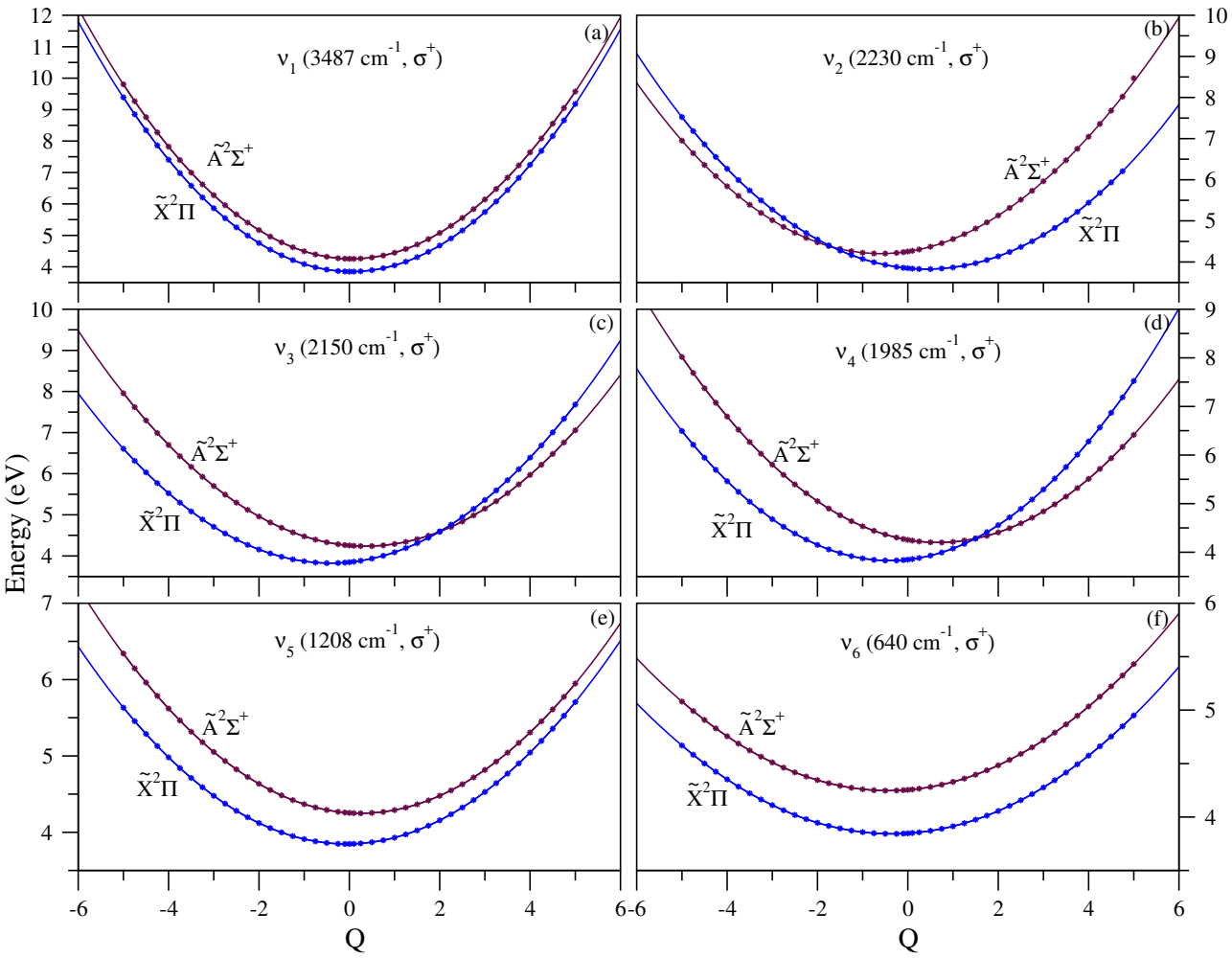

Figure 4.7: Same label as Fig. 4.5 of C_6H.

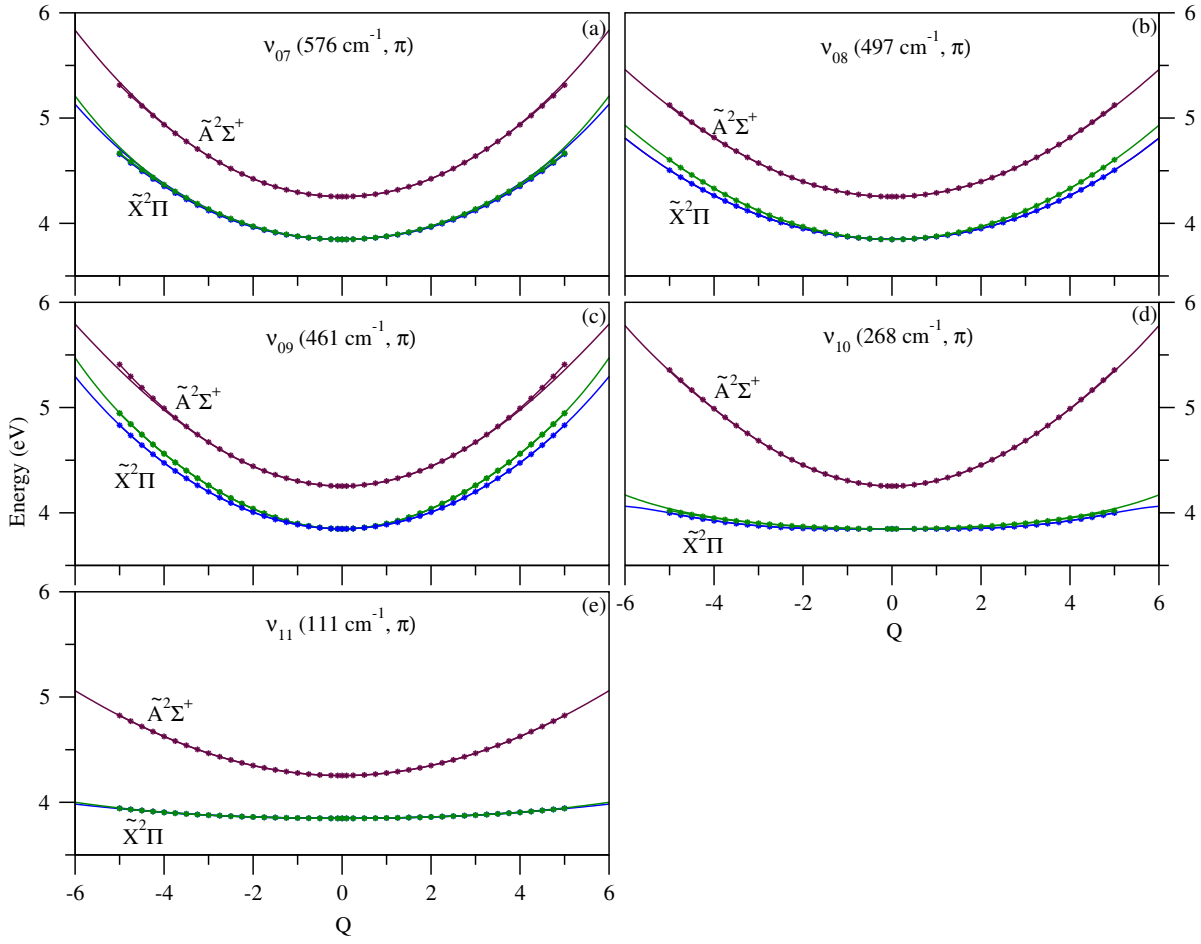

Figure 4.8: Same label as Fig. 4.6 of C_6H.

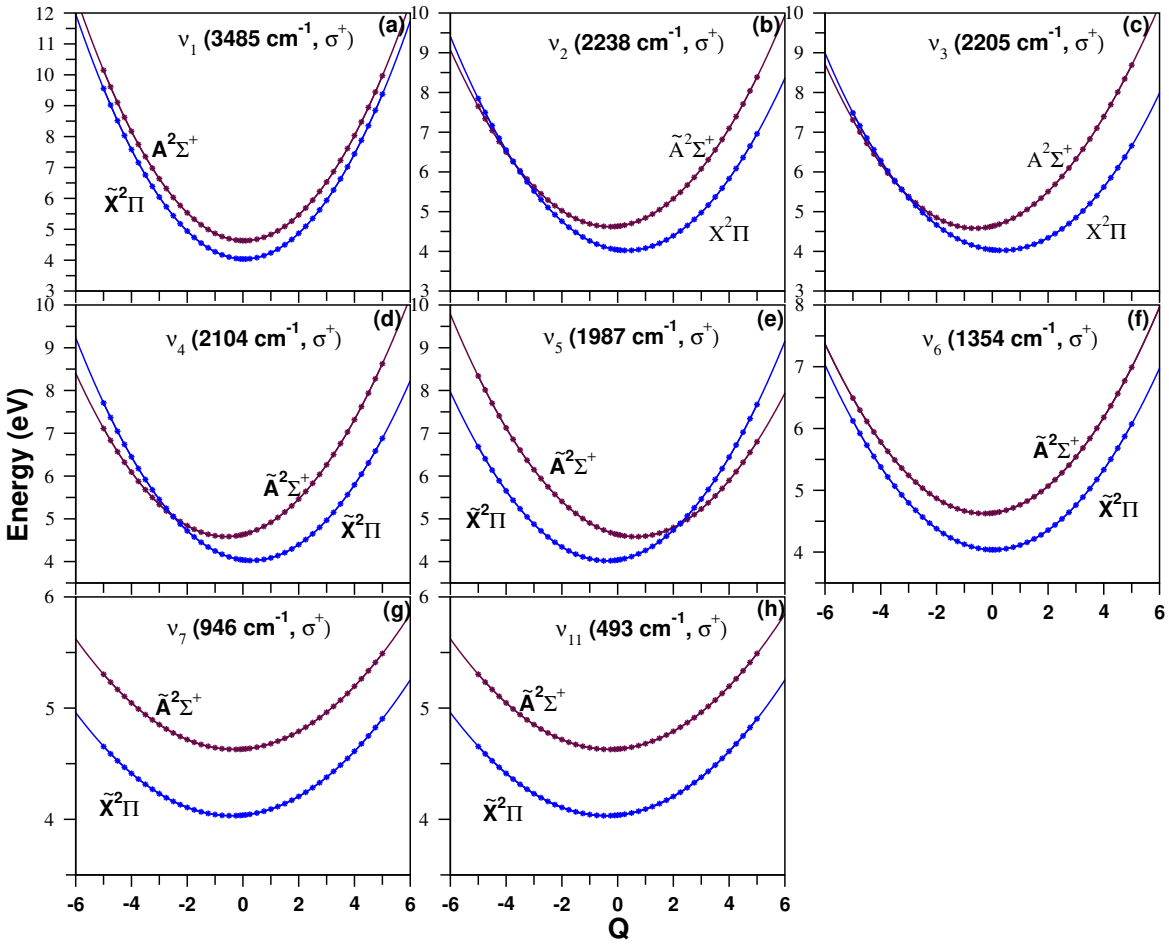

Figure 4.9: Same label as Fig. 4.5 of C_8H.

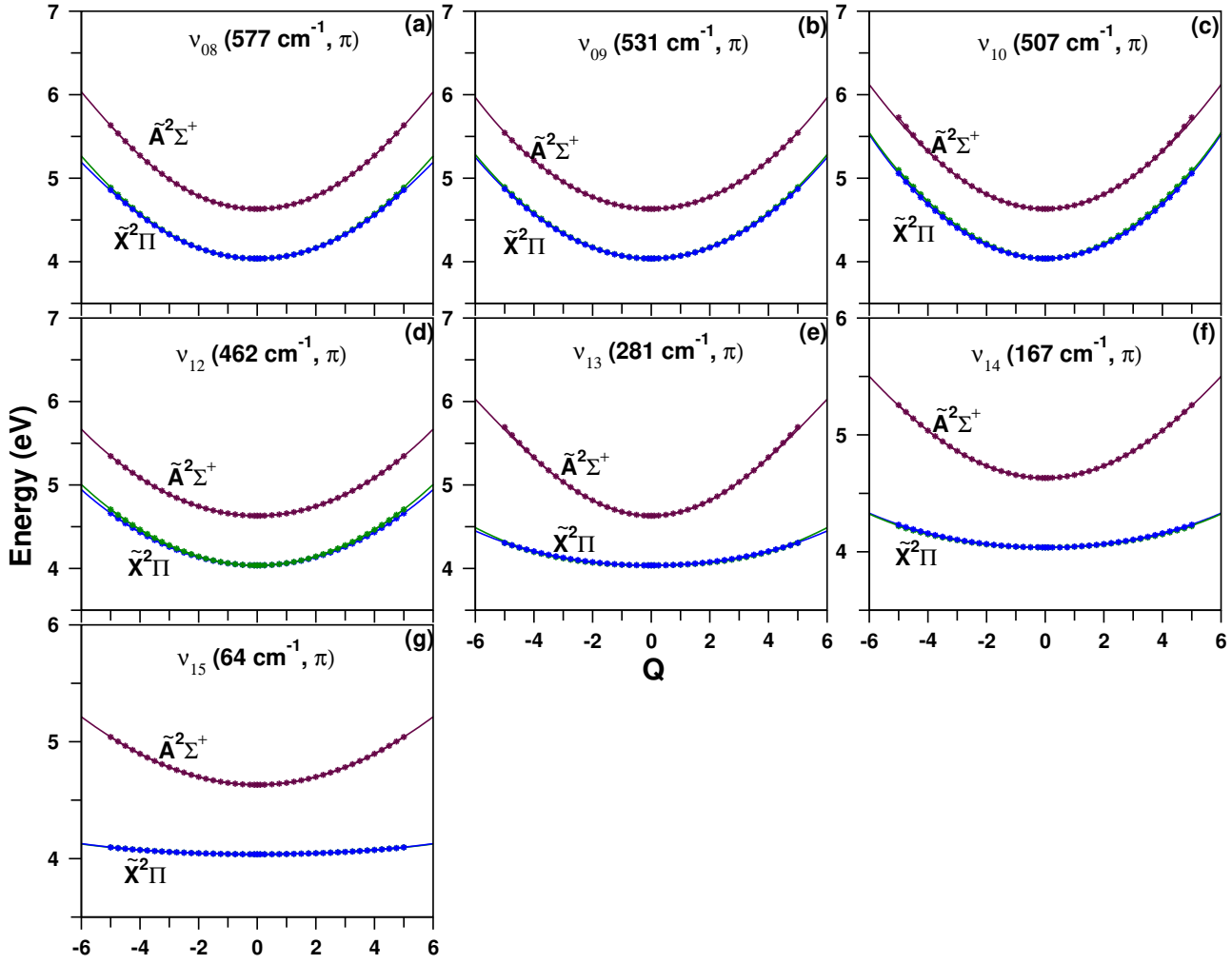

Figure 4.10: Same label as Fig. 4.6 of C_8H.

analysed. A matrix array containing the findings is displayed in Table 4.7. The minimum of a state and the minimum of the intersecting seam are denoted by values in the diagonal and off-diagonal in this instance, respectively. The $\widetilde{X}$ and $\widetilde{A}$ states of C_2H have energy minima at 2.81 and 3.39 eV, respectively. Also at 3.52 eV, the $\widetilde{X}-\widetilde{A}$ CI minimum is located which is only 0.13 eV above the $\widetilde{A}$ state minimum. Then for C_4H, the minima of $\widetilde{X}$ and $\widetilde{A}$ states are located at 3.53 and 3.61 eV respectively. Additionally, the CI minimum between these two states is located at 3.65 eV, meaning only 0.04 eV above the $\widetilde{A}$ state minimum. For C_6H, the minima of $\widetilde{X}$ and $\widetilde{A}$ states, and the CI between the two states are located at 3.77, 4.11, and 4.11 eV respectively. Similarly, for C_8H, the minima of $\widetilde{X}$ and $\widetilde{A}$ states, and the CI between the two states are located at 3.96, 4.45, and 4.46 eV respectively. Overall, the CIs between $\widetilde{X}$ and $\widetilde{A}$ states in case of C_2H is located less than 0.2 eV, in rest of others it is quite close (< 0.05 eV). Consequently, one can expect a significant and rapid electronic population transfer from the $\widetilde{A}$ to $\widetilde{X}$ state contributing for predominant nonadiabatic effects in the nuclear dynamics of all the species.

Table 4.7: VIEs (in eV) of the $\widetilde{X}$ and $\widetilde{A}$ states of $C_{2n}H^-$ calculated at the reference equilibrium geometry of $C_{2n}H$ and compared with the available experimental data.

C_2H	$\widetilde{X}^2\Sigma$	$\widetilde{A}^2\Pi$
$\widetilde{X}^2\Sigma$	2.81	3.52
$\widetilde{A}^2\Pi$		3.39
C_4H	$\widetilde{X}^2\Pi$	$\widetilde{A}^2\Sigma$
$\widetilde{X}^2\Pi$	3.53	3.65
$\widetilde{A}^2\Sigma$		3.61
C_6H	$\widetilde{X}^2\Pi$	$\widetilde{A}^2\Sigma$
$\widetilde{X}^2\Pi$	3.77	4.11
$\widetilde{A}^2\Sigma$		4.11
C_8H	$\widetilde{X}^2\Pi$	$\widetilde{A}^2\Sigma$
$\widetilde{X}^2\Pi$	3.96	4.46
$\widetilde{A}^2\Sigma$		4.45

4.5 Vibronic Structure and Dynamics

The vibrational progressions of $C_{2n}H$ ($n = 1-4$) carbon chains in the first three electronic states i.e., one degenerate and one nondegenerate state ($\widetilde{X}$ and $\widetilde{A}$) of uncoupled spectral envelopes (convoluted through Lorentzian line shape with 30 meV full width half maximum) shown in the Fig. 4.11. In this

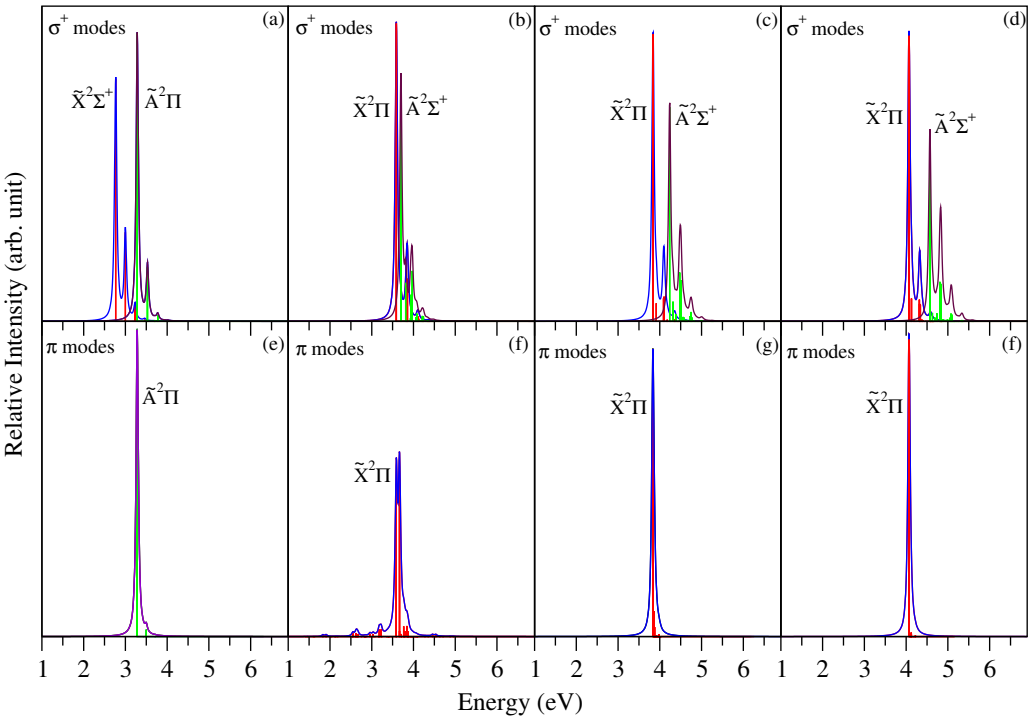

Figure 4.11: The uncoupled $\widetilde{X}$ and $\widetilde{A}$ electronic states of $C_{2n}H$ (n=1-4) vibrational energy level spectrum was calculated using (a) totally symmetric vibrational modes (σ^+) and (b) degenerate vibrational modes (π).

figure, the spectral envelopes presented in each of the panels are the ones resulting from the time-independent matrix diagonalization approach using Lanczos algorithm. Further, the upper panels represent the stick spectra by including totally symmetric σ^+ modes, while the lower panels represent the stick spectra of degenerate π modes.

For C_2H (panel (a) of Fig. 4.11) species, through the inclusion of σ^+ modes (ν_1 & ν_2), the anticipated stick spectra of $\widetilde{X}^2\Sigma$ and $\widetilde{A}^2\Pi$ states is visible here. Consider the $\widetilde{X}^2\Sigma$ state stick spectra originating at energy spacings of $\sim$ 3404 and $\sim$1874 cm^{-1} corresponding to ν_1 and ν_2 respectively. These eigenvalues are also confirmed from the reduced-dimensional vibronic wave packet density plots displayed in Fig. 4.12 and presented in Table 5.12. In panels (a) and (b) of Fig. 4.12, a single node is visible along Q_2 and Q_1 DNDCs dedicated to the fundamental frequencies of ν_2 & ν_1 modes respectively. Further, panel (c) of Fig. 4.12 is assigned to the combination of ν_1 & ν_2 modes due to two nodes simultaneously along their respective Q_1 and Q_2 DNDCs. Moreover, strong Condon activity of ν_2 in the $\widetilde{X}^2\Sigma$ state (cf., Table 4.3) is also confirmed through wave packet density plots in

panels (d), (e), and (f) of Fig. 4.12, dedicated to first, second, and third overtones due to two, three, and four nodes respectively along Q_2 DNDC. Likewise, the subsequent $\widetilde{A}^2\Pi$ state stick spectrum originates at energy spacings of $\sim$ 3400 and $\sim$1974 cm^{-1} corresponding to ν_1 & ν_2 modes respectively. Of note, even in the $\widetilde{A}^2\Pi$ state, the Condon activity of ν_2 is stronger. The assignments are derived from the wave packet density plots of Fig. 4.13, and presented in the Table 5.12. Panels (a) and (b) of Fig. 4.13 exhibits a single node along Q_1 and Q_2 DNDCs dedicated to the fundamental frequencies of ν_1 & ν_2 modes respectively. The successive panels (c) and (d) of Fig. 4.13 are assigned to the combination modes of $\nu_1 + \nu_2$ and $\nu_1 + 2\nu_2$ respectively due to two and three simultaneous nodes along Q_1 and Q_2 DNDCs. The panels (e) and (f) of Fig. 4.13 are assigned to the first overtones of ν_1 & ν_2 respectively due to the apparent two nodes along Q_1 and Q_2 DNDCs. Finally, panels (g) and (h) of Fig. 4.13 are assigned to the second and third overtones of ν_2 due to three and four nodes respectively along Q_2 DNDC.

Table 4.8: Energetically low-lying vibrational energy levels (in cm^{-1}) of the $\widetilde{X}$ and $\widetilde{A}$ electronic states of $C_{2n}H$, $(n = 1 - 4)$ obtained from the uncoupled state calculations.

C_2H				C_4H			
$\widetilde{X}^2\Sigma$		$\widetilde{A}^2\Pi$		$\widetilde{X}^2\Pi$		$\widetilde{A}^2\Sigma$	
Energy	Assignment	Energy	Assignment	Energy	Assignment	Energy	Assignment
0	0_0^0	0	0_0^0	0	0_0^0	0	0_0^0
1874	ν_{20}^{1}	1974	ν_{20}^{1}	889	ν_{40}^{1}	915	ν_{40}^{1}
3404	ν_{10}^{1}	3400	ν_{10}^{1}	2003	ν_{30}^{1}	1831	ν_{40}^{2}
3748	ν_{20}^{2}	3948	ν_{20}^{2}	2146	ν_{20}^{1}	1952	ν_{30}^{1}
5278	$\nu_{10}^{1}+\nu_{20}^{1}$	5374	$\nu_{10}^{1}+\nu_{20}^{1}$	2892	$\nu_{30}^{1}+\nu_{40}^{1}$	2176	ν_{20}^{1}
5622	ν_{20}^{3}	5923	ν_{20}^{3}	3035	$\nu_{20}^{1}+\nu_{40}^{1}$	2869	$\nu_{30}^{1}+\nu_{40}^{1}$
7495	ν_{20}^{4}	6801	ν_{10}^{2}	3503	ν_{10}^{1}	3092	$\nu_{20}^{1}+\nu_{40}^{1}$
		7349	$\nu_{10}^{1}+\nu_{20}^{2}$	4006	ν_{30}^{2}	3504	ν_{10}^{1}
		7899	ν_{20}^{4}	4149	$\nu_{20}^{1}+\nu_{30}^{1}$	3905	ν_{30}^{2}
				4294	ν_{20}^{2}	4008	$\nu_{40}^{2}+\nu_{20}^{1}$
						4137	$\nu_{30}^{1}+\nu_{20}^{1}$
						4351	ν_{20}^{2}
						5267	$\nu_{20}^{2}+\nu_{40}^{1}$
						6304	$\nu_{20}^{2}+\nu_{30}^{1}$

C_6H				C_8H			
$\widetilde{X}^2\Pi$		$\widetilde{A}^2\Sigma$		$\widetilde{X}^2\Pi$		$\widetilde{A}^2\Sigma$	
Energy	Assignment	Energy	Assignment	Energy	Assignment	Energy	Assignment
0	0_0^0	0	0_0^0	0	0_0^0	0	0_0^0
630	ν_{60}^{1}	643	ν_{60}^{1}	485	$\nu_{11_0}^{1}$	493	$\nu_{11_0}^{1}$
1191	ν_{50}^{1}	1213	ν_{50}^{1}	972	$\nu_{11_0}^{2}$	950	ν_{70}^{1}
1260	ν_{60}^{2}	1950	ν_{40}^{2}	1342	ν_{60}^{1}	1357	ν_{60}^{1}
2012	ν_{40}^{1}	2124	ν_{30}^{1}	2006	ν_{50}^{1}	1943	ν_{50}^{1}
2111	ν_{20}^{1}	2180	ν_{20}^{1}	2039	ν_{30}^{1}	2095	ν_{40}^{1}
2140	ν_{30}^{1}	2593	$\nu_{40}^{2}+\nu_{60}^{1}$	2103	ν_{40}^{1}	2145	ν_{30}^{1}
2642	$\nu_{40}^{1}+\nu_{60}^{1}$	2823	$\nu_{20}^{1}+\nu_{60}^{1}$	2202	ν_{20}^{1}	2209	ν_{20}^{1}
2741	$\nu_{20}^{1}+\nu_{60}^{1}$	3163	$\nu_{40}^{1}+\nu_{50}^{1}$	2492	$\nu_{50}^{1}+\nu_{11_0}^{1}$	2437	$\nu_{50}^{1}+\nu_{11_0}^{1}$
2770	$\nu_{30}^{1}+\nu_{60}^{1}$	3337	$\nu_{30}^{1}+\nu_{50}^{1}$	2525	$\nu_{30}^{1}+\nu_{11_0}^{1}$	2588	$\nu_{40}^{1}+\nu_{11_0}^{1}$
		2589	$\nu_{40}^{1}+\nu_{11_0}^{1}$			2639	$\nu_{30}^{1}+\nu_{11_0}^{1}$

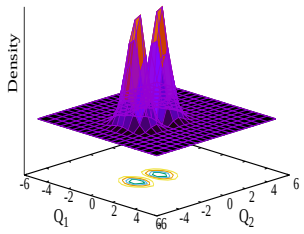

a) 1874 cm^{-1}

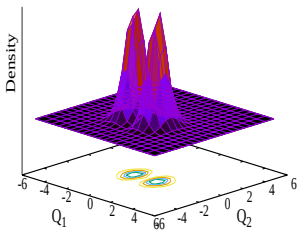

b) 3404 cm^{-1}

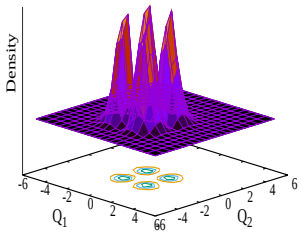

c) 3748 cm^{-1}

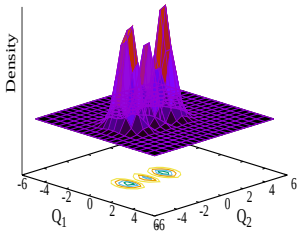

d) 5278 cm^{-1}

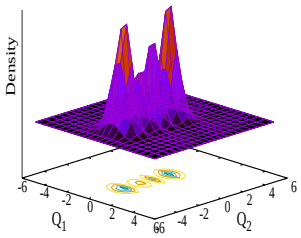

e) 5622 cm^{-1}

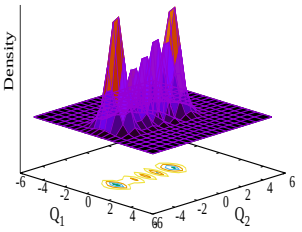

f) 7495 cm^{-1}

Figure 4.12: Probability density of vibronic wave functions of the $\widetilde{X}^2\Sigma$ electronic state of C_2H as a function of nuclear coordinate. Panels a and b represent the fundamentals of v_1 and v_2, respectively. Panel c represents the combination of modes v_1 and v_2. Panels d, e and f are the first, second and third overtones of v_2.

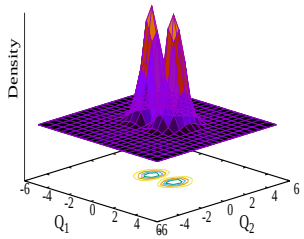

a) 1974 cm^{-1}

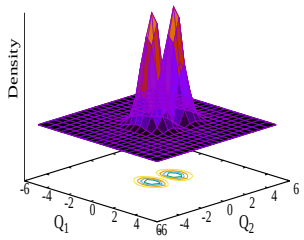

b) 3400 cm^{-1}

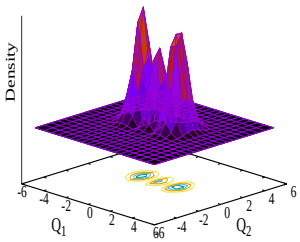

e) 3948 cm^{-1}

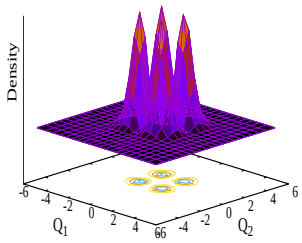

c) 5374 cm^{-1}

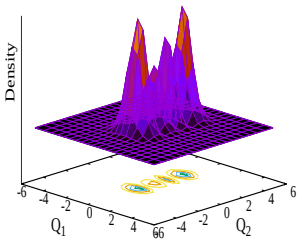

g) 5923 cm^{-1}

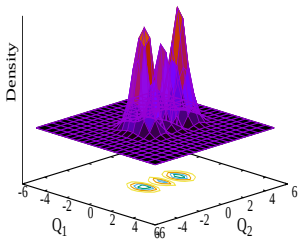

f) 6798 cm^{-1}

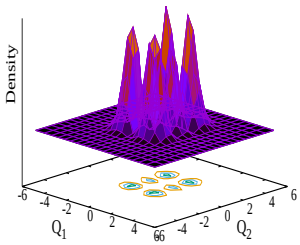

d) 7349 cm^{-1}

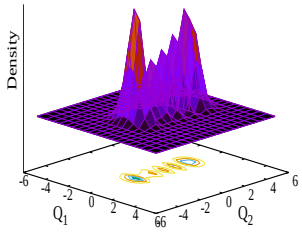

h) 7899 cm^{-1}

Figure 4.13: Probability density of vibronic wave functions of the $\widetilde{A}^2\Pi$ electronic state of C_2H as a function of nuclear coordinate. Panels a and b represent the fundamentals of ν_1 and ν_2, respectively. Panels c and d represent the combinations of ν_1 and ν_2 modes. Panels e and f are the first overtones of ν_1 and ν_2 respectively. Panels g and h represent the second and third overtones of ν_2.

For C_4H (panel (b) of Fig. 4.11) species, through the inclusion of σ^+ modes ($\nu_1, \nu_2, \nu_3,$ & ν_4), the anticipated $\widetilde{X}^2\Pi$ and $\widetilde{A}^2\Sigma$ states' stick spectra is seen here. The $\widetilde{X}^2\Pi$ state stick spectrum originates at ∼3503, ∼2146, ∼2003, and ∼889 cm^{-1} corresponding to fundamental frequencies of ν_1, ν_2, ν_3, and ν_4 modes respectively. In the current $\widetilde{X}^2\Pi$ state, one can realize that the Condon activity of ν_2 and ν_3 modes is significant compared to the weaker Condon activity of the remaining modes (ν_1 & ν_4) from Table 4.4. This observation is also established from the assignments carried out based on wave packet density plots presented in Fig. 4.14 (data given in Table 5.12). Here, panels (a), (b), (c), and (f) of Fig. 4.14 display a single node corroborating for the fundamental frequencies of ν_4, ν_3, ν_2, and ν_1 modes respectively along their corresponding DNDCs. Further, the subsequent panels (d), (e), and (h) corresponds to the combination frequencies of $\nu_3 + \nu_4$, $\nu_2 + \nu_4$, and $\nu_2 + \nu_3$ respectively. Then panels (g) and (i) correspond to first overtone of ν_3 and ν_2 modes along Q_3 and Q_2 DNDCs respectively due to two nodes. Later, the apparent $\widetilde{A}^2\Sigma$ state stick spectra originates at ∼3504, ∼2176, ∼1952, and ∼915 cm^{-1} corresponding to fundamental frequencies of ν_1, ν_2, ν_3, and ν_4 modes respectively. In this context, the Condon activity of ν_2, ν_3, and ν_4 modes is stronger compared to that of ν_1 from Table 4.4. As already pointed out, this proposition is backed with the assignment exercise performed through the wave packet density plots of Fig. 4.15 (data given in Table 5.12). Here, Panels (a), (c), (d), and (g) of Fig. 4.15 correspond to the fundamental frequencies of ν_4, ν_3, ν_2, and ν_1 modes respectively along their corresponding DNDCs. Then the overtones of ν_4, ν_3, and ν_2 are observed in the panels (b), (h), and (k) of Fig. 4.15. Later, various combinations of ν_4, ν_3, and ν_2 are observed in the remaining panels (e), (f), (i), (j), (l), and (m) of Fig. 4.15.

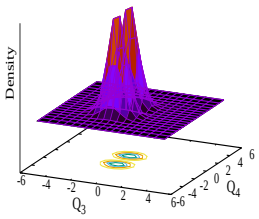

a) 889 cm^{-1}

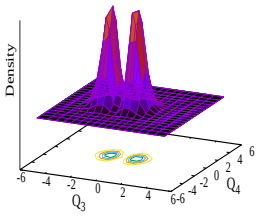

b) 2003 cm^{-1}

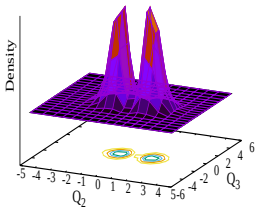

c) 2146 cm^{-1}

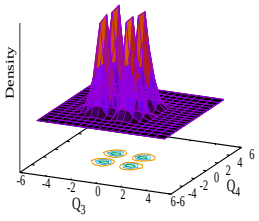

d) 2892 cm^{-1}

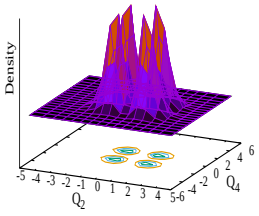

e) 3035 cm^{-1}

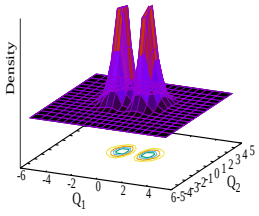

f) 3503 cm^{-1}

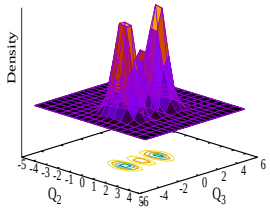

g) 4006 cm^{-1}

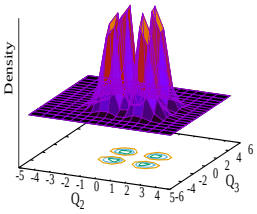

h) 4149 cm^{-1}

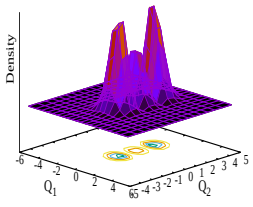

i) 4294 cm^{-1}

Figure 4.14: Probability density of vibronic wave functions of the $\widetilde{X}^2\Pi$ electronic state of C_4H as a function of nuclear coordinate. Panels a, b, c, and f represent the fundamentals of ν_4, ν_3, ν_2, and ν_1 respectively. Panels g and i are the first overtones of ν_3 and ν_2 respectively. Panels d, e, and h represent different combinations of ν_2, ν_3 and ν_4.

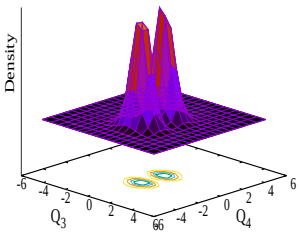

a) 915 cm^{-1}

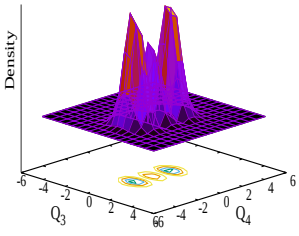

b) 1831 cm^{-1}

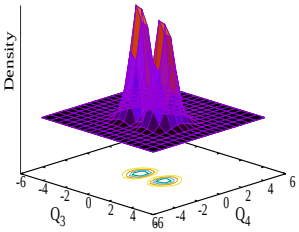

c) 1952 cm^{-1}

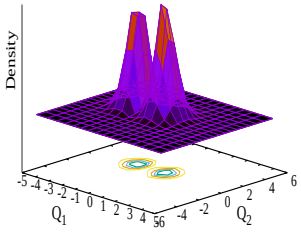

d) 2176 cm^{-1}

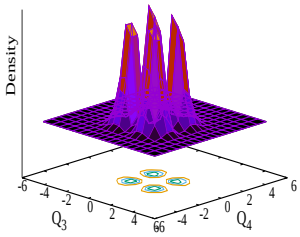

e) 2869 cm^{-1}

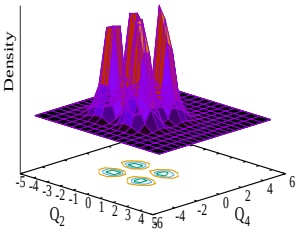

f) 3092 cm^{-1}

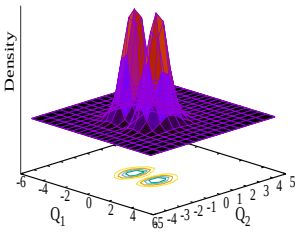

g) 3504 cm^{-1}

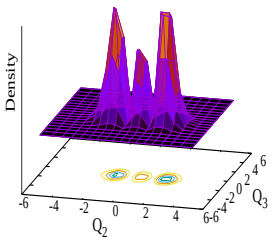

h) 3905 cm^{-1}

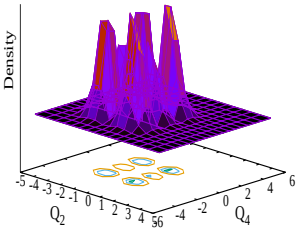

i) 4008 cm^{-1}

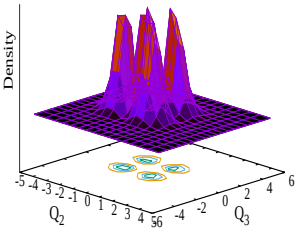

j) 4137 cm^{-1}

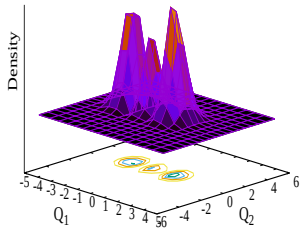

k) 4351 cm^{-1}

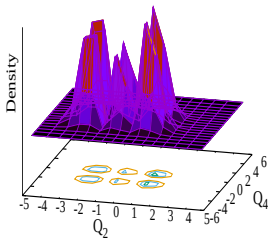

l) 5267 cm^{-1}

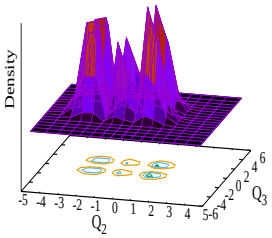

m) 6304 cm^{-1}

Figure 4.15: Probability density of vibronic wave functions of the $\widetilde{A}^2\Sigma$ electronic state of C_4H as a function of nuclear coordinate. Panels a, b, c, and d represent the fundamentals of ν_1, ν_2, ν_3, and ν_4 respectively. Panels e, f, and g represent the first overtones of ν_2, ν_3, and ν_4 respectively. Panels h-m represent different combinations of ν_2, ν_3 and ν_4 modes.

In the similar lines, the $\widetilde{X}^2\Pi$ and $\widetilde{A}^2\Sigma$ states' stick spectra of C_6H and C_8H is shown in panels (c) and (d) of Fig. 4.11. As detailed above, one can interpret the Condon activity and the impact of $\nu_2 - \nu_6$ modes on the stick spectra of C_6H through wave packet density plots (Fig. 4.16 & 4.17) and their corresponding assignments (Table 5.12). Furthermore, the Condon activity and the impact of $\nu_2 - \nu_7$ & ν_{11} on the stick spectra of C_8H through wave packet density plots (Fig. 4.18 & 4.19) and their corresponding assignments (Table 5.12) can be understood.

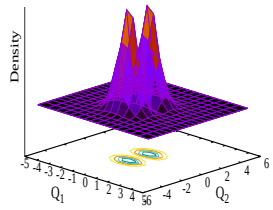

a) 630 cm^{-1}

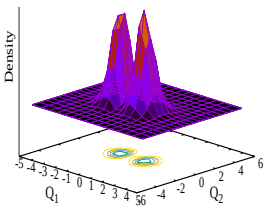

b) 1191 cm^{-1}

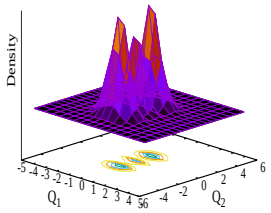

c) 1260 cm^{-1}

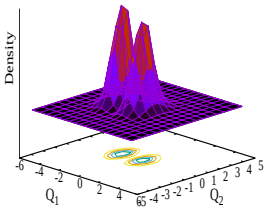

d) 2012 cm^{-1}

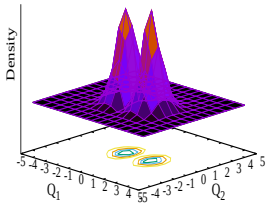

e) 2111 cm^{-1}

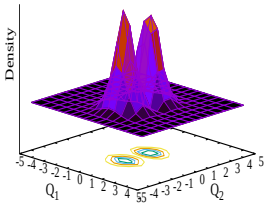

f) 2140 cm^{-1}

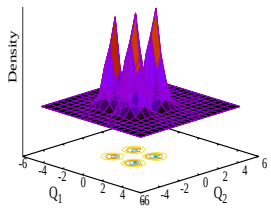

k) 2642 cm^{-1}

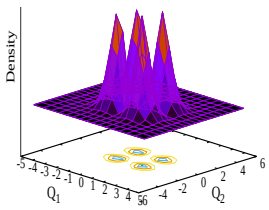

l) 2741 cm^{-1}

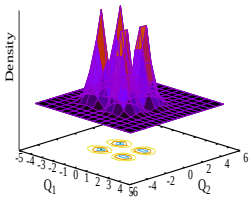

m) 2770 cm^{-1}

Figure 4.16: Probability density of vibronic wave functions of the $\widetilde{A}^2\Sigma$ electronic state of C_6H as a function of nuclear coordinate. Panels a, b, c, and d represent the fundamentals of ν_1, ν_2, ν_3, and ν_4 respectively. Panels e, f, and g represent the first overtones of ν_2, ν_3, and ν_4 respectively. Panels h-m represent different combinations of ν_2, ν_3 and ν_4 modes (please refer to Table 5.12 for more details).

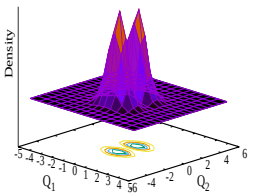

a) 643 cm^{-1}

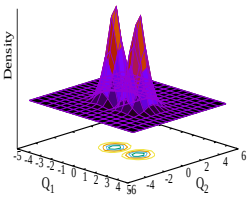

b) 1213 cm^{-1}

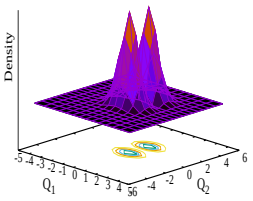

c) 1950 cm^{-1}

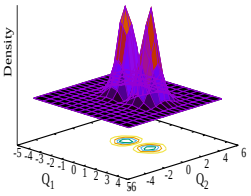

d) 2124 cm^{-1}

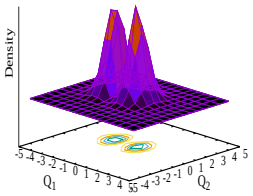

e) 2180 cm^{-1}

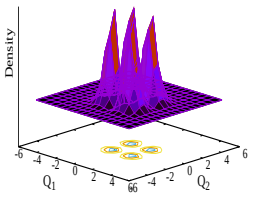

f) 2593 cm^{-1}

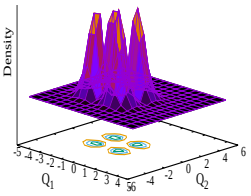

g) 2823 cm^{-1}

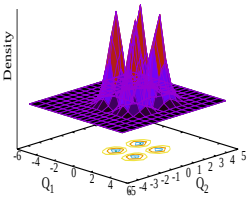

h) 3163 cm^{-1}

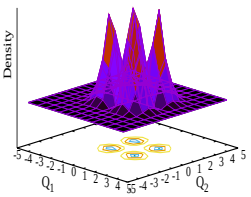

i) 3337 cm^{-1}

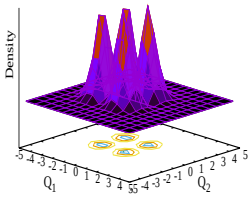

j) 3394 cm^{-1}

Figure 4.17: Probability density of vibronic wave functions of the $\widetilde{A}^2\Sigma$ electronic state of C_6H as a function of nuclear coordinate. Panels a, b, c, and d represent the fundamentals of ν_1, ν_2, ν_3, and ν_4 respectively. Panels e, f, and g represent the first overtones of ν_2, ν_3, and ν_4 respectively. Panels h-m represent different combinations of ν_2, ν_3 and ν_4 modes (please refer to Table 5.12 for more details).

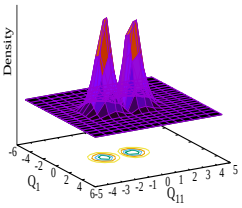

a) 485 cm^{-1}

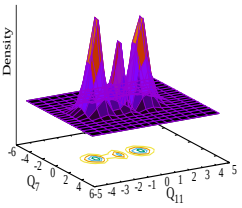

b) 972 cm^{-1}

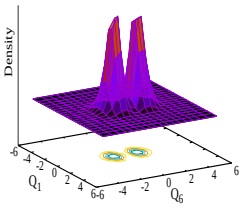

c) 1342 cm^{-1}

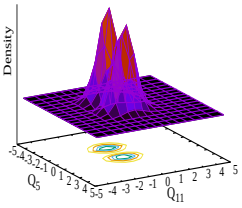

d) 2006 cm^{-1}

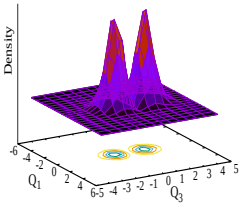

e) 2039 cm^{-1}

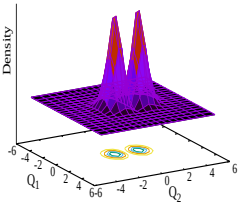

f) 2103 cm^{-1}

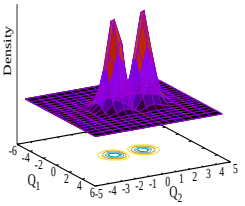

g) 2202 cm^{-1}

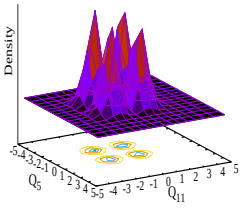

h) 2492 cm^{-1}

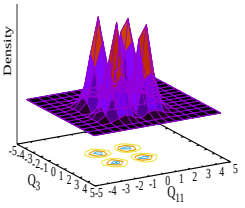

i) 2525 cm^{-1}

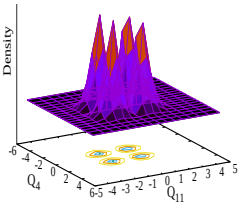

j) 2589 cm^{-1}

Figure 4.18: Probability density of vibronic wave functions of the $\widetilde{A}^2\Sigma$ electronic state of C_6H as a function of nuclear coordinate. Panels a, b, c, and d represent the fundamentals of ν_1, ν_2, ν_3, and ν_4 respectively. Panels e, f, and g represent the first overtones of ν_2, ν_3, and ν_4 respectively. Panels h-m represent different combinations of ν_2, ν_3 and ν_4 modes (please refer to Table 5.12 for more details).

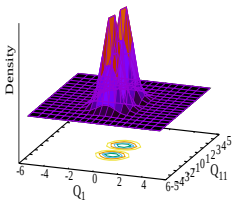

a) 493 cm^{-1}

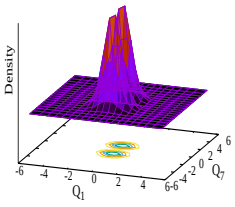

b) 950 cm^{-1}

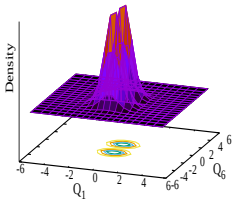

c) 1357 cm^{-1}

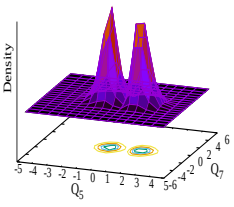

d) 1943 cm^{-1}

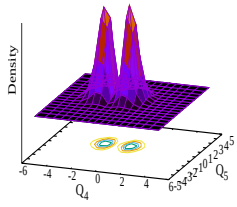

e) 2095 cm^{-1}

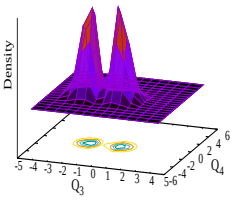

f) 2145 cm^{-1}

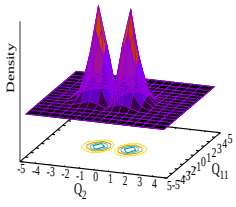

g) 2209 cm^{-1}

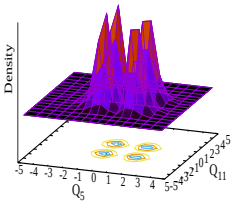

h) 2437 cm^{-1}

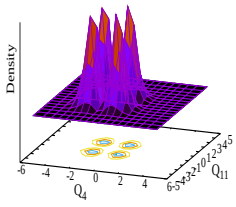

i) 2588 cm^{-1}

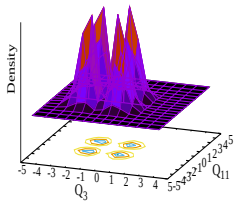

j) 2639 cm^{-1}

Figure 4.19: Probability density of vibronic wave functions of the $\widetilde{A}^2\Sigma$ electronic state of C_6H as a function of nuclear coordinate. Panels a, b, c, and d represent the fundamentals of ν_1, ν_2, ν_3, and ν_4 respectively. Panels e, f, and g represent the first overtones of ν_2, ν_3, and ν_4 respectively. Panels h-m represent different combinations of ν_2, ν_3 and ν_4 modes (please refer to Table 5.12 for more details).

Along the π vibrational modes, the Π electronic states are RT active in fourth order. When the degenerate vibrational modes are distorted, there is significant splitting between the two components. It is anticipated that the vibronic structure of Π states will be greatly impacted by RT coupling of $C_{2n}H$ (see Figs. 4.4,4.6, 4.8, 4.10). The splitting along the π modes of Π states for the mentioned carbon chains is in the decreasing order, indicates that the RT impact likewise diminishing. Tables 4.3,4.4,4.5 and 4.6 provide evidence for this observation by displaying the RT values (γ_i) that are decreasing as chain length increases. Fig. 4.11 displays the partial spectra of C_2H, C_4H, C_6H, and C_8H, respectively, in panels (e), (f), (g), and (h), which were computed using the degenerate RT modes (π). These spectra show how RT coupling contributes to the vibronic structure of Π states.

4.6 Time Dependent Dynamics of $\widetilde{X} - \widetilde{A}$ States

As discussed in the section 'The Hamiltonian' along with RT, this also includes the PRT coupling of the $\widetilde{X} - \widetilde{A}$ states of $C_{2n}H$ through vibrational modes π symmetry. The π vibrational mode's coupling strengths in the $\widetilde{X} - \widetilde{A}$ electronic manifold is substantial, according to the coupling values shown in Table 4.9. All of the modes of $C_{2n}H$ carbon chains are taken into account in the nuclear dynamics calculations to eliminate any room for uncertainty. Using the MCTDH program modules, the dynamical computations were performed by propagating WP on three electronic states (two RT split Π states + one Σ^+ state) of $C_{2n}H$. The initial WP, which corresponds to the reference neutral molecule's vibronic ground state, is vertically promoted to each of the ionic states and propagated in the coupled $\widetilde{X} - \widetilde{A}$ electronic states. To determine the composite vibronic band, the time autocorrelation functions derived from three WP calculations are merged, damped by an exponential function, $e^{(-t/\tau_r)}$ (with τ = 30 fs), and Fourier transformed. Fig. 4.20 displays the available experimental spectra as well as the vibronic band structure of the $\widetilde{X} - \widetilde{A}$ coupled electronic states of $C_{2n}H$ that are determined by these calculations. It is seen from the Fig. 4.20 that the theoretical results are in good agreement with the experimental findings[2]. The vibronic bands of the individual electronic states $\widetilde{X}$ and $\widetilde{A}$ are close in energy and the RT and PRT couplings are having a vital role in the nonadiabatic dynamics.

Table 4.9: Interstate coupling parameters (in eV) of the vibronic Hamiltonian of Eqs. (10) and (11) for the $\widetilde{X}, \widetilde{A}$ electronic states of $C_{2n}H$ ($n = 1-4$) carbon chains estimated from the *ab initio* electronic structure results (see text for details).

Symmetry	Mode	Frequency (eV)	λ_i^{X-A}
C_2H			
π	ν_3	0.0680	0.1018 (1.12)
C_4H			λ_i^{X-A}
π	ν_5	0.0773	0.0594 (0.29)
π	ν_6	0.0542	0.0278 (0.13)
π	ν_7	0.0311	0.0912 (4.29)
C_6H			λ_i^{X-A}
π	ν_7	0.0715	0.0505 (0.24)
π	ν_8	0.0616	0.0403 (0.21)
π	ν_9	0.0572	0.0279 (0.12)
π	ν_{10}	0.0332	0.1129 (5.78)
π	ν_{11}	0.0137	0.0703 (13.16)
C_8H			λ_i^{X-A}
π	ν_8	0.0716	0.0005 (0.00)
π	ν_9	0.0658	0.0280 (0.09)
π	ν_{10}	0.0628	0.0203 (0.05)
π	ν_{12}	0.0573	0.0289 (0.12)
π	ν_{13}	0.0348	0.1140 (5.36)
π	ν_{14}	0.0207	0.0792 (7.31)
π	ν_{15}	0.0080	0.0688 (36.98)

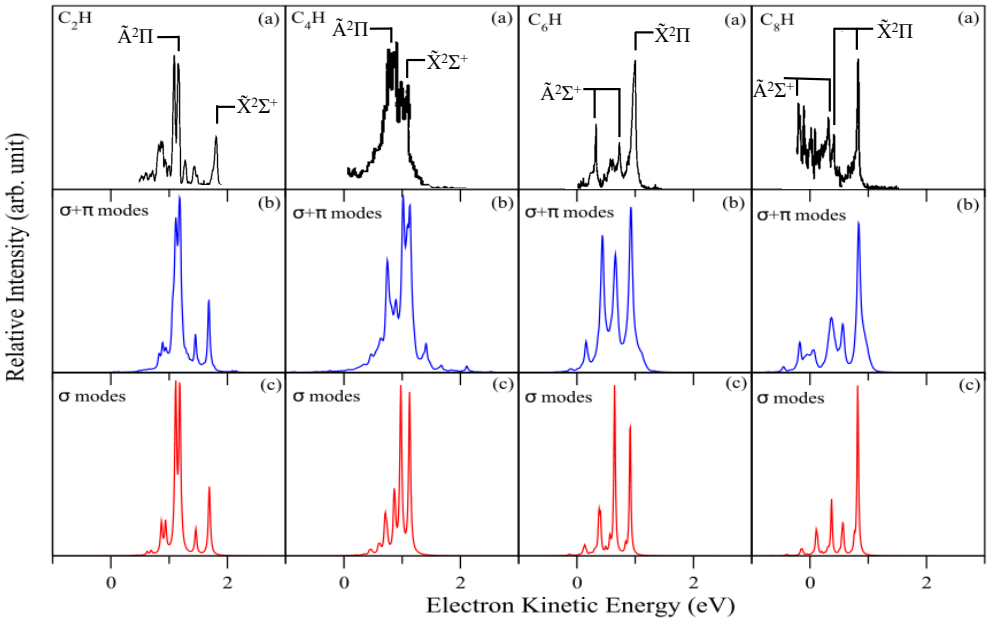

Figure 4.20: Vibronic band structure of the $\widetilde{X}-\widetilde{A}$ coupled electronic states including $\sigma^+ + \pi$ vibrational modes of $C_{2n}H$ (n=1-4) are shown in panels labelled as (b) and just including totally symmetric σ^+ vibrational modes, band structures are shown in panels labelled as (c). Relative intensity (in arbitrary units) is plotted as a function of the energy of the vibronic states of $C_{2n}H$ (n=1-4). The present theoretical results are shown in panels (b) and (c) whereas the experimental results of[2] are shown in panels labelled with (a).

4.7 Internal conversion Dynamics

Figs. 4.21, 4.22, 4.23 and 4.24 helps us to further understand the implications of nonadiabatic coupling on the dynamics, this section examines the time-dependence of the diabatic electronic populations of $C_{2n}H$ ($n = 1-4$) carbon chains in the coupled $\widetilde{X}-\widetilde{A}$ states, encompassing all of the ($\sigma+\pi$) vibrational modes. The magnitude of the PRT coupling that exists among the electronic states determines the population transfer. When WP is initially prepared on the $\widetilde{X}^2\Sigma$ state of C_2H (Fig. 4.21, panel (a)), a significant portion of WP is confined on $\widetilde{X}$ itself. The $\widetilde{X}-\widetilde{A}$ PRT intersection seam (see Table 4.7), which is 0.71 eV greater than the $\widetilde{X}^2\Sigma$ state equilibrium minimum, provides an explanation for this. When WP is placed on a single component of the $\widetilde{A}^2\Pi$ electronic state (let's say x and y) (Fig. 4.21, panels (b) and (c)), the electron population swings between the x/y component of $\widetilde{A}^2\Pi$ and $\widetilde{X}^2\Sigma$ electronic state. This may be explained by the PRT coupling between the two electronic states ($\widetilde{X}^2\Sigma$ and $\widetilde{A}^2\Pi$) via the π vibrational mode, which is considerable (see Table 4.9). Furthermore, the $\widetilde{A}^2\Pi$ state minimum is 3.39 eV, while the PRT intersection minimum of $\widetilde{X}^2\Sigma$-$\widetilde{A}^2\Pi$ is 3.52 eV, which is just 0.13 eV higher, which helps in oscillating the population smoothly. Also, there is a significant RT coupling in the $\widetilde{A}^2\Pi$ state (see Table 4.3). Consequently, the population flow to the second component of the $\widetilde{A}^2\Pi$ state (y/x) is seen.

Around 50% of the population oscillates between the x and y components of $\widetilde{X}^2\Pi$ state in a mirror image pattern when WP is positioned on one of the components (x/y) of $\widetilde{X}^2\Pi$ state of C_4H (see Fig. 4.22, panel (a) and (b)). This indicates a considerable degree of RT impact. The population leakage to the $\widetilde{A}^2\Sigma$ state is quite small as the equilibrium minimum of state $\widetilde{X}^2\Pi$ can neither access the minimum of $\widetilde{A}^2\Sigma$ nor the intersection minimum of $\widetilde{X}^2\Pi$-$\widetilde{A}^2\Sigma$. However, when WP is placed on the $\widetilde{A}^2\Sigma$ state (see 4.22, panel (c)), around 40% of the population moves to the $\widetilde{X}^2\Pi$ state, which is explained by the $\widetilde{X}^2\Sigma$-$\widetilde{A}^2\Pi$ PRT seam minimum, which is just 0.04 eV higher than the $\widetilde{A}^2\Sigma$ state minimum.

In the case of C_6H, around 40% of the population is moved to another component (y/x) of $\widetilde{X}^2\Pi$ state when WP is applied to one of the components (x/y) of $\widetilde{X}^2\Pi$ state (see Fig. 4.23, panels (a) and (b)). Additionally, almost 20% of the population leaks to the $\widetilde{A}^2\Sigma$ state, which is significantly higher than the C_4H, suggesting that the PRT coupling between the $\widetilde{X}^2\Pi$ and $\widetilde{A}^2\Sigma$ states along π modes is higher (cf. Table 4.9). In a similar vein, around 30% of the population gradually moves to the $\widetilde{X}^2\Pi$ state when WP is placed on the $\widetilde{A}^2\Sigma$ state (see Fig. 4.23, panel (c)) since the $\widetilde{X}^2\Pi$-$\widetilde{A}^2\Sigma$ PRT seam minimum and the equilibrium minimum of the $\widetilde{A}^2\Sigma$ state are quasidegenerate. Similarly electronic population dynamics of C_8H, when WP is placed on one of the components (x/y) of $\widetilde{X}^2\Pi$ state (see Fig. 4.24, panels (a) and (b)), curiously 40% of the population is moved to the $\widetilde{A}^2\Sigma$ state and just around 30%

of the population is transferred to the (y/x) component of $\widetilde{X}^2\Pi$ state. This can be the result of higher PRT coupling of $\widetilde{X}^2\Pi$-$\widetilde{A}^2\Sigma$ and low RT impact of $\widetilde{X}^2\Pi$ state, respectively. Similarly, roughly 30% of the population progressively transfers to the $\widetilde{X}^2\Pi$ state when WP is positioned on the $\widetilde{A}^2\Sigma$ state (see Fig. 4.24, panel (c)), since the equilibrium minimum of the $\widetilde{A}^2\Sigma$ state and the $\widetilde{X}^2\Pi$-$\widetilde{A}^2\Sigma$ PRT seam minimum are just 0.01 eV apart.

An extensive description of the nonadiabatic dynamics of all four carbon chains $C_{2n}H$ ($n = 1-4$) is provided by taking into account the cumulative consideration of RT effect within the degenerate Π state along the π coupling vibrational mode (see Tables 4.3,4.4,4.5,4.6), PRT coupling strength between the $\widetilde{X} - \widetilde{A}$ states (see Table 4.9), and also from the static points (see Table 4.7). As the chain length increases, a general tendency is observed in which the impact of PRT increases and the RT effect eventually decreases. The nonadiabatic dynamics of the aforementioned systems has been significantly influenced by these two factors.

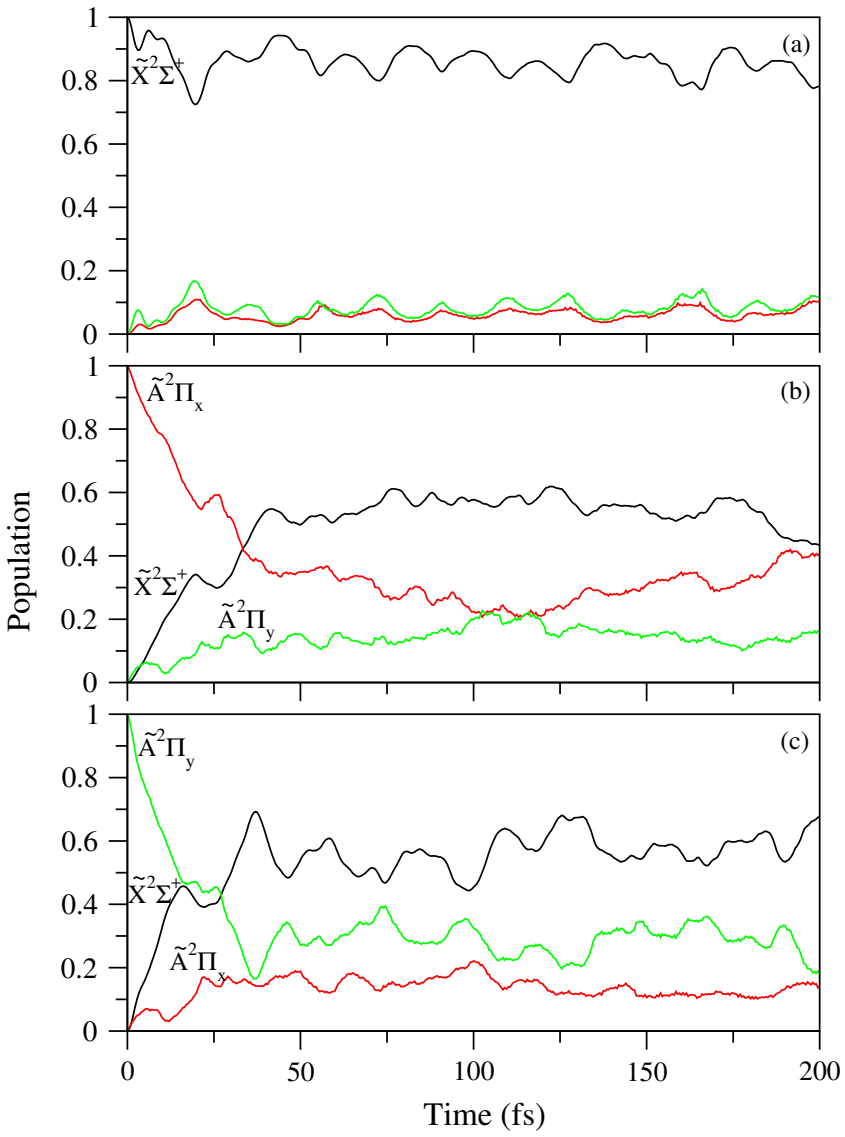

Figure 4.21: Nuclear dynamics of C_2H in the $\tilde{X}$-$\tilde{A}$ coupled states: Time dependence of diabatic electron populations. Panel (a) displays the initial (at t=0) WP on the $\tilde{X}$ electronic state, while panels (b) and (c) display one of the components of the degenerate $\tilde{A}$ state at each time.

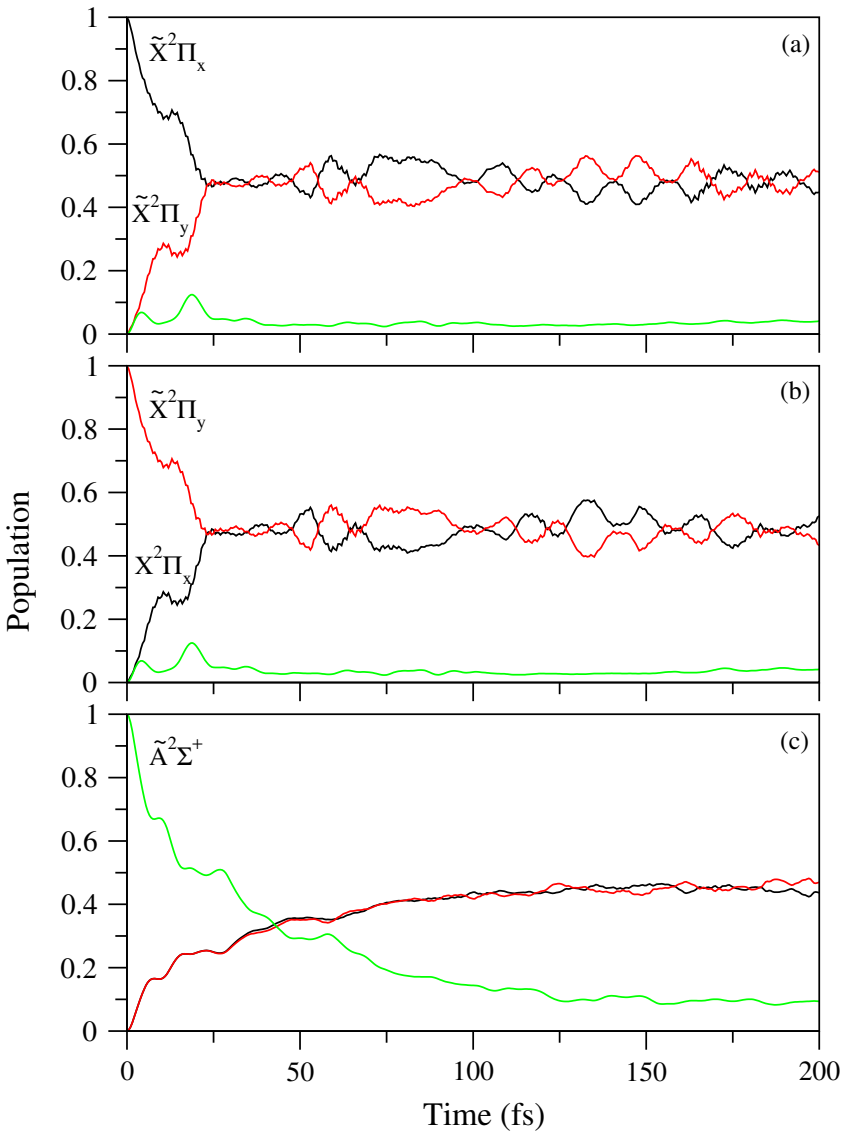

Figure 4.22: Nuclear dynamics of C_4H in the $\tilde{X}$-$\tilde{A}$ coupled states: Time dependence of diabatic electron populations. Panels (a) and (b) display the initial (at t=0) WP on one of the components of the degenerate $\tilde{X}$ state at each time, and panel (c) displays on $\tilde{A}$ electronic state.

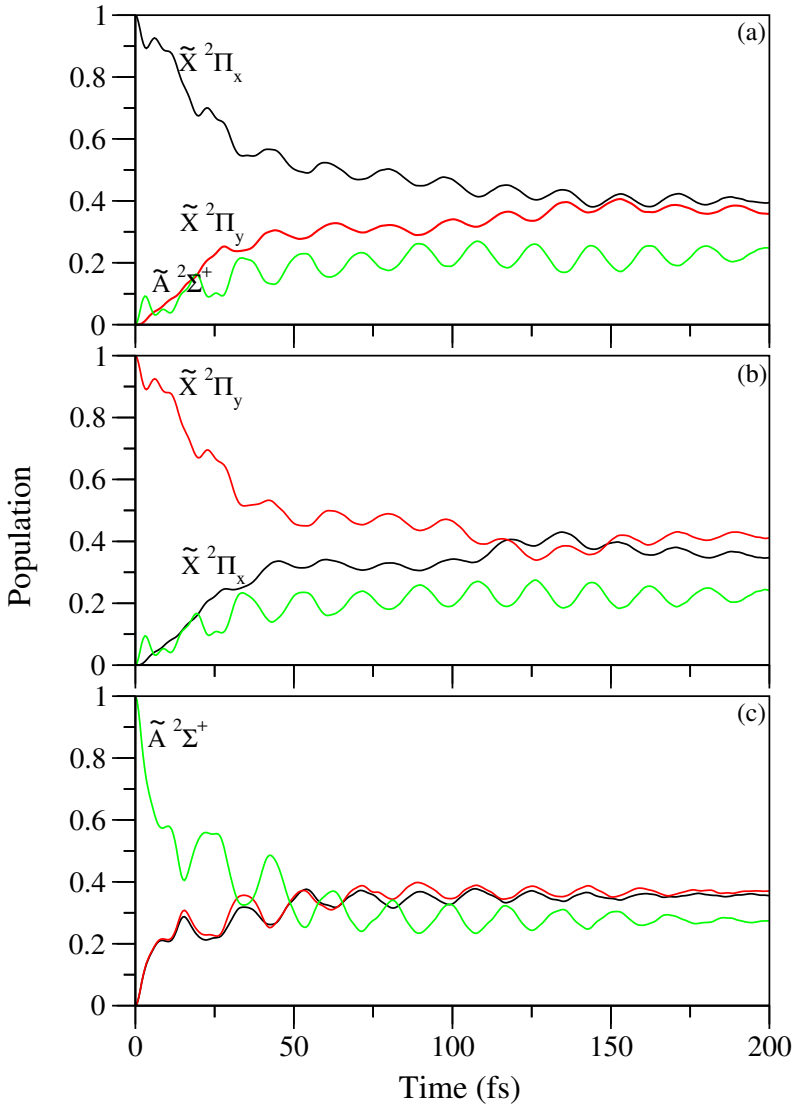

Figure 4.23: Same label as Fig. 4.22 of C_6H.

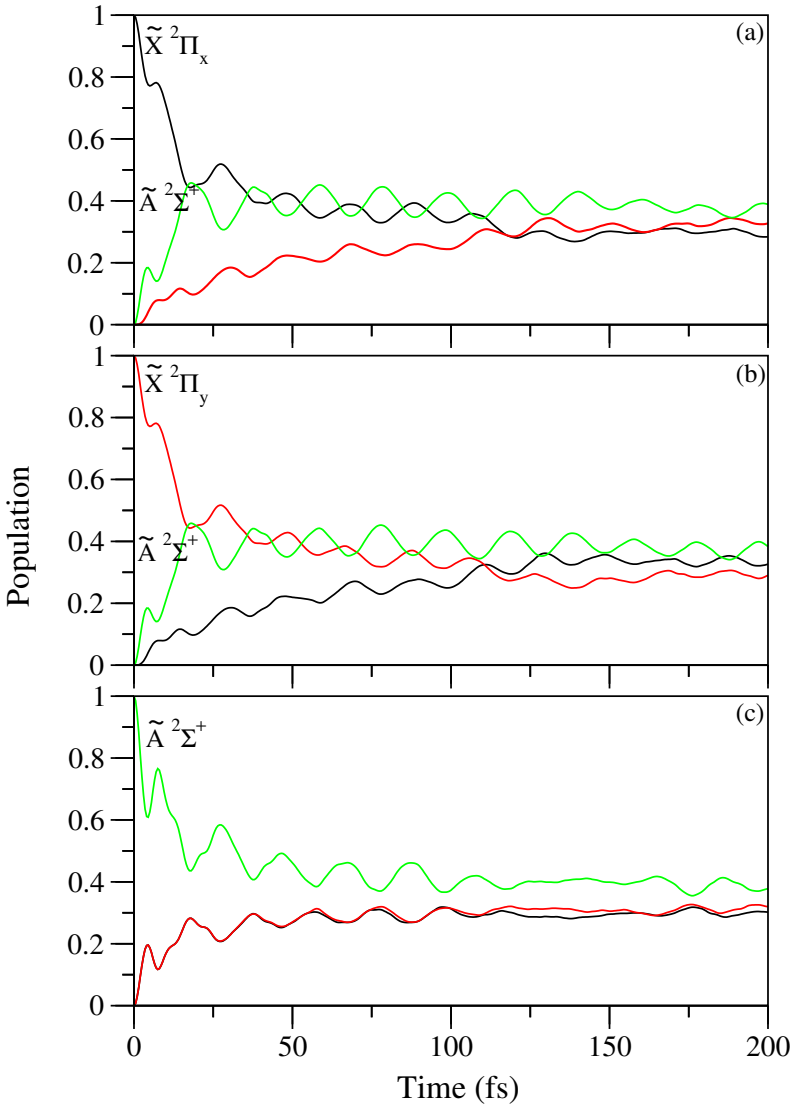

Figure 4.24: Same label as Fig. 4.22 of C_8H.

4.8 Conclusions

In this work, a detailed and exhaustive account of the $C_{2n}H^-$ ($n = 1 - 4$) species and their corresponding neutral species is presented. To achieve this, state-of-the-art *ab initio* electronic structure calculations are carried out and revealed $\widetilde{X}^2\Sigma$ ground state for $n = 1$ and $\widetilde{X}^2\Pi$ ground state for $n > 1$ species. The calculations also supported the extraction of electronic PECs from the three low-lying electronic states of neutral species. The analysis of the former, unfolded that the energy differences among the electronic states and the Franck-Condon activity of the symmetric modes decreased as n increased. Furthermore, the impact of asymmetric modes is found to be significant, but gradually decreased with n in terms of second-order RT coupling. The decrease in energy differences among electronic states resulted in enhanced curve crossings which translated as CIs and helped us anticipate their dominant influence on the dynamics. In this direction, an analysis of the quantitative data of the minima of electronic states and the minima of seams of CIs occurring between various combinations of electronic states is presented. Considering all the relevant couplings and constructing a diabatic Hamiltonian, nuclear dynamics is performed in both uncoupled and coupled frameworks. The uncoupled states results in a time-independent methodology provided us with the vibronic eigenvalues in the form of stick spectra of each electronic state. Based on these results along with the wave packet density plots, assignment of each symmetric vibrational mode and their corresponding overtones and combinations is carried out for all the species. The coupled states results in a time-dependent methodology exhibited excellent accuracy in reproducing the experimental outcomes of each of the species. As a final note on the impact of nonadiabatic effects in all these systems, further deep analysis is carried out with the outcomes of time-dependence of diabatic electronic population picture. Overall, the RT and PRT effects are observed to be following a decreasing and an increasing trends with n respectively.

Chapter 5

Full-dimensional investigation of the photoionization spectrum of benzonitrile (BN)

ABSTRACT

The present investigation employs the state-of-the-art *ab initio* electronic structure and quantum dynamical method to examine the photoionization spectrum of benzonitrile (BN) also called cyanobenzene. A multi-state and multi-mode vibronic coupling model is developed and employed for the purpose. Utilizing both the multi-configuration time-dependent Hartree (MCTDH) and its multi-layer (ML-MCTDH) variant, the dynamics and spectral feature of benzonitrile radical cation ($BN^{\cdot+}$) is examined. The findings from the present theoretical work in conjunction with experimental photoionization spectroscopy aids to the understanding of complex interplay of electronic structural feautures and nuclear dynamics of this complex molecular system. This approach not only elucidates crucial features of individual photoionization bands of BN, but also sheds light on the discrepancies of previous studies as revealed by the reported spectral features. The results contribute further to the understanding of BN's potential applications in various dimensions, highlighting its unique electronic properties influenced by the cyano group. A strong correlation was found between the full dimensional ML-MCTDH findings, the experiment, and reduced dimensional MCTDH calculations. This indicates that the ML-MCTDH method is very efficient, which enabled to understand the finer details of spectral and dynamical features.

5.1 Introduction

In theoretical chemical physics and physical chemistry, it is a significant challenge to describe many-body quantum effects accurately for complex molecules. For small gas phase reactions, a direct method can be utilized, wherein the entire wave function is expanded using static basis functions or configurations that comprehensively cover the Hilbert space of the problem, ensuring numerical convergence. Thanks to advancements in both numerical algorithms and computer hardware, significant advancements have been achieved in recent decades in executing such calculations. Nevertheless, the majority of techniques developed within this framework are not readily adaptable in treating larger systems. The main challenge associated with these conventional full configurational methods is the exponential increase in the number of basis functions relative to the system's size[36;39]. Then in the field of molecular quantum dynamics, the multi-configuration time-dependent Hartree (MCTDH)[35;65;70;130;131] method has emerged as a paradigm tool to treat systems with large electronic and nuclear degrees of freedom fully quantum-mechanically. MCTDH can be interpreted as a technique utilizing highly adaptable time-dependent functions, which adhere to the variational equations originating from the Dirac-Frenkel variational principle. This method converges towards the precise solution and can accommodate a greater number of degrees of freedom (DOFs) compared to quantum dynamics approaches utilizing fixed time-independent functions. More recently, a multi-layer (ML) version of MCTDH has emerged, capable of handling even higher-dimensional systems over 1000 DOFs[36;39;71;72;37;73;38;74;75;76;77;78;79;80;81] quantum mechanically.

In this study, both standard MCTDH (two layers) and ML-MCTDH are employed to investigate the photoionization dynamics of the benzonitrile (BN), C_6H_5CN molecule. The latter, is the simplest aromatic CN-substituted hydrocarbon and apparently is the building block of Polycyclic Aromatic Hydrocarbons (PAHs). Although PAHs are generally to be an established class of interstellar molecules, apparently no particular PAH has been found in the Interstellar Medium (ISM) using rotational spectroscopy or infrared spectroscopic investigations. A large number of PAHs have high rotational partition functions and are either apolar or weakly polar, meaning that their rotational lines are not intense enough to be detected by radioastronomy, making them poor candidates for detection. On the other hand, the CN-group in the BN makes it polar and its permanent dipole moment allows for detecting BN's spectral signature in the ISM using radio telescopes and other astronomical techniques[132].

In organic chemistry, BN's ability to modify band gaps when combined with other materials makes it a crucial component in various fields, such as optoelectronics and photovoltaics[133]. Furthermore, substituted benzenes show electronic transitions between substituent and phenyl moiety, which is also observed in BN. The CN group in BN is known to be bifunctionally interacting with the CN lone pair and phenyl group, resulting in a shift in the molecule's electronic properties. In material

science, the interaction between the cyano group and the phenyl group has been studied extensively in the context of cyano-substituted benzene derivatives and has led to the development of various functional materials[134;135].

A large number of studies have been carried out on the BN molecule, with a plethora of studies encompassing various areas of its chemical and physical properties. Vibrational analysis and assignment studies have also been performed, which have allowed researchers to understand the molecular vibrations of BN better[136]. These studies have been complemented by spectroscopic investigations which probed the ground and excited electronic states of BN by means of photoabsorption and infrared spectroscopy[137]. Furthermore, photoelectron spectroscopy has provided crucial insights into the molecule's electronic structure and its properties[3]. One notable finding is the molecular orbital structure of substituted benzene molecules, where the degenerate e_{1g} orbital of benzene splits into orbitals of b_1 and a_2 symmetry[3]. Interestingly, this trend is also observed in BN, indicating that it shares similarities with its parent benzene molecule. However, there are notable differences, such as the first ionization potential of BN, which is higher than that of benzene[138]. This increase is attributed to the electron density difference in the benzene ring caused by the electron withdrawing cyano group. Specifically, the electron density on the benzene ring is reduced by the cyano group, leading to a higher ionization potential. The results of these analyses have allowed researchers to assign all the peaks to their corresponding vibrations. In this work, we hope to shed light on the missing spectral features of BN and finally provide some new insights on its electronic and vibrational properties.

5.2 Theoretical details

5.2.1 Electronic structure

The geometry optimization of BN is carried out utilizing density functional theory (DFT) using the Becke 3-parameter, Lee, Yang, and Parr (B3LYP) functional, employing the augmented correlation-consistent polarized valence double-zeta (aug-cc-pVDZ) basis set of Dunning[139]. Then obtained the ground state equilibrium geometry and vibrational frequencies with the aid of GAUSSIAN-09 suite of programs[102]. The optimized ground state converges to the C_{2v} symmetry point group see Fig. 5.1. Schematic picture presented in Fig. 5.2, illustrates the molecular orbital correlation between benzene and BN. It demonstrates how the D_{6h} symmetry breaks to C_{2v} upon cyano substitution. The degenerate orbital e_{1g} breaks into two orbitals, b_1 and a_2 symmetry in C_{2v} point group, of which some are stabilized and others are destabilized. This observation explains the shifting of ionized bands with cyano substitution to the parent benzene molecule.

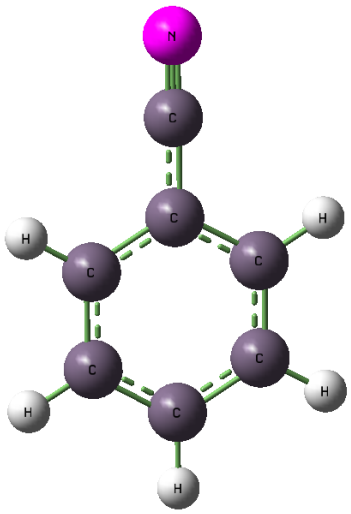

Figure 5.1: Schematic representation of BN'S optimized equilibrium structure in its electronic ground state

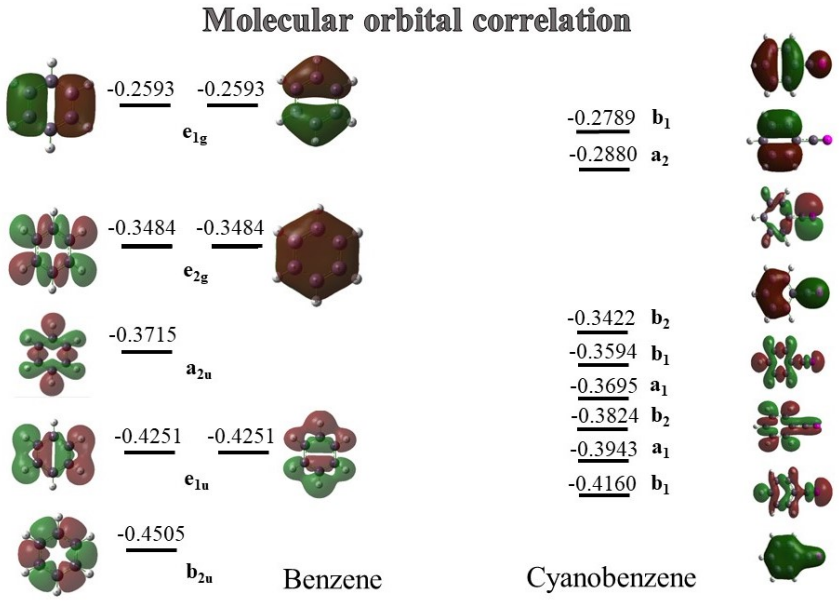

Figure 5.2: Schematic representation of molecular orbital correlation of benzene and BN.

To continue further, the eigenvectors of the force constant matrix are used to calculate the mass-weighted normal coordinates of the vibrational modes. The latter are then converted into dimensionless form by scaling with $\sqrt{\omega_i}$ (in atomic units)[105]. These dimensionless normal displacement coordinate (DNDC) for each vibrational mode, denoted as **Q** in the rest of this paper. The adiabatic potential energies are calculated along the coordinate range, -5.00 (0.25) +5.00, along each vibrational mode. It is important to note here that the reference equilibrium configuration of the molecule lies at $\mathbf{Q} = 0$. The vertical ionization energies (VIEs) at the reference equilibrium geometry are also calculated with the outer valence Green's function (OVGF)[140] method. Ionization potential variant of equation-of-motion coupled cluster singles and doubles (EOMIP-CCSD) methods[13;14] using CFOUR program package[100] are given in the Table 5.1 and compared with the available experimental results. At a first glance, Table 5.1 might appear confusing. However, in this study, the electronic states are energetically ordered as $\widetilde{X}^2B_1 < \widetilde{A}^2A_2 < \widetilde{B}^2B_2 < \widetilde{C}^2B_1 < \widetilde{D}^2A_1 < \widetilde{E}^2B_2 < \widetilde{F}^2A_1 < \widetilde{G}^2B_1$, which differs from the sequence reported previously in the literature[3] as $\widetilde{X}^2B_1 < \widetilde{A}^2A_2 < \widetilde{B}^2B_2 < \widetilde{E}^2B_2 < \widetilde{C}^2B_1 < \widetilde{D}^2A_1 < \widetilde{G}^2B_1 < \widetilde{F}^2A_1$. Such rearrangements of electronic terms can occur when the energy difference between electronic states are minimal. A detailed discussion on this exchange of electronic terms is provided in Section 5. Moreover, VIEs calculated using OVGF and EOMIP-CCSD methods are largely consistent with each other, however, they differ from the experimental findings. While the experimental studies reveal seven photoelectron bands within a certain energy range, our theoretical analyses predict eight bands. The additional band, not observed in the experimental photoelectron spectrum, is elucidated by the current multi-state multi mode vibronic coupling (MMVC) model, with further details discussed in the results and discussion section. Additionally, this study addresses and resolves discrepancies in state symmetries noted between current calculations and earlier predictions at the end of the paper. Later, at each one of the DNDCs ($\mathbf{Q} \lessgtr 0$), the adiabatic energies of eight low-lying electronic states of $BN^{\cdot+}$ are calculated employing the EOMIP-CCSD approach and are illustrated in Figs. 5.3, 5.4, 5.6, 5.7, 5.9 and 5.10.

5.2.2 The Hamiltonian

This study focuses on examining photoionization of BN to the lowest eight doublet electronic states, of $BN^{\cdot+}$ which are energetically close to each other. For this purpose, we developed a MMVC Hamiltonian within a diabatic electronic framework, utilizing DNDC's to represent vibrational modes of the equilibrium reference geometry of BN. The thirty-three vibrational modes of BN undergo transformation in accordance with the irreducible representations (IREPs) of the C_{2v} symmetry point group,

Table 5.1: Energetically lowest eight electronic states of $BN^{\cdot+}$. VIEs (in eV) using OVGF and EOMIP-CCSD methods computed at BN's reference equilibrium geometry and compared with the experimental data[3].

symm.[a]	OVGF[a]	EOMIP-CCSD[a]	Expt.[3]	reported symm.[3]
B_1	9.64	9.71	9.70	B_1
A_2	9.89	9.95	10.13	A_2
B_2	12.01	12.18	11.80	B_2
B_1	12.28	12.50	12.10	B_2
A_1	12.88	12.61	12.62	B_1
B_2	13.00	13.05	13.00	A_1
A_1	13.39	13.32	13.42	B_1
B_1	13.64	13.86	16.50	A_1

[a] This work

as follows,

$$\Gamma_{\text{vib}} = 12a_1 + 7b_1 + 11b_2 + 3a_2. \tag{5.1}$$

Standard group theory selection rules are applied to evaluate the coupling schemes as given below,[11]

$$\Gamma_n \times \Gamma_{Q_s} \times \Gamma_n \supset \Gamma_A, \tag{5.2}$$

$$\Gamma_m \times \Gamma_{Q_c} \times \Gamma_n \supset \Gamma_A. \tag{5.3}$$

Here, Γ_m, Γ_n and Γ_{Q_c} denote the IREPs of the electronic states m, n and the c^{th} vibrational mode, respectively. Wherein, Γ_A represents the totally symmetric irreducible representation (A_1 for C_{2v} point group). Based on the symmetry selection rules outlined above (Eqs. 5.2,5.3), it can be concluded that only the vibrational modes belonging to a_1 symmetry contribute to non-zero intrastate coupling constants, while the modes belonging to b_1, b_2, and a_2 IREPs contribute to non-zero interstate coupling constants.

Taking the mentioned coupling schemes into consideration, the vibronic Hamiltonian is constructed within a diabatic electronic framework, following the standard vibronic coupling theory[11;10;141]. Symbolically, the coupled-states Hamiltonian can be expressed as:

$$\mathcal{H} = \mathcal{H}_0 1_8 + \Delta\mathcal{H}, \tag{5.4}$$

where

$$\mathcal{H}_0 = \mathcal{T}_N + \mathcal{V}_0, \tag{5.5}$$

$\mathcal{H}_0$ refers to the unperturbed Hamiltonian associated with the electronic and vibrational ground state of the reference molecule BN. The quantity $\Delta\mathcal{H}$, indicates the change in electronic energy upon ionization, and 1_8 denotes a (8×8) diagonal matrix (owing to eight electronic states considered in the

present case). The elements of the unperturbed Hamiltonian in terms of the DNDCs of the vibrational modes, within the harmonic approximation, are given as:

$$\mathcal{T}_N = -\frac{1}{2}\sum_i \omega_i \left(\frac{\partial^2}{\partial Q_i^2}\right), \qquad i \in a_1, a_2, b_1, b_2, \tag{5.6}$$

$$\mathcal{V}_0 = \frac{1}{2}\sum_i \omega_i Q_i^2, \qquad i \in a_1, a_2, b_1, b_2, \tag{5.7}$$

where ω_i is the frequency of the vibrational mode, i. For the energetically low-lying eight electronic states, $\Delta\mathcal{H}$ assumes the form

$$\Delta\mathcal{H} = \begin{pmatrix} H_{11} & H_{12} & H_{13} & H_{14} & H_{15} & H_{16} & H_{17} & H_{18} \\ & H_{22} & H_{23} & H_{24} & H_{25} & H_{26} & H_{27} & H_{28} \\ & & H_{33} & H_{34} & H_{35} & H_{36} & H_{37} & H_{38} \\ & & & H_{44} & H_{45} & H_{46} & H_{47} & H_{48} \\ & & & & H_{55} & H_{56} & H_{57} & H_{58} \\ & & h.c. & & & H_{66} & H_{67} & H_{68} \\ & & & & & & H_{77} & H_{78} \\ & & & & & & & H_{88} \end{pmatrix}. \tag{5.8}$$

The elements of this matrix are expanded in a Taylor series around the equilibrium geometry of BN ($\mathbf{Q} = 0$) as[11]

$$\begin{aligned} H_{nn} = E_0^n + \sum_{i\,\in\,a_1} \kappa_i^n Q_i + \frac{1}{2!}\sum_{i\,\in\,a_1,\,a_2,\,b_1,\,b_2} \gamma_i^n Q_i + \frac{1}{2!}\sum_{i,j\,\in\,a_1} \gamma_{ij}^n Q_i Q_j + \frac{1}{3!}\sum_{i\,\in\,a_1} \rho_i^n Q_i^3 + \frac{1}{4!}\sum_{i\,\in\,a_2,\,b_1,\,b_2} \xi_i^n Q_i^4 \\ + \frac{1}{6!}\sum_{i\,\in\,a_2,\,b_1,\,b_2} \delta_i^n Q_i^6\,; \qquad n \in \widetilde{X} - \widetilde{G}, \end{aligned} \tag{5.9}$$

$$H_{nm} = \sum_{i\,\in\,a_2,\,b_1,\,b2} \lambda_i^{nm} Q_i \tag{5.10}$$

In the equations above, n and m are the indices for electronic states, while i and j are used for the vibrational modes. The VIEs, associated with the n^{th} electronic state, is represented by E_0^n. The

quantity κ_i^n defines the linear intra-state coupling parameter. The latter is instrumental in quantifying the shift in the equilibrium position ($\mathbf{Q} \leqslant 0$) of an excited state relative to $\mathbf{Q} = 0$. Furthermore, κ_i^n also represents the first derivative (slope of the curve), ρ_i^n is the third derivative, ξ_i^n is the fourth derivative of energy with respect to $\mathbf{Q}$, while γ_{ij}^n denotes the second derivative of energy with respect to Q_i & Q_j (bi-linear in nature). The parameter λ_i^{nm} denotes the linear inter-state coupling strength existing between the states n and m, coupled via the i^{th} vibrational mode. It is estimated within the framework of linear vibronic coupling theory [11]. Moreover, determining the interstate coupling term $H_{(nm)}$ between electronic states of identical spatial symmetry can be quite complex. To address this challenge, we utilized the direct diabatization technique known as the "four-fold way," originally introduced by Truhlar and co-workers [142;143;144;145;146], to evaluate vibronic coupling among states of same symmetry. For these calculations, we applied the extended multiconfiguration quasi-degenerate perturbation theory (XMCQDPT) method [15;16;147]. The expression below provides an estimate of the coupling strengths between the closely spaced electronic states

$$H_{(nm)} = H_0^{nm} + \sum_{i \in a_1} \lambda_i^{'nm} Q_i + \frac{1}{2!} \sum_{i \in a_1} \gamma_i^{'nm} Q_i^2; \quad n-m \in \widetilde{X}-\widetilde{D}, \widetilde{X}-\widetilde{G}, \widetilde{B}-\widetilde{E}, \widetilde{C}-\widetilde{F}, \widetilde{D}-\widetilde{G} \quad (5.11)$$

In this case, the electronic couplings of the diabatic electronic states taken into consideration are represented by H_0^{nm}.

The parameters required for the Hamiltonian are derived via the Taylor series expansion, fitting the *ab initio* calculated potential energy data . The parameters resulting from the fitting procedure are documented in Tables 5.2, 5.3 and 5.4. Moreover, the diagonal bi-linear coupling parameters, represented as γ_{ij}^n in Equation 5.9, are calculated and presented in Table 5.5. To obtain these, a two-dimensional fitting of the adiabatic *ab initio* electronic energies employing the Levenberg-Marquardt algorithm [17;148] is carried out with MATLAB [149].

5.2.3 Nuclear Dynamics

For large electronic and nuclear degrees of freedom (DOF), the time-dependent matrix diagonalization approach becomes computationally intractable due to a significant rise in the dimensionality. In the latter instance, a novel theoretical framework for the numerically precise solution of the time-dependent Schrödinger equation (TDSE) is developed with the MCTDH approach. This approach is based on discrete variable representation and propagates WPs with a variational ansatz. The system's dimensionality is effectively reduced by its multi-set formulation. Despite being far more sophisticated than the conventional methodology, the MCTDH approach is only applicable to systems with a few tens of degrees of freedom. ML-MCTDH theory is subsequently developed by using a hierar-

chical, dynamic contraction of the basis functions that make up the original SPFs to successfully get around the MCTDH method's bottleneck. This provides a versatile depiction of the complete wave function and creates new opportunities to greatly expand the number of degrees of freedom that can be handled by a numerically precise simulation technique[36;39;71].

In ML-MCTDH, a layered approach is adopted wherein effective modes are selected recursively. Initially, the wave function is expressed in terms of time-dependent functions (first layer) following equations derived from the Dirac-Frenkel variational principle. Instead of using time-independent basis functions, these functions are expressed in terms of lower-dimensional time-dependent functions (second layer), also adhering to the variational principle. Subsequently, these functions can be further expressed in terms of even lower time-dependent functions (subsequent layers) or time-independent functions when reaching the final layer. This approach offers MCTDH a high degree of flexibility and results in a highly compact representation of the wavefunction as shown below[36;39;71]:

$$|\Psi(t)\rangle = \sum_{j_1} \cdots \sum_{j_p} A_{j_1,\ldots,j_p}(t) \prod_{k=1}^{p} |\varphi_{j_k}^{(k)}(t)\rangle \tag{5.12}$$

$$|\varphi_{j_k}^{(k)}(t)\rangle = \sum_{i_1} \cdots \sum_{i_{Q(k)}} B_{i_1,\ldots,i_{Q(k)}}^{k,j_k}(t) \prod_{q=1}^{Q(k)} |v_{i_q}^{(k,q)}(t)\rangle \tag{5.13}$$

$$|v_{i_q}^{(k,q)}(t)\rangle = \sum_{\alpha_1} \cdots \sum_{\alpha_{M(k,q)}} C_{\alpha_1,\ldots,\alpha_{M(k,q)}}^{k,q,i_q}(t) \prod_{\gamma=1}^{M(k,q)} |\xi_{\alpha_\gamma}^{(k,q,\gamma)}(t)\rangle \tag{5.14}$$

Eq. 11, sums over all possible combinations of SPFs $|\varphi_{j_k}^{(k)}(t)\rangle$ for k=1, 2,... p single particle SP group. In Eq. 12, further level in the hierarchy is created by each SPF $|\varphi_{j_k}^{(k)}(t)\rangle$ going through a time-dependent multiconfiguration expansion once again. The SP introduced in Eq. 11 is now referred as the level one (L1) SP. Then, there are multiple level two (L2) SPs in each L1-SP. $Q(k)$ is the number of L2-SP groups in the kth L1-SP group and $|v_{i_q}^{(k,q)}(t)\rangle$ indicates a L2-SPF in the qth L2-SP group. In order to generalise ML-MCTDH, a third layer is introduced as shown in Eq. 13. An arbitrary number of layers can be added by recursively carrying out this technique. $A_{j_1,\ldots,j_p}(t)$, $B_{i_1,\ldots,i_{Q(k)}}^{k,j_k}(t)$, $C_{\alpha_1,\ldots,\alpha_{M(k,q)}}^{k,q,i_q}(t)$ are expansion coefficients of L1, L2, L3 layers. The deepest level of the multilayer hierarchy is reached by stating the SPFs in terms of static configurations.

To carry out the nuclear dynamical computations, the time-independent method to determine the exact positions of the vibronic eigenvalues[109;110] as well as time-dependent method to calculate the broad band spectral envelope and the electronic population dynamics on the coupled electronic states are employed. Fermi's golden rule is utilized to estimate the spectral intensity of the eight $\widetilde{X}^2B_1$, $\widetilde{A}^2A_2$,

$\widetilde{B}^2B_2$, $\widetilde{C}^2B_1$, $\widetilde{D}^2A_1$, $\widetilde{E}^2B_2$, $\widetilde{F}^2A_1$and $\widetilde{G}^2B_1$ electronic states of $BN^{\cdot+}$.

$$I(E) = \sum_{v} |\langle \Psi_v^f | \hat{T} | \Psi_0^i \rangle|^2 \delta(E - E_v^f + E_0^i), \tag{5.15}$$

In the above equation, $|\Psi_0^i\rangle$ is the initial vibronic ground state's wave function with energy E_0^i while the final vibronic state wave function is represented by $|\Psi_v^f\rangle$, with energy E_v^f. The operator $\hat{T}$ characterizes the electron's interaction with external electromagnetic radiation, where E signifies the energy of the incident photon. The reference state, $|\Psi_0^i\rangle$, is assumed to be as follows:

$$|\Psi_0^i\rangle = |\Phi_0\rangle|\chi_0^0\rangle, \tag{5.16}$$

The diabatic electronic state in this case is denoted by $|\Phi\rangle$, and the ground vibrational component of the wave function corresponding to the reference molecule's ground state is denoted by $|\chi\rangle$. Equation (5.16) defines the vibrational component $|\chi\rangle$ as the direct product of harmonic oscillator functions that correspond to the reference state. Using the Lanczos algorithm and a matrix diagonalization technique, $I(E)$ is calculated in the time-independent framework. The squared first component of the Lanczos eigenvectors yields the relative intensity, whereas the eigenvalues accurately show the locations of the vibronic energy levels[11;111;66]. The Fourier transform (Eqs. 5.17 and 5.18) of the WP's time autocorrelation function evolving on the final electronic state in a time-dependent framework can be expressed as

$$I(E) \approx 2\mathrm{Re} \sum_{\mathrm{n}=1}^{8} \int_0^{\infty} \mathrm{e}^{\mathrm{iEt}/\hbar} \langle {}^{\mathrm{n}}_{0} |^{\dagger} \mathrm{e}^{-\mathrm{iEt}/\hbar} |{}^{\mathrm{n}}_{0}\rangle \mathrm{dt}, \tag{5.17}$$

$$\approx 2\mathrm{Re} \sum_{\mathrm{n}=1}^{8} \int_0^{\infty} \mathrm{e}^{\mathrm{iEt}/\hbar} \mathrm{C}^{\mathrm{n}}(\mathrm{t}) \mathrm{dt}, \tag{5.18}$$

The WP launched[70;65;35] on the m^{th} electronic state of $BN^{\cdot+}$ has a time frame autocorrelation function that is provided by $C^n = \langle \Psi^n(t=0) | \Psi^n(t) \rangle$. The vibrational as well as electronic ground state is indicated by, $|\chi_0\rangle$ whereas, the transition dipole matrix is referred as τ. The extended Condon approximation[66] considers the matrix components of τ as constant and relies on the fact that they are independent of the nuclear coordinates in a diabatic electronic basis. Finally, the composite spectrum is calculated by adding together all of the partial spectra that are calculated with WP propagation on every electronic state.

5.3 Results and Discussion

5.3.1 Potential energy surfaces

To understand the details of nuclear dynamics, it is required to understand the detailed topography of the underlying electronic potential energy surfaces (PESs). In the perspective of vibronic coupling theory, we examine the potential energy curves (PECs) obtained from electronic structure calculations (vide supra) as a function of DNDCs for each vibrational degrees of freedom. Naturally, the vibrational modes are predominantly separated according to symmetry, as totally symmetric (a_1) and asymmetric ones (b_1, b_2 and a_2). As already mentioned, the lowest eight electronic states represented as PECs of $BN^{\cdot+}$are presented in Figs. 5.3 and 5.4 for vibrational modes of a_1 symmetry and Figs. 5.6, 5.7, 5.9 and 5.10 for vibrational modes of a_2, b_1 and b_2 symmetry, respectively. We begin the analysis with the symmetric vibrational modes ν_{29}, ν_{24}, ν_{19}, ν_{17}, ν_{14}, ν_{13}, ν_{09}, ν_{07}, ν_{06}, ν_{05}, ν_{03}, and ν_{01} and the results are presented in Figs 5.3 and 5.4.

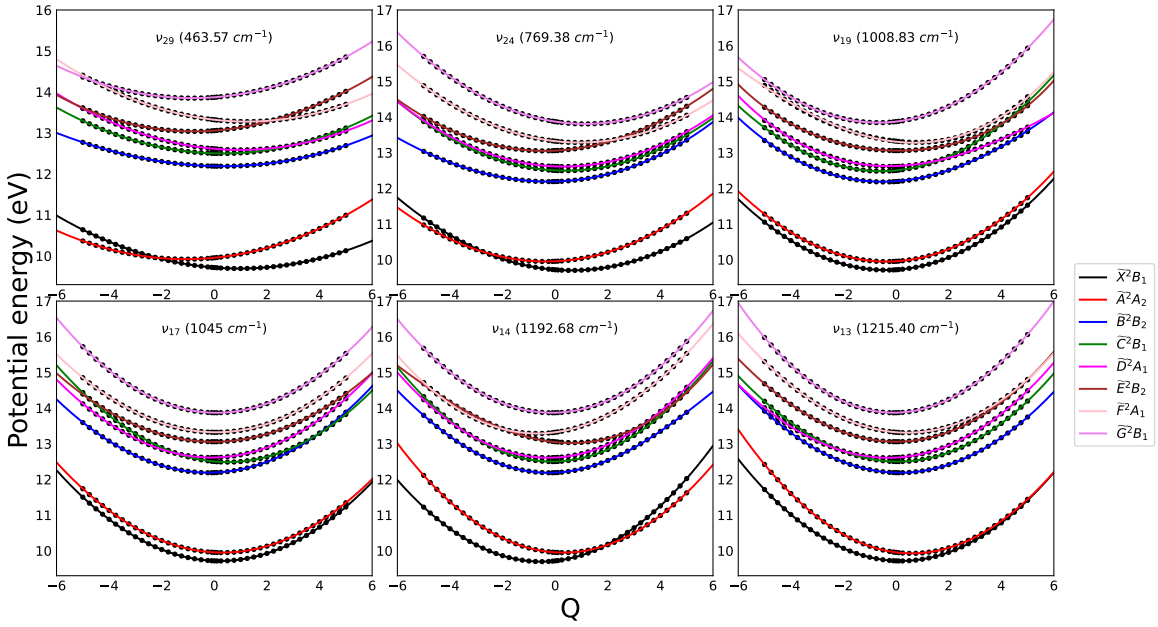

Figure 5.3: One-dimensional cuts of adiabatic electronic energies plotted along the dimensionless normal displacement coordinate of totally symmetric vibrational modes given in $\widetilde{X}^2B_1$, $\widetilde{A}^2A_2$, $\widetilde{B}^2B_2$, $\widetilde{C}^2B_1$, $\widetilde{D}^2A_1$, $\widetilde{E}^2B_2$, $\widetilde{F}^2A_1$and $\widetilde{G}^2B_1$ electronic states of $BN^{\cdot+}$. Solid lines and dots, respectively, represent the potential energies derived from the current theoretical model and computed *ab initio* EOMIP-CCSD.

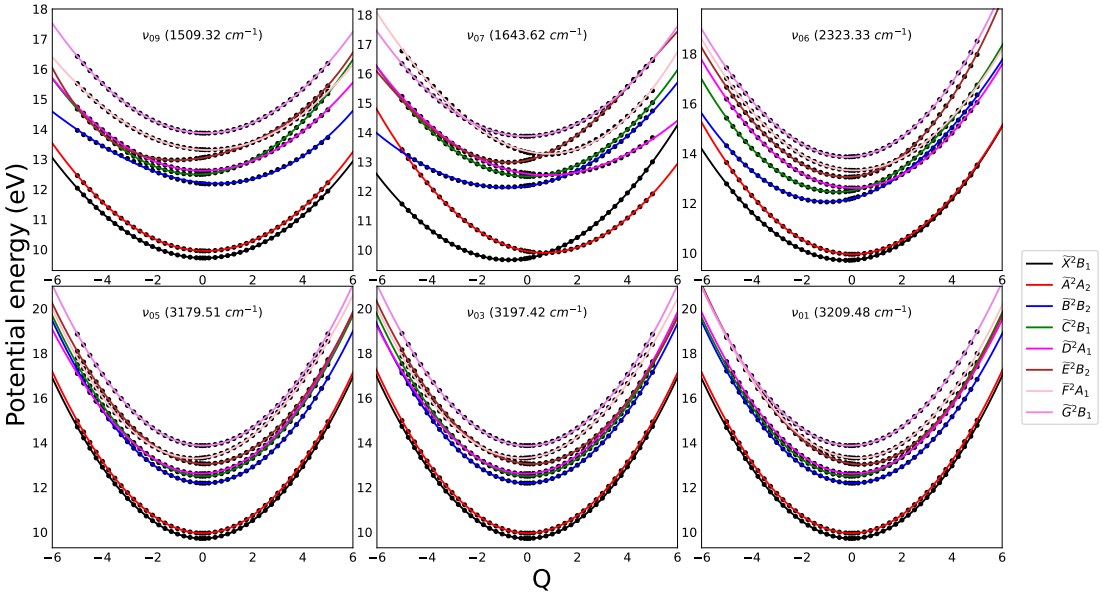

Figure 5.4: Same as the label of Fig. 5.3.

It is already established in the literature that the energy gap between the electronic states is altered by the vibrational modes of a_1 symmetry, also referred as Condon active modes, which adjust the electronic energy minimum away from the reference geometry of the electronic ground state of BN at (Q = 0). As regard to the PECs, the adiabatic electronic energies computed *ab initio* are represented by points, while those derived from the vibronic coupling model discussed in Section 5.2.2 are presented by solid lines. It can be seen that the *ab initio* electronic energies are in good agreement with those calculated from the theoretical model, as elucidated by Eq. 5.9. The fitting parameters extracted from the Taylor series, as displayed in Eq. 5.9, are presented in Tables 5.2, 5.3, and 5.4. It was observed that a third-order Taylor expansion of the Hamiltonian is adequate along the a_1 vibrational modes. Further, Figs. 5.3 and 5.4, shows that almost along all the symmetric vibrational modes, the $\widetilde{X}^2B_1$and $\widetilde{A}^2A_2$ states are energetically quite close over the whole range of nuclear coordinates. It is evident that these states cross along the vibrational modes ν_{07}, ν_{29}, ν_{24}, and ν_{14}. Upon examining the remaining potential curves for the states $\widetilde{B}^2B_2$, $\widetilde{C}^2B_1$, $\widetilde{D}^2A_1$, $\widetilde{E}^2B_2$, $\widetilde{F}^2A_1$, and $\widetilde{G}^2B_1$, several noteworthy intersections amongst them are noticed. Such curve crossings transform to the conical intersections (CIs) in the multidimensional space.

As illustrated in Figs. 5.3 and 5.4, electronic states with same spatial symmetries-namely A_1, B_1, and B_2 exhibit avoided crossings. Such states with identical spatial symmetry can also interact via totally symmetric vibrational modes. This type of uncommon pheneomena is often seen in low-symmetry point groups[150;151;152]. The coupling parameters between these spatially symmetric electronic states are derived from the corresponding adiabatic states using the diabatization approach developed by Truhlar and collaborators[142;143;144;145;146]. The adiabatic electronic states are computed employing

Table 5.2: Linear (κ_i), quadratic (γ_i) and cubic (ρ_i) coupling parameters along totally symmetric modes (a_1) calculated *ab initio* for the $\widetilde{X}^2B_1$-$\widetilde{G}^2B_1$ electronic states of $BN^{\cdot+}$ extracted from EOMIP-CCSD electronic energy data. All values in eV, with dimensionless excitation strength parameters ($\kappa_i^2/2\omega_i^2$) enclosed in parentheses.

Symm	ML-tree labels	Mode	Freq	κ_i ($\kappa_i^2/2\omega_i^2$)	γ_i	η_i	κ_i ($\kappa_i^2/2\omega_i^2$)	γ_i	ρ_i
				$\widetilde{X}^2B_1$			$\widetilde{A}^2A_2$		
a_1	v_1	v_1	0.3979	0.0112 (0.00)	0.0030	-0.0002	0.0076 (0.00)	0.0036	-0.0003
	v_2	v_3	0.3964	-0.0012 (0.00)	0.0044	0.0001	-0.0064 (0.00)	0.0041	0.0000
	v_3	v_5	0.3942	0.0235 (0.00)	0.0058	0.0000	-0.0029 (0.00)	0.0058	-0.0000
	v_4	v_6^*	0.2881	0.0607 (0.02)	-0.0149	0.0023	-0.0080 (0.00)	0.0023	-0.0003
	v_5	v_7^*	0.2038	0.1496 (0.26)	0.0012	-0.0015	-0.1481 (0.26)	0.0126	-0.0006
	v_6	v_9^*	0.1871	-0.0096 (0.00)	-0.0052	-0.0000	-0.0238 (0.00)	0.0037	-0.0000
	v_7	v_{13}^*	0.1507	-0.0277 (0.01)	-0.0027	-0.0005	-0.0935 (0.19)	0.0074	-0.0010
	v_8	v_{14}^*	0.1479	0.0801 (0.14)	0.0046	-0.0000	-0.0463 (0.05)	0.0053	-0.0005
	v_9	v_{17}^*	0.1296	-0.0271 (0.02)	0.0022	-0.0001	-0.0394 (0.05)	-0.0025	0.0000
	v_{10}	v_{19}^*	0.1250	0.0468 (0.07)	0.0008	0.0001	0.0454 (0.07)	-0.0007	0.0001
	v_{11}	v_{24}^*	0.0954	-0.0574 (0.18)	-0.0024	-0.0000	0.0330 (0.06)	-0.0008	-0.0000
	v_{12}	v_{29}^*	0.0575	-0.0504 (0.38)	-0.0041	-0.0001	0.0625 (0.06)	0.0004	0.0000
Symm	ML-tree labels	Mode	Freq	κ_i ($\kappa_i^2/2\omega_i^2$)	γ_i	η_i	κ_i ($\kappa_i^2/2\omega_i^2$)	γ_i	ρ_i
				$\widetilde{B}^2B_2$			$\widetilde{C}^2B_1$		
a_1	v_1	v_1	0.3979	-0.0183 (0.00)	-0.0113	-0.0046	0.0196 (0.00)	0.0022	-0.0003
	v_2	v_3	0.3964	0.0075 (0.00)	-0.0008	-0.0009	-0.0077 (0.00)	0.0034	0.0001
	v_3	v_5	0.3942	-0.0280 (0.00)	-0.0035	-0.0020	0.0006 (0.00)	0.0050	0.0000
	v_4	v_6^*	0.2881	0.2504 (0.37)	-0.0381	-0.0120	0.1741 (0.18)	-0.0018	-0.0102
	v_5	v_7^*	0.2038	0.1212 (0.17)	-0.0559	0.0038	-0.0083 (0.00)	0.0005	-0.0001
	v_6	v_9^*	0.1871	-0.0784 (0.08)	-0.0547	0.0134	0.0484 (0.03)	0.0071	0.0006
	v_7	v_{13}^*	0.1507	-0.0188 (0.00)	-0.0194	0.0005	-0.0103 (0.00)	-0.0154	0.0027
	v_8	v_{14}^*	0.1479	0.0343 (0.02)	-0.0050	-0.0061	0.0169 (0.00)	0.0038	-0.0004
	v_9	v_{17}^*	0.1296	0.0253 (0.01)	-0.0053	0.0008	-0.0656 (0.15)	0.0005	0.0010
	v_{10}	v_{19}^*	0.1250	0.0544 (0.09)	-0.0220	-0.0069	0.0715 (0.16)	-0.0005	0.0000
	v_{11}	v_{24}^*	0.0954	0.0200 (0.02)	-0.0150	0.0028	-0.0365 (0.07)	-0.0008	-0.0003
	v_{12}	v_{29}^*	0.0575	-0.0136 (0.02)	-0.0142	0.0013	-0.0174 (0.04)	0.0009	-0.0000
Symm	ML-tree labels	Mode	Freq	κ_i ($\kappa_i^2/2\omega_i^2$)	γ_i	η_i	κ_i ($\kappa_i^2/2\omega_i^2$)	γ_i	ρ_i
				$\widetilde{D}^2A_1$			$\widetilde{E}^2B_2$		
a_1	v_1	v_1	0.3979	-0.0140 (0.00)	-0.0058	-0.0022	-0.1484 (0.06)	0.0099	0.0053
	v_2	v_3	0.3964	0.0221 (0.00)	-0.0124	0.0050	-0.0708 (0.01)	-0.0137	0.0020
	v_3	v_5	0.3942	0.0234 (0.00)	-0.0146	0.0069	-0.0480 (0.00)	-0.0067	0.0025
	v_4	v_6^*	0.2881	-0.0090 (0.00)	-0.0076	-0.0010	0.0763 (0.03)	0.0538	0.0142
	v_5	v_7^*	0.2038	-0.1190 (0.17)	-0.0522	-0.0056	0.1953 (0.45)	0.0473	-0.0134
	v_6	v_9^*	0.1871	-0.0006 (0.00)	-0.0201	-0.0019	0.1436 (0.29)	-0.0635	-0.0168
	v_7	v_{13}^*	0.1507	0.0394 (0.03)	-0.0199	0.0019	-0.0004 (0.00)	-0.0161	0.0028
	v_8	v_{14}^*	0.1479	0.0378 (0.03)	-0.0042	-0.0006	-0.0778 (0.13)	-0.0277	0.0134
	v_9	v_{17}^*	0.1296	0.0127 (0.00)	-0.0033	0.0003	0.0031 (0.00)	-0.0224	-0.0003
	v_{10}	v_{19}^*	0.1250	0.0253 (0.02)	-0.0290	-0.0109	-0.0090 (0.00)	-0.0412	0.0030
	v_{11}	v_{24}^*	0.0954	-0.0286 (0.04)	-0.0050	-0.0005	0.0355 (0.06)	-0.0074	-0.0016
	v_{12}	v_{29}^*	0.0575	-0.0549 (0.45)	-0.0008	-0.0000	0.0479 (0.34)	0.0030	-0.0018
Symm	ML-tree labels	Mode	Freq	κ_i ($\kappa_i^2/2\omega_i^2$)	γ_i	η_i	κ_i ($\kappa_i^2/2\omega_i^2$)	γ_i	ρ_i
				$\widetilde{F}^2A_1$			$\widetilde{G}^2B_1$		
a_1	v_1	v_1	0.3979	-0.0798 (0.02)	0.0041	0.0020	0.0196 (0.00)	0.0027	-0.0002
	v_2	v_3	0.3964	0.0895 (0.02)	-0.0117	-0.0091	-0.0039 (0.00)	0.0036	0.0001
	v_3	v_5	0.3942	0.1250 (0.05)	-0.0069	-0.0125	0.0007 (0.00)	0.0052	0.0000
	v_4	v_6^*	0.2881	-0.0275 (0.00)	-0.0062	-0.0013	0.0617 (0.02)	0.0039	0.0111
	v_5	v_7^*	0.2038	-0.1926 (0.44)	0.0458	0.0137	0.0131 (0.00)	-0.0007	0.0002
	v_6	v_9^*	0.1871	-0.0381 (0.02)	-0.0224	0.0028	-0.0226 (0.00)	0.0078	-0.0001
	v_7	v_{13}^*	0.1507	-0.0588 (0.07)	-0.0122	0.0021	0.0163 (0.00)	0.0213	-0.0019
	v_8	v_{14}^*	0.1479	0.0996 (0.22)	-0.0038	-0.0043	0.0192 (0.00)	0.0043	0.0000
	v_9	v_{17}^*	0.1296	-0.0073 (0.00)	-0.0075	0.0015	-0.0112 (0.00)	0.0109	-0.0018
	v_{10}	v_{19}^*	0.1250	-0.0803 (0.20)	-0.0134	0.0120	0.0859 (0.23)	0.0044	0.0005
	v_{11}	v_{24}^*	0.0954	-0.0837 (0.38)	-0.0042	0.0001	-0.1135 (0.70)	0.0048	-0.0004
	v_{12}	v_{29}^*	0.0575	-0.0722 (0.79)	0.0010	0.0003	0.0489 (0.36)	0.0015	0.0000

Table 5.3: Quadratic (γ_i), quartic (ξ_i) and sixth-order (δ_i) coupling parameters along the asymmetric modes a_2 and b_1 calculated *ab initio* for the $\widetilde{X}^2B_1$-$\widetilde{G}^2B_1$ electronic states of $BN^{\cdot+}$ extracted from EOMIP-CCSD electronic energy data. All values are in eV.

Symm	ML-tree mode labels	Mode	Freq	γ_i	ξ_i	δ_i	γ_i	ξ_i	δ_i
				$\widetilde{X}^2B_1$			$\widetilde{A}^2A_2$		
a_2	v_{15}	v_{20}^*	0.1220	0.0062	-0.0001	-	0.0049	0.0000	-
	v_{14}	v_{22}	0.1052	-0.0140	0.0002	-	0.0045	-0.0002	-
	v_{13}	v_{30}^*	0.0562	-0.0121	0.0001	-	-0.0331	0.0014	-
b_1	v_{22}	v_{18}^*	0.1252	0.0023	-0.0001	-	-0.0027	0.0000	-
	v_{21}	v_{21}	0.1160	0.0104	-0.0007	-	-0.0117	0.0005	-
	v_{20}	v_{23}	0.0959	0.0095	-0.0002	-	-0.0288	0.0021	-
	v_{19}	v_{25}^*	0.0874	-0.0266	0.0019	-	-0.0195	0.0013	-
	v_{18}	v_{27}^*	0.0721	-0.0153	0.0007	-	-0.0123	0.0004	-
	v_{17}	v_{31}^*	0.0481	-0.0255	0.0009	-	-0.0118	0.0002	-
	v_{16}	v_{33}^*	0.0181	-0.0067	0.0000	-	-0.0123	0.0002	-
Symm	ML-tree mode labels	Mode	Freq	γ_i	ξ_i	δ_i	γ_i	ξ_i	δ_i
				$\widetilde{B}^2B_2$			$\widetilde{C}^2B_1$		
a_2	v_{15}	v_{20}^*	0.1220	-0.0660	0.0031	-	-0.0170	0.0123	-0.0000
	v_{14}	v_{22}	0.1052	-0.0141	-0.0005	-	-0.0083	-0.0007	-
	v_{13}	v_{30}^*	0.0562	-0.0096	0.0000	-	-0.0142	0.0018	-
b_1	v_{22}	v_{18}^*	0.1252	0.0023	-0.0015	-	-0.0566	0.0060	-
	v_{21}	v_{21}	0.1160	0.0006	-0.0012	-	-0.0670	0.0075	-
	v_{20}	v_{23}	0.0959	0.0046	-0.0008	-	-0.0336	0.0047	-
	v_{19}	v_{25}^*	0.0874	-0.0055	-0.0001	-	-0.0202	0.0032	-
	v_{18}	v_{27}^*	0.0721	-0.0026	-0.0002	-	-0.0255	0.0031	-
	v_{17}	v_{31}^*	0.0481	-0.0224	0.0006	-	-0.0375	0.0061	-
	v_{16}	v_{33}^*	0.0181	-0.0280	0.0001	-	-0.0315	0.0012	-
Symm	ML-tree mode labels	Mode	Freq	γ_i	ξ_i	δ_i	γ_i	ξ_i	δ_i
				$\widetilde{D}^2A_1$			$\widetilde{E}^2B_2$		
a_2	v_{15}	v_{20}^*	0.1220	-0.0038	-0.0013	-	-0.0215	0.0127	-0.0000
	v_{14}	v_{22}	0.1052	0.0044	-0.0003	-	-0.0362	0.0020	-
	v_{13}	v_{30}^*	0.0562	-0.0056	-0.0001	-	0.0105	-0.0022	-
b_1	v_{22}	v_{18}^*	0.1252	0.0311	-0.0164	0.0000	-0.0190	0.0013	-
	v_{21}	v_{21}	0.1160	0.0403	-0.0224	0.0000	-0.0163	-0.0004	-
	v_{20}	v_{23}	0.0959	0.0227	-0.0149	0.0000	-0.0021	-0.0003	-
	v_{19}	v_{25}^*	0.0874	0.0078	-0.0066	0.0000	-0.0045	-0.0009	-
	v_{18}	v_{27}^*	0.0721	0.0124	-0.0078	0.0000	-0.0127	0.0001	-
	v_{17}	v_{31}^*	0.0481	0.0326	-0.0166	0.0000	-0.0119	0.0003	-
	v_{16}	v_{33}^*	0.0181	-0.0315	0.0012	0.0000	-0.0127	0.0013	-
Symm	ML-tree mode labels	Mode	Freq	γ_i	ξ_i	δ_i	γ_i	ξ_i	δ_i
				$\widetilde{F}^2A_1$			$\widetilde{G}^2B_1$		
a_2	v_{15}	v_{20}^*	0.1220	-0.0150	0.0014	-	0.0505	-0.0108	-
	v_{14}	v_{22}	0.1052	0.0034	-0.0008	-	-0.0451	0.0076	-
	v_{13}	v_{30}^*	0.0562	-0.0111	0.0002	-	0.0011	-0.0001	-
b_1	v_{22}	v_{18}^*	0.1252	-0.0229	0.0041	-	0.0121	-0.0042	-
	v_{21}	v_{21}	0.1160	-0.0286	0.0070	-	0.0197	-0.0049	-
	v_{20}	v_{23}	0.0959	-0.0244	0.0023	-	-0.0114	0.0005	-
	v_{19}	v_{25}^*	0.0874	0.0077	-0.0022	-	-0.0107	0.0005	-
	v_{18}	v_{27}^*	0.0721	0.0089	-0.0002	-	-0.0134	0.0002	-
	v_{17}	v_{31}^*	0.0481	-0.0066	-0.0001	-	-0.0030	0.0018	-0.0000
	v_{16}	v_{33}^*	0.0181	-0.0123	0.0002	-	-0.0186	0.0027	-

Table 5.4: Quadratic (γ_i), quartic (ξ_i) and sixth-order (δ_i) coupling parameters along the asymmetric modes of b_2 symmetry calculated *ab initio* for the $\widetilde{X}^2B_1$-$\widetilde{G}^2B_1$ electronic states of $BN^{\cdot+}$ extracted from EOMIP-CCSD electronic energy data. All values in eV.

Symm	ML-tree mode labels	Mode	Freq	γ_i	ξ_i	δ_i	γ_i	ξ_i	δ_i
				$\widetilde{X}^2B_1$			$\widetilde{A}^2A_2$		
b_2	ν_{33}	ν_{02}	0.3975	0.0032	-0.0000	-	0.0042	-0.0000	-
	ν_{32}	ν_{04}	0.3955	0.0047	-0.0000	-	0.0057	-0.0000	-
	ν_{31}	ν^*_{08}	0.2001	-0.0954	0.0485	-0.0003	0.1058	-0.0485	0.0000
	ν_{30}	ν_{10}	0.1813	-0.0086	0.0009	-	0.0090	-0.0008	-
	ν_{29}	ν_{11}	0.1676	0.0314	-0.0021	-	0.0308	-0.0017	-
	ν_{28}	ν_{12}	0.1639	0.0099	-0.0003	-	0.0240	-0.0009	-
	ν_{27}	ν_{15}	0.1459	-0.0024	0.0021	0.0000	0.0217	-0.0014	-
	ν_{26}	ν_{16}	0.1363	-0.0022	0.0001	-	0.0031	-0.0002	-
	ν_{25}	ν^*_{26}	0.0785	-0.0332	0.0049	-	0.0261	-0.0049	-
	ν_{24}	ν^*_{28}	0.0692	-0.0060	0.0002	-	-0.0023	0.0001	-
	ν_{23}	ν^*_{32}	0.0207	-0.0109	-0.0001	-	-0.0022	0.0000	-
Symm	ML-tree mode labels	Mode	Freq	γ_i	ξ_i	δ_i	γ_i	ξ_i	δ_i
				$\widetilde{B}^2B_2$			$\widetilde{C}^2B_1$		
b_2	ν_{33}	ν_{02}	0.3975	-0.0027	-0.0015	-	0.0026	-0.0000	-
	ν_{32}	ν_{04}	0.3955	-0.0122	-0.0019	-	0.0042	-0.0000	-
	ν_{31}	ν^*_{08}	0.2001	-0.1070	0.0079	-	0.0060	-0.0001	-
	ν_{30}	ν_{10}	0.1813	-0.0363	-0.0029	-	0.0082	0.0004	-
	ν_{29}	ν_{11}	0.1676	-0.0184	-0.0054	-	0.0122	-0.0011	-
	ν_{28}	ν_{12}	0.1639	-0.0134	-0.0039	-	0.0081	-0.0003	-
	ν_{27}	ν_{15}	0.1459	-0.0044	-0.0004	-	0.0073	-0.0001	-
	ν_{26}	ν_{16}	0.1363	-0.0058	-0.0012	-	0.0079	-0.0000	-
	ν_{25}	ν^*_{26}	0.0785	-0.0304	0.0024	-	-0.0026	0.0000	-
	ν_{24}	ν^*_{28}	0.0692	-0.0361	0.0033	-	-0.0132	-0.0001	-
	ν_{23}	ν^*_{32}	0.0207	-0.0508	0.0009	-	-0.0368	0.0013	-
Symm	ML-tree mode labels	Mode	Freq	γ_i	ξ_i	δ_i	γ_i	ξ_i	δ_i
				$\widetilde{D}^2A_1$			$\widetilde{E}^2B_2$		
b_2	ν_{33}	ν_{02}	0.3975	0.0000	-0.0021	-	-0.0434	0.0077	-
	ν_{32}	ν_{04}	0.3955	-0.0120	0.0022	-	-0.0503	0.0322	-0.0000
	ν_{31}	ν^*_{08}	0.2001	-0.0425	0.0220	-0.0000	-0.1851	0.3688	-0.0012
	ν_{30}	ν_{10}	0.1813	-0.0200	-0.0076	-	-0.0565	0.0273	-0.0000
	ν_{29}	ν_{11}	0.1676	-0.0198	-0.0072	-	-0.0514	0.0109	-
	ν_{28}	ν_{12}	0.1639	-0.0057	-0.0069	-	-0.0570	0.0287	-0.0000
	ν_{27}	ν_{15}	0.1459	-0.0047	-0.0070	-	-0.0246	0.0057	-
	ν_{26}	ν_{16}	0.1363	-0.0004	-0.0003	-	-0.0254	0.0019	-
	ν_{25}	ν^*_{26}	0.0785	0.0103	-0.0039	-	-0.0229	0.0054	-
	ν_{24}	ν^*_{28}	0.0692	0.0164	-0.0135	0.0000	-0.0059	0.0066	-0.0000
	ν_{23}	ν^*_{32}	0.0207	0.0009	-0.0006	0.0000	-0.0209	0.0045	
Symm	ML-tree mode labels	Mode	Freq	γ_i	ξ_i	δ_i	γ_i	ξ_i	δ_i
				$\widetilde{F}^2A_1$			$\widetilde{G}^2B_1$		
b_2	ν_{33}	ν_{02}	0.3975	-0.0018	-0.0006	-	0.0027	-0.0000	-
	ν_{32}	ν_{04}	0.3955	0.0602	-0.0121	-	0.0044	-0.0000	-
	ν_{31}	ν^*_{08}	0.2001	0.1948	-0.1072	0.0000	0.0032	-0.0001	-
	ν_{30}	ν_{10}	0.1813	-0.0452	0.0086	-	0.0078	0.0001	-
	ν_{29}	ν_{11}	0.1676	-0.0458	0.0108	-	0.0145	-0.0013	-
	ν_{28}	ν_{12}	0.1639	0.0008	-0.0082	0.0000	0.0121	-0.0002	-
	ν_{27}	ν_{15}	0.1459	-0.0243	-0.0008	-	0.0064	-0.0001	-
	ν_{26}	ν_{16}	0.1363	-0.0128	0.0001	-	0.0049	0.0001	-
	ν_{25}	ν^*_{26}	0.0785	0.0268	-0.0053	-	-0.0006	0.0000	-
	ν_{24}	ν^*_{28}	0.0692	0.0074	0.0001	-	-0.0148	0.0007	-
	ν_{23}	ν^*_{32}	0.0207	0.0149	-0.0020	-	-0.0233	0.0026	-

Table 5.5: Diagonal bilinear γ_{ij}^{n} parameters (in eV) along the totally symmetric relevant vibrational modes ν_{29}, ν_{24}, ν_{19}, ν_{17}, ν_{14}, ν_{13}, ν_{09}, ν_{07} and ν_{06} of the lowest eight electronic states of $BN^{\cdot+}$.

γ_{ij}	$\widetilde{X}^2B_1$	$\widetilde{A}^2A_2$	$\widetilde{B}^2B_2$	$\widetilde{C}^2B_1$	$\widetilde{D}^2A_1$	$\widetilde{E}^2B_2$	$\widetilde{F}^2A_1$	$\widetilde{G}^2B_1$
γ_{0607}	0.0059	0.0021	0.0697	-0.0080	-0.0086	-0.0845	-0.0052	-0.0111
γ_{2919}	-0.0010	0.0037	0.0192	-0.0016	0.0000	-0.0042	-0.0023	0.0026
γ_{0907}	-0.0002	0.0009	0.0061	0.0074	-0.0031	0.0080	-0.0053	-0.0036
γ_{1309}	-0.0108	0.0024	-0.0014	-0.0040	-0.0013	0.0429	0.0190	0.0050
γ_{2419}	-0.0063	0.0024	-0.0043	-0.0049	-0.0261	-0.0268	-0.0217	-0.0023
γ_{1714}	-0.0037	0.0015	0.0100	0.0020	0.0034	-0.0043	0.0018	-0.0012
γ_{0717}	-0.0036	0.0053	-0.0016	-0.0027	0.0003	-0.0037	0.0153	0.0026
γ_{0714}	-0.0026	0.0053	0.0286	-0.0039	0.0080	0.0079	-0.0187	-0.0049
γ_{0713}	-0.0040	0.0060	0.0388	0.0066	0.0187	-0.0257	0.0084	0.0028
γ_{0629}	0.0054	-0.0025	0.0435	0.0061	0.0057	-0.0345	0.0011	-0.0096
γ_{0624}	-0.0092	0.0018	0.0236	0.0031	-0.0043	-0.0344	0.0037	0.0017
γ_{0619}	0.0017	-0.0011	-0.0094	0.0132	-0.0015	0.0152	0.0058	-0.0135
γ_{0617}	-0.0060	-0.0010	0.0030	-0.0072	0.0009	0.0007	0.0012	0.0154
γ_{0614}	-0.0019	0.0017	-0.0403	0.0025	-0.0062	0.0319	-0.0043	-0.0079
γ_{0613}	0.0109	-0.0050	0.0005	-0.0304	0.0113	0.0229	0.0088	0.0359
γ_{0609}	0.0096	-0.0023	0.0209	-0.0177	0.0073	-0.0099	0.0030	0.0166
γ_{2924}	-0.0011	-0.0035	-0.0153	-0.0000	0.0078	0.0055	0.0072	-0.0059
γ_{2914}	-0.0003	0.0013	0.0167	0.0003	-0.0000	-0.0250	-0.0048	-0.0000
γ_{2409}	-0.0023	0.0003	0.0019	-0.0032	0.0020	-0.0089	0.0125	0.0043
γ_{2407}	-0.0064	0.0012	-0.0287	-0.0039	-0.0258	0.0301	0.0340	-0.0035
γ_{2406}	-0.0092	0.0018	0.0236	0.0031	-0.0043	-0.0344	0.0037	0.0017
γ_{1917}	0.0036	-0.0074	-0.0169	0.0045	-0.0054	-0.0368	-0.0013	-0.0065
γ_{1907}	0.0071	-0.0081	0.0256	-0.0007	-0.0252	-0.0171	0.0437	0.0057
γ_{1409}	0.0024	-0.0006	0.0217	0.0025	0.0048	-0.0340	-0.0113	-0.0024
γ_{1909}	-0.0027	0.0050	-0.0119	0.0025	0.0062	-0.0229	0.0184	-0.0041
γ_{1713}	0.0016	0.0018	-0.0073	-0.0237	-0.0052	0.0059	-0.0014	0.0182
γ_{2909}	0.0006	-0.0013	-0.0008	0.0018	-0.0015	0.0077	-0.0052	-0.0016
γ_{2413}	0.0037	0.0001	0.0107	0.0068	0.0002	-0.0213	-0.0210	-0.0079
γ_{2414}	-0.0024	0.0032	0.0061	-0.0009	0.0048	-0.0158	-0.0059	0.0008
γ_{1914}	0.0048	-0.0042	-0.0000	-0.0014	0.0172	0.0205	-0.0036	0.0054
γ_{1913}	-0.0022	-0.0013	-0.0203	-0.0085	-0.0275	-0.0071	-0.0226	-0.0145
γ_{1709}	0.0094	0.0075	-0.0282	-0.0103	0.0048	-0.0354	0.0117	-0.0026
γ_{2907}	-0.0050	-0.0032	-0.0359	-0.0021	-0.0050	0.0388	-0.0043	-0.0021
γ_{2417}	0.0027	-0.0032	-0.0066	0.0072	0.0003	-0.0177	0.0019	-0.0079
γ_{1413}	0.0031	0.0034	-0.0073	0.0074	0.0133	0.0134	0.0093	-0.0036
γ_{2917}	0.0019	-0.0018	0.0045	0.0004	0.0013	-0.0037	0.0038	0.0001

the XMCQDPT method[15;16;147] with a aug-cc-pVDZ basis set, considering eight electronic states. The active space included 15 electrons distributed over 10 orbitals, denoted as (15,10). All computations were performed using the GAMESS software package[153]. The calculated diabatic PECs along the twelve totally symmetric modes are shown in Fig. 5.5 and the couplings among the same spatial symmetry states are given in Table 5.6.

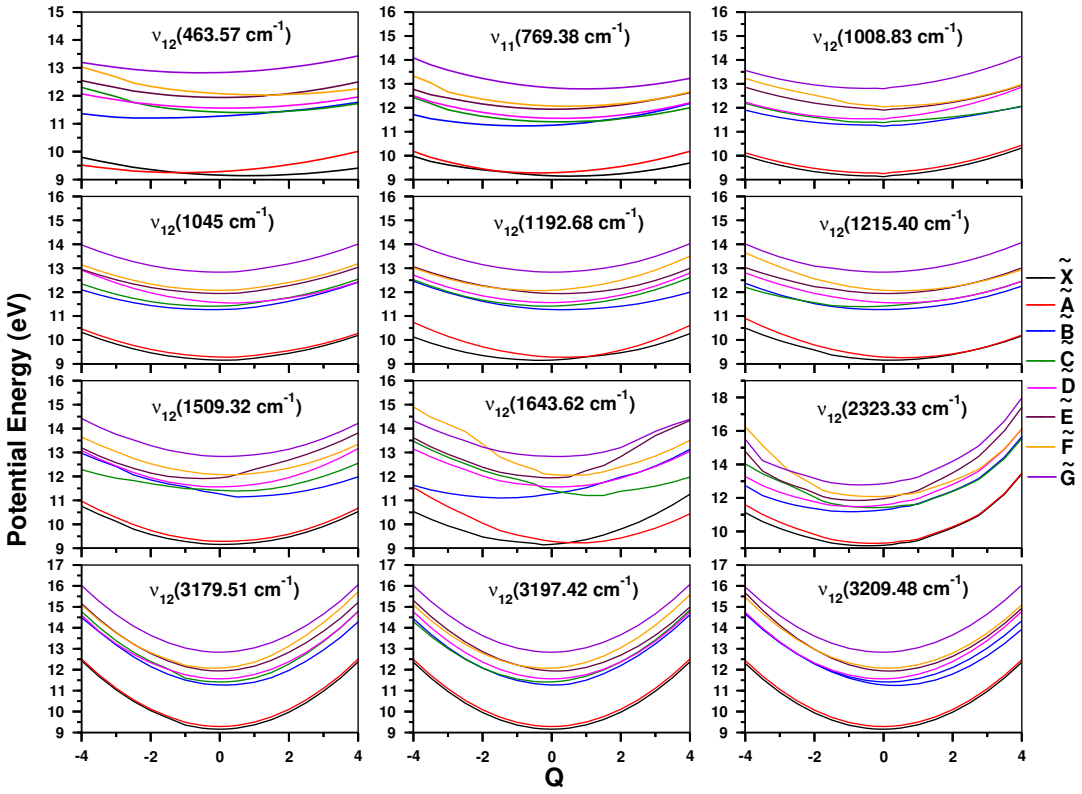

Figure 5.5: One-dimensional cuts of adiabatic electronic energies plotted along the dimensionless normal displacement coordinate of totally symmetric vibrational modes given in $\widetilde{X}$-$\widetilde{G}$ electronic states of $BN^{\cdot+}$

Table 5.6: Interstate coupling parameters (in eV) along a_1 symmetry modes among the same spatial symmetry states of $BN^{\cdot+}$.

a_1	Freq	λ_i'	γ_i'	λ_i'	γ_i'	λ_i'	γ_i'	λ_i'	γ_i'	λ_i'	γ_i'
		$\widetilde{X}-\widetilde{C}$		$\widetilde{X}-\widetilde{G}$		$\widetilde{B}-\widetilde{E}$		$\widetilde{C}-\widetilde{F}$		$\widetilde{D}-\widetilde{G}$	
ν_1	0.3979	-0.0024	0.0001	0.0091	-0.0022	0.0332	0.0036	0.0174	-0.0002	-0.0135	0.0000
ν_2	0.3964	-0.0141	-0.0007	0.0110	0.0019	0.0297	0.0017	-0.0206	0.0010	-0.0051	0.0011
ν_3	0.3942	-0.0081	0.0022	0.0055	-0.0030	-0.0126	-0.0020	-0.0462	-0.0007	-0.0049	0.0005
ν_4	0.2881	-0.1572	-0.0081	-0.1311	-0.0032	0.0693	0.0205	0.0035	0.0028	0.1207	0.0046
ν_5	0.2038	0.0207	-0.0003	0.0156	0.0252	0.0117	0.0227	0.0062	0.0135	0.0042	-0.0118
ν_6	0.1871	0.0831	0.0030	-0.0841	0.0107	-0.1035	-0.0095	-0.0120	0.0100	0.0011	-0.0015
ν_7	0.1507	0.0575	0.0018	0.0031	-0.0085	-0.0125	-0.0002	0.0492	-0.0075	0.0848	-0.0011
ν_8	0.1479	-0.0085	0.0015	0.0086	0.0023	0.0363	0.0185	-0.0235	-0.0014	-0.0071	-0.0015
ν_9	0.1296	-0.0626	0.0032	0.0541	-0.0003	0.0093	0.0047	0.0105	-0.0006	0.0631	-0.0009
ν_{10}	0.1250	-0.0108	-0.0017	0.0226	0.0029	0.0217	0.0027	0.0431	-0.0037	-0.0383	-0.0023
ν_{11}	0.0954	-0.0214	-0.0001	-0.0460	0.0025	0.0095	-0.0004	0.0260	0.0000	-0.0141	-0.0009
ν_{12}	0.0575	0.0224	-0.0005	0.0254	0.0023	-0.0236	0.0038	0.0070	0.0009	-0.0156	-0.0002

The static points on the PESs are crucial to elucidate the dynamical mechanism. For this purpose, the static points such as equilibrium minima of each state and the minimum of CIs between various states is presented in Table 5.7. To calculate these static points, we have employed a constrained minimization algorithm using Lagrange multipliers provided in the Mathematica program module[112]. The analysis shows that $\widetilde{X}^2B_1$ and $\widetilde{A}^2A_2$ states are close enough and the CI between these states is just ∼0.02 eV above the minimum of $\widetilde{A}^2A_2$ state. Then there exists a considerable energy gap ($\sim$ 2 eV) between $\widetilde{A}^2A_2$ and $\widetilde{B}^2B_2$ states with negligible possibility of intersection. This is also observed qualitatively in the PECs. However, the minimum of $\widetilde{B}^2B_2$- $\widetilde{C}^2B_1$ CIs lies very close to the $\widetilde{C}^2B_1$ state equilibrium minima ($\sim$ 0.16 eV) which may result in multiple crossings and nonadiabatic effects. Also, the minimum of $\widetilde{B}^2B_2$- $\widetilde{D}^2A_1$ CIs lies close to the $\widetilde{D}^2A_1$ state equilibrium minimum ($\sim$ 0.15 eV). Quite surprisingly, the $\widetilde{C}^2B_1$- $\widetilde{D}^2A_1$ CI and equilibrium minima of $\widetilde{D}^2A_1$ state are located at $\sim$ 12.52 eV. This might affect the dynamics significantly, which will be addressed later. In a similar line, the $\widetilde{D}^2A_1$- $\widetilde{E}^2B_2$ CI lies very close to equilibrium minima of $\widetilde{E}^2B_2$ state ($\sim$ 0.02 eV). Furthermore, $\widetilde{E}^2B_2$- $\widetilde{F}^2A_1$ and $\widetilde{F}^2A_1$- $\widetilde{G}^2B_1$ CIs lie close to respective minima of $\widetilde{F}^2A_1$ ($\sim$ 0.09 eV) and $\widetilde{G}^2B_1$ ($\sim$ 0.06 eV) states. This validates the observation of several crossings among these electronic states as can be seen in the PECs. Subsequently, through fitting procedure, the resultant Hamiltonian parameters as presented in Table 5.2 displays the Condon activity, or excitation strength ($k_i^2/2\omega_i^2$), for each of the twelve vibrational modes. For each of the eight electronic states, the intensity of the intra-state couplings is indicated by the magnitude of the excitation strength. The vibrational modes with significant excitation strengths, shown in Table 5.2 by asterisks are taken into account in the reduced dimensional MCTDH computations.

Table 5.7: The diagonal entries represent the equilibrium minimum of the given state and off-diagonal entries represent the minimum of various seam of CIs of the electronic states of the $BN^{\cdot+}$ estimated with a second-order vibronic soupling model. All quantities are given in eV.

	$\widetilde{X}^2B_1$	$\widetilde{A}^2A_2$	$\widetilde{B}^2B_2$	$\widetilde{C}^2B_1$	$\widetilde{D}^2A_1$	$\widetilde{E}^2B_2$	$\widetilde{F}^2A_1$	$\widetilde{G}^2B_1$
$\widetilde{X}^2B_1$	9.57	9.83	14.92	26.89	14.91	15.07	20.65	51.36
$\widetilde{A}^2A_2$	-	9.81	12.59	16.81	21.21	14.57	17.47	27.96
$\widetilde{B}^2B_2$	-	-	11.96	12.55	12.54	12.98	13.32	17.19
$\widetilde{C}^2B_1$	-	-	-	12.39	12.52	12.84	13.16	18.73
$\widetilde{D}^2A_1$	-	-	-	-	12.52	12.85	13.59	15.98
$\widetilde{E}^2B_2$	-	-	-	-	-	12.83	13.17	14.05
$\widetilde{F}^2A_1$	-	-	-	-	-	-	13.08	13.80
$\widetilde{G}^2B_1$	-	-	-	-	-	-	-	13.74

Subsequently, we focus on the asymmetric modes and their influence on the electronic states. It is known that the coupling modes that couple two distinct electronic states, as indicated by Eq. 5.2, are the asymmetric vibrational modes of b_1, b_2, and a_2 symmetry. The PECs corresponding to a_2 symmetry (ν_{20}, ν_{22}, ν_{30}) are presented in Fig.5.6, those of b_1 symmetry (ν_{18}, ν_{21}, ν_{23}, ν_{25}, ν_{27}, ν_{31}, ν_{33}) in Fig. 5.7, and those of b_2 symmetry (ν_{02}, ν_{04}, ν_{08}, ν_{10}, ν_{11}, ν_{12}, ν_{15}, ν_{16}, ν_{26}, ν_{28}, ν_{32}) in Figs. 5.9 and 5.10. In comparison to the reference equilibrium C_{2v} geometry at $\mathbf{Q} = 0$, the adiabatic PECs display a symmetric double well form along the b_1 vibrational mode, ν_{31} and b_2 vibrational mode, ν_{32} and ν_{08} with two symmetric minimum at distorted geometry as shown in Fig. 5.8 and 5.11, respectively. The nonadiabatic coupling (interstate coupling) between the energetically close lying electronic states arises due to b_1 and b_2 symmetry vibrational modes, which cause this symmetry breaking[11], sometimes referred to as pseudo-Jahn-Teller (PJT) effect[154]. Thus, it seems that the $BN^{\cdot+}$ molecule is stabilized in the fourth and sixth electronic states at different distorted geometries via vibronic interaction by means of b_1 and b_2 vibrational modes. Here, due to the increased anharmonicity in the framework of the potential cuts, up to a sixth-order Taylor expansion was necessary for a few of the asymmetric vibrational modes. As regard to Fig. 5.7, electronic states $\widetilde{X}^2B_1$and $\widetilde{A}^2A_2$ cross under vibrational modes (ν_{23} and ν_{21}), whereas the other six adiabatic potential energy curves along all the b_1 symmetry modes are at extremely close in energy and some of the states cross over. The electronic states of $\widetilde{X}^2B_1$and $\widetilde{A}^2A_2$ are close to each other in Figs. 5.9 and 5.10, while the remaining six electronic states not only are close in energy, but they cross over among themselves. Tables 5.8, 5.9, 5.10 and 5.11 display the interstate coupling strengths ($\lambda_i^2/2\omega_i^2$) of electronic states through a_2, b_1, and b_2. Asterisks are used to represent the notably high coupling strengths of a_2, b_1, and b_2, vibrational modes which are taken into account in reduced dimensional MCTDH dynamics. Thus, one can anticipate that the nuclear dynamics in these electronic states will be significantly influenced by the vibronic coupling among

the energetically close lying electronic states with required symmetry.

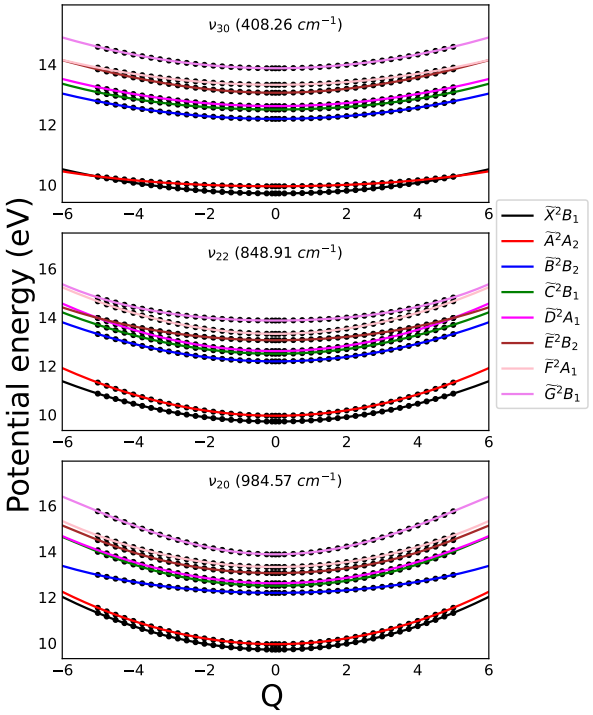

Figure 5.6: Same as the label of Fig. 5.3 along the asymmetric vibrational modes, a_2.

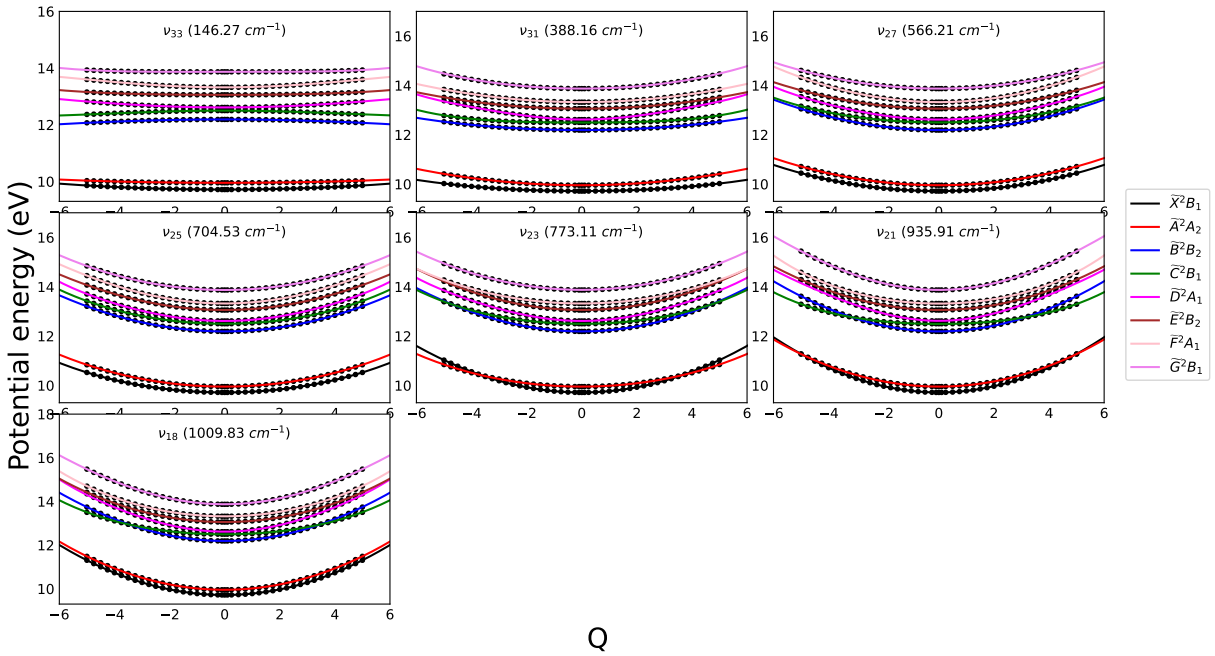

Figure 5.7: Same as the label of Fig. 5.3 along the asymmetric vibrational modes, b_1.

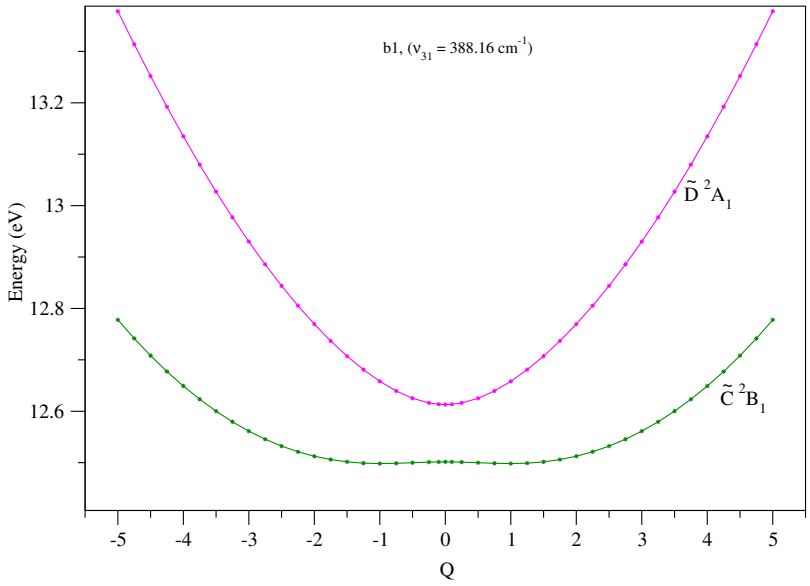

Figure 5.8: The adiabatic potential energy curve showing double well nature along the vibrational mode, ν_{31}.

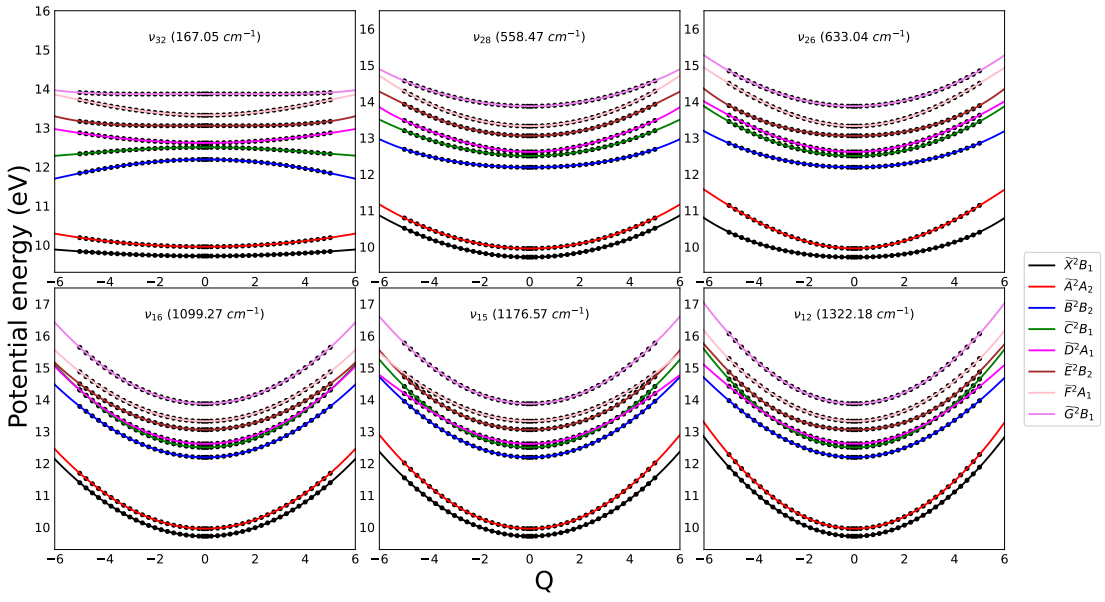

Figure 5.9: Same as the label of Fig. 5.3 along the asymmetric vibrational modes, b_2.

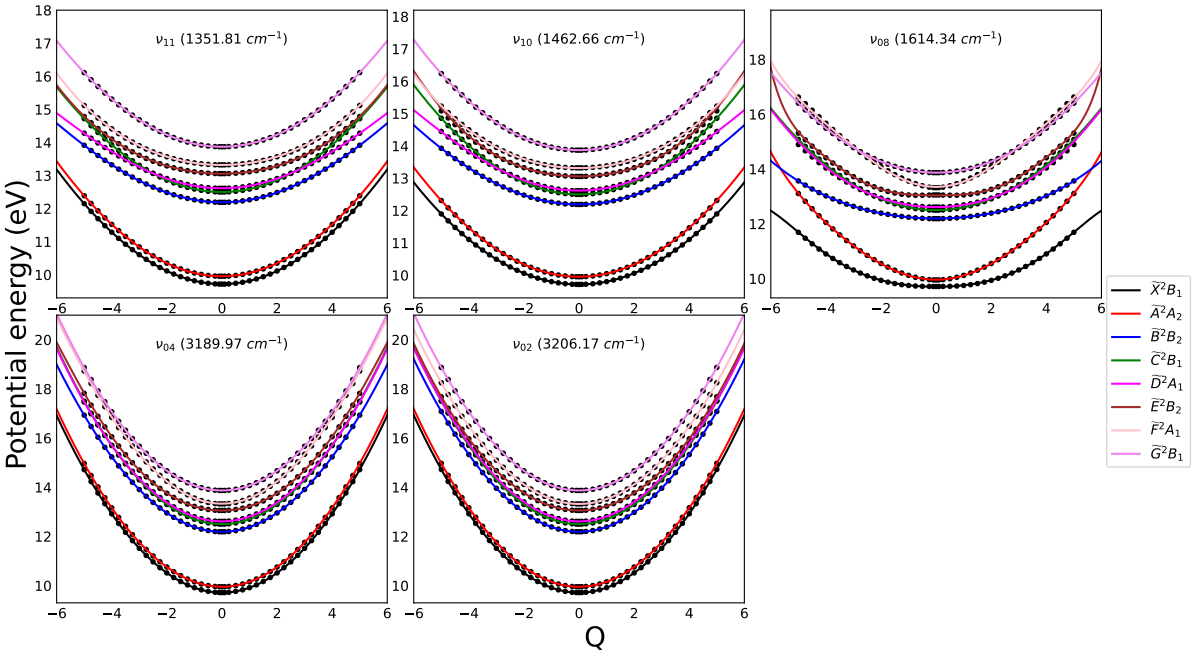

Figure 5.10: Same as the label of Fig. 5.9.

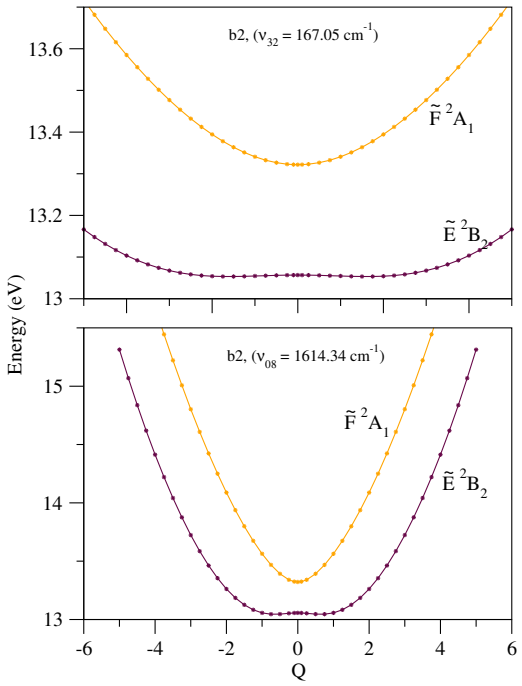

Figure 5.11: The adiabatic potential energy curve showing double well nature along the vibrational modes, v_{32} and v_{08}.

5.3.2 Photoionization and its signature in the experiment

The entire vibronic band structure of the coupled $\widetilde{X}^2B_1$-$\widetilde{A}^2A_2$-$\widetilde{B}^2B_2$-$\widetilde{C}^2B_1$-$\widetilde{D}^2A_1$-$\widetilde{E}^2B_2$-$\widetilde{F}^2A_1$-$\widetilde{G}^2B_1$ electronic states is presented in this section. It is calculated by reduced-dimensional MCTDH calculations

Table 5.8: Interstate coupling parameters (in eV) along a_2 symmetry modes of the vibronic Hamiltonian of Eq. 5.10 for the $\widetilde{X}^2B_1$-$\widetilde{G}^2B_1$ electronic states of $BN^{\cdot+}$ estimated from the *ab initio* electronic structure results (see text for details). Dimensionless excitation strengths ($\lambda_i^2/2\omega_i^2$) are given in the parentheses.

Symm	Mode	ν_{20}^*	ν_{22}	ν_{30}^*
a_2	$\lambda_i^{\widetilde{X},\widetilde{B}}$	0.0391(0.24)	0.0550(0.13)	-
	$\lambda_i^{\widetilde{X},\widetilde{D}}$	0.0677(0.72)	0.1151(0.59)	-
	$\lambda_i^{\widetilde{A},\widetilde{D}}$	0.1337(2.83)	-	-
	$\lambda_i^{\widetilde{A},\widetilde{F}}$	0.1343(2.85)	-	-
	$\lambda_i^{\widetilde{B},\widetilde{C}}$	-	0.0199(0.01)	0.0712(0.17)
	$\lambda_i^{\widetilde{B},\widetilde{G}}$	0.0671(0.71)	-	0.2240(0.70)
	$\lambda_i^{\widetilde{C},\widetilde{E}}$	0.0582(0.53)	-	-
	$\lambda_i^{\widetilde{E},\widetilde{G}}$	-	-	0.1186(0.47)

taking into account twenty with symmetry designations ($9a_1 + 2a_2 + 5b_1 + 4b_2$), vibrational modes. Another set of reduced dimensional MCTDH calculations including bilinear coupling parameters extracted along nine totally symmetric vibrational modes in combinations are performed, (see Table 5.5). Now in order to obtain a relatively complete picture, using optimized ML-trees (cf. Figs. 5.18-5.25) a full dimensional, that is by including all the thirty-three modes ($12a_1+3a_2+7b_1+11b_2$), nonadiabatic dynamics calculations are performed using ML-MCTDH program of Heidelberg MCTDH program module. In addition, to the set of full dimensional calculations, same spatial symmetry couplings shown in the Table 5.6, are incorporated and nonadiabatic dynamics calculations are performed. The parameters required for the construction of Hamiltonian are presented in Tables. 5.1, 5.2, 5.3 and 5.4 and the interstate coupling parameters are given in Tables. 5.8, 5.9, 5.10 and 5.11. The $\widetilde{X}^2B_1$-$\widetilde{A}^2A_2$ electronic manifold has substantial coupling strengths along b_2 symmetry vibrational modes. As can be seen from the coupling parameters presented in Tables 5.10 and 5.11. In contrast, the coupling strength of $\widetilde{A}^2A_2$-$\widetilde{B}^2B_2$ (cf., Table 5.9) is greater than that of $\widetilde{X}^2B_1$-$\widetilde{A}^2A_2$. The coupling strength of $\widetilde{X}^2B_1$-$\widetilde{B}^2B_2$ along a_2 vibrational mode (cf., Table 5.8) is not very strong. There is a significant energy difference, see Table 5.1 between the electronic states $\widetilde{X}^2B_1$and $\widetilde{A}^2A_2$ and the other electronic states $\widetilde{B}^2B_2$-$\widetilde{G}^2B_1$. Therefore, it is unlikely that the coupling of $\widetilde{X}^2B_1$ and $\widetilde{A}^2A_2$ with $\widetilde{B}^2B_2$ and other states would have any impact on the dynamics. Using the ML-MCTDH module full dimensional calculations and the MCTDH program module for reduced dimensional calculations, WPs are performed on eight electronic states. The WP is vertically excited to each ionic state separately and propagated in the coupled electronic manifold for 200 *fs*. To compute the composite vibronic band, the time autocorrelation functions derived from eight WP calculations are combined and damped by an exponential function, $e^{(-t/\tau_r)}$, with $\tau = 33\,fs$, and then Fourier transformed to generate the spectral envelope.

Table 5.9: Same as the label of Table. 5.8 along b_1 symmetry modes.

Symm	Mode	ν^*_{33}	ν^*_{31}	ν^*_{27}	ν^*_{25}	ν_{23}	ν_{21}	ν^*_{18}
b_1	$\lambda_i^{\widetilde{X},\widetilde{D}}$	0.0676(6.97)	0.1991(8.56)	0.1332(1.70)	0.1504(1.48)	-	0.1368(0.69)	0.1367(0.59)
	$\lambda_i^{\widetilde{X},\widetilde{F}}$	0.1093(18.26)	0.1300(3.65)	0.1465(2.06)	0.1703(1.89)	-	-	-
	$\lambda_i^{\widetilde{A},\widetilde{B}}$	-	-	0.0717(0.49)	0.0856(0.48)	0.1346(0.98)	0.0788(0.23)	0.0458(0.06)
	$\lambda_i^{\widetilde{A},\widetilde{E}}$	-	-	-	0.1026(0.68)	0.1404 (1.07)	-	-
	$\lambda_i^{\widetilde{C},\widetilde{D}}$	0.0357(1.94)	0.0581(0.73)	0.0376(0.13)	0.0322(0.06)	0.0484(0.12)	0.0831(0.25)	0.0716(0.16)
	$\lambda_i^{\widetilde{C},\widetilde{F}}$	0.0911(12.68)	0.0859(1.59)	0.0872(0.73)	0.0752(0.37)	0.0515(0.14)	0.1027(0.39)	0.0928(0.27)
	$\lambda_i^{\widetilde{D},\widetilde{G}}$	-	-	-	-	-	-	-
	$\lambda_i^{\widetilde{F},\widetilde{G}}$	-	0.0242(0.12)	-	-	0.0405(0.08)	0.0828(0.25)	0.0694(0.15)

Table 5.10: Same as the label of Table. 5.8 along b_2 symmetry modes.

Symm	Mode	ν^*_{32}	ν^*_{28}	ν^*_{26}	ν_{16}	ν_{15}	ν_{12}	ν_{11}
b_2	$\lambda_i^{\widetilde{X},\widetilde{A}}$	0.0238(0.66)	0.0148(0.02)	0.0697(0.39)	0.0178(0.00)	0.0395(0.03)	0.0302(0.01)	-
	$\lambda_i^{\widetilde{A},\widetilde{C}}$	-	-	-	0.0558(0.08)	-	-	-
	$\lambda_i^{\widetilde{A},\widetilde{G}}$	-	-	-	0.0443(0.05)	-	-	-
	$\lambda_i^{\widetilde{B},\widetilde{D}}$	0.0810(7.67)	0.0747(0.58)	0.0679(0.37)	0.0259(0.01)	-	0.0282(0.01)	-
	$\lambda_i^{\widetilde{B},\widetilde{F}}$	0.1421(23.56)	0.1151(1.38)	0.1294(1.35)	-	-	0.0655(0.08)	-
	$\lambda_i^{\widetilde{D},\widetilde{E}}$	-	-	-	-	-	-	-
	$\lambda_i^{\widetilde{E},\widetilde{F}}$	0.0521(3.17)	0.0279(0.08)	0.0621(0.31)	0.0289(0.02)	-	0.0542(0.05)	0.0199(0.00)

The experimental photoelectron spectrum is shown in panel (a), a reduced-dimensional (as mentioned above) MCTDH spectrum is shown in panel (b), reduced-dimensional MCTDH spectrum including bilinear couplings is presented in panel (c) and the full-dimensional (including all vibrational modes) ML-MCTDH spectrum is shown in panel (d) of Fig. 5.12. Parallelly, the spectrum obtained through full-dimensional ML-MCTDH calculations by incorporating same spatial symmetry couplings is shown in the Fig. 5.13. From the theoretical results, the spectral bands in the energy range $\sim$ 9 to $\sim$15 eV are predicted as $\widetilde{X}^2B_1$-$\widetilde{G}^2B_1$ states. Upon comparison it can be seen that, the general shape and structural features are satisfactorily reproduced by the three theoretical calculations as mentioned above. The whole spectrum appears as two distinct group of bands, one containing bands corresponding to both $\widetilde{X}^2B_1$, $\widetilde{A}^2A_2$ states and the other one appears to corresponds to energetically closely-lying $\widetilde{B}^2B_2$, $\widetilde{C}^2B_1$, $\widetilde{D}^2A_1$, $\widetilde{E}^2B_2$, $\widetilde{F}^2A_1$, and $\widetilde{G}^2B_1$ states of $BN^{\cdot+}$. Also, the PECs shown in Figs. 5.3, 5.4, 5.6, 5.7, 5.9 and 5.10 clearly exhibit the nature of states being separated

Table 5.11: Same as the label of Table. 5.8 along b_2 symmetry modes.

Symm	Mode	ν_{10}	ν^*_{08}	ν_{04}	ν_{02}
b_2	$\lambda_i^{\widetilde{X},\widetilde{A}}$	0.0337(0.01)	0.1409(0.24)	0.0778(0.01)	0.0078(0.00)
	$\lambda_i^{\widetilde{A},\widetilde{C}}$	-	-	-	-
	$\lambda_i^{\widetilde{A},\widetilde{G}}$	-	-	-	-
	$\lambda_i^{\widetilde{B},\widetilde{D}}$	0.0429(0.02)	0.0951(0.11)	0.0164(0.00)	0.0149(0.00)
	$\lambda_i^{\widetilde{B},\widetilde{F}}$	-	0.3193(1.27)	0.1540(0.07)	0.0252(0.00)
	$\lambda_i^{\widetilde{D},\widetilde{E}}$	-	-	-	-
	$\lambda_i^{\widetilde{E},\widetilde{F}}$	-	0.1834(0.42)	0.0991(0.03)	0.0540(0.00)

into two groups due to the energy difference between $\widetilde{X}^2B_1$, $\widetilde{A}^2A_2$ states and the remaining states. Furthermore, the spectral features in the first region show less complicated vibronic structure owing to a weak coupling of $\widetilde{X}^2B_1$ and $\widetilde{A}^2A_2$ states. On the other hand, the second band, exhibits highly complex vibronic structures due to the strong vibronic coupling among $\widetilde{B}^2B_2$, $\widetilde{C}^2B_1$, $\widetilde{D}^2A_1$, $\widetilde{E}^2B_2$, $\widetilde{F}^2A_1$, and $\widetilde{G}^2B_1$ states as revealed by the electronic structure data.

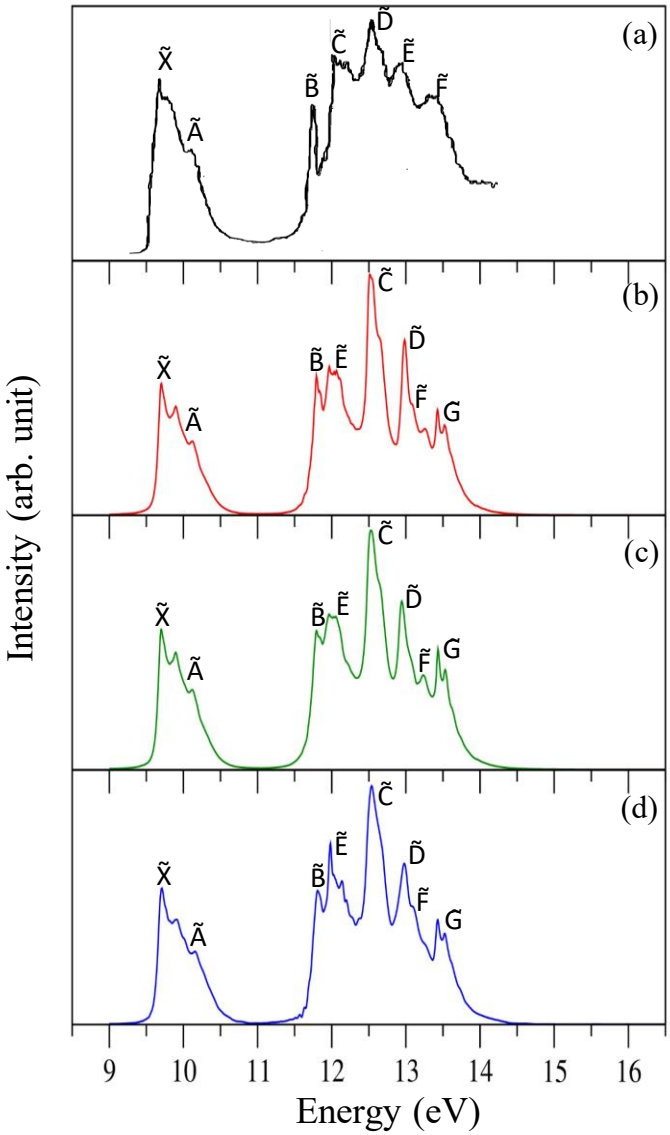

Figure 5.12: Composite Vibronic Band Structure of Coupled $\widetilde{X}^2B_1$-$\widetilde{A}^2A_2$-$\widetilde{B}^2B_2$-$\widetilde{C}^2B_1$-$\widetilde{D}^2A_1$-$\widetilde{E}^2B_2$-$\widetilde{F}^2A_1$-$\widetilde{G}^2B_1$ electronic states of $BN^{\cdot+}$. In panel (b), the band structures calculated using Hamiltonian parameters derived from EOMIP-CCSD energy data via reduced dimensional MCTDH calculations are presented. Panel (c) displays the band structures obtained by including the bilinear coupling incorporated reduced-dimensional MCTDH. Full-dimensional ML-MCTDH calculated band structures are shown in Panel (d), while panel (a) presents the experimental results reproduced from[3].

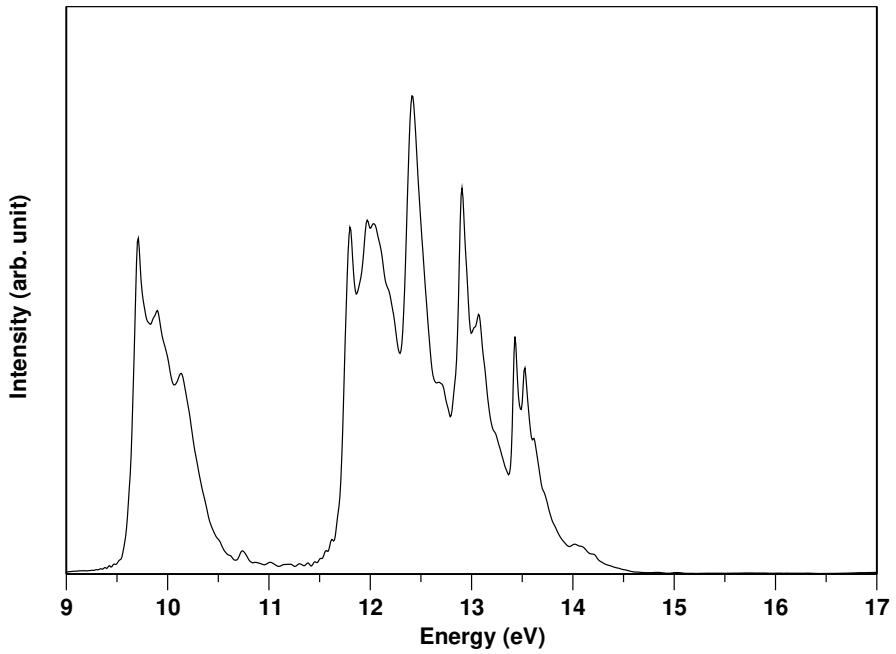

Figure 5.13: Composite vibronic band structure of coupled $\widetilde{X}$-$\widetilde{G}$ electronic states of $BN^{\cdot+}$ using full-dimensional ML-MCTDH by including same spatial symmetry coupling among the electronic states.

Regarding the theoretical methods and their comparison, both reduced-dimensional (panel (b) & (c) of Fig. 5.12) and full-dimensional calculations (panel (d) of Fig. 5.12), also full-dimensional calculations including same spatial symmetry couplings reproduce the features of the experimental observations. While there are not many visible changes in the spectral characteristics compared to panels (b), (c) and (d) and Fig. 5.13, the population dynamics shown in Figs. 5.15 and 5.16 and Fig. 5.17 show notable improvements. Note that, including bilinear coupling terms in the reduced-dimensional MCTDH (panel (c) of Fig. 5.12) had only minor impact on the overall spectrum. However, the full-dimensional spectrum exhibits all the peaks and finer details of the band when compared with the bands of reduced-dimensional spectra of panel (b) and (c). For example, the peak at $\sim$ 12 eV and the vibronic structure thereafter, is clearly visible in the panel (d) of Fig. 5.12.

At this point, it is worthwhile to discuss on the discrepancies of electronic state terms. Although the order of the state symmetries in the current work using the EOMIP-CCSD method, $\widetilde{X}^2B_1 < \widetilde{A}^2A_2 < \widetilde{B}^2B_2 < \widetilde{C}^2B_1 < \widetilde{D}^2A_1 < \widetilde{E}^2B_2 < \widetilde{F}^2A_1 < \widetilde{G}^2B_1$ and the previously predicted work, $\widetilde{X}^2B_1 < \widetilde{A}^2A_2 < \widetilde{B}^2B_2 < \widetilde{E}^2B_2 < \widetilde{C}^2B_1 < \widetilde{D}^2A_1 < \widetilde{G}^2B_1 < \widetilde{F}^2A_1$ [3] did not match, the final coupled states spectrum obtained through all four sets of dynamical calculations (see Fig. 5.12) and Fig. 5.13, confirm that the order of the state symmetries reported in the experiment [3] is appropriate. However, this does not imply that the current study is flawed; rather, it just indicates that the electronic states $\widetilde{C}^2B_1$, $\widetilde{D}^2A_1$, and $\widetilde{E}^2B_2$ were

switched because there was very little energy difference among them. Within the specified energy range, the experimental measurements indicate seven photoelectron bands; our theoretical model yields eight bands. This is one of the most significant findings of this study. Using vibronic coupling theory, the present MMVC, nonadiabatic dynamical treatment predicts the extra band that was not observed in the photoelectron spectrum reported in the literature[3].

5.3.3 Vibrational energy level spectrum of the uncoupled $\widetilde{X}^2B_1$-$\widetilde{G}^2B_1$ electronic states of $BN^{\cdot+}$

Using the Lanczos algorithm combined with a matrix diagonalization technique, the vibrational energy level spectrum of the uncoupled $\widetilde{X}^2B_1$-$\widetilde{G}^2B_1$ electronic states of $BN^{\cdot+}$ is calculated. Nine totally symmetric vibrational modes marked with asterisks in Table 5.2 are used in the theoretical computations, together with the vibronic Hamiltonian of Sec. 5.2.2. Fig. 5.14 display the corresponding convoluted and stick spectra, which were performed using parameters generated from the EOMIP-CCSD electronic energies. 10000 Lanczos iterations are carried out to diagonalize the Hamiltonian of each state represented in the HO basis. The spectral envelopes seen in Fig. 5.14 are produced by convolution of the stick spectrum with a Lorentzian line shape function of 33 meV FWHM. This method allows for the computation of individual transitions, or vibrational progressions, in addition to the spectral envelope. However, this strategy could not be applied for fully coupled states due to the dimensionality problem. Table 5.12 provides the energy eigenvalue and corresponding assignments of the low-lying vibronic levels of the uncoupled $\widetilde{X}^2B_1$, $\widetilde{A}^2A_2$, $\widetilde{B}^2B_2$, $\widetilde{C}^2B_1$, $\widetilde{D}^2A_1$, $\widetilde{E}^2B_2$, $\widetilde{F}^2A_1$and $\widetilde{G}^2B_1$ states. Table 5.12 records the progressions of lines with significant intensities. The findings shown in Table 5.12 show that in every electronic state of $BN^{\cdot+}$, the fundamental nine a_1 vibrational modes are excited. Additionally, it is possible to find the excitation of many combination energy levels. Fig. 5.14, displays the spectrum of $\widetilde{X}^2B_1$ electronic state of $BN^{\cdot+}$, where ν_{29}, ν_{24}, ν_{17} and ν_{07} vibrational modes represent the predominant sequence in this band, with corresponding vibrational progressions found at ∼481, ∼768, ∼1054, and ∼1654 cm^{-1}, respectively. In addition to fundamental vibrational progressions, this band exhibits combination levels that are considerably excited, with peaks located at ∼1249, ∼1696, and ∼2136 cm^{-1}. Vibrational modes ν_{29}, ν_{24}, ν_{14} and ν_9 are dominantly excited whereas ν_{19}, ν_{17}, and ν_{13} exhibit mild excitation in the $\widetilde{B}^2B_2$ state, which is energetically close to the $\widetilde{A}^2A_2$ state (cf. Table 5.12). Peaks are located around ∼516, ∼767, ∼1248 and ∼1524 cm^{-1} and approximately ∼1005, ∼1035, and ∼1214 cm^{-1} separated in that sequence, respectively. Moderately and weakly excited combination levels are also observed at ∼1283 and ∼1522 cm^{-1}, respectively. The computed $\widetilde{X}^2B_1$ and $\widetilde{A}^2A_2$ bands are to be shifted by -0.60 and -0.46 eV, respectively, in order to reproduce the experimental adiabatic ionization position, see Fig. 5.14.

From $\widetilde{B}^2B_2$ to $\widetilde{G}^2B_1$, the ionization bands are complex and close in energy. The switching of electronic bands happened as a result of the extremely small energy difference between the electronic states, as seen in Fig. 5.14. The coupled state spectra displayed in Fig. 5.12 is in good agreement with the order of the electronic state terms presented in the Fig. 5.14. Referring to state $\widetilde{B}^2B_2$'s progressions, vibrational modes ν_{29}, ν_{13}, and ν_{14} are highly excited and peaks are $\sim$ 406, $\sim$1135 and $\sim$1172 cm^{-1} spaced, while the rest are moderately excited. In order to place the computed ionized band $\widetilde{B}^2B_2$ at the experimental adiabatic ionization position, a shift of -0.80 eV is given along the abstica of Fig.5.14. The ionized bands $\widetilde{C}^2B_1$, $\widetilde{D}^2A_1$and $\widetilde{E}^2B_2$ are shifted by -0.48, -0.13 and -1.55 eV respectively to bring them to the experimental band position. Table 5.12, which lists progressions and combination levels, reveals the sticks with good intensity obtained for states $\widetilde{E}^2B_2$, $\widetilde{C}^2B_1$ and $\widetilde{D}^2A_1$. Even if the experimental spectrum (see Fig. 5.12) doesn't show the vibronic band structure of $\widetilde{F}^2A_1$ distinctly, this band unquestionably contributes to the overall shape of the composite spectrum. This band shares parts of its commonality with the eighth electronic band (state $\widetilde{G}^2B_1$) and its major portion falls underneath the sixth electronic band. The vibrational progressions in the seventh and eighth vibronic bands of $\widetilde{F}^2A_1$ and $\widetilde{G}^2B_1$ electronic states, includes fundamental and many combination levels in each band and the peak spacings are given in Table 5.12. To bring the computed ionized bands $\widetilde{F}^2A_1$ and $\widetilde{G}^2B_1$ to the experimental band positions, they are moved by -0.60 and -0.90 eV, respectively.

5.3.4 Internal conversion dynamics

Time-dependent diabatic electronic populations of coupled $\widetilde{X}^2B_1$—$\widetilde{G}^2B_1$ states are analysed here to understand the impact of nonadiabatic coupling effects on the overall dynamics. Figs. 5.15 and 5.16 present the population dynamics during the propagation of the WP till 200 *fs* with an initial excitation on various electronic states. Both Figs. 5.15 and 5.16 contain three columns corresponding to the results obtained from the reduced-dimensional MCTDH (column (i)), bilinear couplings incorporated reduced-dimensional MCTDH (column (ii)), and the full-dimensional ML-MCTDH (column (iii)). Each column in panels (a)-(l) of Figs. 5.15 and 5.16 show multiple rows of panels where WP is initialized on specific electronic states ($\widetilde{X}^2B_1$, $\widetilde{A}^2A_2$, $\widetilde{B}^2B_2$, $\widetilde{C}^2B_1$, $\widetilde{D}^2A_1$, $\widetilde{E}^2B_2$, $\widetilde{F}^2A_1$, $\widetilde{G}^2B_1$) as shown in the respective Figs. 5.15 and 5.16.

In panels (a), (b), and (c) of Fig. 5.15, the propagation initiated from $\widetilde{X}^2B_1$ state, there is a slight electronic population transfer to $\widetilde{A}^2A_2$, $\widetilde{B}^2B_2$, $\widetilde{D}^2A_1$, and $\widetilde{F}^2A_1$ states justifying the corresponding coupling parameters obtained in Tables 5.8, 5.9, 5.10, and 5.11. Although the coupling strengths obtained for vibrational modes of b_1 symmetry between $\widetilde{X}^2B_1$-$\widetilde{D}^2A_1$ (ν_{33}: 6.97 & ν_{31}: 8.56, see Table 5.9) and $\widetilde{X}^2B_1$-$\widetilde{F}^2A_1$ (ν_{33}: 18.26 & ν_{31}: 3.65, see Table 5.9) seems to be stronger than that of $\widetilde{X}^2B_1$-

Table 5.12: Energetically low-lying vibrational energy levels (in cm^{-1}) of the $\widetilde{X}^2B_1$, $\widetilde{A}^2A_2$, $\widetilde{B}^2B_2$, $\widetilde{C}^2B_1$, $\widetilde{D}^2A_1$, $\widetilde{E}^2B_2$, $\widetilde{F}^2A_1$ and $\widetilde{G}^2B_1$ electronic states of $BN^{\cdot+}$ obtained from the uncoupled state calculations. The assignment of the levels with significant intensities of the progressions marked with (+) and are included in the table.

$\widetilde{X}^2B_1$		$\widetilde{A}^2A_2$		$\widetilde{B}^2B_2$		$\widetilde{C}^2B_1$	
Energy	Assignment	Energy	Assignment	Energy	Assignment	Energy	Assignment
0^+	0_0^0	0^+	0_0^0	0^+	0_0^0	0^+	0_0^0
481^+	$\nu_{29_0}^1$	516^+	$\nu_{29_0}^1$	406^+	$\nu_{29_0}^1$	460^+	$\nu_{29_0}^1$
768^+	$\nu_{24_0}^1$	767^+	$\nu_{24_0}^1$	705^+	$\nu_{24_0}^1$	766^+	$\nu_{24_0}^1$
1012^+	$\nu_{19_0}^1$	1005^+	$\nu_{19_0}^1$	930^+	$\nu_{19_0}^1$	1006^+	$\nu_{19_0}^1$
1055^+	$\nu_{17_0}^1$	1035^+	$\nu_{17_0}^1$	1023	$\nu_{17_0}^1$	1050^+	$\nu_{17_0}^1$
1204	$\nu_{13_0}^1$	1214^+	$\nu_{13_0}^1$	1135	$\nu_{13_0}^1$	1152	$\nu_{13_0}^1$
1214^+	$\nu_{14_0}^1$	1248^+	$\nu_{14_0}^1$	1172	$\nu_{14_0}^1$	1209	$\nu_{14_0}^1$
1249^+	$\nu_{24_0}^1+\nu_{29_0}^1$	1283^+	$\nu_{29_0}^1+\nu_{24_0}^1$	1304^+	$\nu_{09_0}^1$	1226	$\nu_{29_0}^1+\nu_{24_0}^1$
1493^+	$\nu_{19_0}^1+\nu_{29_0}^1$	1522^+	$\nu_{29_0}^1+\nu_{19_0}^1$	1399^+	$\nu_{07_0}^1$	1466	$\nu_{29_0}^1+\nu_{19_0}^1$
1536	$\nu_{24_0}^2$	1524	$\nu_{09_0}^1$	2330^+	$\nu_{07_0}^1+\nu_{19_0}^1$	1510	$\nu_{29_0}^1+\nu_{17_0}^1$
1654^+	$\nu_{07_0}^1$	1552	$\nu_{19_0}^1+\nu_{17_0}^1$	2400^+	$\nu_{06_0}^1$	1537^+	$\nu_{09_0}^1$
1686	$\nu_{29_0}^1+\nu_{13_0}^1$	1693^+	$\nu_{07_0}^1$	2704^+	$\nu_{07_0}^1+\nu_{09_0}^1$	1773	$\nu_{24_0}^1+\nu_{19_0}^1$
1696^+	$\nu_{29_0}^1+\nu_{14_0}^1$	1730	$\nu_{13_0}^1+\nu_{29_0}^1$			1816	$\nu_{24_0}^1+\nu_{17_0}^1$
1779	$\nu_{19_0}^1+\nu_{24_0}^1$	1765^+	$\nu_{29_0}^1+\nu_{14_0}^1$			2056^+	$\nu_{19_0}^1+\nu_{17_0}^1$
1822	$\nu_{17_0}^1+\nu_{24_0}^1$	1772	$\nu_{19_0}^1+\nu_{24_0}^1$			2100	$\nu_{17_0}^2$
1972	$\nu_{13_0}^1+\nu_{24_0}^1$	2016	$\nu_{14_0}^1+\nu_{24_0}^1$			2350^+	$\nu_{06_0}^1$
1982	$\nu_{14_0}^1+\nu_{24_0}^1$	2210^+	$\nu_{07_0}^1+\nu_{24_0}^1$				
2136^+	$\nu_{07_0}^1+\nu_{29_0}^1$	2254	$\nu_{19_0}^1+\nu_{14_0}^1$				
2226	$\nu_{14_0}^1+\nu_{19_0}^1$	2284	$\nu_{14_0}^1+\nu_{17_0}^1$				
2262	$\nu_{06_0}^1$	2460	$\nu_{24_0}^1+\nu_{07_0}^1$				
2422^+	$\nu_{07_0}^1+\nu_{24_0}^1$	2463	$\nu_{13_0}^1+\nu_{14_0}^1$				
2869^+	$\nu_{14_0}^1+\nu_{07_0}^1$						

$\widetilde{D}^2A_1$		$\widetilde{E}^2B_2$		$\widetilde{F}^2A_1$		$\widetilde{G}^2B_1$	
Energy	Assignment	Energy	Assignment	Energy	Assignment	Energy	Assignment
0^+	0_0^0	0^+	0_0^0	0^+	0_0^0	0^+	0_0^0
495^+	$\nu_{29_0}^1$	488^+	$\nu_{29_0}^1$	551^+	$\nu_{29_0}^1$	485^+	$\nu_{29_0}^1$
749^+	$\nu_{24_0}^1$	743^+	$\nu_{24_0}^1$	802^+	$\nu_{24_0}^1$	887^+	$\nu_{24_0}^1$
894^+	$\nu_{19_0}^1$	837	$\nu_{19_0}^1$	985^+	$\nu_{19_0}^1$	1025^+	$\nu_{19_0}^1$
1118^+	$\nu_{17_0}^1$	1054^+	$\nu_{14_0}^1$	1015	$\nu_{17_0}^1$	1066^+	$\nu_{17_0}^1$
1133^+	$\nu_{13_0}^1$	1122^+	$\nu_{13_0}^1$	1172^+	$\nu_{13_0}^1$	1210	$\nu_{14_0}^1$
1177^+	$\nu_{14_0}^1$	1231	$\nu_{29_0}^1+\nu_{24_0}^1$	1204^+	$\nu_{14_0}^1$	1300	$\nu_{13_0}^1$
1244^+	$\nu_{24_0}^1+\nu_{29_0}^1$	1367^+	$\nu_{14_0}^1$	1353^+	$\nu_{09_0}^1$	1372^+	$\nu_{29_0}^1+\nu_{24_0}^1$
1408^+	$\nu_{07_0}^1$	1611^+	$\nu_{29_0}^1+\nu_{17_0}^1$	1537^+	$\nu_{29_0}^1+\nu_{17_0}^1$	1510^+	$\nu_{29_0}^1+\nu_{19_0}^1$
1904^+	$\nu_{07_0}^2+\nu_{29_0}^1$	1834^+	$\nu_{07_0}^1$	1724^+	$\nu_{29_0}^1+\nu_{14_0}^1$	1540	$\nu_{09_0}^1$
2527^+	$\nu_{07_0}^1\nu_{17_0}^1$	1856^+	$\nu_{29_0}^1+\nu_{14_0}^1$	1755^+	$\nu_{13_0}^1+\nu_{29_0}^1$	1912^+	$\nu_{19_0}^1+\nu_{24_0}^1$
2542	$\nu_{07_0}^1+\nu_{13_0}^1$	2111^+	$\nu_{14_0}^1+\nu_{24_0}^1$	1787^+	$\nu_{24_0}^1+\nu_{17_0}^1$	1954^+	$\nu_{24_0}^1+\nu_{17_0}^1$
2586	$\nu_{07_0}^1+\nu_{14_0}^1$	2322^+	$\nu_{07_0}^1+\nu_{29_0}^1$	1833^+	$\nu_{07_0}^1$	2092	$\nu_{19_0}^1+\nu_{17_0}^1$
				2006^+	$\nu_{24_0}^1+\nu_{13_0}^1$	2397^+	$\nu_{06_0}^1$
				2094^+	$\nu_{09_0}^2+\nu_{24_0}^1$		
				2339^+	$\nu_{06_0}^1$		
				2384^+	$\nu_{07_0}^2+\nu_{29_0}^1$		
				2558^+	$\nu_{09_0}^2+\nu_{14_0}^1$		
				2635^+	$\nu_{29_0}^2+\nu_{07_0}^1$		

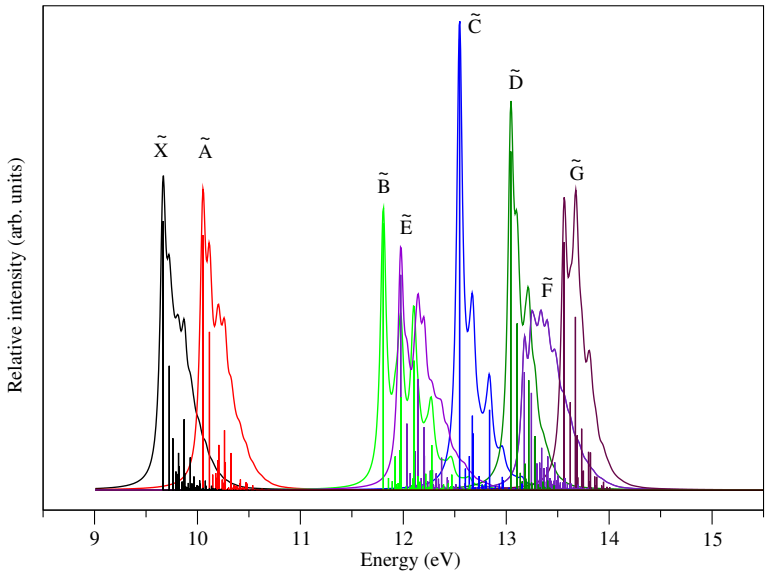

Figure 5.14: The stick vibrational spectrum and the convoluted envelope of the uncoupled $\widetilde{X}^2B_1$, $\widetilde{A}^2A_2$, $\widetilde{B}^2B_2$, $\widetilde{C}^2B_1$, $\widetilde{D}^2A_1$, $\widetilde{E}^2B_2$, $\widetilde{F}^2A_1$and $\widetilde{G}^2B_1$ electronic states of $BN^{\cdot+}$, calculated with nine totally symmetric vibrational modes using the EOMIP-CCSD Hamiltonian parameters.

$\widetilde{A}^2A_2$ (through ν_{32} of b_2 symmetry: 0.66, see Table 5.10) and $\widetilde{X}^2B_1$-$\widetilde{B}^2B_2$ (through ν_{20} of a_2 symmetry: 0.24, see Table 5.8), due to the large separation between $\widetilde{X}^2B_1$ and any of the concerned states here, the population transfer is negligible. Furthermore, comparison among reduced-dimensional, bilinear coupling incorporated reduced-dimensional, and full-dimensional MCTDH shows minor differences in this case.

In panels (d), (e), and (f) of Fig. 5.15, there is a significant population transfer ($\sim$ 80%) to the $\widetilde{X}^2B_1$ state from the initial $\widetilde{A}^2A_2$ state within $\sim$ 15 *fs*. Thereafter, rapid depletion of population of $\widetilde{A}^2A_2$ state and simultaneous major rise in population of $\widetilde{X}^2B_1$ state and minor rise in $\widetilde{D}^2A_1$, and $\widetilde{F}^2A_1$ states is clearly visible. This rapid electronic population transfer to $\widetilde{X}^2B_1$ state originates due to the existence of $\widetilde{X}^2B_1$-$\widetilde{A}^2A_2$ CIs just $\sim$ 0.02 eV above the $\widetilde{A}^2A_2$ state minimum (vide supra). In addition, mild coupling strength observed through vibrational modes of b_2 symmetry between $\widetilde{X}^2B_1$ and $\widetilde{A}^2A_2$ states (through ν_{32} of b_2 symmetry: 0.66, see Table 5.10). Further, the coupling strength obtained between $\widetilde{A}^2A_2$-$\widetilde{D}^2A_1$ (through ν_{20} of a_2 symmetry: 2.83, see Table 5.8) and $\widetilde{A}^2A_2$-$\widetilde{F}^2A_1$ (through ν_{20} of a_2 symmetry: 2.85, see Table 5.8) states is slightly strong. However, owing to the energy difference between $\widetilde{A}^2A_2$-$\widetilde{D}^2A_1$ and $\widetilde{A}^2A_2$-$\widetilde{F}^2A_1$ states, the population transfer is minimal. On the dynamical front, minor differences exist between reduced-dimensional MCTDH and bilin-

ear couplings incorporated reduced-dimensional MCTDH, whereas the results of column (iii) full-dimensional ML-MCTDH stands out showing a different behaviour. Firstly, the population transfer to the $\widetilde{X}^2B_1$ state occurs within $\sim$ 11 *fs* of WP propagation, quicker than that of columns (i) [panel (d)] and (ii) [panel (e)] and secondly minor population transfers to $\widetilde{D}^2A_1$, and $\widetilde{F}^2A_1$ states are more pronounced. Most probably the reason behind this can be attributed to the inclusion of all vibrational modes and the coupling parameters which are additionally included in the ML-MCTDH.

In panels (g), (h), and (i) of Fig. 5.15, there is an apparent population transfer from the initial $\widetilde{B}^2B_2$ state to $\widetilde{X}^2B_1$, $\widetilde{A}^2A_2$, $\widetilde{D}^2A_1$, and $\widetilde{F}^2A_1$ states. Note that, the energy difference between $\widetilde{B}^2B_2$-$\widetilde{A}^2A_2$ and $\widetilde{B}^2B_2$-$\widetilde{X}^2B_1$ states is higher ($\sim$ 2 eV, see Table 5.7) as compared to $\widetilde{B}^2B_2$-$\widetilde{D}^2A_1$ and $\widetilde{B}^2B_2$-$\widetilde{F}^2A_1$ states ($\sim$ 1 eV, see Table 5.7) as seen in the PECs. However, the coupling strengths obtained between $\widetilde{B}^2B_2$-$\widetilde{X}^2B_1$ (through ν_{20} of a_2 symmetry: 0.24, see Table 5.8) and $\widetilde{B}^2B_2$-$\widetilde{A}^2A_2$ (through ν_{23}: 0.98, see Table 5.9) states is lower than that of $\widetilde{B}^2B_2$-$\widetilde{D}^2A_1$ (through ν_{32} of b_2 symmetry: 7.67, see Table 5.10) and $\widetilde{B}^2B_2$-$\widetilde{F}^2A_1$ (through ν_{32} of b_2 symmetry: 23.56, see Table 5.10) states. Surprisingly, a major electronic population is transferred to $\widetilde{X}^2B_1$ and $\widetilde{A}^2A_2$ states after $\sim$ 58 *fs* of WP propagation. This result is more evident from full-dimensional MCTDH dynamics in column (iii) [panel (i)], the population transfer is quite dramatic within $\sim$ 44 *fs*.

Panels (j), (k), and (l) of Fig. 5.15 exhibit rapid and major electronic population transfer ($\sim$60%) from the initial $\widetilde{C}^2B_1$ state to $\widetilde{B}^2B_2$ state and to other states to a minor amount within $\sim$ 45 *fs* of WP propagation. This can be readily attributed to the existence of $\widetilde{C}^2B_1$-$\widetilde{B}^2B_2$ CI just $\sim$ 0.16 eV above the $\widetilde{C}^2B_1$ state minimum and to the mild coupling strength obtained between $\widetilde{B}^2B_2$-$\widetilde{C}^2B_1$ states (through ν_{30} of a_2 symmetry: 0.17, see Table 5.8). Even in this case, the results obtained through full-dimensional MCTDH dynamics in column (iii) [panel (l)], the electronic population transfer happens rather quickly within $\sim$ 20 *fs* of WP propagation.

In Fig. 5.16, panels (a), (b), and (c) exhibit electronic population transfer to the $\widetilde{B}^2B_2$ and $\widetilde{C}^2B_1$ states from the initial $\widetilde{D}^2A_1$ state within $\sim$ 20 fs. Between $\widetilde{B}^2B_2$ and $\widetilde{C}^2B_1$ states, the majority of the population transfer takes place to the $\widetilde{B}^2B_2$ state and a minor amount to the $\widetilde{C}^2B_1$state. This is due to the stronger coupling strength of $\widetilde{D}^2A_1$-$\widetilde{B}^2B_2$ states (through ν_{32} mode of b_2 symmetry: 7.67, see Table 5.10) and weaker coupling strength of $\widetilde{D}^2A_1$-$\widetilde{C}^2B_1$ states (through ν_{33} mode of b_1 symmetry: 1.94, see Table 5.9) respectively. The energy difference between $\widetilde{D}^2A_1$-$\widetilde{B}^2B_2$ states ($\sim$0.02 eV) is slightly higher than that of $\widetilde{D}^2A_1$-$\widetilde{C}^2B_1$ states ($\sim$0 eV) according to Table 5.7. Here, the full-dimensional MCTDH dynamics in column (iii) [panel (c)], displays almost similar results obtained from both the reduced-dimensional MCTDH dynamics (columns (i) [panel (a)] and (ii) [panel (b)]) except for the rise in $\widetilde{B}^2B_2$ state population and simultaneous fall in $\widetilde{C}^2B_1$ state population at $\sim$ 10 *fs*.

Panels (d), (e), and (f) of Fig. 5.16 exhibit electronic population transfer to the $\widetilde{C}^2B_1$, $\widetilde{B}^2B_2$, $\widetilde{D}^2A_1$, and $\widetilde{F}^2A_1$ states in ascending order from the initial $\widetilde{E}^2B_2$ state within $\sim$20 *fs*. The population transfer towards $\widetilde{C}^2B_1$ and $\widetilde{F}^2A_1$ states can be due to the coupling strengths obtained between $\widetilde{C}^2B_1$-$\widetilde{E}^2B_2$ states (0.53, through ν_{20} mode of a_2 symmetry, cf., Table 5.8), and between $\widetilde{F}^2A_1$-$\widetilde{E}^2B_2$ states (3.17, through ν_{32} mode of b_2 symmetry, cf., Table 5.10). Considerable population transfer to the -$\widetilde{C}^2B_1$ state than $\widetilde{F}^2A_1$ state can be due to $\widetilde{C}^2B_1$-$\widetilde{E}^2B_2$ CIs is just $\sim$0.01 eV above the $\widetilde{E}^2B_2$ state minimum and $\widetilde{F}^2A_1$-$\widetilde{E}^2B_2$ CIs is just $\sim$0.09 eV above the $\widetilde{E}^2B_2$ state minimum. Whereas, the population transfer to the $\widetilde{B}^2B_2$ and $\widetilde{D}^2A_1$ states can be due to $\widetilde{B}^2B_2$-$\widetilde{E}^2B_2$ CIs and $\widetilde{D}^2A_1$-$\widetilde{E}^2B_2$ CIs lies $\sim$0.15 eV and $\sim$0.02 eV, respectively above the $\widetilde{E}^2B_2$ state minimum. The results obtained through full-dimensional MCTDH (column (iii) [panel (f)]) contrast the ones obtained from reduced-dimensional dynamics (columns (i) [panel (a)] and (ii) [panel (b)]). The population transfer is delayed and observed initially towards $\widetilde{C}^2B_1$ state, later with a higher proportion towards $\widetilde{B}^2B_2$ state at $\sim$60 *fs*.

Panels (g), (h), and (i) of Fig. 5.16 exhibit electronic population transfer to the $\widetilde{B}^2B_2$, $\widetilde{C}^2B_1$, and $\widetilde{E}^2B_2$ states from the initial $\widetilde{F}^2A_1$ state quite rapidly in such a way that within $\sim$15 *fs* the population of $\widetilde{F}^2A_1$ state is $\sim$90 % depleted. The major proportion of the population is transferred to the $\widetilde{B}^2B_2$, $\widetilde{C}^2B_1$, and $\widetilde{E}^2B_2$ states, with a minor proportion to the $\widetilde{D}^2A_1$ state. The population transfer to the $\widetilde{B}^2B_2$, $\widetilde{C}^2B_1$, and $\widetilde{E}^2B_2$ is dependent upon both coupling strength and static energies. Careful examination reveals that the population transfer occurs uniformly to the $\widetilde{B}^2B_2$, $\widetilde{C}^2B_1$, and $\widetilde{E}^2B_2$ states. The coupling strengths between $\widetilde{B}^2B_2$-$\widetilde{F}^2A_1$ (through ν_{32} mode of b_2 symmetry: 23.56, see Table 5.10), $\widetilde{C}^2B_1$-$\widetilde{F}^2A_1$ (through ν_{33} mode of b_1 symmetry: 12.68, see Table 5.9), and $\widetilde{E}^2B_2$-$\widetilde{F}^2A_1$ (through ν_{32} mode of b_2 symmetry: 3.17, see Table 5.10) seem to justify the population transfer. Also the $\widetilde{B}^2B_2$-$\widetilde{F}^2A_1$ CI, $\widetilde{C}^2B_1$-$\widetilde{F}^2A_1$ CI, and $\widetilde{E}^2B_2$-$\widetilde{F}^2A_1$ CI which are $\sim$0.24 eV, $\sim$ 0.08 eV, and $\sim$0.09 eV, respectively, above the $\widetilde{F}^2A_1$ state minimum adds to the explaination. Whereas $\widetilde{D}^2A_1$-$\widetilde{F}^2A_1$ CIs is $\sim$0.51 eV above the $\widetilde{F}^2A_1$ state minimum justifying the minor population transfer. The results obtained through full-dimensional MCTDH (column (iii) [panel (i)]) displays almost similar nature to the ones obtained from reduced-dimensional dynamics (columns (i) [panel (g)] and (ii) [panel (h)]). Panels (j), (k), and (l) of Fig. 5.16 exhibit electronic population transfer to the $\widetilde{E}^2B_2$ and $\widetilde{F}^2A_1$ states in major proportion and to the $\widetilde{B}^2B_2$, $\widetilde{C}^2B_1$ and $\widetilde{D}^2A_1$ states in minor proportion. This population transfer happens within $\sim$70 *fs* and $\sim$30 *fs* of panels (j) and (l), respectively. The population transfer towards $\widetilde{E}^2B_2$ and $\widetilde{F}^2A_1$ states is justified by coupling strength and energetic factors. The coupling strength between $\widetilde{G}^2B_1$ and $\widetilde{E}^2B_2$ states (through ν_{20} mode of a_2 symmetry) is 0.47 (see Table 5.8) with $\widetilde{G}^2B_1$-$\widetilde{E}^2B_2$ CI located 0.31 eV above the $\widetilde{G}^2B_1$ state minimum. On the other hand, the coupling strength between $\widetilde{G}^2B_1$ and $\widetilde{F}^2A_1$ states (through ν_{21} of b_1 symmetry) is 0.25 (see Table 5.9)

with $\widetilde{G}^2B_1$-$\widetilde{F}^2A_1$ CI located 0.06 eV above the $\widetilde{G}^2B_1$ state minimum. Here, comparison of different dynamics shows that the reduced-dimensional MCTDH displays an equal proportion of population transfer towards $\widetilde{E}^2B_2$ and $\widetilde{F}^2A_1$ states from $\widetilde{G}^2B_1$ state (columns (i) [panel (j)]). The bilinear couplings incorporated reduced-dimensional MCTDH dynamics revealed a dominant population transfer to the $\widetilde{F}^2A_1$ state (columns (ii) [panel (k)]). The full-dimensional MCTDH dynamics resulted in a rather rapid population transfer of $\sim$70% within $\sim$30 *fs* along with a dominant population transfer to the $\widetilde{E}^2B_2$ state (columns (iii) [panel (l)]).

The results obtained by propagating the WP on $\widetilde{X}^2B_1$-$\widetilde{G}^2B_1$ states, respectively, with the incorporation of the same spatial symmetry couplings, are depicted in panels (a)–(h) of 5.17. When the same spatial symmetry couplings are included (see Fig. 5.17), the population profiles differ slightly from the three sets discussed above (see Figs. 5.15 and 5.16). Since this set of calculations show only minor changes in the population profiles, we can hereby conclude the effect of same spatial symmetry couplings is weak.

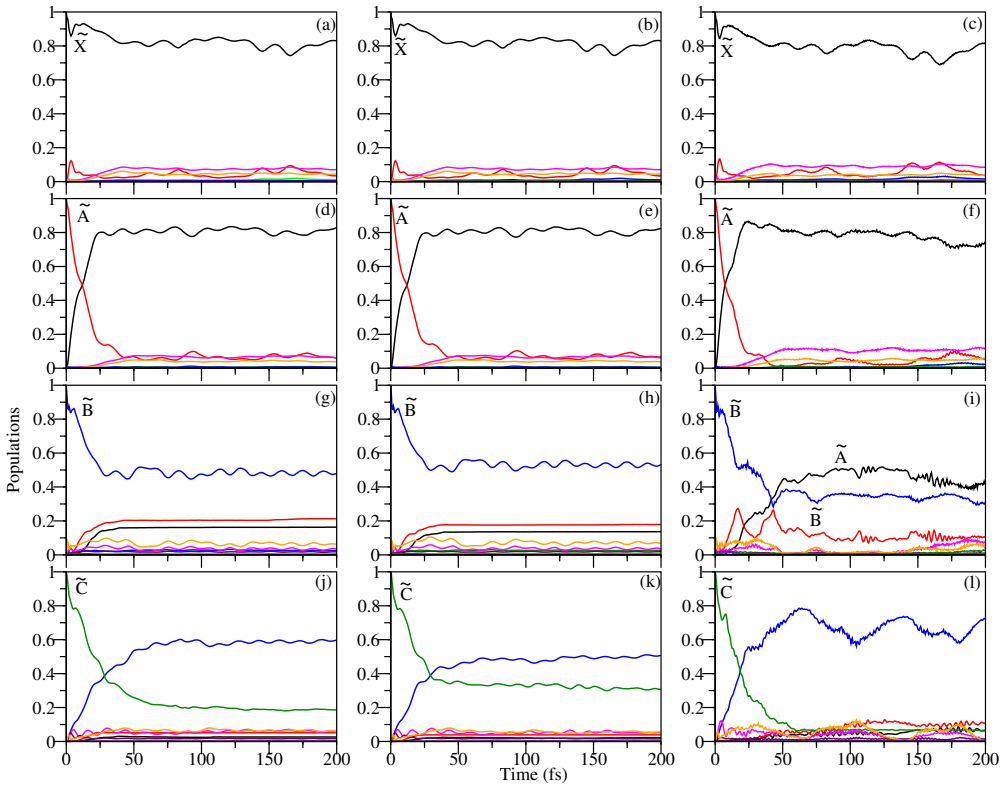

Figure 5.15: Time evolution of the diabatic electronic populations obtained in the coupled $\widetilde{X}^2B_1$-$\widetilde{A}^2A_2$-$\widetilde{B}^2B_2$-$\widetilde{C}^2B_1$-$\widetilde{D}^2A_1$-$\widetilde{E}^2B_2$-$\widetilde{F}^2A_1$-$\widetilde{G}^2B_1$ states situation (using the parameters set derived from the EOMIP-CCSD energy data) by locating an initial WP on each of the $\widetilde{X}^2B_1$, $\widetilde{A}^2A_2$, $\widetilde{B}^2B_2$, and $\widetilde{C}^2B_1$ electronic states separately. Column (i), represents reduced-dimensional MCTDH, column (ii), bilinear couplings incorporated reduced-dimensional MCTDH, and column (iii), full-dimensional ML-MCTDH.

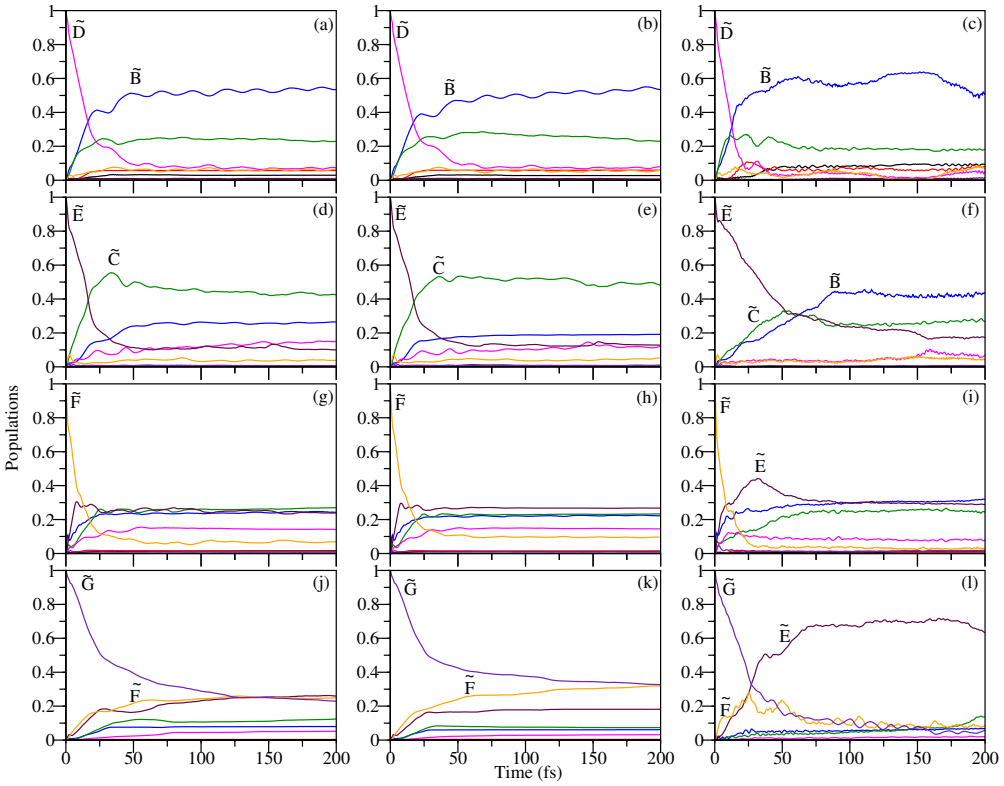

Figure 5.16: Same as the label of Fig. 5.15 by locating an initial WP on each of the $\widetilde{D}^2A_1$, $\widetilde{E}^2B_2$, $\widetilde{F}^2A_1$and $\widetilde{G}^2B_1$ electronic states separately.

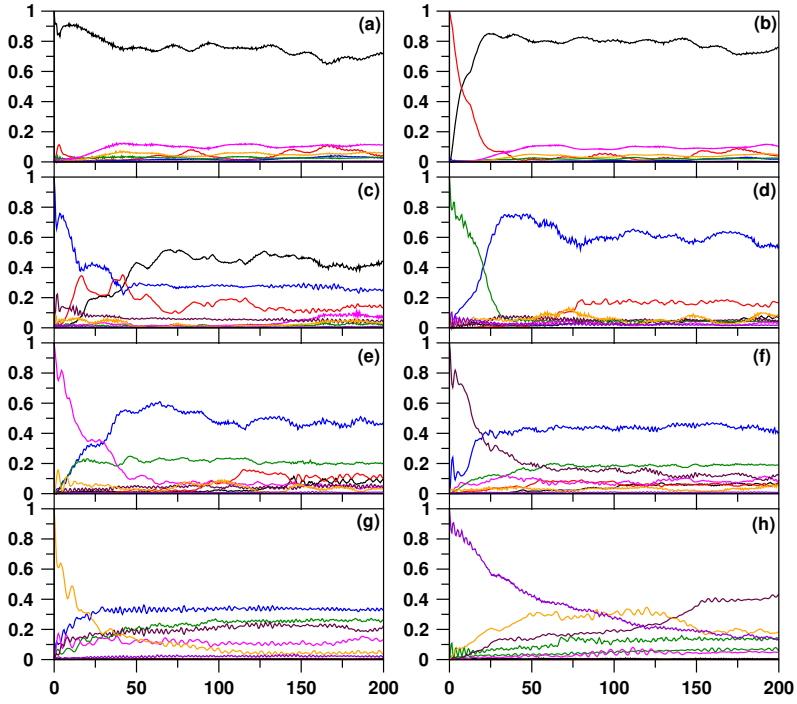

Figure 5.17: Time evolution of the diabatic electronic populations obtained in the coupled $\widetilde{X} - \widetilde{G}$ electronic states of $BN^{\cdot+}$ using full-dimensional ML-MCTDH by including same spatial symmetry coupling among the electronic states.

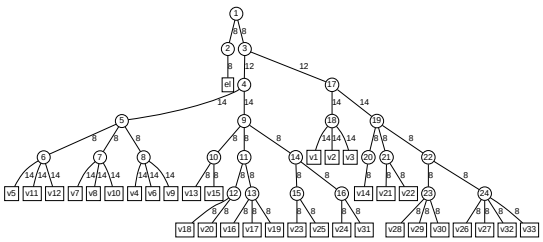

Figure 5.18: The 33D ML-MCTDH simulations of $BN^{\cdot+}$ promted to the $\widetilde{X}^2B_1$ state show the ML-tree structure (ML-MCTDH wavefunction structure). The first layer divides the discrete electronic DOF from the 33 vibrational coordinates, making six layers the maximum depth of the trees. There is also a list of SPFs. Besides the lines joining the squares are the numbers of primitive basis sets to indicate SPFs of the deepest layer.

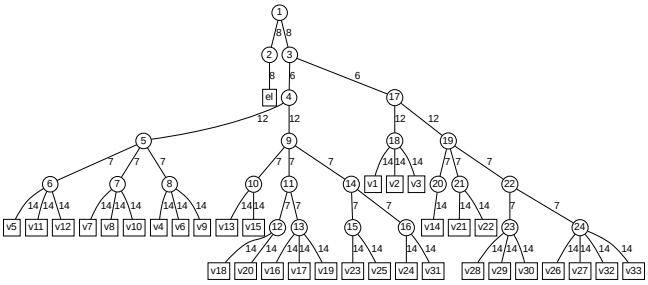

Figure 5.19: Same as the label of Fig. 5.18 promted to the $\widetilde{A}^2A_2$ state.

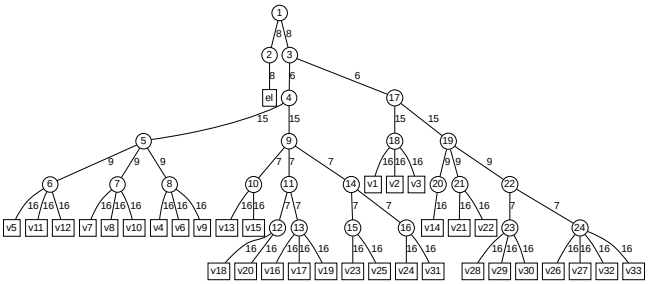

Figure 5.20: Same as the label of Fig. 5.18 promted to the $\widetilde{B}^2B_2$ state.

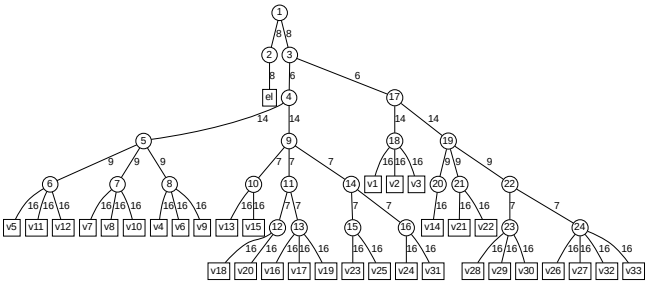

Figure 5.21: Same as the label of Fig. 5.18 promted to the $\widetilde{C}^2B_1$ state.

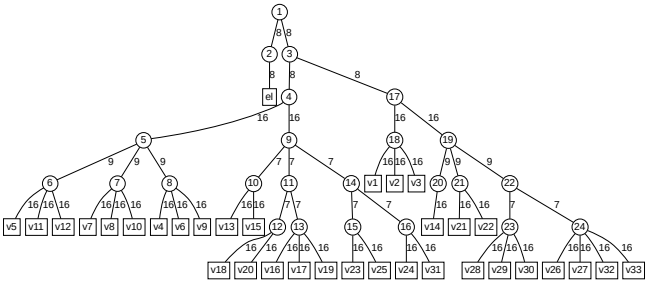

Figure 5.22: Same as the label of Fig. 5.18 promted to the $\widetilde{D}^2A_1$ state.

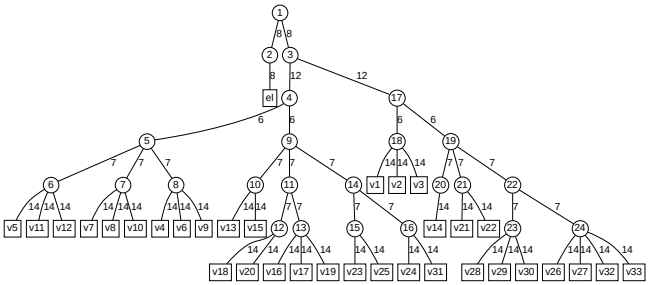

Figure 5.23: Same as the label of Fig. 5.18 promted to the $\widetilde{E}^2B_2$ state.

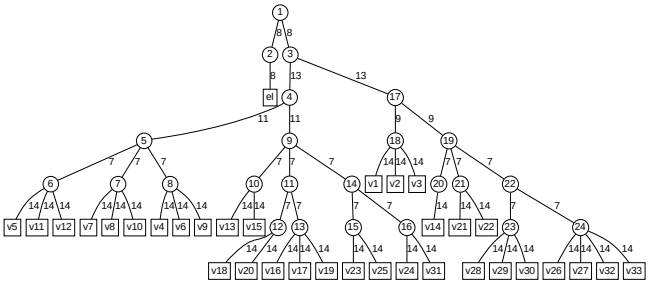

Figure 5.24: Same as the label of Fig. 5.18 promted to the $\widetilde{F}^2A_1$ state.

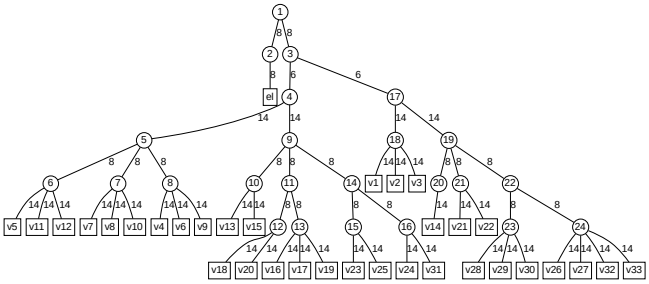

Figure 5.25: Same as the label of Fig. 5.18 promted to the $\widetilde{G}^2B_1$ state.

5.4 Summary and conclusions

The photoelectron spectrum of BN is elucidated by considering eight lowest electronic states and all the vibrational modes. Extensive electronic structure calculations are performed using *ab initio* quantum chemistry techniques. Subsequently, the PECs are constructed along all the vibrational modes. The electronic structure results are used to generate a model vibronic Hamiltonian in a diabatic electronic basis using the DNDC of the vibrational modes. The basic symmetry selection rules and standard vibronic coupling theory are used to assess the coupling between various electronic states. As the study of PECs reveals a complex structure of electronic states, we observed a distinct separation of ($\widetilde{X}^2B_1$-$\widetilde{A}^2A_2$) from the remaining ($\widetilde{B}^2B_2$-$\widetilde{G}^2B_1$) electronic states. Based on the distinctive features of the PECs and the parameters derived from the model Hamiltonian, fascinating dynamics are expected.

With the hope, we moved forward with four distinct approaches for the time-dependent nuclear dynamics calculations. The first approach involves reduced-dimensional dynamics with twenty carefully chosen vibrational modes out of 33. Similarly to reduced-dimensional, bilinear couplings are included in the second. In the full-dimensional approach, all the thirty three vibrational modes are included and in the final same spatial symmetry couplings are added to the full-dimensional set. We note that there is a strong agreement between the available experimental spectrum and the theoretical spectrum that is reproduced using these four approaches. Full-dimensional dynamics results have provided a detailed outcomes when compared with both the reduced-dimensional dynamics results. It is a difficult effort to choose vibrational modes collectively for eight electronic states in a complex system like BN. The advantage of including all the modes contributed to an improvement of full-dimensional dynamics results. As already noted, the experimental photoelectron spectra possesses broadly two bands, one with the $\widetilde{X}^2B_1$, $\widetilde{A}^2A_2$ states and the other with the remaining states $\widetilde{B}^2B_2$-$\widetilde{G}^2B_1$. However, a distinctive ordering of electronic state symmetries is given to the second band. The significant nonadiabatic coupling and energy closeness between the electronic states can be the cause of this.

Chapter 6

Summary and Outlook

The present work provides a comprehensive account of nonadiabatic coupling effects in three different molecular systems, each belonging to a different symmetry point group. By combining high-level *ab initio* electronic structure calculations, construction of diabatic vibronic Hamiltonians, and both time-independent and time-dependent nuclear dynamics simulations, the vibronic structures and electronic state dynamics of these systems were explored in detail. While the chosen species are, cyanogen (C_2N_2), carbon monohydride anions $C_{2n}H^-$ (n = 1–4), and BN which are chemically diverse, they share a unifying theme: their symmetry properties strongly influence electronic degeneracies, vibronic couplings, which pave the path to study variety of nonadiabatic effects that manifests in molecular spectroscopy and chemical dynamics.

In the first chapter, the cyanogen molecule was studied which possesses $D_{\infty h}$ symmetry point in its equilibrium geometry. This high symmetry plays a decisive role in defining the degeneracies of the low-lying electronic states, particularly the doubly degenerate $\widetilde{X}^2\Pi_g$ and $\widetilde{C}^2\Pi_u$ states. It also dictates the vibronic activity of vibrational modes, with symmetric stretching vibrations being strongly Condon active and degenerate modes coupling through the Renner-Teller effect. Theoretical vibronic band structures, compared against the experimental work of Baker et al., revealed the dominance of the C≡N stretching mode (ν_1), which formed progressions in all four states. For instance, the $\widetilde{A}^2\Sigma_g^+$ state remained dynamically isolated due to the absence of energetically accessible glancing degeneracy at the equilibrium geometry of the reference state, leads to the prediction of long-lived radiative emission. In contrast, population redistribution in the $\widetilde{B}^2\Sigma_u^+$ and $\widetilde{C}^2\Pi_u$ states demonstrated how symmetry-allowed couplings promote nonradiative transitions. Thus, the linear $D_{\infty h}$ symmetry framework both constrains and enables the observed vibronic structure and dynamics of $C_2N_2^+$.

The second chapter addressed the carbon monohydride anions $C_{2n}H^-$ (n = 1-4), belonging to the $C_{\infty v}$ symmetry point group. This axial symmetry, distinct from the inversion-symmetric $D_{\infty h}$ case

of C_2N_2, plays a pivotal role in shaping the electronic structure trends across the series. Ground state symmetries were identified as $\widetilde{X}^2\Sigma$ for n = 1 and $\widetilde{X}^2\Pi$ for n > 1, reflecting the interplay between orbital ordering and symmetry constraints. Potential energy curves were then constructed for the lowest three electronic states of the neutral species. Analysis of these curves revealed clear trends. As the chain length (n) increases, the energy gaps between different electronic states become smaller as was known from text books highlighting the fundamental particle-in-a-box model. At the same time, the Condon activity of symmetric vibrational modes also decreases. In contrast, asymmetric vibrational modes initially play a significant role through second-order Renner-Teller coupling, but their impact gradually weakens as 'n' grows. The decrease in energy gaps with increase in chainlength also increases the number of curve crossings between electronic states. These crossings, which manifest as CIs, influenced the dynamics of the system. A detailed analysis of the minima of both the electronic states and the seams of the CIs was calculated to quantify their positions and roles. Next, a diabatic Hamiltonian was constructed that included all relevant couplings. Using this, nuclear dynamics was performed with both time-independent (uncoupled states) and time-dependent (coupled states) approaches. In the uncoupled framework, the vibronic eigenvalues were obtained, producing stick spectra for each electronic state. From these results and the associated wave packet density plots, vibrational progressions, overtones, and combination bands were identified and assigned for all species. In the coupled framework, the time-dependent dynamics gave results that agree very well with the experimental observations, confirming the accuracy of the theoretical approach. Finally, the time evolution of diabatic electronic populations was analyzed in detail. This provided further insight into the role of nonadiabatic effects across the series. The results showed two clear trends: the influence of the Renner-Teller effect decreases as n increases, while the nonadiabatic effect becomes more prominent with increasing chain length. Overall, this chapter demonstrates how increasing the length of the $C_{2n}H^-$ chains systematically modifies their vibronic behavior. The observed trends, in energy gaps, vibrational activity, and the balance between RT and nonadiabatic couplings, highlight the strong connection between molecular size, symmetry, and nonadiabatic dynamics.

The third chapter focused on the BN molecule, which belongs to the lower C_{2v} symmetry point group. This reduced symmetry, compared to the linear $D_{\infty h}$ and $C_{\infty v}$ point groups of the previous systems, results in electronic states of nondegenerate symmetry labels (e.g., $\widetilde{X}^2B_1$, $\widetilde{A}^2A_2$, $\widetilde{B}^2B_2$), while still allowing strong vibronic couplings due to their close energetic proximity. The complexity of BN lies in the coexistence of eight low-lying electronic states and 33 vibrational modes, creating a dense vibronic manifold. The construction of diabatic vibronic Hamiltonian using derivative nonadiabatic couplings revealed a natural separation of the ($\widetilde{X}^2B_1$, $\widetilde{A}^2A_2$) states from the higher-lying manifold ($\widetilde{B}^2B_2$–$\widetilde{G}^2B_1$), consistent with the experimentally observed two-band photoelectron spectrum. However, the lower

C_{2v} symmetry permits numerous vibronic interactions that complicate the band structure. Nuclear dynamics calculations, performed with reduced- and full-dimensional models, demonstrated that including all 33 vibrational modes was essential to capture the subtle couplings and achieve quantitative agreement with experiment. While reduced models provided qualitative insights, the full dimensional consideration was necessary to reproduce the intricate band structure and vibrational contributions. The BN case thereby illustrates how lower symmetry molecule, combined with strong state proximity, amplifies nonadiabatic complexity.

When viewed collectively, these three case studies emphasize the role of symmetry in governing vibronic structures and dynamics. In the high-symmetry $D_{\infty h}$ system of C_2N_2, degeneracies and RT couplings define the dynamics but also restrict nonadiabatic pathways. In the axial $C_{\infty v}$ carbon monohydride chains, systematic modulation of vibronic activity with molecular size is observed, producing predictable trends in RT and nonadiabatic effects. In the lower symmetry C_{2v} BN system, the absence of high-symmetry constraints and the presence of many vibrational modes amplify coupling opportunities, demanding full dimensional treatments. Across these distinct symmetry frameworks, a common set of nonadiabatic processes, Renner-Teller splitting, and conical intersections are computed and analyzed. These insights not only resolve long-standing spectral puzzles, but also provide a predictive framework for extending vibronic coupling theory to complex systems and low-symmetry systems of astrophysical importance.

- The present work has primarily focused on light-atom molecular systems. A natural extension is to investigate linear transition-metal complexes, where the interplay of Renner-Teller distortions and spin-orbit coupling (SOC) produces complex spin-vibronic dynamics. These systems demand multi-state vibronic Hamiltonian parameterized with relativistic ab initio methods, and their study will provide insights into SOC-driven nonadiabatic mechanisms in functional materials.

- Another promising avenue is the systematic treatment of open-shell linear systems with triplet states, where spin contamination complicates the construction of diabatic Hamiltonian. Incorporating spin-Renner-Teller couplings and mixed-spin conical intersections into vibronic models will be essential for capturing the accurate dynamics. Such studies will advance our understanding of nonradiative relaxation in radicals and spin-forbidden processes of importance in photochemistry.

- With the advancement of computational methodologies, particularly the multi-layer multi-configurational time-dependent Hartree (ML-MCTDH) approach, we are now well equipped to tackle complex systems of biologically relevant size. Extending vibronic coupling theory

within this framework will enable detailed investigations of photophysics and excited-state dynamics in biomolecules, providing microscopic insights into nonadiabatic relaxation, energy transfer, and photostability mechanisms central to biology and photochemistry.

Chapter 7

Appendix

Appendix I: The Renner-Teller Hamiltonian of the degenerate Π electronic state of symmetric linear molecule

Symmetric linear molecules belong to the $D_{\infty h}$ symmetry point group which possess doubly degenerate electronic state like $\Pi, \Delta, \cdots$ etc. It is found that linear molecule[34] like $C_2N_2^+$ possesses vibrational modes of σ_g^+, σ_u^+, π_g and π_u symmetry only. Due to the lack of δ vibrational modes in linear molecules degenerate Π electronic states are **RT active** in second-order along π modes and Δ electronic states are **RT active** in fourth-order along these modes (see text for the corresponding selection rules). The symmetry selection rules read

$$\Pi_g \otimes \Pi_g \supset \delta_g + \sigma_g^+ + \sigma_g^- \tag{A1}$$

$$\Pi_u \otimes \Pi_u \supset \delta_g + \sigma_g^+ + \sigma_g^- \tag{A2}$$

The electronic Hamiltonian for the doubly degenerate Π electronic state can be derived as follows. Let φ_x and φ_y be the two components of the Π state. In polar coordinate (ρ, φ) the two components of Π state can be written as

$$|\varphi_x > \;=\; \rho\, cos\varphi \tag{A3}$$

$$|\varphi_y > \;=\; \rho\, sin\varphi\ . \tag{A4}$$

In complex coordinates the components of the Π state can be written as

$$|\varphi_+> \;=\; \varphi_x + i\varphi_y = \rho\, e^{i\varphi} \tag{A5}$$

$$|\varphi_-> \;=\; \varphi_x - i\varphi_y = \rho\, e^{-i\varphi}\ . \tag{A6}$$

The degenerate π_g or π_u vibrational mode lifts the electronic degeneracy of the Π state. Let Q_x and Q_y be the two components of a π_g (or π_u) vibrational mode. In polar coordinate one can write

$$Q_x \;=\; \rho\, cos\varphi \tag{A7}$$

$$Q_y \;=\; \rho\, sin\varphi\ . \tag{A8}$$

Analogous to the state representation, Q_x and Q_y (in complex coordinates) can be written as

$$Q_+ \;=\; Q_x + iQ_y = \rho\, e^{i\varphi} \tag{A9}$$

$$Q_- \;=\; Q_x - iQ_y = \rho\, e^{-i\varphi}\ . \tag{A10}$$

The rotation operations on the above functions reads

$$C_\varphi|\varphi_+> \;=\; e^{i\varphi}|\varphi_+> \tag{A11}$$

$$C_\varphi|\varphi_-> \;=\; e^{-i\varphi}|\varphi_->\,, \tag{A12}$$

and

$$C_\varphi\, Q_+ \;=\; e^{i\varphi}Q_+ \tag{A13}$$

$$C_\varphi\, Q_- \;=\; e^{-i\varphi}Q_-\ . \tag{A14}$$

Now the 2× 2 diabatic electronic Hamiltonian for the Π electronic state can be written as

$$H_{el} = \begin{bmatrix} S_{11} & S_{12} \\ S_{12}^* & S_{22} \end{bmatrix}\ . \tag{A15}$$

In the above matrix Hamiltonian 1 and 2 are the 'x' and 'y' components of degenerate Π electronic

state. The elements of this matrix Hamiltonian can be expanded in a Taylor series. In this article, the Hamiltonian of the doubly degenerate Π electronic state is expanded up to sixth-order as follows

$$\begin{aligned} H_{el} \quad &= W^{(0)} + W^{(1)}_{+}Q_{+} + W^{(1)}_{-}Q_{-} + W^{(2)}_{++}Q^{2}_{+} + W^{(2)}_{--}Q^{2}_{-} + W^{(2)}_{+-}Q_{+}Q_{-} + W^{(2)}_{-+}Q_{+}Q_{-} \\ &+W^{(3)}_{++}Q^{3}_{+} + W^{(3)}_{--}Q^{3}_{-} + W^{(3)}_{+-}Q^{2}_{+}Q^{1}_{-} + W^{(3)}_{-+}Q^{1}_{+}Q^{2}_{-} + W^{(4)}_{++}Q^{4}_{+} + W^{(4}_{--}Q^{4}_{-} \\ &+W^{(4)}_{+-}Q^{3}_{+}Q^{1}_{-} + W^{(4)}_{-+}Q^{1}_{+}Q^{3}_{-} + W^{(4)}_{+-}Q^{2}_{+}Q^{2}_{-} + W^{(4)}_{-+}Q^{2}_{+}Q^{2}_{-} + W^{(5)}_{++}Q^{5}_{+} + W^{(5}_{--}Q^{5}_{-} \\ &+W^{(5)}_{+-}Q^{4}_{+}Q^{1}_{-} + W^{(5)}_{-+}Q^{1}_{+}Q^{4}_{-} + W^{(5)}_{-+}Q^{3}_{+}Q^{2}_{-} + W^{(5)}_{-+}Q^{2}_{+}Q^{3}_{-} + W^{(6)}_{++}Q^{6}_{+} + W^{(6}_{--}Q^{6}_{-} \\ &+W^{(6)}_{+-}Q^{5}_{+}Q^{1}_{-} + W^{(6)}_{-+}Q^{1}_{+}Q^{5}_{-} + W^{(6)}_{-+}Q^{4}_{+}Q^{2}_{-} + W^{(6)}_{-+}Q^{2}_{+}Q^{4}_{-} + W^{(3)}_{+-}Q^{3}_{+}Q^{3}_{-} + W^{(3)}_{-+}Q^{3}_{+}Q^{3}_{-} \ . \end{aligned} \tag{A16}$$

The operation of C_{φ} on the above Hamiltonian reads

$$\begin{aligned} H_{el} \quad &= \quad W^{(0)} + W^{(1)}_{+}e^{i\varphi}Q_{+} + W^{(1)}_{-}e^{-i\varphi}Q_{-} + W^{(2)}_{++}e^{2i\varphi}Q^{2}_{+} + W^{(2)}_{--}e^{-2i\varphi}Q^{2}_{-} \\ &+ \quad W^{(2)}_{+-}e^{i\varphi}e^{-i\varphi}Q_{+}Q_{-} + W^{(2)}_{-+}e^{-i\varphi}e^{i\varphi}Q_{-}Q_{+} + W^{(3)}_{++}e^{3i\varphi}Q^{3}_{+} + W^{(3)}_{--}e^{-3i\varphi}Q^{3}_{-} \\ &+ \quad W^{(3)}_{+-}e^{2i\varphi}e^{-i\varphi}Q^{2}_{+}Q^{1}_{-} + W^{(3)}_{-+}e^{i\varphi}e^{-2i\varphi}Q^{1}_{+}Q^{2}_{-} + W^{(4)}_{++}e^{4i\varphi}Q^{4}_{+} + W^{(4}_{--}e^{-4i\varphi}Q^{4}_{-} \\ &+ \quad W^{(4)}_{+-}e^{3i\varphi}e^{-i\varphi}Q^{3}_{+}Q^{1}_{-} + W^{(4)}_{-+}e^{i\varphi}e^{-3i\varphi}Q^{1}_{+}Q^{3}_{-} + W^{(4)}_{+-}e^{2i\varphi}e^{-2i\varphi}Q^{2}_{+}Q^{2}_{-} + W^{(4)}_{-+}e^{-2i\varphi}e^{2i\varphi}Q^{2}_{+}Q^{2}_{-} \\ &+ \quad W^{(5)}_{++}e^{5i\varphi}Q^{5}_{+}W^{(5}_{--}e^{-5i\varphi}Q^{5}_{-} + W^{(5)}_{+-}e^{4i\varphi}e^{-i\varphi}Q^{4}_{+}Q^{1}_{-} + W^{(5)}_{-+}e^{i\varphi}e^{-4i\varphi}Q^{1}_{+}Q^{4}_{-} + W^{(5)}_{-+}e^{3i\varphi}e^{-2i\varphi}Q^{3}_{+}Q^{2}_{-} \\ &+ \quad W^{(5)}_{-+}e^{2i\varphi}e^{-3i\varphi}Q^{2}_{+}Q^{3}_{-} + W^{(6)}_{++}e^{6i\varphi}Q^{6}_{+} + W^{(6}_{--}e^{-6i\varphi}Q^{6}_{-} + W^{(6)}_{+-}e^{5i\varphi}e^{-i\varphi}Q^{5}_{+}Q^{1}_{-} \\ &+ \quad W^{(6)}_{-+}e^{i\varphi}e^{-5i\varphi}Q^{1}_{+}Q^{5}_{-} + W^{(6)}_{-+}e^{4i\varphi}e^{-2i\varphi}Q^{4}_{+}Q^{2}_{-} + W^{(6)}_{-+}e^{2i\varphi}e^{-4i\varphi}Q^{2}_{+}Q^{4}_{-} \\ &+ \quad W^{(3)}_{+-}e^{3i\varphi}e^{-3i\varphi}Q^{3}_{+}Q^{3}_{-} + W^{(3)}_{-+}e^{-3i\varphi}e^{3i\varphi}Q^{3}_{+}Q^{3}_{-} \ . \end{aligned} \tag{A17}$$

Upon simplification it assumes the form

$$\begin{aligned}
H_{el} &= W^{(0)} + W^{(1)}_{+} e^{i\varphi} Q_{+} + W^{(1)}_{-} e^{-i\varphi} Q_{-} + W^{(2)}_{++} e^{2i\varphi} Q^{2}_{+} + W^{(2)}_{--} e^{-2i\varphi} Q^{2}_{-} \\
&+ W^{(2)}_{+-} Q_{+} Q_{-} + W^{(2)}_{-+} Q_{-} Q_{+} + W^{(3)}_{++} e^{3i\varphi} Q^{3}_{+} + W^{(3)}_{--} e^{-3i\varphi} Q^{3}_{-} \\
&+ W^{(3)}_{+-} e^{i\varphi} Q^{2}_{+} Q^{1}_{-} + W^{(3)}_{-+} e^{-i\varphi} Q^{1}_{+} Q^{2}_{-} + W^{(4)}_{++} e^{4i\varphi} Q^{4}_{+} + W^{(4}_{--} e^{-4i\varphi} Q^{4}_{-} \\
&+ W^{(4)}_{+-} e^{2i\varphi} Q^{3}_{+} Q^{1}_{-} + W^{(4)}_{-+} e^{-2i\varphi} Q^{1}_{+} Q^{3}_{-} + W^{(4)}_{+-} Q^{2}_{+} Q^{2}_{-} + W^{(4)}_{-+} Q^{2}_{+} Q^{2}_{-} \\
&+ W^{(5)}_{++} e^{5i\varphi} Q^{5}_{+} + W^{(5)}_{--} e^{-5i\varphi} Q^{5}_{-} + W^{(5)}_{+-} e^{3i\varphi} Q^{4}_{+} Q^{1}_{-} + W^{(5)}_{-+} e^{-3i\varphi} Q^{1}_{+} Q^{4}_{-} + W^{(5)}_{-+} e^{i\varphi} Q^{3}_{+} Q^{2}_{-} \\
&+ W^{(5)}_{-+} e^{-i\varphi} Q^{2}_{+} Q^{3}_{-} + W^{(6)}_{++} e^{6i\varphi} Q^{6}_{+} + W^{(6}_{--} e^{-6i\varphi} Q^{6}_{-} + W^{(6)}_{+-} e^{4i\varphi} Q^{5}_{+} Q^{1}_{-} \\
&+ W^{(6)}_{-+} e^{-4i\varphi} Q^{1}_{+} Q^{5}_{-} + W^{(6)}_{-+} e^{2i\varphi} Q^{4}_{+} Q^{2}_{-} + W^{(6)}_{-+} e^{-2i\varphi} Q^{2}_{+} Q^{4}_{-} \\
&+ W^{(3)}_{+-} Q^{3}_{+} Q^{3}_{-} + W^{(3)}_{-+} Q^{3}_{+} Q^{3}_{-} \; . \qquad \text{(A18)}
\end{aligned}$$

Now the elements of the matrix Hamiltonian [Eq. (A15)] reads

$$\begin{aligned}
S_{11} = < \varphi_{+} | H_{el} | \varphi_{+} > = & \quad < e^{i\varphi} \varphi_{+} | H_{el} | e^{i\varphi} \varphi_{+} > \qquad \text{(A19)} \\
= & \quad < \varphi_{+} | H_{el} | \varphi_{+} > , \qquad \text{(A20)}
\end{aligned}$$

and

$$S_{22} = < \varphi_{-} | H_{el} | \varphi_{-} > \; . \qquad \text{(A21)}$$

These elements required to be symmetry invariant. Therefore the terms of Eq. (A18) which do not contain any $e^{\pm i\varphi}$ factor are collected. This consideration yields

$$\begin{aligned}
S_{11} &= < \varphi_{+} | H_{el} | \varphi_{+} > = W^{(0)} + W^{(2)}_{+-} Q_{+} Q_{-} + W^{(2)}_{-+} Q_{-} Q_{+} + W^{(4)}_{+-} Q^{2}_{+} Q^{2}_{-} + W^{(4)}_{-+} Q^{2}_{-} Q^{2}_{+} \\
&+ W^{(6)}_{+-} Q^{3}_{+} Q^{3}_{-} + W^{(6)}_{-+} Q^{3}_{-} Q^{3}_{+} \; , \qquad \text{(A22)} \\
S_{22} &= < \varphi_{-} | H_{el} | \varphi_{-} > = W^{(0)} + W^{(2)}_{+-} Q_{+} Q_{-} + W^{(2)}_{-+} Q_{-} Q_{+} + W^{(4)}_{+-} Q^{2}_{+} Q^{2}_{-} + W^{(4)}_{-+} Q^{2}_{-} Q^{2}_{+} \\
&+ W^{(6)}_{+-} Q^{3}_{+} Q^{3}_{-} + W^{(6)}_{-+} Q^{3}_{-} Q^{3}_{+} \; . \qquad \text{(A23)}
\end{aligned}$$

It can be seen that, $S_{11} = S_{22}$, now

$$\begin{aligned}
S_{12} = < \varphi_{+} | H_{el} | \varphi_{-} > = & \quad < e^{i\varphi} \varphi_{+} | H_{el} | e^{-i\varphi} \varphi_{-} > \qquad \text{(A24)} \\
= & \quad e^{-2i\varphi} < \varphi_{+} | H_{el} | \varphi_{-} > \; . \qquad \text{(A25)}
\end{aligned}$$

Therefore the terms which contain $e^{-2i\varphi}$ coefficient would correspond to the symmetry invariant

expression of S_{12}. Collecting those terms from Eq. (A18) gives rise to

$$S_{12} =< \varphi_+|H_{el}|\varphi_- >= W^{(2)}_{--}Q_-Q_- + W^{(4)}_{+-}Q^1_+Q^3_- + W^{(6)}_{+-}Q^2_+Q^4_- \tag{A26}$$

Now a unitary transformation is carried out to bring the Hamiltonian back to the real representation. Defining such a unitary matrix as

$$U = \frac{1}{\sqrt{2}}\begin{bmatrix} 1 & -i \\ 1 & i \end{bmatrix} . \tag{A27}$$

It can be seen that $U^{-1} = U^\dagger$; $UU^\dagger = \mathbf{1}$ and $U^\dagger = (U^*)^T$.

Now,

$$H_{real} = U^\dagger H_{el} U . \tag{A28}$$

Using Eq. (A15) and the U matrix the following expression follows

$$H_{real} = \frac{1}{2}\begin{bmatrix} S_{11} + S_{22} + (S_{12} + S^*_{12}) & -iS_{11} + iS_{22} - i(S^*_{12} - S_{12}) \\ iS_{11} - iS_{22} - i(S^*_{12} - S_{12}) & S_{11} + S_{22} - (S_{12} + S^*_{12}) \end{bmatrix} . \tag{A29}$$

Using Eqs. A9, A10 and A22 one can write

$$\begin{aligned} S_{11} = \quad & W^{(0)} + W^{(2)}_{+-}Q_+Q_- + W^{(2)}_{-+}Q_-Q_+ + W^{(4)}_{+-}Q^2_+Q^2_- + W^{(4)}_{-+}Q^2_-Q^2_+ \\ & + W^{(6)}_{+-}Q^3_+Q^3_- + W^{(6)}_{-+}Q^3_-Q^3_+ && \text{(A30a)} \\ = \quad & W^{(0)} + W^{(2)}_{+-}(Q_x + Q_{iy})(Q_x - Q_{iy}) + W^{(2)}_{-+}(Q_x - Q_{iy})(Q_x + Q_{iy}) \\ & + W^{(4)}_{+-}(Q_x + Q_{iy})^2(Q_x - Q_{iy})^2 + + W^{(4)}_{-+}(Q_x - Q_{iy})^2(Q_x + Q_{iy})^2 \\ & + W^{(6)}_{+-}(Q_x + Q_{iy})^3(Q_x - Q_{iy})^3 + W^{(6)}_{-+}(Q_x - Q_{iy})^3(Q_x + Q_{iy})^3 && \text{(A30b)} \\ = \quad & W^{(0)} + (W^{(2)}_{+-} + W^{(2)}_{-+})(Q^2_x + Q^2_y) + (W^{(4)}_{+-} + W^{(4)}_{-+})(Q^2_x + Q^2_y)^2 \\ & + (W^{(6)}_{+-} + W^{(6)}_{-+})(Q^2_x + Q^2_y)^3 . && \text{(A30c)} \end{aligned}$$

Similarly using Eqs. A9, A10 and A23 one obtains

$$\begin{aligned} S_{22} &= W^{(0)} + (W^{(2)}_{+-} + W^{(2)}_{-+})(Q_x^2 + Q_y^2) + (W^{(4)}_{+-} + W^{(4)}_{-+})(Q_x^2 + Q_y^2)^2 \\ &\quad + (W^{(6)}_{+-} + W^{(6)}_{-+})(Q_x^2 + Q_y^2)^3 \ . \end{aligned} \tag{A31}$$

Eqs. A9, A10 and A26 yields

$$\begin{aligned} S_{12} = &\quad W^{(2)}_{--} Q_- Q_- + W^{(4)}_{+-} Q_+^1 Q_-^3 + W^{(6)}_{+-} Q_+^2 Q_-^4 \\ = &\quad W^{(2)}_{--} (Q_x - iQ_y)^2 + W^{(4)}_{+-} (Q_x + iQ_y)^1 (Q_x - iQ_y)^3 + W^{(6)}_{+-} (Q_x + iQ_y)^2 (Q_x - iQ_y)^4 \\ = &\quad W^{(2)}_{--} (Q_x^2 + 2iQ_xQ_y - Q_y^2) + W^{(4)}_{+-} (Q_x^4 - 2iQ_xQ_y^3 - 2iQ_x^3Q_y - Q_y^4) \\ &\quad + W^{(6)}_{+-} (Q_x^6 - Q_x^2Q_y^4 + Q_x^4Q_y^2 - Q_y^6 - 2iQ_x^5Q_y^1 - 2iQ_x^1Q_y^5 - 4iQ_x^3Q_y^3) \ , \end{aligned} \tag{A32}$$

and

$$\begin{aligned} S_{12}^* = W^{(2)}_{--} (Q_x^2 - 2iQ_xQ_y - Q_y^2) + W^{(4)}_{+-} (Q_x^4 + 2iQ_xQ_y^3 + 2iQ_x^3Q_y - Q_y^4) \\ + W^{(6)}_{+-} (Q_x^6 - Q_x^2Q_y^4 + Q_x^4Q_y^2 - Q_y^6 + 2iQ_x^5Q_y^1 + 2iQ_x^1Q_y^5 + 4iQ_x^3Q_y^3) \ . \end{aligned} \tag{A33}$$

Now

$$(S_{12} + S_{12}^*) = 2W^{(2)}_{--} [Q_x^2 - Q_y^2] + 2W^{(4)}_{+-} [Q_x^4 - Q_y^4] + 2W^{(6)}_{+-} [Q_x^6 - Q_y^6 - Q_x^2Q_y^4 + Q_x^4Q_y^2] \ . \tag{A34}$$

and

$$-i(S_{12}^* - S_{12}) = 4W^{(2)}_{--} Q_xQ_y + 4W^4_{+-} (Q_x^1Q_y^3 + Q_x^3Q_y^1) + 4W^6_{+-} (Q_x^5Q_y^1 + Q_x^1Q_y^5 + 2Q_x^3Q_y^3) \ . \tag{A35}$$

Now the final elements of the matrix Hamiltonian are given by

$$
\begin{aligned}
(H_{11}) = \quad & \frac{1}{2}[S_{11}+S_{22}+S_{12}+S_{12}^{*}]\,, \\
= \quad & \frac{1}{2}[2(W^{(0)}+(W_{+-}^{(2)}+W_{-+}^{2})(Q_x^2+Q_y^2)+W_{--}^{(2)}(Q_x^2-Q_y^2)+(W_{+-}^{(4)}+W_{-+}^{4})(Q_x^2+Q_y^2)^2+ \\
& W_{+-}^{(4)}(Q_x^4-Q_y^4)+(W_{+-}^{(6)}+W_{-+}^{6})(Q_x^2+Q_y^2)^3+W_{+-}^{(6)}(Q_x^6-Q_y^6-Q_x^2Q_y^4+Q_x^4Q_y^2)\,, \\
= \quad & W^{(0)}+(W_{+-}^{(2)}+W_{-+}^{2})(Q_x^2+Q_y^2)+W_{--}^{(2)}(Q_x^2-Q_y^2)+(W_{+-}^{(4)}+W_{-+}^{4})(Q_x^2+Q_y^2)^2+ \\
& W_{+-}^{(4)}(Q_x^4-Q_y^4)+(W_{+-}^{(6)}+W_{-+}^{6})(Q_x^2+Q_y^2)^3+W_{+-}^{(6)}(Q_x^6-Q_y^6-Q_x^2Q_y^4+Q_x^4Q_y^2)\,. \qquad \text{(A36)} \\
(H_{22}) = \quad & \frac{1}{2}[S_{11}+S_{22}-(S_{12}+S_{12}^{*})]\,, \\
= \quad & W^{(0)}+(W_{+-}^{(2)}+W_{-+}^{2})(Q_x^2+Q_y^2)-W_{--}^{(2)}(Q_x^2-Q_y^2)+(W_{+-}^{(4)}+W_{-+}^{4})(Q_x^2+Q_y^2)^2- \\
& W_{+-}^{(4)}(Q_x^4-Q_y^4)+(W_{+-}^{(6)}+W_{-+}^{6})(Q_x^2+Q_y^2)^3-W_{+-}^{(6)}(Q_x^6-Q_y^6-Q_x^2Q_y^4+Q_x^4Q_y^2)\,. \qquad \text{(A37)} \\
(H_{12}) = \quad & \frac{1}{2}(-iS_{11}+iS_{22}-iS_{12}^{*}+iS_{12})\,, \\
= \quad & 2W^{(2)}(Q_xQ_y)+2W^{4}(Q_x^1Q_y^3+Q_x^3Q_y^1)+2W^{6}(Q_x^5Q_y^1+Q_x^1Q_y^5+2Q_x^3Q_y^3)\,. \qquad \text{(A38)}
\end{aligned}
$$

The coefficients appearing in the above equations have the following definition as appeared in the text [Eqs. (6-10)]

$$
\begin{aligned}
& W^{(0)} = E_{\Pi}\,, \\
& (W_{+-}^{(2)}+W_{-+}^{(2)}) = \gamma^{(2)}\,, \\
& W_{--}^{(2)} = \eta^{(2)}\,, \\
& (W_{+-}^{(4)}+W_{-+}^{(4)}) = \xi^{(4)}\,, \\
& W_{+-}^{(4)} = \delta^{(4)}\,, \\
& (W_{+-}^{(6)}+W_{-+}^{(6)}) = \sigma^{(6)}\,, \\
& W_{+-}^{(6)} = \rho^{(6)}\,,
\end{aligned}
$$

Inserting them in Eqs. A36, A37, A38 the RT Hamiltonian for the Π state as written in the text is obtained

$$
\begin{aligned}
(H_{real})_{11} = \quad & E_{\Pi}+\gamma^{(2)}(Q_x^2+Q_y^2)+\eta^{(2)}(Q_x^2-Q_y^2)^2+\xi^{(4)}(Q_x^2+Q_y^2)^2+\delta^{(4)} \\
& (Q_x^4-Q_y^4)+\sigma^{(6)}(Q_x^2+Q_y^2)^3+\rho^{(6)}(Q_x^6-Q_y^6-Q_x^2Q_y^4+Q_x^4Q_y^2) \qquad \text{(A39)} \\
(H_{real})_{22} = \quad & E_{\Pi}+\gamma^{(2)}(Q_x^2+Q_y^2)-\eta^{2}(Q_x^2-Q_y^2)^2+\xi^{(4)}(Q_x^2+Q_y^2)^2-\delta^{(4)} \\
& (Q_x^4-Q_y^4)+\sigma^{(6)}(Q_x^2+Q_y^2)^3-\rho^{(6)}(Q_x^6-Q_y^6-Q_x^2Q_y^4+Q_x^4Q_y^2) \qquad \text{(A40)} \\
(H_{real})_{12} = \quad & 2\eta^{(2)}Q_xQ_y+2\delta^{4}(Q_x^1Q_y^3+Q_x^3Q_y^1)+2\rho^{6}(Q_x^5Q_y^1+Q_x^1Q_y^5+2Q_x^3Q_y^3)\,. \qquad \text{(A41)}
\end{aligned}
$$

Appendix II: Irreducible representation of linear chains of $C_{\infty v}$ point group symmetry with N carbon and hydrogen atoms

The carbon chains $C_{2n}H^{-}$ ($n = 1 - 4$) examined in this study have equilibrium geometry of $C_{\infty v}$ point group symmetry. In terms of correlation, the highest Abelian point group with $C_{\infty v}$ is C_{2v}. The correlation table between vibrational modes and electronic states is shown below. The molecule has been proposed to be on the Y-Z plane, with the X-axis perpendicular to the molecular plane, as shown in Fig. 4.1 and 4.2.

The orthogonality theorem is used to develop a generic equation for the symmetry representation of a linear molecule with N atoms that belongs to the $C_{\infty v}$ equilibrium symmetry point group whose highest abelian point group is C_{2v}.

The derivation for n odd number of atoms (where, n = 3,5,...9).

C_{2v}	E	$C_2(z)$	$\sigma(xz)$	$\sigma(yz)$
Γ_{red}	3n	-n	n	n

Now the components of C_{2v} point group reduces to :

$$\eta_{A_1} = \frac{1}{4}[3n - n + n + n] = \frac{1}{4}[4n] = n \tag{A42}$$

$$\eta_{A_2} = \frac{1}{4}[3n - n - n - n] = 0 \tag{A43}$$

$$\eta_{B_1} = \frac{1}{4}[3n + n + n - n] = \frac{1}{4}[4n] = n \tag{A44}$$

$$\eta_{B_2} = \frac{1}{4}[3n + n - n + n] = \frac{1}{4}[4n] = n \tag{A45}$$

$$\tag{A46}$$

Now,

$$\Gamma_{total} = nA_1 + nB_1 + nB_2 \tag{A47}$$

$$= nA1 + n(B1 + B2) \tag{A48}$$

$$= n\sigma^{+} + n\pi \tag{A49}$$

$$\Gamma_{rotational} = 1A_2 + 1B_1 + 1B_2 \tag{A50}$$

$$= 0 + 1\pi \tag{A51}$$

Since, C_n is linear, rotation along z-axis, R_z should be ignored. So, A_2 vanishes from here.

$$\Gamma_{translational} = \quad 1A_1 + 1B_1 + 1B_2 \tag{A52}$$

$$= \quad 1\sigma^+ + 1\pi \tag{A53}$$

Now,

$$\Gamma_{vibrational} = \quad \Gamma_{total} - \Gamma_{rotational} - \Gamma_{translational} \tag{A54}$$

$$= \quad nA_1 + n(B_1 + B_2) - (B_1 + B_2) - A_1 - (B_1 + B_2) \tag{A55}$$

$$= \quad (n-1)\sigma^+ + (n-2)\pi \tag{A56}$$

It demonstrates that there are no δ vibrational modes in linear odd-numbered molecules. Because of this, its degenerate electronic states (Π) have degenerate π vibrational modes, which make them second-order Renner-Teller (RT) active.

Correlation table (from Herzberg's book) :

$C_{\infty v}$	C_{2v}	vib mode
Σ^+	A_1	σ^+
Σ^-	A_2	σ^-
Π	B_1+B_2	π

Bibliography

[1] C. Baker, David Warren Turner, and William Charles Price. High resolution molecular photoelectron spectroscopy. iii. acetylenes and aza-acetylenes. *Proc. Roy. Soc.*, 308(1492):19–37, 1968.

[2] T. R. Taylor, C. Xu, and D.M. Neumark. *J. Chem. Phys.*, 108:10018, 1998.

[3] R. Griebel, G. Hohlneicher, and F. Dorr. *J. Elec. Spec. Rel. Phen*, 4:185, 1974.

[4] Carol E. Wayne and Richard P. Wayne. *Photochemistry*. Oxford University Press, 08 2023.

[5] David L. Nelson and Michael M. Cox. *Lehninger Principles of Biochemistry*. W. H. Freeman and Company, New York, 7th edition, 2017.

[6] Nabil A. Shaath. Ultraviolet filters. *Photochemical & Photobiological Sciences*, 9(4):464–469, 2010.

[7] Michael Grätzel. *Photoelectrochemical Cells*. CRC Press, 2006.

[8] Chester F. Carlson. Electrophotography. *Journal of the Franklin Institute*, 230(4):457–464, 1940.

[9] M. Born and R. Oppenheimer. Zur quantentheorie der molekeln. *Annalen der Physik*, 389(20):457–484, 1927.

[10] C. J. Ballhausen and A. E. Hansen. The jahn–teller effect in chemistry. *Annual Review of Physical Chemistry*, 23:15–34, 1972.

[11] H. Köppel, W. Domcke, and L. S. Cederbaum. Multimode molecular dynamics beyond the born-oppenheimer approximation. *Adv. Chem. Phys.*, 57:59–246, Jan 1984.

[12] G. Fischer. *Vibronic Coupling: The Interaction Between the Electronic and Nuclear Motions*. Academic Press, London, 1984.

[13] Monika Musiał, Stanisław A. Kucharski, and Rodney J. Bartlett. Equation-of-motion coupled cluster method with full inclusion of the connected triple excitations for ionized states: Ip-eom-ccsdt. *J. Chem. Phys.*, 118(3):1128–1136, 2003.

[14] Yannick J. Bomble, Jamal C. Saeh, John F. Stanton, Péter G. Szalay, Mihály Kállay, and Jürgen Gauss. Equation-of-motion coupled-cluster methods for ionized states with an approximate treatment of triple excitations. *J. Chem. Phys.*, 122(15):154107, 2005.

[15] Hajime Nakano. *J. Chem. Phys.*, 99(10):7983–7992, 1993.

[16] Hajime Nakano. *Chem. Phys. Lett.*, 207(4-5):372–378, 1993.

[17] K. Levenberg. *Q. Appl. Math.*, 2:164, 1944.

[18] R. Renner. *Zeitschrift für Physik*, 92:172, 1934.

[19] E. Teller. *Journal of Physical Chemistry*, 41:109, 1937.

[20] H. A. Jahn and E. Teller. *Proceedings of the Royal Society of London. Series A, Mathematical and Physical Sciences*, 161:220, 1937.

[21] Wolfgang Domcke and David R. Yarkony. Role of conical intersections in molecular spectroscopy and photoinduced chemical dynamics. *Annual Review of Physical Chemistry*, 63:325–352, 2012.

[22] Hermann Köppel and Wolfgang Domcke. In Paul von Ragué Schleyer, editor, *Encyclopedia of Computational Chemistry*, page 3166. Wiley, New York, 1998.

[23] Jane K. Cullum and Ralph A. Willoughby. *Lanczos Algorithms for Large Symmetric Eigenvalue Computations: Volume 1, Theory*, volume 3 of *Progress in Scientific Computing*. Birkhäuser, Boston, MA, 1985.

[24] J. von Neumann and E. P. Wigner. Über das verhalten von eigenwerten bei adiabatischen prozessen. *Physikalische Zeitschrift*, 30:467–470, 1929.

[25] H. Köppel, L. S. Cederbaum, W. Domcke, and S. S. Shaik. Multimode molecular dynamics beyond the born-oppenheimer approximation. *Angewandte Chemie International Edition in English*, 22(3):210–211, 1983.

[26] W. Domcke, D. R. Yarkony, and H. Köppel, editors. *Conical Intersections: Electronic Structure, Dynamics and Spectroscopy*. World Scientific, Singapore, 2004.

[27] H. A. Jahn. The problem of degeneracy in quantum mechanics. *Proceedings of the Royal Society of London. Series A, Mathematical and Physical Sciences*, 164:117–138, 1938.

[28] I. B. Bersuker. *The Jahn-Teller Effect*. Cambridge University Press, Cambridge, 2006.

[29] H. Köppel, L. S. Cederbaum, and S. Mahapatra. Theory of the jahn-teller effect. In M. Quack and F. Merkt, editors, *Handbook of High-Resolution Spectroscopy*, volume 2, pages 1395–1441. John Wiley & Sons, 2011.

[30] S. Mahapatra. Multidimensional nonadiabatic dynamics: A non-born–oppenheimer perspective of photochemistry. *Accounts of Chemical Research*, 42(8):1004–1015, 2009.

[31] I. B. Bersuker and V. Z. Polinger. *Vibronic Interactions in Molecules and Crystals*. Springer-Verlag, Berlin, 1989.

[32] H. L. Dai and R. W. Field. *Molecular Dynamics and Spectroscopy by Stimulated Emission Pumping*. World Scientific, Singapore, 1995.

[33] P. Rosmus and G. Chambaud. The renner–teller effect and the role of electronically degenerate states in molecular ions. In C. Y. Ng, editor, *Photoionization and Photodetachment*, volume 10A, chapter 5, pages 292–361. World Scientific, Singapore, 2000.

[34] H. Köppel, W. Domcke, and L. S. Cederbaum. Theory of vibronic coupling in linear molecules. *J. Chem. Phys.*, 74(5):2945–2968, 1981.

[35] M.H. Beck, A. Jäckle, G.A. Worth, and H.-D. Meyer. The multiconfiguration time-dependent hartree (mctdh) method: a highly efficient algorithm for propagating wavepackets. *Phys. Rep.*, 324(1):1–105, 2000.

[36] Haobin Wang and Michael Thoss. *J. Chem. Phys.*, 119(3):1289, 2003.

[37] Haobin Wang, David E. Skinner, and Michael Thoss. *J. Chem. Phys.*, 125(17):174502, 2006.

[38] Haobin Wang and Michael Thoss. *J. Phys. Chem. A.*, 111(41):10369, 2007.

[39] Haobin Wang. *J. Phys. Chem. A.*, 119(29):7951, 2015.

[40] B. H. Lengsfield and D. R. Yarkony. Nonadiabatic interactions between potential energy surfaces: Theory and applications. *Advances in Chemical Physics*, 82:1–71, 1992.

[41] M. Born and K. Huang. *Dynamical Theory of Crystal Lattices*. Oxford University Press, New York, 1954.

[42] W. Pauli Jr. Über die gesetzmäßigkeiten des anomalen zeemaneffektes. *Annalen der Physik*, 373:177–240, 1922.

[43] P. Güttinger. Das verhalten von atomen im magnetischen drehfeld. *Zeitschrift für Physik*, 73:169–184, 1932.

[44] H. Hellmann. Zur rolle der kinetischen elektronenenergie für die zwischenatomaren kräfte. *Zeitschrift für Physik*, 85:180–190, 1933.

[45] R. P. Feynman. Forces in molecules. *Physical Review*, 56:340–343, 1939.

[46] R. Englman. *The Jahn-Teller Effect in Molecules and Crystals*. Wiley-Interscience, New York, 1972.

[47] W. Lichten. Avoided level crossings in diatomic molecules. *Physical Review*, 164:131–142, 1967.

[48] F. T. Smith. Diabolical degeneracy. *Physical Review*, 179:111–123, 1969.

[49] T. F. O'Malley. Theory of electronic interactions in molecular collisions. In D. R. Bates and I. Estermann, editors, *Advances in Atomic and Molecular Physics*, volume 7, pages 223–274. Academic Press, 1971.

[50] W. Domcke and G. Stock. Theory of ultrafast nonadiabatic excited-state processes and their spectroscopic detection in real time. *Advances in Chemical Physics*, 100:1–169, 1997.

[51] M. Baer. Adiabatic and diabatic representations for atom–molecule collisions: Treatment of the reactive problem. *Chemical Physics*, 15:49–63, 1976.

[52] M. Baer. The born–oppenheimer approximation and beyond. *Chemical Physics Letters*, 35(1):112–118, 1975.

[53] C. A. Mead and D. G. Truhlar. On the determination of born–oppenheimer nuclear motion wave functions including complications due to conical intersections and identical nuclei. *The Journal of Chemical Physics*, 77(12):6090–6098, 1982.

[54] V. Sidis. Nonadiabatic transitions in molecular collisions. In *Advances in Chemical Physics*, volume 82, pages 73–194. John Wiley & Sons, 1992.

[55] T. Pacher, L. S. Cederbaum, and H. Köppel. Approximate treatment of multichannel vibronic dynamics: The model system formalism. In *Advances in Chemical Physics*, volume 84, pages 293–391. John Wiley & Sons, 1993.

[56] A. Thiel and H. Köppel. Multimode vibronic dynamics in the pyrazine molecule: A wave packet study. *The Journal of Chemical Physics*, 110(19):9371–9383, 1999.

[57] W. Lichten. Avoided crossings of molecular terms. *Physical Review*, 131(1):229–236, 1963.

[58] H. C. Longuet-Higgins. The intersection of potential energy surfaces in polyatomic molecules. *Proceedings of the Royal Society of London. Series A, Mathematical and Physical Sciences*, 344(1637):147–156, 1975.

[59] R. K. Preston and J. C. Tully. Molecular dynamics with electronic transitions. *The Journal of Chemical Physics*, 54(9):4297–4304, 1971.

[60] G. Hirsch, P. J. Bruna, R. J. Buenker, and S. D. Peyerimhoff. Ab initio study of the potential energy surfaces of low-lying electronic states of nh_2^+. *Chemical Physics*, 45:335–349, 1980.

[61] H.-J. Werner and W. Meyer. A quadratically convergent multiconfiguration-self-consistent field method with simultaneous optimization of orbitals and ci coefficients. *The Journal of Chemical Physics*, 74(9):5802–5807, 1981.

[62] H. Köppel, J. Gronki, and S. Mahapatra. Dynamics near conical intersections: Photoelectron spectra and wave packet calculations. *The Journal of Chemical Physics*, 115(5):2377–2388, 2001.

[63] Y. E. Perlin and M. Wagner, editors. *The Dynamical Jahn-Teller Effect in Localized Systems*. North-Holland, Amsterdam, 1984.

[64] E. B. Wilson Jr., J. C. Decius, and P. C. Cross. *Molecular Vibrations: The Theory of Infrared and Raman Vibrational Spectra*. McGraw-Hill, New York, 1955.

[65] H.-D. Meyer, U. Manthe, and L. S. Cederbaum. The multi-configurational time-dependent hartree approach. *Chem. Phys. Lett.*, 165(1):73–78, 1990.

[66] W. Domcke, H. Köppel, and L. S. Cederbaum. Spectroscopic effects of conical intersections of molecular potential energy surfaces. *Mol. Phys.*, 43(4):851–875, 1981.

[67] H. Köppel and W. Domcke. Conical intersections and nonadiabatic dynamics. In P. v. R. Schleyer, editor, *Encyclopedia of Computational Chemistry*, pages 3166–3192. Wiley, New York, 1998.

[68] E. J. Heller. Time-dependent approach to semiclassical dynamics. *The Journal of Chemical Physics*, 68(5):3891–3897, 1978.

[69] G. A. Worth, M. H. Beck, A. Jäckle, and H.-D. Meyer. The mctdh package, version 8.2, 2000. H.-D. Meyer, Version 8.3 (2002), Version 8.4 (2007). See http://mctdh.uni-hd.de.

[70] U. Manthe, H.□D. Meyer, and L. S. Cederbaum. Wave□packet dynamics within the multiconfiguration hartree framework: General aspects and application to nocl. *J. Chem. Phys.*, 97(5):3199–3213, 1992.

[71] Oriol Vendrell and Hans-Dieter Meyer. *J. Chem. Phys.*, 134(4):044135, 2011.

[72] Samrit Mainali, Fabien Gatti, Dmitri Iouchtchenko, Pierre-Nicholas Roy, and Hans-Dieter Meyer. *J. Chem. Phys.*, 154(17):174106, 2021.

[73] Haobin Wang and Michael Thoss. *J. Chem. Phys.*, 124(3):034114, 2006.

[74] Till Westermann, Ralf Brodbeck, Alexander B. Rozhenko, Wolfgang Schoeller, and Uwe Manthe. *J. Chem. Phys.*, 135(18):184102, 2011.

[75] Qingyong Meng and Hans-Dieter Meyer. *J. Chem. Phys.*, 138(1):014313, 2013.

[76] Jan Schulze, Mohamed F. Shibl, Mohammed J. Al-Marri, and Oliver Kühn. *J. Chem. Phys.*, 144(18):185101, 2016.

[77] Yu Xie, Jie Zheng, and Zhenggang Lan. *J. Chem. Phys.*, 142(8):084706, 2015.

[78] Jie Zheng, Yu Xie, Shengshi Jiang, and Zhenggang Lan. *J. Phys. Chem. C.*, 120(3):1375, 2016.

[79] Qingyong Meng and Hans-Dieter Meyer. *J. Chem. Phys.*, 146(18):184305, 2017.

[80] David Mendive-Tapia, Thiago Firmino, Hans-Dieter Meyer, and Fabien Gatti. *Chem. Phys.*, 482:113, 2017.

[81] David Mendive-Tapia, Etienne Mangaud, Thiago Firmino, Aurélien de la Lande, Michèle Desouter-Lecomte, Hans-Dieter Meyer, and Fabien Gatti. *J. Phys. Chem. B.*, 122(1):126, 2018.

[82] G. A. Worth, M. H. Beck, A. Jäckle, and H.-D. Meyer. The mctdh package, version 8.2, 2000. H.-D. Meyer, Version 8.3 (2002), Version 8.4 (2007); O. Vendrell and H.-D. Meyer, Version 8.5 (2011). See http://mctdh.uni-hd.de.

[83] M. Nsangou, M. L. Senent, and M. Hochlaf. Theoretical investigations of cyanogen anion. *Chem. Phys.*, 355:164–168, 2009.

[84] M. Winnewisser. Interstellare moleküle und mikrowellenspektroskopie i. *Chem. Unserer. Zeit.*, 18:1–16, 1984.

[85] H. W. Kroto. The spectra of interstellar molecules. *Int. Rev. Phys. Chem.*, 1(3):309–376, 1981.

[86] M. Bell, P. Feldman, and H. Matthews. Cyanopolyyne absorption in the direction of cassiopeia. *A. Astron. Astrophys.*, 101:13–16, 1981.

[87] Athena Coustenis, Bruno Bézard, Daniel Gautier, A. Marten, and Robert E. Samuelson. Titan's atmosphere from voyager infrared observations: Iii. vertical distributions of hydrocarbons and nitriles near titan's north pole. *Icarus*, 89:152–167, 1991.

[88] M. C. McCarthy, J.-U. Grabow, M. J. Travers, W. Chen, C. A. Gottlieb, and P. Thaddeus. Laboratory detection of the carbon chains HC[TINF]15[/TINF]n and HC[TINF]17[/TINF]n. *Astrophys. J.*, 494(2):L231–L234, feb 1998.

[89] L. M. Woodney, M. F. A'Hearn, and Schleicher. Morphology of hcn and cn in comet hale–bopp (1995 o1). *Icarus*, 157:193–204, 2002.

[90] Karen Magee-Sauer, Michael J. Mumma, Michael A. DiSanti, Neil Dello Russo, and Terrence W. Rettig. Infrared spectroscopy of the ν3 band of hydrogen cyanide in comet c/1995 o1 hale–bopp. *Icarus*, 142(2):498–508, 1999.

[91] Ewine F. van Dishoeck. Astrochemistry of dust, ice and gas: introduction and overview. *Faraday Discuss.*, 168:9–47, 2014.

[92] William Huggins. Preliminary note on the photographic spectrum of comet b 1881. *Procs. Roy. Soc.*, 33(216-219):1–3, 1882.

[93] R. L. Hudson and M. H. Moore. Reactions of nitriles in ices relevant to Titan, comets, and the interstellar medium: formation of cyanate ion, ketenimines, and isonitriles. *Icarus*, 172(2):466–478, dec 2004.

[94] C. K. Møller and B. P. Stoicheff. High resolution raman spectroscopy of gases: Iv. rotational raman spectrum of cyanogen. *Can. J. Phys.*, 32(10):635–638, 1954.

[95] Arthur G. Maki. High□resolution infrared spectra of cyanogen and cyanogen□15n2. *J. Chem. Phys.*, 43(9):3193–3199, 1965.

[96] Wagner B. De Almeida and Alan Hinchliffe. An ab initio study of the c2n2 molecule: Nccn, cnnc and cncn species. *J. Mol. Struct.*, 206(1):77–87, 1990.

[97] L. S. Cederbaum, W. Domcke, and W. Von Niessen. A theoretical photoelectron spectrum of cyanogen by a green-function method. *Chem. Phys.*, 10(2):459–470, 1975.

[98] L. S. Cederbaum, G. Hohlneicher, and W. Von Niessen. On the breakdown of the koopmans' theorem for nitrogen. *Chem. Phys. Lett.*, 18(4):503–508, 1973.

[99] Thom H. Dunning. Gaussian basis sets for use in correlated molecular calculations. i. the atoms boron through neon and hydrogen. *J. Chem. Phys.*, 90(2):1007–1023, 1989.

[100] J. F. Stanton, J. Gauss, L. Cheng, M. E. Harding, D. A. Matthews, and P. G. Szalay. CFOUR, Coupled-Cluster techniques for Computational Chemistry, a quantum-chemical program package. With contributions from A.A. Auer, R.J. Bartlett, U. Benedikt, C. Berger, D.E. Bernholdt, S. Blaschke, Y. J. Bomble, S. Burger, O. Christiansen, D. Datta, F. Engel, R. Faber, J. Greiner, M. Heckert, O. Heun, M. Hilgenberg, C. Huber, T.-C. Jagau, D. Jonsson, J. Jusélius, T. Kirsch, K. Klein, G.M. KopperW.J. Lauderdale, F. Lipparini, T. Metzroth, L.A. Mück, D.P. O'Neill, T. Nottoli, D.R. Price, E. Prochnow, C. Puzzarini, K. Ruud, F. Schiffmann, W. Schwalbach, C. Simmons, S. Stopkowicz, A. Tajti, J. Vázquez, F. Wang, J.D. Watts and the integral packages MOLECULE (J. Almlöf and P.R. Taylor), PROPS (P.R. Taylor), ABACUS (T. Helgaker, H.J. Aa. Jensen, P. Jørgensen, and J. Olsen), and ECP routines by A. V. Mitin and C. van Wüllen. For the current version, see http://www.cfour.de.

[101] Chr. Møller and M. S. Plesset. Note on an approximation treatment for many-electron systems. *Phys. Rev.*, 46:618–622, Oct 1934.

[102] M. J. Frisch, G. W. Trucks, H. B. Schlegel, G. E. Scuseria, M. A. Robb, J. R. Cheeseman, G. Scalmani, V. Barone, B. Mennucci, G. A. Petersson, H. Nakatsuji, M. Caricato, X. Li, H. P. Hratchian, A. F. Izmaylov, J. Bloino, G. Zheng, J. L. Sonnenberg, M. Hada, M. Ehara, K. Toyota, R. Fukuda, J. Hasegawa, M. Ishida, T. Nakajima, Y. Honda, O. Kitao, H. Nakai, T. Vreven, J. A. Montgomery, Jr., J. E. Peralta, F. Ogliaro, M. Bearpark, J. J. Heyd, E. Brothers, K. N. Kudin, V. N. Staroverov, R. Kobayashi, J. Normand, K. Raghavachari, A. Rendell, J. C. Burant, S. S. Iyengar, J. Tomasi, M. Cossi, N. Rega, J. M. Millam, M. Klene, J. E. Knox, J. B. Cross, V. Bakken, C. Adamo, J. Jaramillo, R. Gomperts, R. E. Stratmann, O. Yazyev, A. J. Austin, R. Cammi, C. Pomelli, J. W. Ochterski, R. L. Martin, K. Morokuma, V. G. Zakrzewski, G. A. Voth, P. Salvador, J. J. Dannenberg, S. Dapprich, A. D. Daniels, O. Farkas, J. B. Foresman, J. V. Ortiz, J. Cioslowski, and D. J. Fox. Gaussian 09 Revision E.01. Gaussian Inc. Wallingford CT 2009.

[103] Minh Tho Nguyen. Isocyanogen (ncnc) and diisocyanogen (cnnc): Structures and some spectroscopic properties. *Chem. Phys. Lett.*, 157(5):430–435, 1989.

[104] Y. H. Ding, X. R. Huang, Z. S. Li, and C. C. Sun. Theoretical study on potential-energy surface of c2n2. *J. Chem. Phys.*, 108(5):2024–2027, 1998.

[105] E. B. Wilson, J. C. Decius, P. C. Cross, and Benson R. Sundheim. Molecular vibrations: The theory of infrared and raman vibrational spectra. *J. Electrochem. Soc.*, 102(9):235C, 1955.

[106] Llewellyn H. Jones. Force field of cyanogen from vibrational spectra of isotopic species. *J. Mol. Spectrosc.*, 49(1):82–90, 1974.

[107] G.J. Cartwright, D. O'Hare, A.D. Walsh, and P.A. Warsop. The rotational and vibrational structure of the 2500Å system of cyanogen. *J. Mol. Spectrosc*, 39(3):393–399, 1971.

[108] S. Rajagopala Reddy, Arpita Ghosh, and S. Mahapatra. Electronic spectroscopy of carbon chains (c2n+1, n = 7–10) of astrophysical importance. i. quantum chemistry. *J. Chem. Phys.*, 151(5):054303, 2019.

[109] Cornelius Lanczos. An iteration method for the solution of the eigenvalue problem of linear differential and integral operators. *J. Res. Natl. Bur. Stand. B*, 45:255–282, 1950.

[110] J. Cullum and R.A. Willoughby. *Lanczos Algorithms for Large Symmetric Eigenvalue Problems*, volume I and II. SIAM, 1985.

[111] Paul von Ragué Schleyer, Peter R Schreiner, Schaefer III, et al. *Encyclopedia of Computational Chemistry*. John Wiley and sons, 1998.

[112] Wolfram Research Inc. Mathematica Version 8.0. Champaign, Illinois, 2010.

[113] Hans-Dieter Meyer, Frédéric Le Quéré, Céline Léonard, and Fabien Gatti. Calculation and selective population of vibrational levels with the multiconfiguration time-dependent hartree (mctdh) algorithm. *Chem. Phys.*, 329(1):179–192, 2006.

[114] Loïc Joubert Doriol, Fabien Gatti, Christophe Iung, and Hans-Dieter Meyer. Computation of vibrational energy levels and eigenstates of fluoroform using the multiconfiguration time-dependent hartree method. *J. Chem. Phys.*, 129(22):224109, 2008.

[115] GA Worth, MH Beck, Andreas Jäckle, and Hans-Dieter Meyer. The mctdh package, version 8.4 (2007). *The MCTDH Package, Version 8.4 (2007)*, 2019.

[116] E. B. Jochnowitz and J. P. Maier. *Mol. Phys.*, 106:2093, 2008.

[117] J. H. Kiefer, S. S. Sidhu, R. D. Kern, K. Xie, H. Chen, and L. B. Harding. *Combust. Sci. Technol.*, 82:101, 1992.

[118] T. Pino, M. Tulej, G. Güthe, M. Pachkov, and J. P. Maier. *J. Chem. Phys.*, 116:6126, 2002.

[119] E. Herbst and Y. Osamura. *Astrophys. J.*, 679:1670, 2008.

[120] E. Garand, T. I. Yacovitch, J. Zhou, S. M. Sheehan, and D. M. Neumark. *Chem. Sci.*, 1:192, 2010.

[121] J. Zhou, E. Garand, and D. M. Neumark. *J. Chem. Phys.*, 127:114313, 2007.

[122] K. M. Ervin and W. C. Lineberger. *J. Phys. Chem.*, 95:1167, 1991.

[123] R. Tarroni and S. Carter. *J. Chem. Phys.*, 119:12878, 2003.

[124] D. E. Woon. *Chem. Phys. Lett.*, 244:45, 1995.

[125] M. Perić, B. Engels, and S. D. Peyerimhoff. *J. Mol. Spectrosc.*, 150:56, 1991.

[126] S. Graf, J. Geiss, and S. Leutwyler. *J. Chem. Phys.*, 114:4542, 2001.

[127] Peter Botschwina and Rainer Oswald. Coupled cluster calculations for (potential) interstellar anions: The c2nh(-) series (n=2–6). *International Journal of Mass Spectrometry*, 277(1):180–188, 2008. Electron-induced atomic and molecular processes: A special issue honoring Eugen Illenberger on his 65th birthday.

[128] Jia Zhou, Etienne Garand, and Daniel M. Neumark. *The Journal of Chemical Physics*, 127(15):154320, 10 2007.

[129] Jr. Dunning, Thom H. Gaussian basis sets for use in correlated molecular calculations. I. The atoms boron through neon and hydrogen. *The Journal of Chemical Physics*, 90(2):1007–1023, 01 1989.

[130] Hans-Dieter Meyer and Graham Worth. *Theor. Chem. Acc.*, 109:251, 06 2003.

[131] H.-D. Meyer, F. Gatti, and G. A. Worth. Wiley-VCH, Weinheim, 2009.

[132] B. A. McGuire, A. M. Burkhardt, S. Kalenskii, C. N. Shingledecker, A. J. Remijan, E. Herbst, and M. C. McCarthy. *Sci.*, 359:202, 2018.

[133] Sung Yong Byeon, Kyung Hyung Lee, and Jun Yeob Lee. *J. Mater. Chem. C*, 8:5832, 2020.

[134] A. R. Dixon, K. Dmitry, and S. Andrei. *J. Chem. Phys.*, 143:134306, 2015.

[135] R. Yamamoto, S. Ishikawa, T. Ebata., and N. Mikami. *J. Raman. Spectrosc.*, 31:295, 2000.

[136] Y. Dimitrova. *J. Mol. Struc.*, 39:241, 1997.

[137] B. N. Rajasekhar, V. Dharmarpu, A. K. Das, A. Shastri, A. Veeraiah, and S. Krishnakumar. *J. Quant. Spec. & Rad. Trans.*, 283:108159, 2022.

[138] T. Kobayashi and S. Nagakura. *Bul. Chem. Soc. Japan*, 47:2563, 1974.

[139] Jr. Dunning, Thom H. *J. Chem. Phys.*, 90(2):1007–1023, 01 1989.

[140] L. S. Cederbaum and W. Domcke. John Wiley & Sons, Ltd, 1977.

[141] G. Fischer. *Vibronic Coupling*. Academic Press, London., 1984.

[142] Hiroki Nakamura and Donald G. Truhlar. *J. Chem. Phys.*, 115(22):10353–10372, 2001.

[143] Hiroki Nakamura and Donald G. Truhlar. *J. Chem. Phys.*, 117(12):5576–5593, 2002.

[144] Hiroki Nakamura and Donald G. Truhlar. *J. Chem. Phys.*, 118(15):6816–6829, 2003.

[145] Kuan Yin Yang, Xiao Xu, Jingjing Zheng, and Donald G. Truhlar. *Chem. Sci.*, 5:4661–4680, 2014.

[146] Yong-Shi Shu, Zoltán Varga, Suttipong Kanchanakungwankul, Ling Zhang, and Donald G. Truhlar. *J. Phys. Chem. A*, 126(5):992–1018, 2022.

[147] Alexander A. Granovsky. *J. Chem. Phys.*, 134(21):214113, 2011.

[148] D. W. Marquardt. *J. Appl. Math.*, 11:431, 1963.

[149] The MathWorks Inc. Matlab optimization toolbox, version 9.13.0 (r2020a), 2020.

[150] Harald Köppel, Lorenz S. Cederbaum, and Wolfgang Domcke. *Chem. Phys.*, 69:175–183, 1982.

[151] Banafsheh Nikoobakht and Harald Köppel. *Mol. Phys.*, 119(21):e1958019, 2021.

[152] Banafsheh Nikoobakht and Harald Köppel. *Phys. Chem. Chem. Phys.*, 24:12433–12441, 2022.

[153] Michael W. Schmidt, Kim K. Baldridge, Jerry A. Boatz, Stephen T. Elbert, Mark S. Gordon, Jan H. Jensen, Shiro Koseki, Nikita Matsunaga, Kiet A. Nguyen, Shujun Su, Theresa L. Windus, Michel Dupuis, and John A. Montgomery Jr. *J. Comput. Chem.*, 14(11):1347–1363, 1993.

[154] Isaac B. Bersuker. *Chem. Rev.*, 113(3):1351–1390, 2013.

Publications

1. **Rani, M.**, Arun Kumar, K., & Susanta, M. Photoionization Bands of Cyanogen: Multi-Mode Vibronic Coupling and Renner-Teller Effects. *ChemPhysChem*, 24, e202200882 (1-14), (2023).

2. Ajay, K., **Rani, M.**, & Susanta, M. Vibronic Coupling in Formamide Radical Cation: A Full-dimensional Approach. *Journal of Computational Chemistry*, 1–6 (2025).

3. Mohammad, A., **Rani, M.**, & Susanta, M. Laser driven S-CH3 Photodissociation Dynamics of Thioanisole on a New Potential Energy Surface. *Journal of Chemical Sciences*, (2025). *(accepted)*

4. Nagarajan, S., Srivastava, A., Ishtiyak, M., **Rani, M.**, & Pal, S. Cycloruthenates(iii) with CNO Pincer-like Ligands: Regioselective Metallation of N -(4-R -Benzoyl)-N -(2-Naphthylidene)Hydrazines. *Journal of Organometallic Chemistry*, 975, 1 (2022).

5. **Rani, M.**, & Susanta, M. Full-Dimensional Investigation of the Photoionization Spectrum of Cyanobenzene. *(Soon to be submitted)*

6. **Rani, M.**, & Susanta, M. Vibronic Coupling and Renner-Teller Effects on Linear Carbon Chains, $C_{2n}H^-$ ($n = 1 - 4$). *(Soon to be submitted)*

Conferences attended

1. Poster presentation in ‘DAE Symposium on Current Trends in Theoretical Chemistry (CTTC-2020)’ Sep 2021, BARC, Mumbai, India.
2. Poster presentation in ‘17th Theoretical Chemistry Symposium (TCS-2021)’, Dec 2021, IISER Kolkata, India.
3. Oral presentation in ‘20th Annual In-House Symposium CHEMFEST-2023.’
4. Poster presentation in ‘Quantum System in Chemistry, Physics, and Biology (QSCP-XXVI)’, Oct 2023, Ashoka University, India.
5. Attended workshop, ‘MCTDH Summer School July-2023’, Heidelberg, Germany.

Renner-Teller effects and Vibronic Coupling: Full-dimensional Nonadiabatic Dynamics of Linear carbon chains and Cyanobenzene

by MAMILWAR RANI

Submission date: 13-Oct-2025 12:48PM (UTC+0530)
Submission ID: 2779685521
File name: MAMILWAR_RANI.pdf (4.08M)
Word count: 51150
Character count: 202481

Renner-Teller effects and Vibronic Coupling: Full-dimensional Nonadiabatic Dynamics of Linear carbon chains and Cyanobenzene

ORIGINALITY REPORT

23%	9%	22%	5%
SIMILARITY INDEX	INTERNET SOURCES	PUBLICATIONS	STUDENT PAPERS

PRIMARY SOURCES

1	Mamilwar Rani, Arun Kumar Kanakati, Susanta Mahapatra. "Photoionization Bands of Cyanogen: Multi-Mode Vibronic Coupling and Renner-Teller Effects", ChemPhysChem, 2023 Publication	15%
2	chemistry.uohyd.ac.in Internet Source	2%
3	Submitted to University of Hyderabad, Hyderabad Student Paper	2%
4	Samala Nagaprasad Reddy, S. Mahapatra. "Theoretical Study on Molecules of Interstellar Interest. I. Radical Cation of Noncompact Polycyclic Aromatic Hydrocarbons", The Journal of Physical Chemistry A, 2013 Publication	1%
5	Vadala Jhansi Rani, Arun Kumar Kanakati, S. Mahapatra. "Multi-state and Multi-mode Vibronic Coupling Effects in the Photoionization Spectroscopy of Acetaldehyde", The Journal of Physical Chemistry A, 2022 Publication	<1%
6	Haobin Wang. "Multilayer Multiconfiguration Time-Dependent Hartree Theory", The Journal	<1%

Susanta Mahapatra
Senior Professor
School of Chemistry
University of Hyderabad
Hyderabad-500046, TS, India.

of Physical Chemistry A, 2015
Publication

7	Rudraditya Sarkar, S. Mahapatra. " Theoretical study of photodetachment spectroscopy of hydrogenated boron cluster anion H B7− and its deuterated isotopomer ", The Journal of Chemical Physics, 2017 Publication	<1 %
8	Arun Kumar Kanakati, S. Mahapatra. "Vibronic coupling in the first six electronic states of pentafluorobenzene radical cation: Radiative emission and nonradiative decay", The Journal of Chemical Physics, 2021 Publication	<1 %
9	fdocument.org Internet Source	<1 %
10	S. Rajagopala Reddy, Arpita Ghosh, S. Mahapatra. " Electronic spectroscopy of carbon chains (C , = 7–10) of astrophysical importance. I. Quantum chemistry ", The Journal of Chemical Physics, 2019 Publication	<1 %
11	Samala Nagaprasad Reddy, S. Mahapatra. "Theoretical Study on Molecules of Interstellar Interest. II. Radical Cation of Compact Polycyclic Aromatic Hydrocarbons", The Journal of Physical Chemistry B, 2015 Publication	<1 %
12	T. Mondal, A. J. C. Varandas. "Quadratic coupling treatment of the Jahn-Teller effect in the triply-degenerate electronic state of CH4+: Can one account for floppiness?", The Journal of Chemical Physics, 2012 Publication	<1 %

13	Karunamoy Rajak, Arpita Ghosh, S. Mahapatra. "Vibronic Coupling in the First Five Electronic States of Dicyanodiacetylene Radical Cation", The Journal of Physical Chemistry A, 2018 Publication	<1 %
14	Samrit Mainali, Fabien Gatti, Dmitri Iouchtchenko, Pierre-Nicholas Roy, Hans-Dieter Meyer. "Comparison of the multi-layer multi-configuration time-dependent Hartree (ML-MCTDH) method and the density matrix renormalization group (DMRG) for ground state properties of linear rotor chains", The Journal of Chemical Physics, 2021 Publication	<1 %
15	Arpita Ghosh, Karunamoy Rajak, Arun Kumar Kanakati, S. Mahapatra. "Renner-Teller and pseudo-Renner-Teller interactions in the electronic ground and excited states of the dicyanoacetylene radical cation: Assignment of vibronic spectrum and elucidation of nonradiative and radiative decay mechanisms", Computational and Theoretical Chemistry, 2019 Publication	<1 %
16	Rudraditya Sarkar, Susanta Mahapatra. " Vibronic coupling in the first four electronic states of CH F ", Molecular Physics, 2015 Publication	<1 %
17	V. Sivaranjana Reddy. "Vibronic interactions in the photodetachment spectroscopy of phenide anion", The Journal of Chemical Physics, 2007 Publication	<1 %

18	Susanta Ghanta. "Photophysics and photostability of pyrimidine molecule and its radical cation: a theoretical study", Molecular Physics, 2016 Publication	<1 %
19	"Multidimensional Quantum Dynamics", Wiley, 2009 Publication	<1 %
20	Arun Kumar Kanakati, Vadala Jhansi Rani, Susanta Mahapatra. "The Jahn-Teller and pseudo-Jahn-Teller effects in propyne radical cation", Physical Chemistry Chemical Physics, 2022 Publication	<1 %
21	T. Mondal, S. Rajagopala Reddy, S. Mahapatra. "Photophysics of fluorinated benzene. III. Hexafluorobenzene", The Journal of Chemical Physics, 2012 Publication	<1 %
22	T. Mondal, S. Mahapatra. "Photophysics of fluorinated benzene. II. Quantum dynamics", The Journal of Chemical Physics, 2010 Publication	<1 %
23	Susanta Mahapatra. "Structure and dynamics of electronically excited molecular systems", WIREs Computational Molecular Science, 2021 Publication	<1 %
24	T. Mondal, S. Mahapatra. "Complex Dynamics at Conical Intersections: Vibronic Spectra and Ultrafast Decay of Electronically Excited Trifluoroacetonitrile Radical Cation", The Journal of Physical Chemistry A, 2008 Publication	<1 %

25	V. Sivaranjana Reddy, S. Mahapatra. "Electronic nonadiabatic interactions and ultrafast internal conversion in phenylacetylene radical cation", The Journal of Chemical Physics, 2009 Publication	<1 %
26	Daniel M. Neumark. " Slow Electron Velocity-Map Imaging of Negative Ions: Applications to Spectroscopy and Dynamics ", The Journal of Physical Chemistry A, 2008 Publication	<1 %
27	"The Jahn-Teller Effect", Springer Science and Business Media LLC, 2009 Publication	<1 %
28	www.x-mol.com Internet Source	<1 %
29	"Advances in Chemical Physics", Wiley, 1984 Publication	<1 %
30	S. Rajagopala Reddy, S. Mahapatra. "Theoretical study of photodetachment processes of anionic boron clusters. II. Dynamics", The Journal of Chemical Physics, 2012 Publication	<1 %
31	Karunamoy Rajak, Arpita Ghosh, Susanta Mahapatra. "Vibronic Coupling in the First Five Electronic States of Dicyanodiacetylene Radical Cation", The Journal of Physical Chemistry A, 2018 Publication	<1 %
32	V. Sivaranjana Reddy, Samala Nagaprasad Reddy, S. Mahapatra. "Ultrafast dynamics of electronically excited diborane radical cation", Theoretical Chemistry Accounts, 2015	<1 %

Publication

33	Wu, Ming, and Trevor J. Sears. "STUDIES OF THE RENNER–TELLER EFFECT IN NCO BY SEP SPECTROSCOPY", Advanced Series in Physical Chemistry, 1995. Publication	<1 %
34	Arun Kumar Kanakati, Vadala Jhansi Rani, Rudraditya Sarkar, Susanta Mahapatra. "Elucidation of vibronic structure and dynamics of first eight excited electronic states of pentafluorobenzene", The Journal of Chemical Physics, 2022 Publication	<1 %
35	idr.l2.nitk.ac.in Internet Source	<1 %
36	T. S. Venkatesan, S. Mahapatra. "Exploring the Jahn-Teller and pseudo-Jahn-Teller conical intersections in the ethane radical cation", The Journal of Chemical Physics, 2005 Publication	<1 %
37	Susanta Mahapatra, Gireesh M. Krishnan. "Photoelectron spectroscopy of chlorine dioxide and its negative ion: A quantum dynamical study", The Journal of Chemical Physics, 2001 Publication	<1 %
38	ijfcs.ut.ac.ir Internet Source	<1 %
39	pubs.rsc.org Internet Source	<1 %
40	Thoss, M.. "Quantum dynamical simulation of ultrafast molecular processes in the condensed phase", Chemical Physics, 20060306	<1 %

Publication

41	digital.lib.washington.edu Internet Source	<1 %
42	Rudraditya Sarkar, S. Mahapatra. " Vibronic Dynamics of Electronic Ground State of CH F and Its Deuterated Isotopomer ", The Journal of Physical Chemistry A, 2016 Publication	<1 %
43	hdl.handle.net Internet Source	<1 %
44	nzdr.ru Internet Source	<1 %
45	Rudraditya Sarkar, S. Rajagopala Reddy, S. Mahapatra, H. Köppel. " On the Jahn–Teller effect in the electronic ground state of CH 3 F + ", Chemical Physics, 2017 Publication	<1 %
46	arxiv.org Internet Source	<1 %
47	discovery.researcher.life Internet Source	<1 %
48	Applications of Topological Methods in Molecular Chemistry, 2016. Publication	<1 %
49	ia803001.us.archive.org Internet Source	<1 %
50	Roberto Improta, Fabrizio Santoro, Lluís Blancafort. "Quantum Mechanical Studies on the Photophysics and the Photochemistry of Nucleic Acids and Nucleobases", Chemical Reviews, 2016 Publication	<1 %
	Submitted to University of Birmingham	

51	Student Paper	<1 %
52	Arpita Ghosh, S. Rajagopala Reddy, Susanta Mahapatra. " Electronic spectroscopy of carbon chains (C , = 7–10) of astrophysical importance. II. Quantum dynamics ", The Journal of Chemical Physics, 2019 Publication	<1 %
53	T. S. Venkatesan, S. Mahapatra, L. S. Cederbaum, H. Köppel. " Theoretical Investigation of Jahn−Teller Dynamics in the E‘ Electronic Ground State of the Cyclopropane Radical Cation ", The Journal of Physical Chemistry A, 2004 Publication	<1 %
54	assets.researchsquare.com Internet Source	<1 %
55	Arpita Ghosh, Samala Nagaprasad Reddy, S. Rajagopala Reddy, S. Mahapatra. " Vibronic Coupling in the X̃ Π –Ã Π Band System of Diacetylene Radical Cation ", The Journal of Physical Chemistry A, 2016 Publication	<1 %
56	Atkins, Peter, de Paula, Julio, Friedman, Ronald. "Physical Chemistry", Physical Chemistry, 2017 Publication	<1 %
57	U. Priyanka, Aishwarya Paul, T. Mondal. "Vibronic coupling and ultrafast relaxation dynamics in the first five excited singlet electronic states of bithiophene", The Journal of Chemical Physics, 2024 Publication	<1 %

58 Vincent Pohl, Jean Christophe Tremblay. "Adiabatic electronic flux density: A Born-Oppenheimer broken-symmetry ansatz", Physical Review A, 2016 <1%
Publication

Exclude quotes	On	Exclude matches	< 14 words
Exclude bibliography	On		